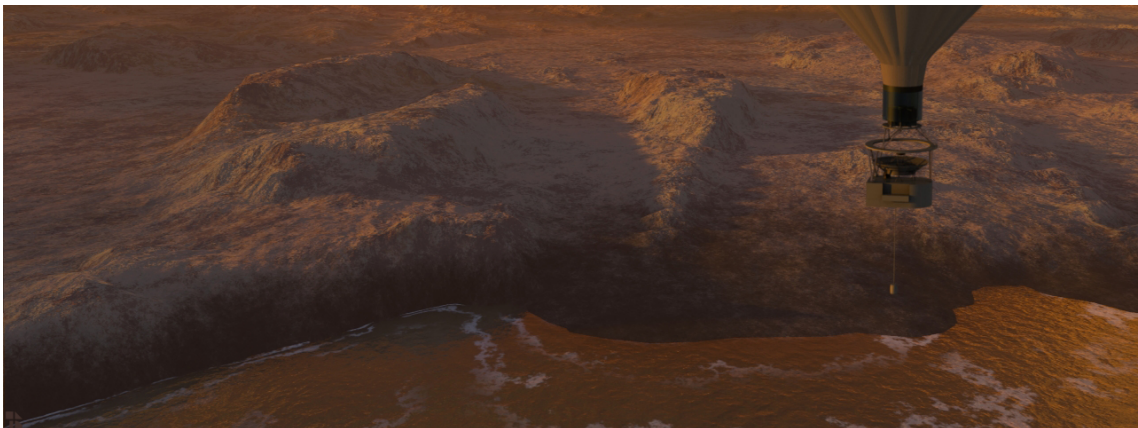

Gravitational signature of Titan's (sub) surface lakes

Discovering the composition of the lakes using a MEMS micro
gradiometer mounted on a balloon

R. M. C. Spiteri
1045458

September 22, 2008



[Courtesy: NASA]

DELFT UNIVERSITY OF TECHNOLOGY
FACULTY OF AEROSPACE ENGINEERING

This research was carried out at the research group:

Astrodynamics & Satellite Systems
Department of Earth Observation and Space Systems
Faculty of Aerospace Engineering
Delft University of Technology
Kluyverweg 1, 2629 HS Delft
The Netherlands

Printed in The Netherlands
Copyright 2008 © by R. M. C. Spiteri

This document was typeset with $\text{\LaTeX} 2_{\epsilon}$.

Gravitational signature of Titan's (sub) surface lakes

Discovering the composition of the lakes using a MEMS micro
gradiometer mounted on a balloon

R. M. C. Spiteri
1045458



Dr. L. L. A. Vermeersen
DELFT UNIVERSITY OF TECHNOLOGY



Dr. J. M. Smit
STICHTING RUIMTEVAART ONDERZOEK NEDERLAND

This page is intentionally left blank

Preface

This report is the final report of the thesis work of Lindy Spiteri, student at the faculty of Aerospace Engineering, Delft University of Technology. To graduate for the master Space Engineering, profile space mission design, research was done to see if a MEMS micro-gradiometer can detect lakes on the surface of Saturn's moon Titan and extract density information from the gravity measurements made from these lakes.

Readers only interested in the different aspects of the research done are referred to chapter 2 for information about Titan, chapter 3 on gradiometry and chapter 4 for the theoretical background on the gravity field. The models used is described in chapter 5 and the analysis done in chapter 6. Readers only interested in the beautiful figures I created are referred to appendices E and F.

First of all I want to thank my supervisors, Bert Vermeersen of Delft University of Technology and Martijn Smit of SRON. Next to that I want to thank professor Klees for all the fruitful meetings to enlarge my understanding of the gravitational potential and a special thanks goes to my fellow students in rooms 9.06 and 9.03, especially Elja, for their enthusiasm, help and nice lunches. Finally I would like to thank my roommate Kevin and my boyfriend Joost for their support throughout the year.

Enjoy reading!

Delft, **September 22, 2008**
Lindy Spiteri



Contents

Preface	ii
Summary	ix
List of symbols	xiii
List of abbreviations	xv
List of figures	xvii
List of tables	xix
1 Introduction	1
2 Titan	3
2.1 The Saturnian system	3
2.1.1 Saturn η	3
2.1.2 In orbit around Saturn	3
2.2 Observing Titan: missions to the moon of Saturn	5
2.2.1 Voyager	6
2.2.2 Cassini–Huygens mission	6
2.2.3 Cassini Equinox Mission	10
2.2.4 Future missions	11
2.3 The interior of Titan	15
2.3.1 Planet formation	16
2.3.2 The interior structure of Titan	17
2.4 The surface of Titan	20
2.4.1 The Huygens landing site	20
2.4.2 Imaging by the Cassini orbiter	21
2.5 The atmosphere	23
2.5.1 The atmospheric profile	23
2.5.2 Molecular composition	24
2.5.3 Titan’s (organic) haze	24
2.5.4 Titan’s methane cycle	25
2.5.5 Clouds	28
2.5.6 Winds	29
	iii

3	Gradiometry	31
3.1	Gravimetry from space	31
3.1.1	Measuring the gravity field	31
3.1.2	Gravimetric missions	34
3.2	Balloon–borne gravimetry	36
3.3	Theoretical background on gradiometry	36
3.3.1	Theoretical background on gradiometric measurements in general	37
3.3.2	Observation equations for SGG	38
3.4	The specifications of gradiometers	40
3.4.1	The performance of a gradiometer	40
3.4.2	GOCE gradiometer	42
3.4.3	MEMS–technology used for miniaturize instruments	42
4	The gravity field of a planet	47
4.1	Gravitational potential	47
4.1.1	Hydrostatic and isostatic equilibrium	48
4.1.2	Moment of inertia of a planet	51
4.1.3	Spherical harmonic representation of the gravitational potential	52
4.1.4	Alternative representations of gravitational fields	55
4.2	Gravity gradients	58
4.2.1	Gravity gradients of point mass	58
4.2.2	Gravity gradients of the single layer method	59
4.2.3	Gravity gradients of the point mass method	60
4.3	Tidal potential	61
4.3.1	Background theory on the tidal potential	61
4.3.2	Tidal Love numbers	62
4.3.3	Induced tidal potential	63
4.3.4	Tidal dissipation	63
4.4	Tidal parameters of Titan	65
5	Modeling the gravity field of the lakes on the surface of Titan	75
5.1	Modeling the gravity field	75
5.1.1	Modeling the gravity field of Titan	75
5.1.2	Modeling the lakes as a single mass layer	76
5.2	Initial conditions: reference system and source points	78
5.2.1	Reference coordinate system	78
5.2.2	Selecting and discretizing the lakes from the northern hemisphere	81
5.3	The tidal potential at the surface of Titan	81
5.3.1	The tidal potential at the surface of Titan	81
5.3.2	The time–varying part of the tidal potential	83
6	Analysis of the gradients measured in the vicinity of lakes on Titan	85
6.1	Gravitational potential and gravity gradients of the lake area	85
6.1.1	Gravitational potential of the lakes	85
6.1.2	Gravity gradients of the lakes	88
6.2	Simulation of a passive balloon in the atmosphere of Titan	88

6.3	Gradients measured at different altitudes throughout the atmosphere of Titan . . .	90
6.3.1	Gradients measured at different balloon altitudes	93
6.3.2	Fluctuation in the gradients of Titan	95
6.4	Combining the gradients of multiple lakes	95
6.5	Gradients along different trajectories of the balloon	96
6.5.1	The trajectories plotted in 2D	98
6.5.2	The trajectories plotted in 3D	100
6.6	Influence of different lake densities	101
6.7	Gradients due to subsurface lakes	102
6.8	Determining the lake density using the least-squares method	104
6.8.1	Theoretical background on the least-squares method	104
6.8.2	The least-squares method applied to the system of gradient equations . . .	105
6.8.3	Variance of the computed lake density for different observation sets	106
7	Discussion	111
7.1	Conclusions	111
7.2	Recommendations	113
A	Definitions	121
B	Properties of methane and ethane	125
C	Legendre polynomials	127
D	Tidal parameters of Titan	129
E	Time-dependent part of the tide-raising potential	135
F	Miscellaneous figures belonging to chapter 6	141
G	Computed layer density of the lakes and variance of the observations	161

Summary

Titan, the largest moon of Saturn, has a significant atmosphere in which it hosts a methane cycle in resemblance to the Earth's hydrological cycle, including clouds, rain and surface lakes. One of the key questions within the science community today is what the origin is of the methane on Titan. Methane is one of the chemicals produced by life forms. Is some kind of bacteria active on Titan? Was it incorporated in the interior at the time of formation or is it formed and stored in the interior? One way to learn more about the interior of a celestial body is by doing gravity measurements, using a so-called gravity gradiometer.

The Titan and the Saturn System Mission is a joint venture between ESA and NASA (TBC), a combination from studies for Cosmic Vision 2015–2025 and Outer Planet Flagship Mission. As part of *in situ* investigation components a hot-air balloon will be released in the atmosphere of Titan. One of the instruments on board of the gondola of the hot-air balloon will be a micro-gradiometer, as initially proposed by SRON, the Netherlands Institute for Space Research, since the conventional gradiometers are far too bulky and heavy to send on a planetary mission.

Pictures taken by instruments on board of the Cassini spacecraft prove that lakes are present at the polar regions of Titan. The composition of these lakes is still unknown, though it is believed that these lakes consist of a hydrocarbon mixture. With the area of the lakes known, gradiometer measurements could resolve for the density of these lakes. It is the aim of this research if a MEMS micro-gradiometer on board of a hot air balloon floating in the atmosphere of Titan can detect (sub-)surface lakes. Can then the density of the lakes be resolved from the gradients? With what accuracy can the gradiometer resolve for the density of the lakes?

A basic model of the gravity gradients of Titan is created using MATLAB. One of the problems that was encountered creating such a model is that not much information on the global gravitational field of Titan is available. The classic approach using a spherical harmonic representation is not possible, as there is not enough data yet. Therefore the mass layer method, which assumes the gravitational potential of lakes can be represented by a single mass layer on the surface of Titan, is used to model two lakes. The lakes are selected from a Cassini image of the northern polar region.

Different simulations are done in order to see what the effect is of balloon altitude, of different trajectories along which measurements can be done, of different densities of the lakes, in order to see how the lake density influences the gravity gradients, and of the location of the lakes with respect to the surface of Titan. When changing one of these parameters, the influence can directly be noted in the gradients simulated. The strength of the gravity gradients decreases with altitude and it is shown that the measurements at higher altitudes are not sufficiently accurate. The same holds for sub-surface lakes: the further the lake is located beneath the surface of Titan, the weaker

the gradients.

The gradients that are measured along the axis of the chosen reference system (the diagonal gradients) give a larger difference in magnitude than the off-diagonal gradients, and thus are better measurable. The least-squares method is used to compute the lake density from the observations simulated. The accuracy of the computed density is the same for computations using only the diagonal gradients of the gravity tensor as for computations using the complete gravity tensor. Concluding, the diagonal gradients give the larger part of the information and it is therefore very important to emphasize the sensitivity of the part of the gradiometer that will measure the diagonal gradients.

The models used in this research are very basic models. The models show that a gradiometer can give a lot of information on the lakes on Titan. Due to its high sensitivity many small surface features can be distinguished and in combination with visual data it can be powerful tool to determine the interior structure locally.

List of symbols

Constants		
AU	Astronomical unit	149.60×10^6 km
c	Speed of light	3×10^5 km/s
G	Gravitational constant	6.673×10^{-11} m ³ /kg s ²
k_B	Boltzmann constant	$1.3806504 \times 10^{-23}$ J/K

Symbol		Unit
a	Semi-major axis	[km]
\mathbf{a}	Acceleration	[m/s ²]
A	Design matrix (LS-technique)	
b	Baseline	[m]
c	Damping factor	
C	Covariance matrix (LS-technique)	
\bar{C}_{nm}	Normalized spherical harmonic coefficients	
d	Distance	[m]
e	Eccentricity	
$\frac{dE}{dt}$	Energy dissipation	
f_{ice}	Ice mass fraction	
$f_{silicate}$	Silicate mass fraction	
\mathbf{F}	Force	[N]
\mathbf{g}	Gravitational force	[N]
g_B	Bouger gravity anomaly	
g_p	Gravitational acceleration	[m/s ²]
$g_p(obs)$	Observed gravity	[m/s ²]
g_0	Unperturbed surface gravity of a celestial body	[m/s ²]
\mathbf{G}	Tidal force	[N]
GM	Planetocentric constant	[km ³ /s ²]
h	Height	[m]
h_2	Displacement Love number	
i	Inclination	[°]
I_p	Moment of inertia	
J_n	Gravitational moments	

Continued on the next page

CONTENTS

Symbol		Unit
k	Spring constant	[N/m]
k_f	Fluid Love number	
k_2	Secular Love number	
k_2^a	Atmospheric Love number	
k_2^l	Load Love number	
k_2^s	Solid body Love number	
L_m	Mean longitude	[°]
m	Mass	[kg]
M	Mass of a planet or moon	[kg]
M	Mean anomaly	[°]
n	Mean orbital motion	[/s]
N	Noise current or voltage	
p	Pressure	[Pa]
p_c	Pressure in the centre of a planet	[Pa]
\tilde{p}_{S_2}	Amplitude of the two-degree atmospheric tide	
$P_n(\cos \vartheta)$	Legendre polynomials	
\tilde{P}_{nm}	Fully normalized Legendre functions	
q_r	Harmonic coefficient	
q_t	Tidal parameter	
Q	Quality factor	
Q_{tidal}	Effective tidal dissipation factor	
r	Radial distance	[m]
\mathbf{R}	Rotation Matrix	
R	Radius	[m]
R_c	Radius of the core of a celestial body	[km]
R_e	Equatorial radius of a celestial body	[km]
R_p	Polar radius of a celestial body	[km]
$\ddot{\mathbf{R}}$	Acceleration	[m/s ²]
S	Surface	[m ²]
$S_{detected}$	Signal current or voltage	
\tilde{S}_{nm}	Normalized spherical harmonic coefficients	
S_Γ	Power Spectral Density	[E/√Hz]
t	Time	[s]
T	Temperature	[K]
v	Velocity	[m/s]
V	Total perturbing potential	[m ² /s ²]
V_g	Gravitational potential	[m ² /s ²]
V_p	Periodic part of the total perturbing potential	[m ² /s ²]
V_r	Rotational potential	[m ² /s ²]
V_s	Static part of the total perturbing potential	[m ² /s ²]

Continued on the next page

Symbol		Unit
$V_t = V_{tidal}$	tidal potential	$[m^2/s^2]$
$V_{t,i} = V_{tidal,induced}$	Induced tidal potential	$[m^2/s^2]$
\mathbf{x}	Measurement point	
\mathbf{x}	Parameter vector (LS–technique)	
y	Doppler radio signal	
\mathbf{y}	Observation vector (LS–technique)	
\mathbf{y}	Source point	
δg_T	Terrain correction factor	
Δg_B	Bouger correction	
Δg_{FAA}	Free air correction	
Δh_g	Geoid height anomaly	[m]
Δp	Increase pressure	[Pa]
Δv	Relative velocity	[m/s]
Δz	Increase in height	[m]
α	Regularization parameter (LS–technique)	
α_e	Energy coupling coefficient of the mechanical to electrical conversion	
$\mathbf{\Gamma}$	Gravity tensor	[E]
Γ_{ij}	Gradiometer measurement	
Γ_n	Gravity gradient noise	$[E/\sqrt{Hz}]$
$\frac{\sigma(\Gamma)}{\Gamma}$	Measurement precision	
δ	Lag of the tidal bulge	[°]
ϵ	Sensor noise energy	
ϵ	Residual vector (LS–technique)	
$\zeta(e)$	Eccentricity dependent factor	
η	Obliquity	[°]
θ	Colatitude	[°]
λ	Longitude	[°]
Λ	Response coefficient	
$\Lambda_{2,0}$	Tidal response coefficient	
μ	Density	$[kg/m^2]$
μ_e	Elastic shear modulus	[Pa]
μ_{12}	Reduced mass	
ρ	Density	$[kg/m^3]$
$\bar{\rho}$	Mean density	$[kg/m^3]$
ρ_c	Density of the core	$[kg/m^3]$
ρ_C	Density of the crust	$[kg/m^3]$
ρ_{ice}	Ice density	$[kg/m^3]$
ρ_M	Density of the mantle	$[kg/m^3]$

Continued on the next page

CONTENTS

Symbol		Unit
ρ_{sil}	Silicate density	[kg/m ³]
σ	Standard deviation	
σ_R	surface of a sphere	[m ²]
τ	Investigation time	[s]
φ	Latitude	[°]
χ	Measure of the longitude of the node of the equator on the orbit with respect to the pericenter of the orbit	
ω	Argument of the perigee	[°]
ω_d	Mechanical self resonance factor	
ω_{rot}	Rotational period of a planet	[°/s]
Ω	Right ascension of the ascending node	[°]
Ω^2	Centrifugal acceleration	[m/s ²]
$\dot{\Omega}$	Angular acceleration	[m/s ²]
Subscripts		
m	Spherical harmonic order	
n	Spherical harmonic degree	
S	Saturn	
T	Titan	

List of abbreviations

ACP	Aerosol Collector and Pyrolyzer
ASI	Agenzia Spaziale Italiana
AU	Astronomical Unit
CAPS	Cassini Plasma Spectrometer
CCN	Cloud Condensation Nuclei
CDA	Cosmic Dust Analyzer
CHAMP	CHALLENGING Minisatellite Payload
CIRS	Composite Infrared Spectrometer
CoM	Center of Mass
DISR	Descent Imager/Spectral Radiometer
DWE	Doppler Wind Experiment
EJSM	Europa and the Jupiter System Mission
ESA	European Space Agency
ESTEC	European Space Technical Center
FFT	Fast Fourier Transform
GCM	General Circulation Model
GCMS	Gas Chromatograph and Mass Spectrometer
GOCE	Gravity field and steadystate Ocean Circulation Explorer
GPS	Global Positioning System
GRACE	Gravity Recovery And Climate Experiment
HASI	Huygens Atmosphere Structure Instrument
INMS	Ion and Neutral Mass Spectrometer
INS	Inertial Navigation System
IR	Infrared
ISS	Imaging Science Subsystem
JPL	Jet Propulsion Laboratory
JSST	Joint Science Definition Team
LS	Least-Squares
MAG	Dual-Technique Magnetometer
MEMS	Micro-Electronic-Mechanical-System
MIMI	Magnetospheric Imaging Instrument
MMRTG	Multi-Mission Radioisotope Thermoelectric Generator
MoI	Moment of Inertia
NASA	National Aeronautics and Space Administration

Continued on the next page

CONTENTS

OPFM	Outer Planet Flagship Mission
PPI	Pressure Profile Instrument
PSD	Power Spectral Density
RADAR	Cassini Radar
RPWS	Radio and Plasma Wave Spectrometer
RSS	Radio Science Subsystem
RTG	Radioisotope Thermoelectric Generator
SAR	Synthetic Aperture Radar
SGG	Satellite Gravity Gradiometry
SH	Spherical Harmonics
SNR	Signal-to-Noise Ratio
SP	Sub-Saturn Point
SRON	Stichting Ruimtevaart Onderzoek Nederland
SSP	Surface Science Package
SST	Satellite-to-Satellite Tracking
TandEM	Titan and Enceladus Mission
TEM	TEMperature sensors
TNEA	Total Noise Equivalent Acceleration
TSSM	Titan and the Saturn System Mission
UV	Ultraviolet
UVIS	Ultraviolet Imaging Spectrograph
VIMS	Visible and Infrared Mapping Spectrometer

List of Figures

2.1	Saturn's A ring seen in ultraviolet light	4
2.2	Titan as seen in the visible band	6
2.3	Artist impression of the Titan explorer	14
2.4	Simulation of different trajectories of a passive balloon	15
2.5	The phase diagram of water	18
2.6	A possible interior structure of Titan	19
2.7	The surface of Titan as seen by the DISR instrument	20
2.8	SAR image of the lakes at the northern hemisphere	21
2.9	The atmospheric temperature profile as measured by the HASI instrument	23
2.10	Temperature and the pressure profile as measured by Huygens instruments	24
2.11	A simplified photochemical scheme on the haze formation	25
2.12	Titan's methane cycle	25
2.13	The methane mole fraction in Titan's atmosphere	26
3.1	The Meissl scheme	34
3.2	Artist impression of the GOCE spacecraft	35
3.3	A sketch showing the exaggerated motions of a gondola underneath a balloon	37
3.4	Forces between three bodies	37
3.5	The MEMS market in 2005	42
3.6	Cross-section of a MEMS accelerometer	44
3.7	The proposed micro-gradiometer	45
4.1	Static isostatic equilibrium	50
4.2	The different types of spherical harmonics	54
4.3	The higher order coefficients of the spherical harmonics	54
4.4	Point P and point Q in a Titan centered reference system	60
4.5	The body with mass m is perturbed by a body with mass $M_{perturber}$	61
4.6	The three interior models used	65
4.7	A priori values of J_2 for differet phase lag angles δ	70
4.8	The expected probability distribution of the observed values for the Love number	71
4.9	Radial structure and density distribution of Titan	73
5.1	Gravitational potential for an arbitrary point on the z -axis	77
5.2	The lake can be seen as a 'hole' in the homogeneous sphere	77
5.3	The global Titan reference system and the local north-oriented reference system	78
5.4	The gravity gradients in the local north-oriented reference system	79
5.5	The gravity gradients in the Titan centered reference system	80
5.6	The gradients plotted in the local north-oriented reference system	80

LIST OF FIGURES

5.7	SAR image and the discretization of the lakes at the northern hemisphere	81
5.8	The time-dependent part of the tide-raising potential	84
6.1	The gravitational potential of lake 01	86
6.2	The gravitational potential of lake 02	86
6.3	The gravitational potential of the two lakes, $d = 20$ km	87
6.4	The gravitational potential of the two lakes, $d = 100$ km	87
6.5	The gravity gradients of lake 01	89
6.6	The gravity gradients of lake 02	89
6.7	The trajectory along 79°N crossing both lakes	90
6.8	Schematic representation of the location of the measurements	91
6.9	Diagonal gradients up to an altitude of 20 km	92
6.10	Off-diagonal gradients up to an altitude of 20 km	92
6.11	The diagonal gradients at an altitude of 2, 6 and 10 km	93
6.12	The off-diagonal gradients at an altitude of 2, 6 and 10 km	94
6.13	The off-diagonal gradients of Titan and of lake 01	95
6.14	The diagonal gradients of lake 01 and lake 02 separately and combined	96
6.15	The off-diagonal gradients of lake 01 and lake 02 separately and combined	97
6.16	The different trajectories of the balloon as used in the simulations	97
6.17	V_{xx} along different trajectories, plotted in 2D	98
6.18	V_{yz} along different trajectories, plotted in 2D	99
6.19	The measured gradient V_{xx} along different trajectories, plotted in 3D	100
6.20	The diagonal gradients for different lake-densities	101
6.21	The diagonal gradients for different lake-densities	102
6.22	The diagonal gradients for sub-surface lakes at different depths	103
6.23	The off-diagonal gradients for sub-surface lakes at different depths	103
6.24	The results of the LS estimation, $\sigma_{ij} = 0.17$ Eötvös	107
6.25	The results of the LS estimation zoomed in on the part below the red line	108
D.1	A priori values of C_{22} for different phase lag angles δ	131
D.2	A priori values of S_{22} for different phase lag angles δ	131
D.3	Summary of the model results for a primordial $\text{NH}_3 \cdot \text{H}_2\text{O}$ ocean of 5 wt.% NH_3	132
D.4	Summary of the model results for a primordial $\text{NH}_3 \cdot \text{H}_2\text{O}$ ocean of 15 wt.% NH_3	133
D.5	Mass fractions of rock/iron and ice plus subsurface ocean for various core heat production rates	134
E.1	The time-dependent part of the tide-raising potential, days 1 and 2	136
E.2	The time-dependent part of the tide-raising potential, days 3 and 4	136
E.3	The time-dependent part of the tide-raising potential, days 5 and 6	137
E.4	The time-dependent part of the tide-raising potential, days 7 and 8	137
E.5	The time-dependent part of the tide-raising potential, days 9 and 10	138
E.6	The time-dependent part of the tide-raising potential, days 11 and 12	138
E.7	The time-dependent part of the tide-raising potential, days 13 and 14	139
E.8	The time-dependent part of the tide-raising potential, days 15 and 16	139
F.1	The gravitational potential of lake 01 and lake 02	141

F.2	The gravitational potential of lake 01 and lake 02	142
F.3	The gravitational potential of the lakes, $d = 10$ km	142
F.4	The gravitational potential of the lakes, $d = 30$ km	143
F.5	The gravitational potential of the lakes, $d = 40$ km	143
F.6	The gravity gradient V_{xx} of lake 01 and lake 02	144
F.7	The gravity gradient V_{xy} of lake 01 and lake 02	145
F.8	The gravity gradient V_{xz} of lake 01 and lake 02	145
F.9	The gravity gradient V_{yx} of lake 01 and lake 02	146
F.10	The gravity gradient V_{yy} of lake 01 and lake 02	146
F.11	The gravity gradient V_{yz} of lake 01 and lake 02	147
F.12	The gravity gradient V_{zx} of lake 01 and lake 02	147
F.13	The gravity gradient V_{zy} of lake 01 and lake 02	148
F.14	The gravity gradient V_{zz} of lake 01 and lake 02	148
F.15	Diagonal gradients up to an altitude of 1000 km	149
F.16	Off-diagonal gradients up to an altitude of 1000 km	150
F.17	Diagonal gradients up to an altitude of 100 km	150
F.18	Off-diagonal gradients up to an altitude of 100 km	151
F.19	The diagonal gradients at an altitude of 10 km	152
F.20	The off-diagonal gradients at an altitude of 10 km	152
F.21	The diagonal gradients of Titan and superimposed with the gradients of lake 01	153
F.22	V_{yy} along different trajectories, plotted in 2D	154
F.23	V_{zz} along different trajectories, plotted in 2D	154
F.24	V_{xy} along different trajectories, plotted in 2D	155
F.25	V_{xz} along different trajectories, plotted in 2D	155
F.26	V_{yy} along different trajectories, plotted in 3D	156
F.27	V_{zz} along different trajectories, plotted in 3D	156
F.28	V_{xy} along different trajectories, plotted in 3D	157
F.29	V_{xz} along different trajectories, plotted in 3D	157
F.30	V_{yz} along different trajectories, plotted in 3D	158
F.31	The off-diagonal gradients for different lake-densities	159
F.32	The off-diagonal gradients for different lake-densities	159
F.33	The diagonal gradients for sub-surface lakes, $d = 10$ km	160
F.34	The off-diagonal gradients for sub-surface lakes, $d = 10$ km	160
G.1	The results of the LS estimation, $\sigma_{ij} = 1$ Eötvös	164
G.2	The results of the LS estimation zoomed in on the part below the red line	164
G.3	The results of the LS estimation, $\sigma_{ij} = 2.6$ Eötvös	165
G.4	The results of the LS estimation zoomed in on the part below the red line	165

List of Tables

2.1	Characteristics of Saturn	4
2.2	Characteristics of Titan	5
2.3	Date of the Cassini flybys at Titan and the flyby altitudes	9
2.4	Properties of different hydrocarbon mixtures, pure methane and pure ethane	22
3.1	Characteristics of the GOCE three-axis diagonal gradiometer	42
3.2	Specifications of a micro-gravity gradiometer	44
4.1	Complex Love numbers and mass load coefficients	66
4.2	The dissipation rates for the various interior models of Titan	67
4.3	Love numbers as a function of three interior models	68
5.1	Estimation of mean values for V_f induced by several celestial bodies	82
6.1	The maximum difference in magnitude of the gravity gradients	88
6.2	The location of the measurement point and the area of the lakes	91
6.3	The results of the LS estimation for measurement sets 6, 8 and 9	109
B.1	Properties of methane at a pressure of 1.5 bar	125
B.2	Properties of ethane at a pressure of 1.5 bar	125
B.3	Additional data methane and ethane	126
D.1	Different interior models of Titan	129
F.1	The location of the measurement point and the area of the lakes	149
G.1	The density and variance computed for the perfect measurement sets	161

Introduction

Titan, the largest moon of Saturn, amazes us every time again and again. This moon, orange in appearance, has a significant atmosphere in which it hosts a methane cycle in resemblance to the Earth's hydrological cycle, including clouds, rain and surface lakes. One of the key questions within the science community today is what the origin is of the methane on Titan. Methane is one of the chemicals produced by life forms. Is some kind of bacteria active on Titan? Was it incorporated in the interior at the time of formation or is it formed and stored in the interior? One way to learn more about the interior of a celestial body is by doing gravity measurements, using a so-called gravity gradiometer.

TandEM – Titan and Enceladus mission, was proposed in response to ESA's Cosmic Vision 2015–2025 call for proposals, a mission with the goal of exploring the two of the moons of Saturn *in situ*, Titan and Enceladus, to understand their atmosphere, surface and interior. TandEM was selected for further studies within the Cosmic Vision plan, but the mission is a candidate for NASA's outer planet flagship missions too. Therefore ESA and NASA have started a collaboration on the mission studies: Titan and the Saturn System Mission (TSSM). As part of *in situ* investigation components a hot-air balloon would be released in the atmosphere of Titan. One of the instruments on board of the gondola of the hot-air balloon would be a MEMS micro-gradiometer, as initially proposed by SRON, the Netherlands Institute for Space Research.

Measuring the gravity field from space using a gradiometer has not been done before. GOCE, the gravity field and steady-state ocean circulation explorer to be launched in October 2008, will be the first satellite carrying a gradiometer on board. A lot is expected from GOCE: it will determine gravity-field anomalies with an accuracy of 1 Gal, the geoid with an accuracy of 1–2 cm and the spatial resolution will be better than 100 km. This gradiometer, however, is far too bulky and heavy to send on a planetary mission. GOCE is a dedicated mission with no other scientific instruments on board. It is clear that such a configuration is not possible for planetary missions: it would require too much money and mission time for the science return that would then be achieved.

Pictures taken by instruments on board of the Cassini spacecraft prove that lakes are present at the polar regions of Titan. The composition of these lakes is still unknown, though it is believed that these lakes consist of a hydrocarbon mixture. With the area of the lakes known, gradiometer measurements could resolve for the density of these lakes. Can a MEMS micro-gradiometer on board of a hot air balloon floating in the atmosphere of Titan detect (sub-) surface lakes? Can then the density of the lakes be resolved from the gradients? With what accuracy can the gradiometer resolve for the density of the lakes?

To find the answers to these questions a model will be created using a computer program called MATLAB. One of the problems that will be encountered creating such a model is that not much information on the global gravitational field of Titan is available. The classic approach using a spherical harmonic representation is not possible, as there is not enough data yet. Before creating the model several assumptions are made:

- The gradiometer is not damaged during the journey toward Titan and during deployment in Titan's atmosphere. It arrives at Titan fully functional
- The gradiometer is a perfect instrument (no noise, instantaneous measurements)
- The position of the gradiometer with respect to the moon is known accurately
- The gravity field is simulated locally

Starting from these assumptions a very basic model of the gravity gradients of Titan is created. From the lakes as seen by Cassini at the northern polar region a selection is made and modeled as mass anomalies. Finally several datasets are created and the density is resolved from the simulated measurements using the least-squares method.

This report is built up as follows: an introduction to Titan is given in the next chapter. It gives a description on what is known about the planet and recent discoveries are mostly included. Gradiometry, the technique used to measure the gravity gradients of the gravitational potential, and the gradiometer, the instrument used to measure the gravity gradients, are discussed in chapter 3. Chapter 4 describes the theory behind the gravitational and tidal potential. Chapter 5 describes the model that is created and chapter 6 provides an analysis of the results from the model. Finally, chapter 7 finishes this report with conclusions and recommendations.

Titan

Discovered in 1655 by Christian Huygens, Saturn's largest moon, Titan, is the second largest satellite in the solar system (after Ganymede of Jupiter). Christiaan Huygens was a Dutch mathematician, astronomer and physicist. In 1659 *Systema Saturnium* was published, in which he revealed a full exposition of his observations of the system of Saturn, the determination of the period of the moon he had discovered and an explanation of his new theory on Saturn's appearance [21]. This chapter will try to give a complete picture of the moon Huygens discovered. It will start with an introduction to the Saturnian system in which Titan is located and it will give some characteristics of Titan (section 2.1). Hereafter past and future missions to Titan are discussed. Section 2.3 elaborates on the formation of planets and interior of Titan, two closely related subjects. Most of what nowadays is known on the surface characteristics of Titan will be described in section 2.4 and finally, in section 2.5, several aspects of the atmosphere will be treated.

2.1 The Saturnian system

This section will start with a brief introduction into the system of Saturn, the planet around which Titan is in orbit. Next to that some main orbital and physical elements of Titan are presented.

2.1.1 Saturn η

Saturn, the second largest planet (after Jupiter) in our solar system is named after a major Roman god: Saturnus, the god of agriculture and harvest and father of Jupiter. This planet is classified as a gas giant, with a radius of approximately 60,000 km and a gaseous atmosphere. The planet itself mainly consists of hydrogen, a small amount of helium and other trace elements. The inner core of Saturn consists of rock, surrounded by a thick layer of metallic hydrogen, with a mass more than ten times as large as the mass of the Earth. The main physical characteristics and orbital elements are given in table 2.1. Though all four outer planets have a system of rings, that of Saturn is the most distinctive. Its appearance is bright and it can be seen through a simple telescope. The rings are mainly composed out of ices, rocks and dust. Pictures of the so-called A ring made in the ultraviolet light (UV), see figure 2.1, clearly show distinctive features of the rings. Saturn is orbited by at least sixty known satellites, of which Titan is the largest. Together with Mimas, Enceladus, Tethys, Dione, Rhea and Iapetus it is one of the more massive moons, which has become a spheroid under its own gravitation.

2.1.2 In orbit around Saturn

Titan is the twentieth most distant moon of Saturn and is frequently described as a satellite with planet-like characteristics. It has an atmosphere, seasons due to the approximately 26.7° inclina-

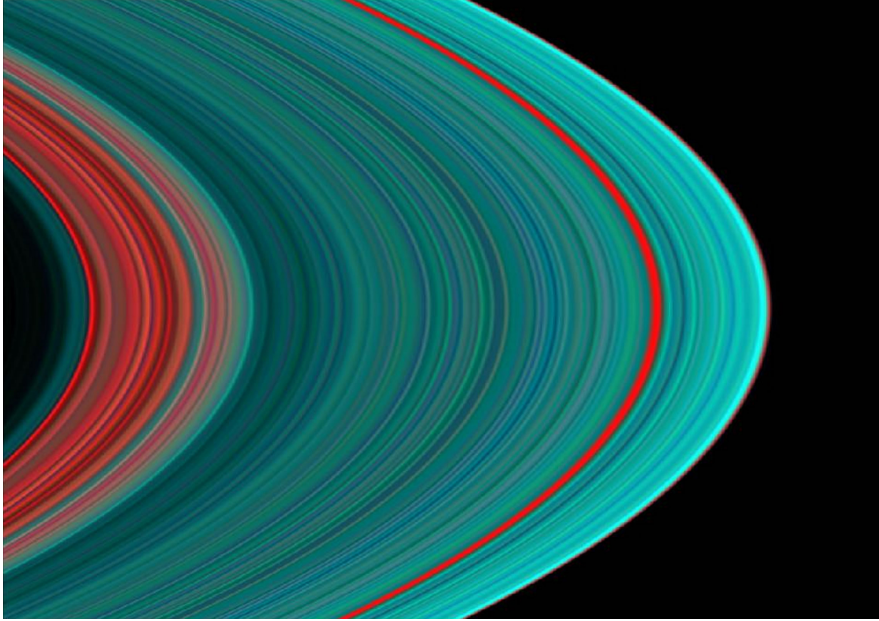


Figure 2.1: Saturn's A ring seen in ultraviolet light. From the inside out, the 'Cassini division' in faint red on the left is followed by the A ring in its entirety. The A ring begins with a 'dirty' interior of red followed by a general pattern of more turquoise as it spreads away from the planet, which indicates denser material made up of ice. The red band, roughly three-quarters of the way out in the A ring, is known as the 'Encke Gap' [Courtesy: ESA].

Table 2.1: Characteristics of Saturn [7].

<i>Mean orbital elements</i>	
Semi-major axis (a)	9.5428244 AU
Eccentricity (e)	0.055509
Inclination (i)	2.4889°
Orbital period	29.423519 yr
Ω	113.666°
ω	93.057°
Mean longitude (L_m)	50.077°
Aphelion distance	10.11595804 AU
Perihelion distance	9.04807635 AU
<i>Physical data</i>	
Mass	568.46 · 10 ²⁴ kg
Density	687.3 kg/m ³
Equatorial radius	60 268 ± 4 km
Polar radius	54 364 ± 10 km
Rotational period	10 ^h 39 ^m 22 ^s .4
Obliquity	26.73°
Surface gravity	8.96 ± 0.01 m/s ² (0.914 g)
Geometric albedo	0.47
Planetocentric constant (GM)	3.79 · 10 ¹⁶ m ³ /s ²

tion to the ecliptic of Saturn, a diameter roughly 50% larger than Earth's moon and it is 80% more massive. Titan, Venus, Mars and Earth are the only bodies in our solar system with a significant atmosphere, making Titan the only moon in our solar system which resembles an Earth-like planet. The dense smog layer in Titan's atmosphere makes it impossible to probe the satellite's

surface in visible wavelengths, only in far infrared (IR) (the longer wavelengths) and with the use of radar sounding a glimpse of the surface can be seen. Spectra of the atmosphere show the smog layer to consist of various hydrocarbons, nitriles and some carbon oxide compounds [7].

The orbit of Titan is, just like most of the planetary satellites, prograde¹ and synchronous with respect to Saturn, which means that the orbital period of 15.945 days is equal to the rotational period of the satellite. The sidereal period of Saturn is 10,759 days (29.42 years), which gives the duration of one season on Titan to be 7.365 years.

Titan has a 3:4 orbital resonance² with another, smaller, moon of Saturn, Hyperion. The gravitational acceleration at the surface of Titan is 1.35 m/s^2 , 0.14 times the gravitational attraction at the surface of the Earth. The surface pressure is 1.5 bar, 1.5 times the surface pressure of the Earth (1 bar). The orbital elements and other physical characteristics of Titan can be found in table 2.2.

Table 2.2: *Characteristics of Titan ([29] and [62]).*

<i>Mean orbital elements</i>	
Semi-major axis (a)	$1.22187 \cdot 10^6 \text{ km}$
Eccentricity (e)	0.0292
Inclination (i)	0.28°
Orbital period	15.945421 Earth days
Rotation period	Synchronous
<i>Physical data</i>	
Equatorial radius	$2575 \pm 2 \text{ km}$
Mass	$1345.53 \cdot 10^{20} \text{ kg}$
Density	$1880 \pm 4 \text{ kg/m}^3$
Surface temperature	94 K
Surface pressure	1496 hPa (1.5 bar)
Surface gravity	1.352 m/s^2 (0.14 g_{Earth})
Geometric albedo	0.21
Planetocentric constant (GM)	$8978.13 \pm 0.06 \text{ km}^3/\text{s}^2$

2.2 Observing Titan: missions to the moon of Saturn

Pioneer 11 passed the moon Titan at a distance of 360,000 kilometers on September 2, 1979, taking five images which constructed the first picture of Titan from outer space, see the left picture of figure 2.2. In 1980 the Voyager 1 spacecraft deliberately made a detour, terminating its Grand Tour to the outer planets, to make more images of Titan and its atmosphere. The first Voyager picture is shown in the middle of figure 2.2. Nowadays the Cassini spacecraft sends high-resolution images, not only in the visible wavelength, back to the Earth. The left picture of figure 2.2 was made on its approach to Titan. All images show that Titan is covered in an orange haze, a feature of Titan's dense atmosphere. It is colored orange because methane particles which reside in Titan's atmosphere absorb all wavelengths in the visible band, except the orange wavelength.

¹see appendix A

²see appendix A

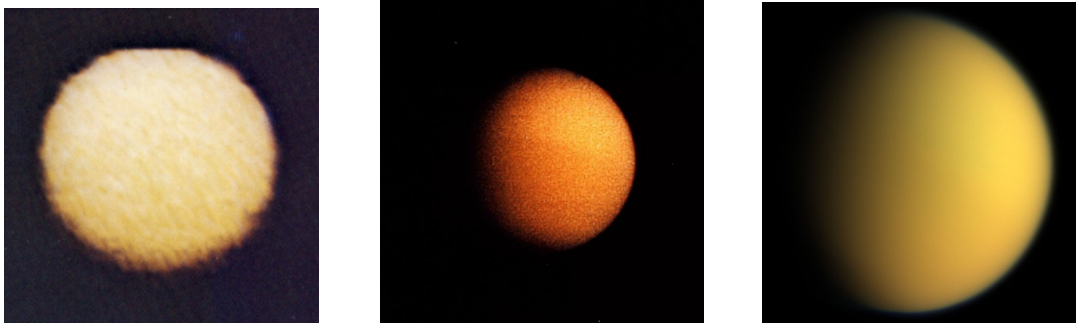


Figure 2.2: Titan as seen in the visible band by Pioneer 11 (left) [Courtesy: NASA], Voyager 1 (middle) [Courtesy: NASA] and Cassini (right) [Courtesy: ESA].

2.2.1 Voyager

The original goal of the Voyager missions was to make a closeup study of Jupiter and Saturn, Saturn's rings, and the larger moons of the two planets. The two Voyagers were both launched from Cape Canaveral, Florida, aboard a Titan–Centaur rocket, Voyager 2 on August 20, 1977 and Voyager 1 on September 5, 1977. Until now Voyager 1 and 2 explored all the giant planets of the outer solar system, Jupiter, Saturn, Uranus and Neptune; 48 of their moons; and the unique system of rings and magnetic fields these planets possess. As of February 2008, Voyager 1 was at a distance of 15.7 billion kilometers (105.3 AU) and Voyager 2 at a distance of 12.7 billion kilometers (85 AU) from the Sun. Currently five science investigation teams are still participating in the Interstellar Mission, as the Voyager mission is renamed to. It is expected that both spacecraft will have their electrical power and attitude control propellant to continue operating until around 2020, though with loss in subsystem redundancy [28].

The trajectory as designed for Voyager 1 was to send the spacecraft past Titan and behind Saturn's rings. Until then scientists believed that Titan was the largest satellite in our solar system, because the measurements were limited to the top of the haze. On its close approach Voyager diametric radio occultation showed that Titan's surface was actually below a haze and that Titan is slightly smaller than Ganymede. Though the surface cannot be seen on Voyager pictures, several detached haze layers can be seen. Another distinctive feature that was seen was a dark hood around the north pole, where the haze layers merge with the main layer. Under the better viewing conditions of Voyager 2, the hood was found to be a dark ring around the pole. Next to that the southern hemisphere was slightly brighter than the northern, which possibly is a result of seasonal effects. The Voyagers flew past Titan when the season was equivalent of mid–April and early May on Earth, or early spring in the northern hemisphere and early fall in the south on Titan [28].

2.2.2 Cassini–Huygens mission

The Cassini–Huygens mission to Saturn is a joint endeavour of ESA, NASA and the Italian space agency, Agenzia Spaziale Italiana (ASI). The Cassini spacecraft carries twelve instruments in orbit around Saturn and the Huygens lander escorted another six instruments to the surface of Titan. Cassini–Huygens is the largest interplanetary spacecraft ever built. It lifted off from Cape

Canaveral on October 15, 2007 aboard a Titan IVB–Centaur rocket and used several gravity assists³ to reach its final destination: the Saturnian system. During the nominal mission lifetime, which ended June 2008, Cassini has completed 75 orbits around Saturn, 44 close fly–bys of Titan, and numerous fly–bys of Saturn’s other icy moons [11]. Last April, a mission extension was approved by NASA and the Cassini spacecraft will continue its journey for at least two more years around Saturn and its moons, under the name of Cassini Equinox, see section 2.2.3.

The Cassini orbiter

The Cassini spacecraft is 6.7 m high and 4 m wide and alone weighs 2125 kg. The Huygens probe adds another 349 kg and including 3.1 tonnes of propellant, the launch mass of Cassini–Huygens was 5.82 tonnes. Three Radioisotope Thermoelectric Generators (RTGs) provide power for the complete spacecraft including the instruments, computers, radio transmitters, attitude thrusters and reaction wheels. Communication can be done using the high–gain or one of the two low–gain antennae mounted on the spacecraft. At the moment the primary function of the high–gain antenna is to support communication with Earth, next to that it is used for scientific experiments. During the first part of its voyage to Saturn, the high–gain antenna was positioned toward the Sun such that it could function as a shield to protect the spacecraft’s instruments from solar radiation. The low–gain antennae are only used for communication in emergency situations such as a power failure on board of the spacecraft. The twelve scientific instruments on board are [11]:

- Cassini Plasma Spectrometer (CAPS) explores plasma (highly ionized gas) within and near Saturn’s magnetic field
- Cosmic Dust Analyzer (CDA) studies ice and dust grains in and near the Saturn system
- Composite Infrared Spectrometer (CIRS) measures infrared energy from the surface, atmosphere and rings of Saturn and its moons to study their temperature and compositions
- Ion and Neutral Mass Spectrometer (INMS) examines neutral and charged particles near Titan, Saturn and moons to learn more about their atmospheres and ionospheres
- Imaging Science Subsystem (ISS) takes pictures in visible, UV and near–IR light
- Dual–Technique Magnetometer (MAG) studies Saturn’s magnetic field and its interactions with the solar wind, the rings and the moons of Saturn
- Magnetospheric Imaging Instrument (MIMI) images Saturn’s magnetosphere and measures interactions between the magnetosphere and the solar wind, a flow of ionized gases streaming out from the Sun
- Cassini Radar (RADAR) maps surface of Titan using radar imager to pierce the veil of haze. It is used to measure heights of surface features too
- Radio and Plasma Wave Spectrometer (RPWS) investigates plasma waves (generated by ionized gases flowing out from the Sun or orbiting Saturn), natural emissions of radio energy and dust

³see appendix A

- Radio Science Subsystem (RSS) searches for gravitational waves⁴ coming from beyond the solar system; studies the atmosphere, rings and gravity fields of Saturn and its moons by measuring telltale changes in radio waves sent from the spacecraft
- Ultraviolet Imaging Spectrograph (UVIS) measures ultraviolet energy from atmospheres and rings to study their structure, chemistry and composition
- Visible and Infrared Mapping Spectrometer (VIMS) identifies the chemical compositions of the surfaces, atmospheres and rings of Saturn and its moons by measuring colours of visible light and infrared energy emitted or reflected

The Cassini orbiter has flown by Titan several times already, but more flybys are still planned. After the data became available from the Huygens lander and earlier Titan encounters, the density in the upper atmosphere was discovered to be greater than originally expected. Hence some of the 'lower' flyby altitudes had to be adjusted to a higher altitude, otherwise the air-drag of the upper atmosphere might have changed the orbit of the Cassini spacecraft too much. Table 2.3 gives an overview of all past and coming flybys of the nominal mission of the Cassini orbiter and it is indicated which altitudes were revised. For more recent information on these flybys and on flybys with other moons of Saturn, see the Cassini–Huygens website [11].

The Huygens landing probe

On January 14, 2005, the Huygens lander descended into the atmosphere of Titan. Using three different parachutes in sequence to ensure a soft landing, the Huygens probe made a two and a half hour trip before it finally reached the surface. The probe carried six scientific instruments, protected by a hard shell which functioned as a brake and as thermal protection during the descent. The instruments were mainly meant to analyze Titan's atmosphere and surface [11]:

- The Aerosol Collector and Pyrolyzer (ACP) collected aerosols for chemical-composition analysis
- The Descent Imager/Spectral Radiometer (DISR) took images and made spectral measurements using sensors covering a wide spectral range. A few hundred meters before impact, the instrument switched on its lamp and acquired spectra of the surface material
- The Doppler Wind Experiment (DWE) used radio signals to deduce atmospheric properties. The drift of the probe caused by the winds in Titan's atmosphere induced a measurable Doppler shift in the carrier signal. Other radio-signal-perturbing effects such as the swinging motion of the probe was detected from the signal too
- The Gas Chromatograph and Mass Spectrometer (GCMS) identified and analyzed the various elements within the atmosphere. It was equipped with gas samplers too, which were filled at high altitudes and analyzed during descent when more time was available.
- The Huygens Atmosphere Structure Instrument (HASI) used its sensors to measure the physical and electrical properties of the atmosphere. It had an on-board microphone too, to record sounds, see [11] for this recording

⁴see appendix A

Table 2.3: Date of the Cassini flybys at Titan and the flyby altitudes. As stated in September 2007.

Titan flyby	Flyby date	Alt. (km)	Titan flyby	Flyby date	Alt. (km)
2004			2007		
TA	October 26	1200	T23	January 13	1000 ¹
TB	December 13	1200	T24	January 29	2631
2005			T25	February 22	1000 ¹
Huygens descent	January 14	60 000	T26	March 10	980 ¹
T3	February 15	1577	T27	March 26	1010 ¹
T4	March 31	2402	T28	April 10	990 ¹
T5	April 16	1025	T29	April 26	980 ¹
T6	August 22	3758	T30	May 12	690 ¹
T7	September 07	1025	T31	May 28	960
T8	October 28	1451	T32b	June 13	950 ¹
T9	December 26	10 409	T33	June 29	1932
2006			T34	July 19	1332
T10	January 15	2043	T35	August 31	3212
T11	February 27	1813	T36	October 02	975 ¹
T12	March 19	1951	T37	November 19	1000 ¹
T13	April 30	1855	T38	December 5	1300
T14	May 20	1879	T39	December 20	970 ¹
T15	July 2	1906	2008		
T16	July 22	950 ¹	T40	January 05	1010 ¹
T17	September 07	1000 ¹	T41	February 22	1000 ¹
T18	September 23	960 ¹	T42	March 25	1000 ¹
T19	October 09	980 ¹	T43	May 12	1000 ¹
T20a	October 25	1030 ¹	T44	May 28	1348
T21	December 12	1000 ¹			
T22	December 28	1300			

¹Revised altitudes [47]

- The Surface Science Package (SSP) is a suite of sensors which determined the physical properties of the surface at the impact site and provided information on its composition. The package includes an accelerometer to measure the impact deceleration, sensors which measured the index of refraction, temperature, thermal conductivity, heat capacity, speed of sound, and dielectric constant of the material at the impact site

The Huygens probe was designed to land and survive on liquid material, since this was what the scientists at the time expected.

Discoveries by Cassini and remaining questions

Next to not finding a global ocean, the Cassini–Huygens mission has discovered many important features of Titan. Here a short list of the most important discoveries [45]:

- Ethane and ethane clouds were observed that varied over time
- Fluvial channels, lakes and seas were imaged by Cassini radar
- A strong indication of evaporating methane/ethane from the ground has been found

- Evidence for cryovolcanism has been found
- Surface deposits of carbon dioxide have been detected
- A non-synchronous spin was measured. This could indicate the presence of a subsurface ocean, see section 5.3

The major question that remains open is what is the source of Titan's methane and what the sink is for its organic products. Cassini data suggest that Titan's climate has not been static in the history of the solar system and may still be changing today, but no real evidence is given so far [68].

More remains unanswered by the Cassini mission, to give some examples [45]:

- What are the lakes made of? What is flowing in the rivers?
- Is there active volcanism? What kinds of tectonics?
- How are the polymers made in the atmosphere? What is the energy source?
- When and how do the heavy rains occur?
- Is there a rock/metal core? How thin is the crust?
- Is ammonia present and what is the loss rate of the major gases?
- What are the organics at Titan's surface? What is the potential for life?

Considering this is not even the complete list of questions, a lot still has to be discovered. Maybe Cassini will still solve some of these questions the coming years, but a future mission to Titan might be able solve the remaining mysteries on this fascinating moon of Saturn.

2.2.3 Cassini Equinox Mission

June 30 marked the end of the original Cassini-Huygens mission and with this end the Cassini Equinox mission started. The mission will run from July 2008 to September 2010. The mission extension will build further on the primary mission, principal mission objectives are given by ([30] and [11]):

- To study the Saturnian moons, in particular Titan and Enceladus, in more detail
- To monitor seasonal effects on Titan and Saturn
- To explore new regions of the Saturnian magnetosphere
- To observe the unique ring geometry of the Saturn equinox in August 2009 - when sunlight will pass directly through the plane of the rings

The focus in the study on the moons on Saturn will lie on Titan and Enceladus. Titan, because of its similarity with (future) Earth and Enceladus, because of the potential habitability of the moon [30].

In August 2009, Saturn's autumnal equinox⁵ will occur, then the sun shines directly on the equator illuminating the rings of Saturn in a different way. Past observations, when the rings were illuminated from the south, revealed complex dynamics and interactions with the moons. This time Cassini will monitor seasonal changes as the angle of sunlight shifts to the top of the ring plane and the northern hemispheres of Saturn and its moons ([30] and [11]).

2.2.4 Future missions

Titan has a lot for us to discover and it is worth a visit again. With the call for proposals for ESA's Cosmic Vision two missions to the outer planets were selected for further studies: TandEM, to Titan and Enceladus, in the Saturn system and Laplace, to Europa in the Jupiter system. Both studies are candidates for NASA's Outer Planet Flagship Mission (OPFM) too and now the forces are joint in two mission studies: Europa and the Jupiter System Mission (EJSM) and Titan and the Saturn System Mission (TSSM). In the autumn of 2008 the decision will be made whether to go back to either Jupiter or Saturn and the implementation of this mission will start in 2009.

TANDEM - Titan and Enceladus mission

The initial TandEM concept consists of two moderately-sized spacecraft to be launched around 2020. One is defined as a Titan-Enceladus orbiter, carrying Enceladus landers, and the other will be a carrier for Titan in situ investigation elements, the Titan hot-air balloon (Montgolfière) and three mini-probes [4].

The Titan-Enceladus orbiter would deliver up to two Enceladus landers, which would perform in situ seismic, temperature, and possibly compositional measurements. The data relay will be provided by the orbiter during the flybys of Enceladus approximately every 8.25 days. After permanent orbit insertion of Titan, the Montgolfière and surface probe investigations will take place. The orbiter then will be maneuvered to a polar orbit around Titan to perform optimized Titan orbital science and to provide telecom support to the Titan in situ elements [4].

The principal mission objectives are driven by the question the Cassini-Huygens mission raised, and are given in short:

- Titan space environment: thorough investigation of Titan's atmosphere, ionosphere and exosphere, as well as its plasma and magnetic field
- Titan's neutral atmosphere: to obtain more data on temperature, pressure, CH₄ and C₂H₆ humidity, wind fields, internal structure and evolution of clouds, haze characteristics, evaporation rates and temperature over the lakes, surface composition and thermal properties, volumetric changes in lakes and river systems and solar partitioning
- Titan's surface: to obtain (high-resolution) infrared stereo and radar surface mapping, locally and globally and in-situ measurements of surface material from a variety of locations
- Enceladus: to perform measurements as mentioned above for Enceladus' jets, plumes and surface

⁵see appendix A

- Titan and Enceladus interiors and origins: to explore the interiors of Titan and Enceladus by quantifying spatial and temporal variations of topography, gravity field and magnetic field (if any), to determine the composition of the interior and surface materials, proportions of noble gases and isotopic ratios
- Investigation of the astrobiological features by, among others, isotopic and molecular composition, molecular structure of Titan's aerosols and of its various surface materials, to do a chemical analysis of the ejecta produced by cryovolcanism and to investigate molecular and isotopic composition of Enceladus' plumes

More information on the TandEM mission can be found at the mission website [68].

Outer Planet Flagship Mission

The mission studies of the OPFM have embraced Titan as study object because of its low gravity and a thick atmosphere, which make Titan accessible for *in situ* exploration. This allows a broader range of scientific instruments to be taken on this exploration and therefore Titan, "the rich and diverse body offering extraordinary scientific return, is an excellent choice for the next Flagship mission" [70].

The targets of Titan system science include among others geology, meteorology, chemistry, geophysics, space physics and hydrology. To address all these parts the Titan Explorer (TE) mission architecture, includes a separate orbiter, lander, and balloon. The mission to be launched in 2018 will arrive at Titan, through two Venus and two Earth flybys, in 2028. An Atlas V 551 will carry all three elements, an orbiter, a lander and a balloon, housed in individual aeroshells [70].

The orbiter will have a nominal mission life time of four years and it will carry twelve instruments. Thus it will facilitate radio science to provide global mapping, remote sensing observations and *in situ* upper atmospheric measurements. The orbiter design utilizes aerocapture in Titan's atmosphere to save 4 km/s of velocity change capability. The direct-entry lander, build upon the experience from Huygens and Mars missions, will carry eight instruments and will in particular allow for seismic measurements and direct analysis of surface composition. The aerial vehicle, a Montgolfière (hot-air) balloon, can circumnavigate Titan using zonal winds and taking measurements with five instruments. This Balloon inflates during entry and descent and remains near an altitude of 10 km to bridge the science gap between the orbiter and lander scales, notably providing widespread meter-scale imaging of the surface and subsurface radar sounding [70].

The two objectives of the OPFM are defined by four investigations and listed in order of priority [70]:

1. Titan: an evolving Earth-like system

- Determine the composition and transport of volatiles and condensates in the atmosphere and at the surface, including hydrocarbons and nitriles, on both regional and global scales, in order to understand the hydrocarbon cycle. Determine the climatological and meteorological variations of temperature, clouds, and winds

- Characterize and assess the relative importance today and throughout time of Titan's geologic, marine, and geomorphologic processes, e.g. cryovolcanic, aeolian, tectonic, fluvial, hydraulic, impact, and erosion
- Determine the role of the interaction of Titan's upper atmosphere and ionosphere with Saturn's magnetosphere in determining the evolution and climatology of Titan's atmosphere, especially the loss of materials and as a source of free energy and heat for driving the chemistry and dynamics. Determine the chemical pathways by which the nascent tholin formation takes place in the upper atmosphere
- Determine the state of internal differentiation. Understand the heat sources and thermal evolution of Titan. Determine if Titan has a metallic core and an intrinsic magnetic field. Determine the extent and origin (tidal vs. tectonic) of Titan's geodynamic activity

2. Titan's organic inventory: a path to prebiological molecules

- Determine the chemical pathways leading to formation of complex organics at all altitudes in the Titan atmosphere and their modification and deposition on the surface with particular emphasis on ascertaining the extent of organic chemical evolution on Titan
- Determine geochemical constraints on bulk composition, the delivery of nitrogen and methane to the surface, and exchange of surface materials with the interior over geologic time
- Determine where chemical modification of organics on the surface may have occurred, in particular, possible hydrolysis of tholins by transient liquid water into pyrimidines, amino acids, e.g. via impact melt or cryovolcanic deposits.
- Determine the depth of any subsurface liquid water ocean, its thickness and electrical conductivity, and the lateral variations in thickness and rigidity of the overlying icy crust

More detailed information can be found in the public release version of the Titan Explorer Flagship Mission Study [70].

Titan and the Saturn System Mission

TSSM is a joint venture between ESA and NASA, a combination from studies for Cosmic Vision and OPFM, as described previously. The now phase 2 study has an important constrained applied: aerocapture cannot be used, due to its technological immaturity. This led at the NASA side to a rethink of the mission: because of mass limitations, limited orbital payload can be included, but there is an opportunity to investigate other parts of the Saturn system (e.g. Enceladus) because science is possible prior to Titan orbit insertion. The main objectives of the TSSM are [45]:

- To produce a breakthrough in scientific advancement in understanding Titan, a very Earth-like system
- To achieve major advance beyond Voyager and Cassini by carrying out focused Titan exploration initiatives
- To conduct dedicated remote sensing (using an orbiter) and *in situ* campaigns

To achieve this, three teams were set up: a Joint Science Definition Team (JSDT), a mission engineering team for the orbiter (at JPL) and a mission engineering team for the *in situ* vehicle (at ESTEC). The JDST is responsible for the level 1 science requirements, the hierarchical definition of the scientific goals and the definition of the straw man payload. The two engineering teams will focus on the mission requirements, mission architecture, data return and the systems requirements document for both their own part [45].

The main mission goals are to investigate the moons Titan and Enceladus and their connection to the overall Saturn system. The scientific objectives that will be addressed follow from the Cosmic Vision and the Flagship studies as described previously.

The Titan orbiter will be optimized for Titan science and will have a Cassini-like design [9]. The *in situ* vehicle studies at ESTEC include a hot-air balloon, a lander, probe(s) or a recently suggested submarine [45].

Initial concepts of a Titan Montgolfière look very promising. The combined heat source for the local gas of the atmosphere and the electrical source for the Montgolfière would be a Multi-Mission Radioisotope Thermoelectric Generator (MMRTG). The Montgolfière would be released from an entry aeroshell and inflated during descent, full inflation would be reached above 10 km. Following inflation, the Montgolfière would float around Titan's globe carried by the winds. At mid-latitudes, it is estimated that the balloon would circle the globe in about six months and with a designed lifetime of at least one year this would mean at least two circumnavigations of Titan's globe. Altitude control will be autonomously by using a vent valve in the top of the balloon, steered by on-board software, which will get its information from attitude and altitude sensors. Payload options to be studied for the Montgolfière range in mass from 10 to 30 kg. Among the large list of *in situ* payload options, see [9], the gradiometer can be found and it is thus still an option to be part of the instruments to be selected for the gondola under the balloon.



Figure 2.3: Artist impression of the Titan explorer [Courtesy: NASA].

Balloons in the atmosphere of Titan

Because of the prospect of a future mission to Titan, a review was performed on the key factors of different aerial platforms, see [41] and a study on possible trajectories for a passive balloon, see [74].

A wide variety of balloon concepts were investigated, including concepts that were not within the NASA Flagship study. The main focus of the review was on heat and electrical energy supply as well as different buoyancy options. The design driver is the radioisotope power supply, with which a large platform can be designed and thus having the advantages for a large scientific payload and long lifetime. Because of the thermal output of this power supply a Montgolfière would be an ideal solution in terms of longevity, weight performance, easy inclusion of attitude control and the possibility for including propulsion and surface sampling options. Inclusion of small radioisotope power sources was not researched in depth, mainly because these power supplies are still under development, though this might be a very attractive possibility in the (near) future.

Another option is a battery-powered gas balloon, which would reside in the troposphere (up to 40 km) and stratosphere (40-320 km, see section 2.5 for more details). The longevity of these balloons would only be a couple of days and with very low data return, both very unfavorable [41].

A two dimensional version of the Titan global circulation model (GCM) of Titan's atmosphere has been developed, see [52] and [54]. This model describes multiple coupling between dynamics, haze, chemistry and radiative transfer. Using the prediction of the winds on Titan included in this model, eighteen hypothetical massless passive balloons are released in the atmosphere, under the assumption that they remain at a constant altitude and have no dynamics of their own relative to the wind. The balloons are released at two different altitudes, two and twenty km, and at nine different latitudes (80°N, 60°N, 40°N, 20°N, 0°, 20°S, 40°S, 60°S, 80°S). Results of the simulation for balloons released at an altitude of two km are given in figure 2.4. Though the model is largely hypothetical, it might give small indication on the path a possible passive balloon would take, released at certain latitudes and during certain seasons [74].

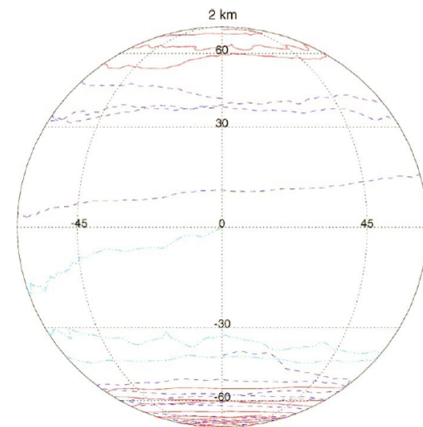


Figure 2.4: Simulation of different trajectories of a passive balloon at an altitude of 2 km [74].

2.3 The interior of Titan

The interior of a planet or satellite can not be observed directly. Nevertheless it is possible to derive information on the interior from direct observable parameters, such as the mass, size and shape of the body. Using information on the gravitational field and rotation rate of a celestial body, estimations can be made on the degree of concentration of mass at center of that body. The gravitational field can to some extent be determined from the orbit of (natural) satellites or rings. If evidence for volcanism and plate tectonics are found, constraints can be set on the thermal

environment below the surface of a planet. Energy output provides information on the thermal structure of the interior [7].

This section will start with a short description on the formation of planets and the outer satellites, after which the possibilities for the interior of Titan is discussed. This section concludes with some comments on how gravity measurements can be used to infer the interior structure.

2.3.1 Planet formation

By understanding the formation of the solar system, much can be said about the interior of the planets in the solar system. Elements assumed to be found in the early solar nebula were the building blocks for what eventually became the planets that are orbiting the Sun nowadays. Combining this with the chemical compounds found nowadays on Titan, it is possible to trace back how Titan was formed and hence what kind of material was incorporated into its interior.

Formation of the planets in the solar system

Astrophysical models suggest that flattened circumstellar disks are a natural byproduct of star formation. These protoplanetary disks originate from the collapse of rotating molecular cloud cores, where a significant fraction of the materials in the core falls onto a rotationally supported disk orbiting the pressure-supported (proto) star. The disk has the same initial elemental composition as the growing star, in our solar system the Sun. At sufficient distance from the Sun it was cool enough for a small percentage of the material to cool down into solid form. Within a few AU of the Sun this dust was mainly composed of rock-forming compounds, whereas further away a more or less equal amount of ices (H_2O , CH_4 , CO , etc) was present in solid form next to the rocky solids. What happens during and after the infall stage is still poorly understood. The disk was then very active and probably highly turbulent, most likely due to a mismatch of specific angular momentum of the gas hitting the disk with that required to maintain keplerian motion, gravitational instabilities, viscous and magnetic forces [7].

The micrometer-sized dust grows to kilometer-sized planetesimal, which by different perturbations lead to accretion. Accretion is the process where the planetesimal, by means of their own gravity, gain mass by collection of interstellar gases and objects. Eventually solid bodies in the inner solar system formed the terrestrial planets. The planetary cores, which have several times the mass of the Earth, formed the outer solar system. These massive cores were able to gravitationally attract and keep substantially amounts of gaseous material from the solar nebula. This was not the case with the less massive planetesimal, the terrestrial planets. The gases in their current atmospheres are formed from material that was incorporated in the solid planetesimal. The current low eccentricities of the orbits of the outer planets imply that some damping process has been taken place, for instance accretion/ejection of small planetesimal or interactions with residual gas within the protoplanetary disk. For a more in depth discussion on planet formation see chapter 12 of [7].

Formation of planetary satellites in the outer solar system

The previous section indicates that the interior of a planet or moon is highly dependent on the environment in which it was created. Hence satellites being created in the same solar nebula, at more or less the same time, have a lot in common.

The satellites that are in orbit closest to the giant planets (near the Roche limit⁶, for Saturn this limit is at 147,000 km) are in general quite small and consist mainly of rock. These moons were formed very close to their planet and at high temperatures, so most probably the water-ice is completely evaporated during formation. Planetary rings are formed at the location where the tidal forces from the planet are large enough to break up the small bodies held together solely by their own gravity, though the rings seen today are not the same as were formed billions of years ago (see [7] for more information on planetary rings). In the outer regions, small bodies orbit the four outer planets in a highly eccentric and inclined orbits. This diversity in satellites orbiting a planet suggest that not all the satellites are formed in the same manner.

Most planetary systems have regular and irregular satellites. The regular satellites are the moons that orbit the planet in a low eccentric, prograde orbit near the equatorial plane of the planet. This implies that these satellites were formed by a solid body accretion process, in the same manner the planets were formed around the Sun, within the protoplanetary disk surrounding the planet. These disks could very well contain material from the outer portions of the protoplanet's envelope, or material that is directly captured from the protoplanetary disk. The irregular satellites are the small bodies orbiting the planet in the high eccentric, high inclined orbits, and it is believed that these satellites are captured in the planetary system from heliocentric orbits which passed through our solar system. These satellites are composed largely of water-ice with only a small amount of rock. [7].

From the sixty known satellites orbiting Saturn, 38 are classified as irregular satellites, of which nine orbit Saturn with a prograde orbit and 29 in a retrograde orbit. Eight have the title of inner satellites and only ten are classified as regular satellites, of which Titan is one [29]. The remaining 4 have not been classified, since it is not clear to which group they belong yet.

2.3.2 The interior structure of Titan

When comparing Titan's density and radius to other moons, it is an intermediate between the Jovian satellites Ganymede and Callisto. The densities of these satellites indicate that their interiors are mostly composed of ice and silicates. However Titan has a significant atmosphere, dominated by nitrogen and methane, which suggests that the interior is enriched with more volatile ices. These volatile ices, in the case of Titan $\text{NH}_3 \cdot \text{H}_2\text{O}$ and $\text{CH}_4 \cdot \text{H}_2\text{O}$, have similar densities to 'normal' water-ice. The lower temperature in the less massive proto-Saturnian nebula, compared to the proto-Jovian nebula, favored the incorporation of a larger amount of volatiles [62].

⁶see appendix A

Theoretical models of the interior of Titan

At the moment, no data on the Moment-of-Inertia (Mol) factor is present. This factor can restrict the possibilities for the interior of Titan significantly. Hence only using theoretical models, in analogy of the Jovian satellites, some constraints on the interior of Titan can be given. The presence of the substances such as methane found in the atmosphere suggests a certain amount of volatiles incorporated within Titan's interior. Next to that, the interior of Titan should have a mechanism to compensate for the methane lost in the atmosphere (see section 2.5). This makes it plausible that, since observations by the Cassini spacecraft never found a global ocean, a sub-surface ammonia-water ocean is present underneath the ice-I mantle (see figure 2.5, ice-I is often used in analogy to ice-Ih). Simulations show that if Titan's current interior is totally solid, it presumably has always been in this state and would give strong constraints on the formation of Titan. On the other hand, if a liquid layer was formed during accretion, it should still be present nowadays and it might contain a significant fraction of ammonia [71].

So, most likely Titan's interior is differentiated in an iron and rock core and an icy mantle. Planetary differentiation is the process during planet formation where the denser particles will sink to the center of a planet and the less denser materials will rise to the surface and thus create the mantle. Undifferentiated planet models represent a planet where such a differentiation between core and mantle has not been taken place. The mantle of Titan, considering the pressure and temperature of the moon, is a layer of ice I. Water ice is a major constituent of the planets and satellites in the outer Solar System. Depending on the pressure and temperature, water-ice can take at least fifteen different crystalline forms. The various crystalline forms are mainly represented by the temperature and the pressure; the higher the pressure, the more densely the water molecules are packed. Figure 2.5 shows the phase diagram of water, the different phases of water-ice are well understood compared to for instance ammonia and methane ices or mixtures of these. To get a better understanding more experimental data is required, such as experimental work on nitrogen-water, ammonia-water and ammonia-methane-water systems at high pressures and low temperatures [58].

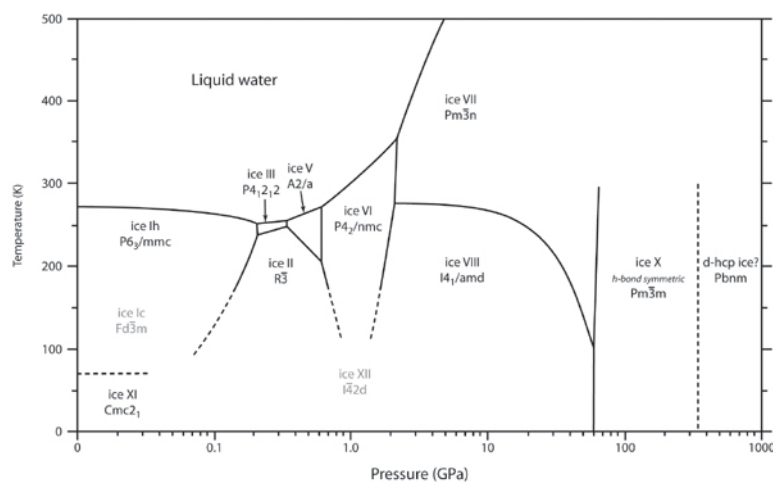


Figure 2.5: The phase diagram of water [Courtesy: Fortes].

Titan's core

Evolution of Titan's core has been researched for two extreme cases [58]: (1) CI chondrite and (2) EH enstatite chondrite. Chondrites⁷ are stones of meteoric origin, characterized by the small round granules called chondrules⁸. If the chondrites of case (1) were included in the planetoids, the present core of Titan will probably be a well-mixed convecting layer with an average temperature of 1400 K, and a thick cold thermal boundary layer, having a total radius of $r_{core} = 1870$ km [58]. If the chondrites were EH chondrites (case (2)), Titan's core most probably will be divided into two layers: an inner liquid iron core, (thickness $r_{liquid\ iron} \approx 910$ km), surrounded by a well-convecting silicate layer (thickness $r_{silicate\ layer} \approx 800$ km) [58].

Gravity measurements and the interior

The thickness of the sub-surface ocean largely depends on the amount of volatiles incorporated in the mantle, the actual radiogenic heating of the core and the heat transfer through the surface. These properties are still unknown, but based on models which couple Titan's orbital eccentricity to its interior assumptions about these properties are made. The presence of volatiles in the sub-surface ocean lowers the freezing temperature of the ocean, hence lowering the temperature of the ice I layer and increasing its viscosity. This influences the heat transfer through the surface again, making the estimation of the thickness of the sub-surface ocean very hard [62].

Theory shows that the Love numbers are linearly related to the ice shell thickness [62]. The tidal Love number is a measure of the response to the gravitational pull of a nearby body. The orbital eccentricity of Titan causes tidal variations of the quadrupole moments from which the second degree potential Love number k_2 will be derived, k_2 being related to the interior structure and rheological properties [62]. Thus, when the Love numbers and the quadrupole moments of the gravity field, J_2 and C_{22} , are known, the interior structure can be inferred. With four ideal flybys, two at Titan's periapsis and two at Titan's apoapsis [55], J_2 and C_{22} can be determined from Doppler tracking of the perturbation of the Cassini orbiter (see section 3.1). Section 4.3 will treat these computations and accompanying estimations of the expected Love numbers.

Low tidal dissipation rates are more consistent with a primordial origin of Titan's significant orbital eccentricity that otherwise should have been damped to smaller values over the age of the solar system. This will be treated extensively in section 4.4.

⁷see appendix A

⁸see appendix A

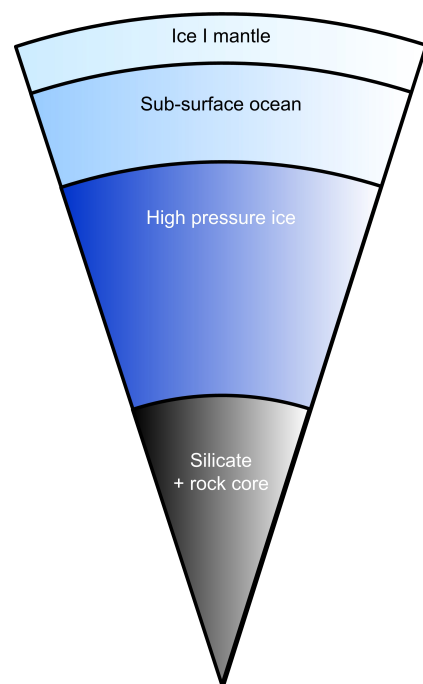


Figure 2.6: A possible interior structure of Titan.

The most likely interior of Titan

Looking at the research done until now, scientists in Europe at the moment believe that the interior structure will be divided, from surface to center, into an ice–Ih layer, an ammonia rich water liquid layer, a high–pressure ice layer (mainly phases V and VI) and a rocky core [71], see figure 2.6.

2.4 The surface of Titan

Scientists have speculated about Titan’s surface for a long time. To compensate for the methane lost due to ionization in the outer atmosphere and other natural processes, initial speculations were that Titan should be completely covered by a deep hydrocarbon ocean. But quite the contrary was found when the Huygens probe landed on the surface of Titan, as will be described in this section.

2.4.1 The Huygens landing site

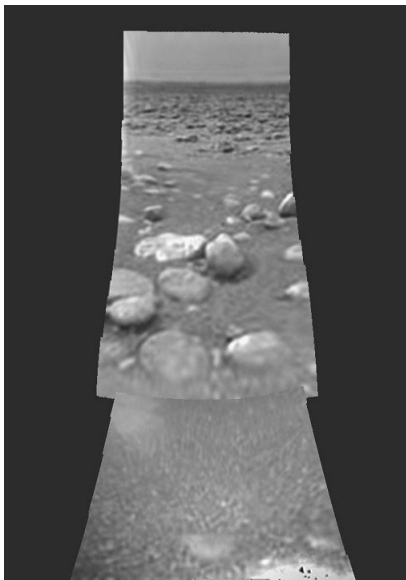


Figure 2.7: *The surface of Titan as seen by the DISR instrument on the Huygens probe [Courtesy: ESA].*

The surface of the Huygens landing site was neither hard, like for instance solid ice, nor the expected liquid. The probe landed on a surface that consists of a solid, granular material having either a low or zero cohesion or a fluid component, resulting in a mixture of wet sand or a textured tar/wet clay. The possibility that the measurements made by the Huygens probe are of one of the cobbles resting on the surface, instead of the surface itself, cannot be ruled out [93]. A view of Titan’s surface at the Huygens landing spot, made by DISR on board of the Huygens probe is given in figure 2.7. Although no liquid bodies were directly imaged by the DISR instrument, it found a compelling evidence for fluid flow on the surface of Titan. At least a few structures that were seen on the pictures suggest that there are cryovolcanic flows on the surface.

The GCMS instrument on board of the Huygens probe measured during the descent an increased amount of methane toward the surface, while the nitrogen count rate remained constant [65]. Methane, ethane and propane are liquids at Titan’s surface conditions. In the photochemical models of Titan, propane is produced only 1/40th as abundantly as ethane [42]. This, in combination with the measurements made by the GCMS at the surface of Titan, shows that ethane and methane should be present at Titan’s surface. The presence of cyanogen (C_2N_2), benzene and CO_2 is most probable [50].

2.4.2 Imaging by the Cassini orbiter

The radar on the Cassini orbiter has until now observed dunes, lakes, cryovolcanic features, river-like channels, degraded impact craters and mountains. Although many new insights are given, it should be kept in mind that these results are only based on 20% coverage of Titan's surface of which most taken from the northern hemisphere and equatorial regions.

Lakes on the surface of Titan

Though the descent of the Huygens probe did not reveal a global ocean, Cassini observations have shown areas on the radar images darker than other patches of area, see figure 2.8. These large radar-dark areas are interpreted as lakes. The hypothesis that these lakes are filled with hydrocarbons is supported by their very low reflectivity and morphological similarities to lakes on Earth. If the lakes are not filled with liquid hydrocarbons, it might be that the patches seen are depressions and channels formed in the past, which have now been filled by a very low-density deposit that is darker (that is the lower the reflectivity of the deposit, the darker the features will be observed in the pictures) than any observed elsewhere on Titan. Approximately 68% of Titan's north polar region above 60 degrees is now covered by SAR-images obtained by Cassini, but only 12% of the south polar region is mapped. The dark pathes found on the southern polar region do have the same backscatter as the northern lakes [40].

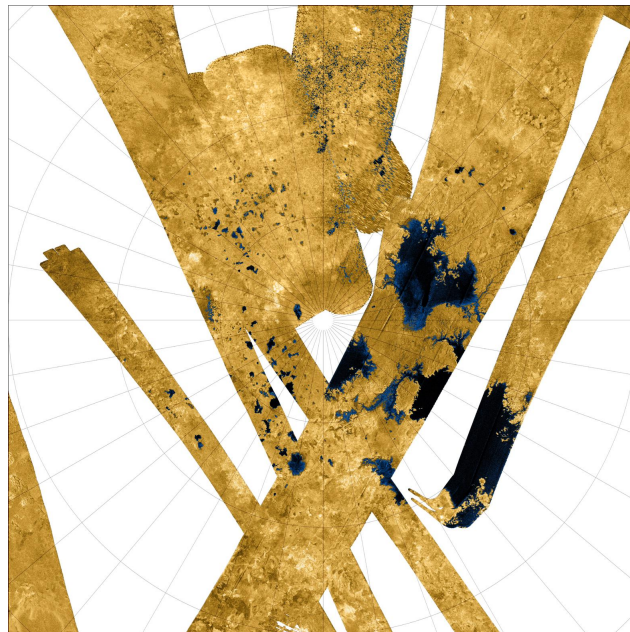


Figure 2.8: SAR image of the lakes at the northern hemisphere. Compilation made of different pictures during Cassini fly-bys [40].

To determine the depth of the lakes from the Cassini images, terrestrial analogs are used as a guide. Thus, the smaller lakes ($\sim 100 \text{ km}^2$) are estimated to have a depth of the order of 10 m, while the depth of the large seas is estimated to be ten times or more larger [42]. The exact composition of the liquid/sand in the lakes is still unknown. According to [48] the lakes at the surface consist of a liquid hydrocarbon mixture. Table 2.4 gives the density and composition of the two

mixtures as suggested in [48], together with the density of pure methane and pure ethane [82].

Table 2.4: Properties of the different hydrocarbon mixtures as proposed in [48], pure methane and pure ethane at 1.5 bar [82].

Constituents (per mole)	Temperature [K]	Density [kg/m ³]
<i>Case 1: pure methane</i> 1 CH ₄	92.7	448.90
<i>Case 2: pure ethane lake</i> 1 C ₂ H ₆	92.4	649.43
<i>Case 3: mixture I</i> 0.35 CH ₄ , 0.6 C ₂ H ₆ , 0.05 N ₂	92.5	547
<i>Case 4: mixture II</i> 0.08 CH ₄ , 0.9 C ₂ H ₆ , 0.02 N ₂	92.5	620.5

Spectroscopic data of Ontario Lacus in Titan's south-polar region, obtained by Cassini VIMS, indicate that ethane, probably in liquid solution with methane, nitrogen and other low-molecular-mass hydrocarbons. This lake-like feature was already found in 2005 with the use of Cassini's ISS narrow-angle camera.

Dunes at the equatorial region of Titan

As the lakes are a distinct feature of Titan's poles, dunes are found at the equatorial region up to 30°, where about 40% of the surface is covered by 1–2 km longitudinal sand dunes. The height of the largest dunes are estimated to be around 150 m and the average thickness about 30 m. These estimations are all made by comparing the dunes at Titan with the longitudinal dunes present on Earth [42].

Mountains

Prior to Cassini it was believed that impact structures would dominate the topography on Titan, because these features are dominant on Ganymede and Callisto. Then mountains and mountain ranges would be central peaks and rims of craters, but none of this was revealed by Cassini. The highly elevated regions, which can be indicated as mountains, are estimated to cover 1% of Titan surface. By using shading effects on the radar images and by making quantitative estimations by shape-from-shading (radarclinometry) several of these mountain features have been observed more closely and measured. Mountains up to a height of 1930 m and with an average slope of 37.2° are found in widely varying locations around Titan. If internal processes are responsible for this widespread variety of mountains, these processes have not been localized adequately. What the images do indicate is that erosion has been or currently is active at the surface of Titan. The age of a typical mountain is estimated between 20 and 100 million years, on geological timescales this is very young [51].

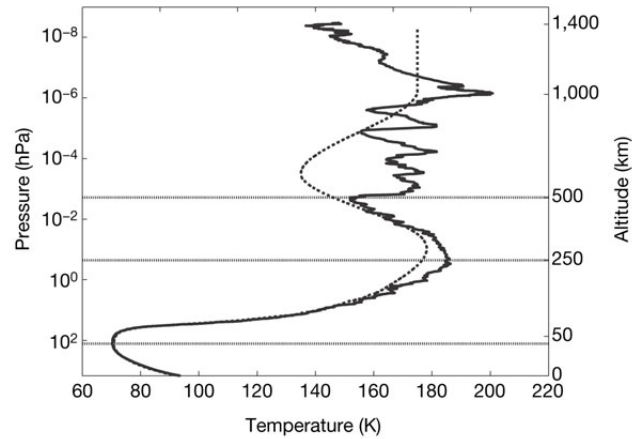


Figure 2.9: The atmospheric temperature profile of Titan's atmosphere as measured by the HASI instrument (solid line) compared to the engineering model (dashed line) [15].

2.5 The atmosphere

As mentioned before, Titan has a significant atmosphere. This section will describe the distinct features of Titan's atmosphere. The temperature profile is mostly based on observations and measurements, while the composition of the haze and the functioning of the methane cycle are more hypothetical. The formation of clouds and the existence of winds are partly based on a theory applicable to Earth and partly on recent observations of the Cassini–Huygens mission.

2.5.1 The atmospheric profile

During the descent of the Huygens probe, HASI determined the density of the atmosphere, from which the temperature and pressure were derived. The atmosphere was encountered earlier than expected, already at an altitude of 1500 km it could be detected. The HASI instrument characterized the thermosphere, between 500 and 1020 km, by the presence of temperature variations due to dynamic phenomena, for instance gravity waves and gravitational tides [15]. A minimum temperature value of 152 K was measured at 490 km altitude, which could indicate the mesopause. Hereafter the temperature of the stratosphere increased while descending, until a value of approximately 186 K at 250 km and 0.3 Pa. Temperatures in the lower part of the mesosphere and the upper part of the stratosphere all were about 5–10 K higher than predicted by models. From 150 km downwards the temperature is directly measured by temperature (TEM) sensors and the pressure by the pressure profile instrument (PPI), see figure 2.10. The solid line represents the measurements of the two units, while the circles (ingress) and crosses (egress) are the values obtained by Voyager 1 radio occultation. The tropopause, indicated by the minimum temperature reached during the descent, was encountered at 44 km (70.4 K, 115 hPa). The surface temperature measured was 93.65 ± 0.25 K and the pressure was $1467 \text{ hPa} \pm 1 \text{ hPa}$, within expectations [15].

The HASI temperature profile of the lower atmosphere was compared to Voyager data and the comparison suggests that the atmosphere is uniform and slowly changing at the mid latitudes [15]. The question does remain if the profile measured by HASI is valid throughout the entire atmosphere of Titan, only at mid-latitudes or locally.

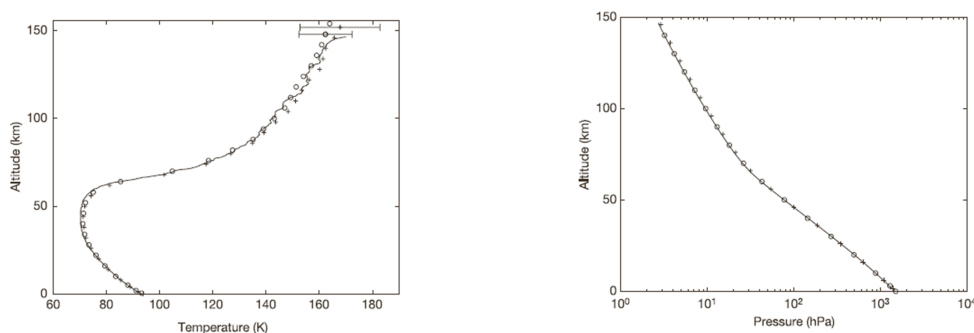


Figure 2.10: Temperature profile (left) and the pressure profile (right) as measured by Huygens instruments [15].

The engineering model of Titan's atmosphere resembles more or less that of the Earth. According to the models the surface pressure is 1.46 bar and the temperature 93 K. The troposphere extends to the tropopause at an altitude of approximately 40 km (140 hPa, ± 70 K). Above the tropopause the stratosphere extends, where at 320 km altitude the temperature reaches a minimum value of 177 K and the pressure drops to about 5–6 Pa. Increasing the altitude, the temperature decreases again. In contradiction to the profile measured by the HASI instrument, the models locate the mesopause at a height of 800 km (135 K, 0.01 Pa). The reason for this difference is not clear. In the outer atmosphere the temperature rises to temperature of roughly 180 K (0.01–0.03 Pa) at ~ 800 km [7].

2.5.2 Molecular composition

At the surface of Titan the atmosphere consists for roughly 95% of Nitrogen (N_2) and 5% of methane (CH_4). Higher in the atmosphere the percentage is about 98% N_2 and 2% CH_4 . GCMS observations of the lower atmosphere and surface have identified traces of ethane (C_2H_6), propane (C_3H_8), benzene (C_6H_6), cyanogen (C_2N_2), carbon dioxide (CO_2) and hydrogen cyanide (HCN). Of the noble gases only traces of Argon (^{36}AR and ^{40}AR) could be identified, see [50].

2.5.3 Titan's (organic) haze

The smog layer covering Titan is formed at an altitude of 300 to 500 km, by organic aerosols, consisting of hydrocarbons (e.g. HCN) and nitriles (e.g. NH_3). Aerosols are small particles, which reside in the atmosphere. The haze in the upper atmosphere reflects 30% of the incident sunlight and as much as 40% is absorbed, resulting in an anti-greenhouse effect, cooling the surface by nine Kelvin. On the other hand the troposphere acts as a thermal blanket, warming the surface roughly for twenty Kelvin compared to the situation in the absence of a troposphere. Net the surface of Titan is warmed eleven degrees with respect to its equilibrium [46].

Evidence is found that complex negatively charged hydrocarbon molecules, tholins, are formed at an altitude of around 1000 km. At this altitude, methane and nitrogen is destroyed under influence of sunlight and energetic particles, which then will form larger, more complex molecules and eventually tholins, see figure 2.11. These heavy molecules (radii of ~ 260 nm) are gravita-

tionally bound to Titan and will fall back to the lower atmosphere, where they indeed are found by the ACP (Aerosol Collector and Pyrolyzer) on board of the Huygens probe [25]. The high linear polarization and the strong forward scattering of the particles imply that the haze particles are small monomers [19]. The radius of the monomers as measured by the DISR instrument is $0.05 \mu\text{m}$, though the data indicate that larger radii are possible too. A better estimate of the size will be available after the analysis of the solar aureole measurements made. These are measurements made during the descent of the Huygens probe through the haze upwards, looking at the brightness of the visible spectra of the Sun. Other observations by DISR probe demonstrated that there was significant haze opacity at all altitudes during the descent, which would imply that the haze extends all the way down to the surface [76].

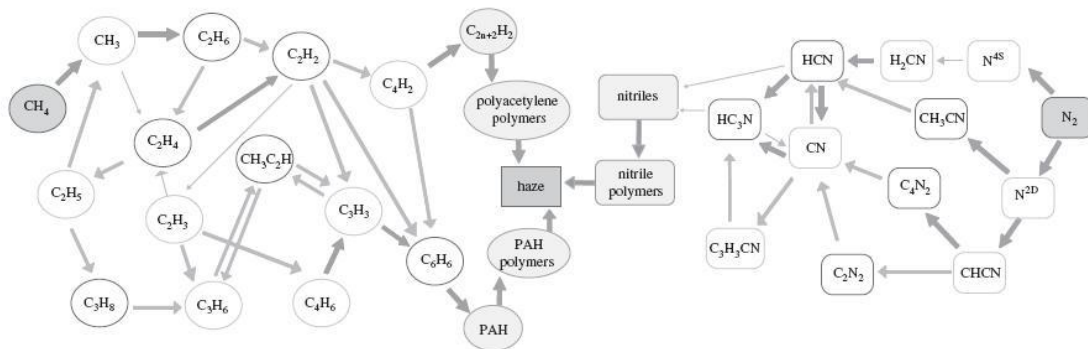


Figure 2.11: A simplified photochemical scheme on the haze formation in Titan's atmosphere [1].

2.5.4 Titan's methane cycle

It is strongly believed that the methane on Titan functions in the same way as water on Earth, that is, a methane cycle on Titan exists similar to the terrestrial hydrological cycle, involving clouds, rain and surface liquids, see figure 2.12. Methane, just as water, can exist as gas, ice and liquid. At 1.5 bar and a temperature of 94 K, methane and ethane are in the liquid phase, see appendix B. Looking at the atmospheric profile (figure 2.9) and pictures of the northern hemisphere made by Cassini, it is plausible that the methane and ethane do exist in liquid form, though a lot remains uncertain about the function of methane on Titan. The source of the methane is yet unknown, either it arrived at Titan at the time of its formation or it is/was produced on Titan. Methane is one of the organic molecules produced by life forms; hence the question arises if the methane found on Titan is an indication for the presence of bacteria or if it is formed by some geological process. Up till now no concrete evidence is found for the microbio-

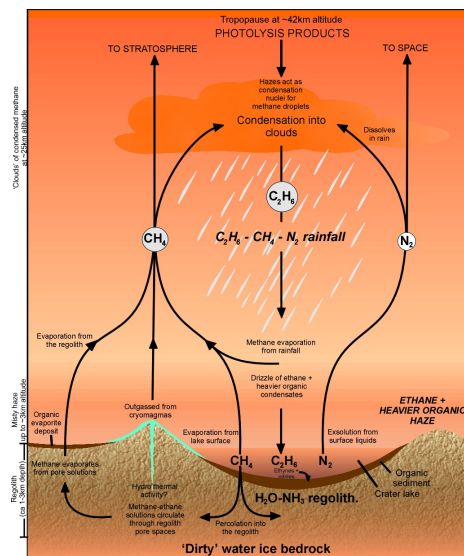


Figure 2.12: A simplified picture of Titan's methane cycle.

ological production of methane. The methallogical cycle is expected to be a closed cycle; however current data are inadequate for evaluation of the recirculation of methane from the surface into the interior.

Removal of methane from the atmosphere

The methane on Titan is removed from the atmosphere by two chemical processes: photochemistry and condensation.

In the ionosphere (above 700 km) methane is destroyed by photolysis, the process where under influence of photons chemical compounds are broken down. The shorter wavelengths (below 140 nm) initiate the production of short-lived, fast-reacting radicals, which subsequently form ethane (C_2H_6) or will react with other atmospheric molecules (see figure 2.11). The ethane diffuses downwards and condensates in a region of about 15 km, just above the tropopause. Though the ethane mixing ratio below 15 km is uniform, the amount of ethane that condenses is expected to vary, due to temperature changes at the surface and in the troposphere. On the surface the amount of ethane is expected to compete with the haze material, which is formed in comparable amounts [1].

In the troposphere methane is removed by condensation. The methane mole fraction as measured by the Huygens GCMS is given in figure 2.13. In the stratosphere the value is constant, and the uniform mixing in the lower stratosphere and upper troposphere was as expected too. Below an altitude of 32 km to approximately 8 km, the methane mole fraction gradually increased, from 8 km until the surface the value remained more or less constant ($4.92 \pm 0.25 \cdot 10^{-2}$). This could indicate evaporation of liquid methane, and a possibility of rain, representative features of the methallogical cycle. This only holds if there is a system that if methane is transported from the surface to the interior, it circulates back out to the surface again, just as water does on Earth. It is believed that there are two plausible possibilities for the condensation of methane: (1) CH_4 vapour over pure CH_4 liquid and (2) N_2 dissolved in CH_4 liquid. These two possibilities are described extensively in [1] and will not be treated here any further.

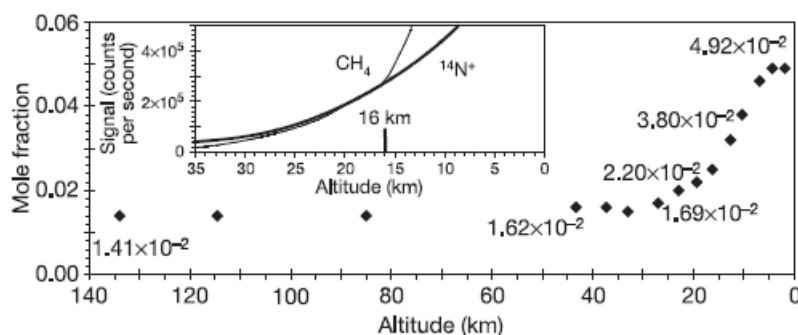


Figure 2.13: The methane mole fraction in Titan's atmosphere as measured by the Huygens GCMS instrument [1].

Hydrogeochemical source of the methane

It is believed that the interior of Titan does not permit recycling of the on the surface deposited hydrocarbons back into methane, which means that the replenishment of methane into the atmosphere has to come from another source. A possibility is that methane could be deposited in the interior as methane clathrate⁹ from the subnebula. Of the noble gases that could have been deposited in the interior of Titan during formation, xenon is trapped at a temperature close to that required for methane. Due to the absence in GCMS measurements of large amounts of heavy noble gases, especially xenon, this is a less likely option. Thus, as mentioned before, it is believed that either biology or geology is responsible for the methane production on Titan [1].

Another possibility is the production of methane by water–rock reactions. In oceans on Earth, seawater hydrolysis the oxidized magnesium (Mg) and iron (Fe) rich silicates into serpentinite, a process called serpentization¹⁰. End products of this process are methane and hydrogen sulfide, for more details on the key geochemical reactions see [1]. On Earth these gases provide an energy source for deep sea chemotroph micro–organisms, organisms that obtain energy by the oxidation of electron–donating–molecules in their environment. On Titan these gases would be expected to be released from the surface, but the Huygens GCMS instrument found no evidence of H₂S or other sulfur compounds at the surface.

These water–rock reactions usually take place under high temperatures, temperatures only found at Titan’s core. Recently discoveries in oceans on Earth have shown that these reactions can occur at lower temperatures. The low–temperature serpentization mechanism proves more promising, though not enough laboratory data on this process is present. A chemical model on formation of CH₄ on Mars yields, if scaled up to Titan’s surface area and assuming Titan’s interior is made up of half water–half rock, a value comparable to the amount of methane found on Titan today. Though looking over geologic time, the amount of methane would be much larger. So though the analogy between Titan and Mars does not hold exactly, it does show that hydrochemical processes are capable of producing large amounts of methane to restore the amount lost in the atmosphere as discussed in this section. More laboratory data on the low–temperature serpentization process is needed to prove this mechanism. The produced methane can easily be stored as a stable clathrate–hydrate, which has been found in terrestrial oceans, and models show it should exist in the interiors of Mars and Titan too [1].

Methane outgassing

In order to replenish the mentioned loss of the methane from the atmosphere, the CH₄ stored in the interior needs to be released back into the atmosphere. Indirect evidence of outgassing has been found on Cassini images, where possible cryovolcanoes are indicated. Direct evidence can only be found by the detection of radiogenic argon (⁴⁰Ar). Radiogenic argon is a decay product of potassium (⁴⁰K), which presumably is incorporated in the core at time of formation (see section 2.3). The half–life of ⁴⁰K is 1.3 billion years, which implies that the conversion of ⁴⁰K into ⁴⁰Ar must have been completed billions of years ago. The mole fraction of ⁴⁰Ar measured by GCMS ($4.32 \pm 0.1 \times 10^{-5}$) is roughly one–half the expected value, assuming Titan’s rocky interior is simi-

⁹see appendix A

¹⁰see appendix A

lar to that of the Earth and the outgassing just as efficiently. The exact release rate of methane can only be found after thorough understanding of Titan's interior, however when scaling the rate of volcanism of Earth and Venus to Titan's surface area, it seems sufficient to recover from the loss by photochemistry [1].

The possibility that methane outgasses by another system remains one of the possibilities too, and together with the cryovolcanism this could bring even a larger amount of methane back into the atmosphere. Still uncertainties are present about the amount of methane present at Titan's surface and the composition of Titan's interior and the manner in which methane is replenished into the atmosphere. The complete cycle as discussed here is still largely hypothetical.

2.5.5 Clouds

The methane clouds on Titan cover less than 1% of the total surface area. Though the existence of clouds is now confirmed, no significant signature of rain is found yet [15]. The last couple of years research has been done and proposed solutions have been put forward, but still the origin and composition of the clouds are not fully understood [7].

Formation of clouds

To form clouds small particles, Cloud Condensation Nuclei (CCN), are needed. The surface tension of water is not high enough to solely form a cloud. On Earth these CCN are for instance desert sand, sea salt or other particles that are dispersed in the atmosphere. These particles do not necessarily have to be injected in the atmosphere from the surface, particles from outer space could behave as CCN too.

Evidence for clouds on Titan

To confirm the existence of clouds on Titan, observations were done with the W. M. Keck telescope using the speckle imaging technique. Speckle imaging is a high resolution technique that works well on bright objects such as Titan. The wavelength range of 1.95–2.29 μm includes both a strong methane absorption band and a window where methane absorption is nearly zero, so that light can penetrate to the surface. The clouds detected using adaptive optics techniques with narrow band imaging with the Gemini and Keck telescopes in December 2001, were located near Titan's South Pole. Observations with the W. M. Keck telescope confirm that the bright spots seen at the southern hemisphere in October 1998 are clouds and not surface features or artifacts of the speckle reduction process [17].

Nature of the clouds

After the confirmation of the discovery of clouds on Titan, more research was done on this phenomenon. Large storms near the South pole and long (stringy) clouds only at certain latitudes have been observed. Titan's circulation dictates the 40°S latitude of Titan's clouds. There has been no observed correlation with the cloud activity and Titan's orbital position so far and the clouds tendency to appear only at certain longitudes suggests a correlation to the surface – this is still largely uncertain due to the multiple active centers within the clouds [18]. A possible solution could be the existence of cryovolcanism on Titan's surface. Another possibility is that the clouds

are present due to convection from lakes. Until now, lakes have only been identified in the polar regions, so a connection between the two seems evident.

Recent observations [19] have reported a polar ethane cloud at the northern hemisphere. Until now, clouds were detected only at southern latitudes. The particles composing the northern cloud are smaller than the particles composing the southern methane clouds, apart from this the clouds' characteristics are all consistent with the condensation of ethane. This could indicate that there is a difference in the cloud composition depending on the hemisphere being observed. A possible influence of seasons, but this has not been confirmed. The northern cloud was only found at an altitude of 30–50 km, above 60 km none was observed [19].

The Huygens descent probe measurements support the existence of clouds. On basis of methane humidity measurements it is most likely the probe passed through an optically thin cloud of methane ice from 30–20 km altitude and droplets of methane–nitrogen liquid from 16–7 km. The publication [44] supports the existence of clouds with the help of measurements with the tilt sensors of the SSP too. As the Huygens probe floated under the parachute through Titan's atmosphere there was a lot of buffeting, even though the air itself was fairly still. Based on knowledge of turbulent cloud layers on Earth, it was shown from Huygens data that the probe must have passed through a turbulent cloud layer.

2.5.6 Winds

The knowledge of the winds is based on models developed over the years. The models often comprehend a part of Titan's dynamics, for instance Risbeth et al. (2000) [58] developed a dynamical model of Titan's thermosphere and Zhu and Strobel (2005) [94] a model on the equatorial super-rotation (i.e. at the equatorial region of Titan the winds flow significantly faster than the planet rotates, ~ 110 m/s at 0.1 hPa) in Titan's stratosphere. Rannou et al. (2004) have combined the major part of the knowledge into a coupled dynamics–microphysics model of Titan's atmosphere. This section will focus on the commonalities of the models and what was measured during the descent of the Huygens probe.

Predictions made by the models

On Titan an equator–to–pole like Hadley circulation exists. Hadley cell circulation is the atmospheric circulation caused by the heating of the air at the equator, which subsequently will flow to the lower pressure regions, the poles. Here the air cools down and will flow back again to the equator. The influence of the sun on the heating of the air at the equator is considered to be minimal, the influence of the Hadley circulation will not be large. Studies with CIRS on board of Cassini support this Hadley type of circulation. The measurements show an increase in volatiles toward the north pole, which is consistent with polar subsidence [69].

Prograde zonal winds are estimated to be about 100 m/s, occurring in the upper stratosphere ([58], [53] and [94]). The zonal winds are caused by the difference in temperature between the day and the night side of the moon; on Titan day–night temperature difference (at solar maximum) is about $\Delta T = 20$ K at an altitude of 800 km. At solar minimum these effects are expected to be a few degrees less. Thermospheric winds causing circulation in the atmosphere are estimated

to have speeds around 60 m/s and are of major influence for the dynamical constants. The circulation pattern suggested by Rishbeth et al. (2000) [58] differs largely from that of the Earth. The possibility exists that Saturn's magnetosphere is forcing some of the winds on Titan, but too little is known about both the magnetosphere of Saturn and Titan [58].

Gravitational winds in Titan's atmosphere

The proximity of Saturn and the eccentric orbit of Titan forces gravitational tides in Titan's atmosphere. According to the model used in [75], the atmospheric response is a prograde propagating tidal wave, with a diurnal (daily) frequency and zonal (in West–East direction) phase speed of $c_\varphi = 3.87 \cos \vartheta$ m/s, where ϑ represents the co-latitude, restricted to the troposphere and stratosphere with an upper boundary at approximately 300 km. While the zonal wind remains prograde, since the background circulation is stronger than the tidal amplitude, the meridional (in North–South direction) wind changes direction twice per Titan day and four times along the parallel of latitude. Instantaneous wind speeds of 5 m/s have been found in the simulations. In the lower atmosphere the tidal amplitudes are quite small, at the tropopause (~ 40 km) the maximum temperature amplitude is approximately 0.3 K and the horizontal wind components are approximately 2 m/s. In the troposphere and above 150 km, the horizontal tidal winds reach amplitudes of 4 m.

In the upper atmosphere (above the stratopause ~ 300 km) the tidal waves reach nonlinear amplitudes due an approximate exponential growth by $p_0(r)^{-1/2}$ where p_0 is the background pressure and r radial distance from the center of Titan, positive outward. According to [66] gravitational tides are an important component of the structure of Titan's upper atmosphere. Unlike gravity waves forced by for instance topography or convective and frontal systems, the forcing frequency, zonal phase speed, longitudinal wave number and forcing potential of gravitational tides will be precisely known and predictions can be made using primitive equation models once the background pressure, mass density temperature and wind fields are well characterized, see [66].

Huygens descent and winds

During the Huygens descent Doppler measurements were performed by the tracking stations. These measurements show that a zonal wind of about 100 m/s exists at an altitude of 140 km, and that it is decreasing steadily toward the surface. Next to that the data shows that the wind dropped to almost 0 m/s around 80 km altitude and that a reversal of the west–east zonal drift in the lowest 7 km is present [44].

By assembling the mosaics made by the DISR instrument, a reconstruction of the descent path of the Huygens spacecraft can be made. The found trajectory indicates that the probe was slowly drifting westward, caused by the prograde winds, slowing down from 50 km altitude to 30 km altitude and more rapidly to 20 km onwards. The last kilometers of the descent the wind dropped to zero and reversed around an altitude of 7 km, near the expected top of the planetary boundary producing a west–northwestwardly motion [76]. The Huygens probe has only made measurements on one location. To verify if the models and speculations really are correct, a whole series of measurements at different places in the atmosphere is desired.

Gradiometry

Over the century, gravity had been measured in a lot of different ways: from the Eötvös torsion balance until gravimetry from space. The traditional method of measuring the Earth's gravity field, as Eötvös initiated with his curvature and horizontal variometer, is based on comparing the differences in how a 'test mass' responds to the gravitational attraction at different locations on the surface of the Earth. Although data on gravity have been collected from many parts of the world by traditional means, they vary considerably in quality and are incomplete. The process of acquiring data on land and at sea is very time-consuming and expensive; global coverage with data of a consistent quality would take decades. With the need for a global map of the Earth's gravity field [20], and the recent progress in improving accuracy of the instrumentation, the obvious solution is to make gravity observations from space.

Section 3.1 describes different techniques for measuring the gravity field from space, whereas section 3.2 focuses on balloon-borne gravimetry. Theoretical background on these measurements is given in the next section, section 3.3. This chapter concludes by looking at the instrument itself and the technology used to miniaturize the GOCE gradiometer, which is too large to use on planetary missions.

3.1 Gravimetry from space

There are various ways to determine the components of the gravity gradient tensor from space. To do this several missions have been initiated to determine the gravity field of the Earth the last decade. Gravimetry is the measurement of the gravitational field, either its magnitude or its properties. This can be done using a (combination of) different measuring techniques, explained first. Hereafter the (future) missions dedicated to measurements of the Earth's gravitational field are shortly described.

3.1.1 Measuring the gravity field

Gravimetric measurements can be made using a gravimeter or gradiometer or by tracking (natural) satellites of a celestial body. At the moment there are three ways to measure the gravity field of a planet from space, by (1) Earth-based tracking of a spacecraft, (2) satellite-to-satellite tracking (SST) or (3) by satellite gravity gradiometry (SGG).

Earth-based tracking of spacecraft

Earth-based tracking of spacecraft is the oldest technique of the three. From the beginning of spaceflight it is used to determine where a spacecraft is. The first observations made use of data

based on optical data, while nowadays radiometric Doppler data is used for orbit determination. The measurement technique exploits precise phase measurements of a microwave beam generated from a stable frequency reference at a ground station, transmitted to the spacecraft and coherently sent back to earth by means of a transponder. At the ground stations the frequency shift [55]:

$$\frac{\Delta v}{v} = y \quad (3.1)$$

and the relative velocity Δv

$$\Delta v = cy \quad (3.2)$$

are measured with an investigation time τ . Here $c = 3 \cdot 10^5$ km/s represents the speed of light and y the Doppler radio signal. Due to the Doppler shifts in radio signals between the satellite and the ground station, perturbations can be seen in the orbit. From these perturbations the gravity field can roughly be determined.

The flyby geometry has a strong effect in the combined determination of J_2 and C_{22} . It is difficult to measure both J_2 and C_{22} from the same flyby, J_2 can be best determined from a polar orbit and C_{22} from an equatorial orbit [2]. In an equatorial flyby, the purely radial acceleration due to the second degree zonal harmonic (J_2) can be separated from the acceleration caused by the sectoral term C_{22} , by looking at the difference in the variation compared to the distance from the body. In addition, the velocity variation perpendicular to the flyby-plane (the quantity provided by Doppler data) is smaller than for a high inclination flybys. These facts make equatorial flybys better suited to determine the non-zonal harmonics, the same holds for determination of the J_2 term in a polar orbit. The geometry affects the estimation of J_2 and C_{22} in another way too: Doppler measurements are sensitive only to the line-of-sight component of the velocity. This inherent geometrical symmetry of the problem (rotations in the line of sight do not change the observables) may result in nearly singular matrices and large estimation errors, if the data arc is too short [24].

Satellite-to-satellite tracking

SST is based on the same principle as Earth-based tracking of satellites. Instead of measuring from a fixed point on the Earth, another satellite is used to determine the position of the reference satellite. There are two types of SST: high-low and low-low SST. With high-low SST one satellite orbits a celestial body in a high orbit, while the other reference satellite orbits the body in a low orbit. Around the Earth, GPS-satellites are used for precise positioning of the low-flying reference satellite. In the low-low formation, the distance between two satellites in the same orbit is measured. This distance changes due to the changes in the gravitational field of the body, which on its turn changes due to internal mass distribution. Hence from the variance in the distance between the two satellites, the gravity field is retrieved. An advantage of SST above Earth-based tracking is that SST is able to give nearly continuous, high-precision and three-dimensional information of the gravity field.

Satellite gravity gradiometry

SGG is based on measured accelerations, the difference in acceleration is the gradient in the gravitational acceleration. Using three pairs of three accelerometers located at different points, the variations in X, Y and Z-direction can be measured and the various components of the gravity gradient tensor can be determined. Defining a gradiometer measurement as Γ_{ij} , a measurement of a one component gradiometer can be defined as [59]:

$$\Gamma_{ij} = \frac{a_j(B) - a_j(A)}{b_{AB}^i} = \frac{\Delta a_j}{b^i} \quad (3.3)$$

Here, i represents the direction of the baseline and b_{AB}^i the length of the baseline between the two proof masses A and B . Subscript j gives the direction the accelerometers are oriented in the a local reference frame and a_j gives the acceleration measured. Measurement precision ($\frac{\sigma(\Gamma)}{\Gamma}$) is determined by the standard deviation $\sigma(a)$ of the two accelerometer measurements [m/s^2], which are assumed to be identical, and the uncertainty of the baseline, $\sigma(b)$, is given as [59]:

$$\frac{\sigma(\Gamma)}{\Gamma} = 2 \frac{\sigma(a)}{\Delta a} + \frac{\sigma(b)}{b} = 2 \frac{\sigma(a)}{\Gamma \cdot b} + \frac{\sigma(b)}{b} \quad (3.4)$$

If the baseline is rigid, assuming thermal expansion of the structure can be neglected, the term $\sigma(b)/b$ is equal to zero and the relative precision of a gradiometer is determined by the precision of the accelerometer measurement and the length of the baseline. This means that when the baseline length is increased, the gradiometer precision increases as well. Hence increase in baseline length is an important aspect to increase gradiometric performance, provided that error sources due to other sensor elements have to stay below this level [59].

One of the main problems with observing gravity using a satellite mounted gradiometer is the fact that the strength of the a gravitational field decreases with altitude. This is very good shown by the Meissl scheme, see figure 3.1, which is based on the representation by spherical harmonics. The horizontal lines represent the amplification gained when measuring a derivative of gravitational potential. The vertical lines show the damping which increases with altitude. The orbit of a satellite must therefore be as low as possible to observe the strongest gravitational signal. However, the lower the orbit the more air-drag the satellite experiences, which causes disturbances in the motion of the satellite. Atmospheric drag is not the only non-gravitational acceleration that influences the measurements, others are:

- Direct solar pressure radiation
- Pressure of the planet's albedo
- Pressure of the planet's infrared radiation

All these accelerations are measured together with the gravitational accelerations by the gradiometer, and have to be 'subtracted' from the signal in order to derive the best possible gravity-field model. On the GOCE satellite (see next section) active drag compensation and angular control will be used in order to maintain its extremely low orbital altitude of 250 km and to compensate for the effect of non-gravitational forces [59].

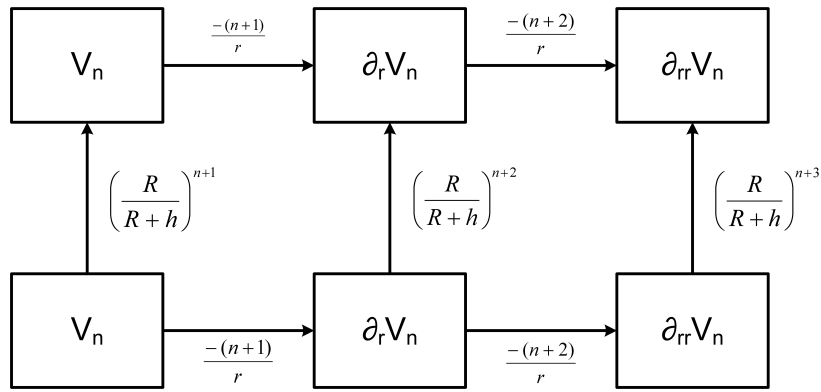


Figure 3.1: The Meissl scheme, which shows the damping factors (vertical) and amplification factors (horizontal) for a signal constituent V_n of degree n [35].

3.1.2 Gravimetric missions

In the past several missions to determine the gravitational field of the Earth have been launched and are still flying. The CHALLENGING Minisatellite Payload (CHAMP), launched in 2000, determines gravitational anomalies using the high–low SST technique. The two Gravity Recovery And Climate Experiment (GRACE) satellites, still in orbit, use the low–low SST principle. The Gravity field and steady–state Ocean Circulation Explorer (GOCE), expected launch October 2008, will use a combination of SGG and high–low SST to determine the Earth’s gravity field with a precision of 1 mGal.

CHALLENGING Minisatellite Payload

Orbiting at a an altitude of approximately 400 km and using the high GPS satellites at an altitude of around 20,000 km, it led to an improvement of up to two orders of magnitude in accuracy in global gravity models for features of up to a few thousand kilometers. For example, there has been a significant improvement in the data from polar regions, which are difficult to access from the ground. With CHAMP temporal changes in the gravitational field due to global mass redistributions, which are in general small, slow and large–scaled, can be recovered with a higher signal/noise ratio and an increased spectral resolution too [20]. By this, a discrimination between various signal sources becomes possible. The most interesting temporal gravity variations causing a global signature, result from atmospheric mass redistributions, ocean circulation, sea level changes due to polar ice melting or aggregation, and the visco–elastic response of the Earth’s lithosphere to past and present loads [16].

Gravity Recovery And Climate Experiment

GRACE makes use of satellite–to–satellite tracking between two low–flying satellites. The twin satellites GRACE–A and GRACE–B fly in formation, about 200 km apart, at an altitude of 400 km. In addition, both satellites track signals transmitted by the GPS constellation. The goal of the GRACE mission is to determine both the static as the time–variable components of the Earth’s gravity field.

The two satellites can be seen as a one component gradiometer with a very long baseline to

achieve a high accuracy. The distance between the two satellites is constantly communicated via a microwave K-band ranging instrument. As the gravitational field changes beneath the satellites - correlating to changes in mass (topography) of the surface beneath - the orbital motion of each satellite is changed. This change in orbital motion causes the distance between the satellites to expand or contract and can be measured using the K-band instrument. From this, the fluctuations in the Earth's gravitational field can be determined [78].

Gravity field and steady-state Ocean Circulation Explorer

GOCE is one of the core missions of ESA's Living Planet Programme. GOCE will have a nominal mission duration of 20 months. The short mission duration is due to the relatively large atmospheric drag the spacecraft experiences in its, for a satellite, extremely low orbit of 250 km altitude. The low orbit is needed to receive as strong a possible measurement of the gravity gradients, which get weaker with increasing altitude. It uses the combination of high-low SST and SGG, because it is not possible to map the complete gravity field at all spatial scales with the same quality only with the gradiometer. The gradiometer is used to measure high resolution features of the gravity field while GPS is used to obtain low-resolution data. The combination of these two principles provides the opportunity to derive a global geoid model with a 100 km spatial resolution and 1–2 cm accuracy. Gravity-field anomalies can be determined with an accuracy of 1 mGal ($1 \text{ mGal} = 10^{-5} \text{ m/s}^2$) [20].

GOCE is equipped with three pairs of 3-axis accelerometers, which by differential measurements act as a conventional gradiometer. In addition, it has a high quality 12-channel GPS receiver and a laser retro-reflector enabling tracking by ground-based lasers. The spacecraft has a rigid structure with fixed solar wings and no movable parts single. Its body is octagonal, about five meters long and one meter in diameter, the cross-section is minimized in the direction of flight to reduce atmospheric drag and it has tail fins which act as passive stabilizers [10]. All these features make GOCE look like a spy plane from a movie, see figure 3.2.

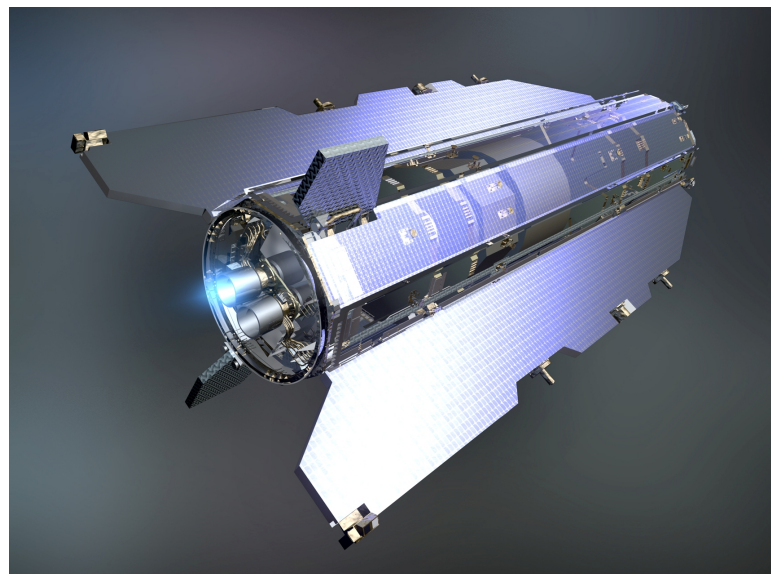


Figure 3.2: Artist impression of the GOCE spacecraft [Courtesy: ESA].

3.2 Balloon-borne gravimetry

Acquiring gravimetric data from airborne platforms is nowadays very common, even commercially exploited in the oil and gas industry to identify pockets of oil and gas within the Earth's crust. Balloon-borne gravimetry is, on the contrary, not at all common. A balloon operates in a dynamic, largely unpredictable environment. To see what the influence on gravimetric measurements is, balloon borne gravimetry on Earth is treated in this section. It is assumed that a balloon in the atmosphere of Titan behaves in the same way. Though the experimental results are very limited, a description is given in this section.

On Earth in late September 1983, gravity measurements from a high-altitude balloon, DUCKY Ia, were made to verify global and upward-continued gravity models. A second flight in DUCKY II was made in October 1985. The first flight was intended to provide balloon motion and environment data with a preliminary estimate of the quality of measured gravity values and showed that tracking was the most difficult problem. Therefore the second flight included differential GPS tracking, tested the use of differential GPS tracking and measured gravity at altitude [39].

The gravimeter package that is suspended underneath the balloon senses accelerations due to balloon motions as well as gravitational acceleration, therefore these motions must be very accurately accounted for in gravity estimation. Additional instrumentation is required to measure as many balloon motions as possible, such as rotation, bobbing and swaying, see figure 3.3. Therefore during the DUCKY experiments independent measurements were made of the balloon motions by an inertial navigation package (three accelerometers, three rate gyros, three-axis magnetometer and two tiltmeters) combined with ground tracking (X, Y and Z position and velocity). In the second flight a radar transponder and a GPS receiver was added [38].

For the specified time interval (1 second) during which the measurements were made, the variation of the balloon accelerations was expected to be significantly greater than the variations expected in the Earth's gravity field. According to [39] the independent measurements will allow for separation of balloon-induced accelerations from gravitational acceleration to 1 mGal, using tracking data to an accuracy of about 5 cm/s in velocity for Eötvös corrections, and position to 1 m. The results of the first flight were successful [38] and a preliminary look to the raw data for the entire flight is given in [38], but no conclusion were drawn yet. The second flight was, according to [39], a success too, but results of these flight were never published and not accessible.

Later studies by C. Jekeli, [26] and [27], focused on the feasibility of using GPS in conjunction with an inertial navigation system (INS) to measure the gravity vector on a moving platform, specifically a high altitude balloon. This studied showed that the the errors, which were dominated by GPS related errors, needed to be reduced to make the GPS/INS a feasible gravimetry system.

3.3 Theoretical background on gradiometry

State-of-the-art methods for determination of gravitational fields from satellites use two or more proof masses and measure the relative motion of these proof masses. This can be done by measuring dynamically relative forces or angular momenta [35]. First the general formulae for gra-

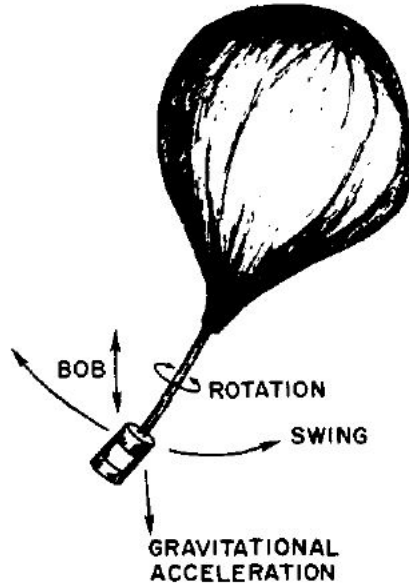


Figure 3.3: A sketch by A. R. Lazarewicz [38] showing the exaggerated motions of a gondola underneath a balloon. Each of these motions contribute to the vertical acceleration vector, thus confusing the gradiometer data.

diometry are derived, then the observation equations for SGG are given.

3.3.1 Theoretical background on gradiometric measurements in general

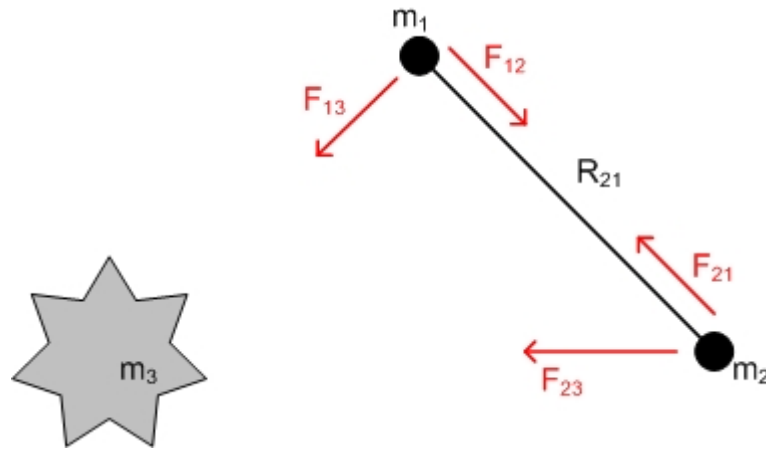


Figure 3.4: Forces between three bodies, F_{23} is the force where m_2 is attracted m_3 . Note that $F_{21} = -F_{12}$.

Suppose \mathbf{K}_{ij} is the force acting on m_i in the gravitational field of m_j i.e. m_i is attracted by m_j , see figure 3.4. The equation of motion of the proof masses m_1 and m_2 in the gravitational field of m_3 can then be written according to Newton's second law as [35]:

$$\mathbf{F} = m\mathbf{a} \Rightarrow m_2\ddot{\mathbf{R}}_2 = \mathbf{F}_{12} + \mathbf{F}_{23} \quad \text{and} \quad m_1\ddot{\mathbf{R}}_1 = \mathbf{F}_{13} + \mathbf{F}_{12} = \mathbf{F}_{13} - \mathbf{F}_{21} \quad (3.5)$$

where $\ddot{\mathbf{R}}_i$ represents the acceleration of the proof masses $i = 1, 2$. The relative acceleration vector

between the proof masses m_1 and m_2 is defined as $\ddot{\mathbf{R}}_{12} = \ddot{\mathbf{R}}_2 - \ddot{\mathbf{R}}_1$, which using equation 3.5 can be written as:

$$\ddot{\mathbf{R}}_{12} = \frac{1}{m_1} \mathbf{F}_{13} + \frac{1}{\mu_{12}} \mathbf{F}_{21} \quad (3.6)$$

where μ_{12} is the reduced mass

$$\mu_{12} = \frac{m_1 m_2}{m_1 + m_2}$$

Because $\mathbf{F}_{23} = m_2 \mathbf{g}_3(\mathbf{R}_2)$ and $\mathbf{F}_{13} = m_1 \mathbf{g}_3(\mathbf{R}_1)$, using $\mathbf{g} = \nabla V$, equation 3.6 can be rewritten as [35]:

$$\mu_{12} \ddot{\mathbf{R}}_{12} = \mu_{12} (\mathbf{g}_3(\mathbf{R}_2) - \mathbf{g}_3(\mathbf{R}_1)) + \mathbf{F}_{12} \quad (3.7)$$

where the term

$$\mu_{12} (\mathbf{g}_3(\mathbf{R}_2) - \mathbf{g}_3(\mathbf{R}_1)) = \mathbf{G}_{(21)3}$$

is a tidal force: it is the *difference* between the gravitational interaction of proof masses m_1 and m_2 with body m_3 . Summarizing, the equation of motion of proof mass m_2 relative to proof mass m_1 , both under influence of a third body m_3 is given as:

$$\mu_{12} \ddot{\mathbf{R}}_{12} = \mathbf{G}_{(21)3} + \mathbf{F}_{21} \quad (3.8)$$

If body m_3 is for instance a celestial body, then $\mathbf{g}_3(\mathbf{R}) = \nabla V(\mathbf{R})$, where V is the gravitational potential of that celestial body.

The tidal force $\mathbf{G}_{(21)3}$ can be determined in two different ways: (i) using the kinematic $\mathbf{R}_{12}(t)$ of the relative motion between two satellites m_1 and m_2 or (ii) by direct measurement. Two different gradiometer concepts can be used to measure the tidal force directly, namely (a) inline gradiometry or (b) cross-component gradiometry. The concept of inline gradiometry works as follows: the distance between the two proof masses is kept constant and the relative acceleration vector in line of the two masses is measured. In cross-component gradiometry the two proof masses are rigidly connected and the angular momentum generated by the tidal field is measured [35].

3.3.2 Observation equations for SGG

A gradiometer usually measures the force difference with respect to the center of mass (CoM) of the satellite, point S . Now, $\mathbf{g}_3(\mathbf{R}_i)$, with $i = 1, 2$, can be expanded in a Taylor series around point S , where $R_S = \frac{R_1 + R_2}{2}$ [35]:

$$\mathbf{g}_3(\mathbf{R}_i) = \mathbf{g}_3(\mathbf{R}_S) = \nabla \mathbf{g}_3(\mathbf{R}_S) (\mathbf{R}_i - \mathbf{R}_S) + O(|\mathbf{R}_i - \mathbf{R}_S|^2), \quad i = 1, 2.$$

Because the distance between the two proof masses (\mathbf{R}_{12}) is very small, quadratic and higher order terms can be neglected. Thus the tidal force $\mathbf{G}_{(21)3}$ can be approximated by:

$$\mathbf{G}_{(21)3} \approx \mu_{12} \nabla \nabla V(\mathbf{R}_S) \mathbf{R}_{12}$$

The tensor $\nabla\nabla V$ is called the gravitational tensor Γ . The elements of Γ are the second derivatives of the gravitational potential. Equation 3.8, which gives the equation of motion of proof mass m_2 relative to proof mass m_1 , both under influence of a third body (as shown in figure 3.4), can now be approximated as [35]:

$$\mu_{12}\ddot{\mathbf{R}}_{12} \approx \mu_{12}\Gamma(\mathbf{R}_S)\mathbf{R}_{12} + \mathbf{F}_{21} \quad (3.9)$$

When the gravitational interaction between the two proof masses is small (for instance if the masses m_1 and m_2 are small) \mathbf{F}_{12} can be neglected. Then the acceleration vector of m_2 relative to m_1 is approximated by [35]:

$$\ddot{\mathbf{R}}_{12} \approx \Gamma(\mathbf{R}_S)\mathbf{R}_{12} \quad (3.10)$$

This equation is used as basic functional model for satellite gravity gradiometry. For instance with the in-line gradiometer concept, the distance $|\mathbf{R}_{12}|$ is kept constant and the relative acceleration $\ddot{\mathbf{R}}_{12}$ is measured.

A gradiometer on board of the satellite, rotates, though slow, in inertial space. The force actually measured by the gradiometer is gravity and not gravitation. If \mathbf{r}_i is the vector pointing from the CoM of the balloon (point S , which is assumed to be identical with the origin of the reference system of the gradiometer) to a proof mass m located at O_i , then the measurable acceleration of the proof mass in a rotating reference frame with rotation vector ω can be given as [35]:

$$\mathbf{a}_i = (\nabla V_i - \nabla V_S) - \dot{\omega} \times \mathbf{r}_i - \omega \times (\omega \times \mathbf{r}_i) \quad (3.11)$$

where V_i and V_S are the gravitational potential at O_i and S respectively. The linear acceleration of the proof mass induced by the gravitational potential is denoted by $(\nabla V_i - \nabla V_S)$, the linear acceleration of the proof mass induced by the satellite's angular accelerations is given by $\dot{\omega} \times \mathbf{r}_i$ and the centrifugal acceleration of the proof mass induced by the satellite angular rotation is given by $-\omega \times (\omega \times \mathbf{r}_i)$. Expanding ∇V_i in a Taylor series around the CoM (point S):

$$\nabla V_i = \nabla V_S + \nabla\nabla V_S \mathbf{r}_i + O(|\mathbf{r}_i|^2) \quad (3.12)$$

Since $|\mathbf{r}_i|$ is very small, equation 3.12 can be approximated by [35]:

$$\nabla V_i \approx \nabla V_S + \nabla\nabla V_S \mathbf{r}_i \quad (3.13)$$

combining this with equation 3.11:

$$\mathbf{a}_i = \nabla\nabla V_S \mathbf{r}_i - \dot{\omega} \times \mathbf{r}_i - \omega \times (\omega \times \mathbf{r}_i) \quad (3.14)$$

where

$$\nabla\nabla V = \Gamma = \begin{pmatrix} V_{xx} & V_{xy} & V_{xz} \\ V_{yx} & V_{yy} & V_{yz} \\ V_{zx} & V_{zy} & V_{zz} \end{pmatrix}, \quad \mathbf{r}_i = \begin{pmatrix} r_{x,i} \\ r_{y,i} \\ r_{z,i} \end{pmatrix}, \quad \omega = \begin{pmatrix} \omega_x \\ \omega_y \\ \omega_z \end{pmatrix}, \quad \dot{\omega} = \begin{pmatrix} \dot{\omega}_x \\ \dot{\omega}_y \\ \dot{\omega}_z \end{pmatrix} \quad (3.15)$$

here subscripts x, y and z denote the axis belonging to the reference system fixed to the gradiometer. Evaluating $\dot{\underline{\omega}} \times \mathbf{r}_i$ and $\underline{\omega} \times (\underline{\omega} \times \mathbf{r}_i)$, equation 3.11 can be approximated by (for the complete derivation see [35]):

$$\mathbf{a}_i \approx (\Gamma - \dot{\underline{\Omega}} - \underline{\Omega}^2) \Big|_S \mathbf{r}_i \quad (3.16)$$

with

$$\underline{\Omega}^2 = \begin{pmatrix} -(\omega_y^2 + \omega_z^2) & \omega_x \omega_y & \omega_x \omega_z \\ \omega_y \omega_z & -(\omega_x^2 + \omega_z^2) & \omega_y \omega_z \\ \omega_z \omega_x & \omega_z \omega_y & -(\omega_x^2 + \omega_y^2) \end{pmatrix}, \quad \dot{\underline{\Omega}} = \begin{pmatrix} 0 & -\dot{\omega}_z & -\dot{\omega}_y \\ \dot{\omega}_z & 0 & -\dot{\omega}_x \\ \dot{\omega}_y & \dot{\omega}_x & 0 \end{pmatrix} \quad (3.17)$$

From measurements in a rotating frame fixed to the satellite (equation 3.16) the gravitational tensor (Γ) cannot be measured directly, but only the sum of the gravitational acceleration, the centrifugal acceleration (the term $\underline{\Omega}^2$) and the angular acceleration (the term $\dot{\underline{\Omega}}$).

3.4 The specifications of gradiometers

The traditional method of measuring the Earth's gravity field is based on comparing the differences in how a 'test mass' responds to the gravitational attraction at different locations on the surface of the Earth. Nowadays gravity can be measured from space using a so-called gradiometer. MEMS technology is used to develop a micro-gradiometer, since the now existing technology, used in the GOCE satellite, is far too heavy and big to implement in a mission to (the moons of) outer planets.

This section describes first the values used to indicate the performance of a gradiometer in general, then gives characteristics of the gradiometer on board of GOCE and concludes with MEMS, the technology used to miniaturize gradiometers.

3.4.1 The performance of a gradiometer

There are several values that indicate the performance of an accelerometer or gravimeter: the sensitivity of the instrument, Total Noise Equivalent Acceleration (TNEA), the Power Spectral Density (PSD) and the Signal-to-Noise Ratio (SNR).

Sensitivity

The sensitivity of a gradiometer is proportional to the mass, m , over the spring constant, k , [13]:

$$\text{sensitivity} \propto \frac{m}{k} = \frac{1}{\omega_d^2} \quad (3.18)$$

where ω_d is a mechanical self resonance factor.

Total Noise Equivalent Acceleration

The TNEA is defined by the total mass, if the output signals are simply averaged and noise is not correlated [92]:

$$TNEA = \frac{\sqrt{4k_B T c}}{m} = \sqrt{\frac{4k_B T \omega_d}{Q m}} \quad (3.19)$$

with k_B the Boltzmann constant, T the temperature in Kelvin, c the damping factor, Q a quality factor, m the mass of the proof mass and ω_d the mechanical self resonance factor. Equation 3.19 shows that mechanical noise can be reduced by increasing the proof mass size and reducing damping. A combination of N accelerometers improves the TNEA by a factor of $N^{-1/2}$, hence it is defined by total mass, if output signals are simply averaged and noise is not correlated [13].

Power Spectral Density

Power spectral density function (PSD) shows the strength of the variations (energy) as a function of frequency. In other words, it shows at which frequencies variations are strong and at which frequencies variations are weak. The unit of PSD is energy per frequency (width) and one can obtain energy within a specific frequency range by integrating PSD within that frequency range. Computation of PSD is done directly by a method called the Fast Fourier Transform (FFT) or by computing the autocorrelation function and then transforming it [6]. The PSD for all gravity gradiometers is given by [13]:

$$S_\Gamma = \Gamma_n^2 = \frac{8}{mb^2} \left(\frac{k_B T \omega_d}{Q(f)} + \frac{\omega_d^2}{2\alpha_e} \epsilon(f) \right) \quad (3.20)$$

where:

- Γ_n the gravity gradient noise
- b is the base line of the two test masses
- m the mass of one of the test masses
- k_B the Boltzmann constant
- T the temperature in Kelvin
- $\omega_d = 2\pi f$ is the mechanical resonance frequency of the differential mode
- Q the quality factor of the resonance mode, in the case of a differential gradiometer the damping coefficient for the differential mode $Q = \tau_d^{-1}$
- α_e the energy coupling coefficient of the mechanical to electrical conversion
- ϵ is the sensor noise energy

The first term in the expression represents the mechanical and thermal noise, the second term the sensor noise energy. The mechanical noise, which is known as the Brownian noise, is thus given as [13]:

$$S_\Gamma = \frac{8}{mb^2} \left(\frac{k_B T \omega_d}{Q(f)} \right) \quad (3.21)$$

Signal-to-Noise Ratio

The SNR is defined as the detected signal in the measurement (the signal current or voltage, $S_{detected}$) to the noise (noise current or voltage, N) in that same measurement [31]:

$$SNR = \frac{S_{detected}}{N} \tag{3.22}$$

3.4.2 GOCE gradiometer

On board of the GOCE satellite will be the first gradiometer flown into space. It is a three-axis electrostatic gradiometer, that will measure gravity gradients in all spatial directions and specifically designed to measure the stationary gravity field. The main characteristics of the GOCE gradiometer are given in table 3.1 below.

Table 3.1: Characteristics of the GOCE three-axis diagonal gradiometer [Courtesy: ESA].

Design Measurement Bandwidth (MBW)	5×10^{-3} to 10^{-1} Hz
Baseline length	0.5 m
gravity gradient resolution	$10 \text{ mE}/\sqrt{\text{Hz}}$
Sensitivity (detection noise)	
Measurement bandwidth	$< 10^{-12} \text{ m/s}^2 \sqrt{\text{Hz}}$
Extended bandwidth (10^{-5} to 1 Hz)	$< 10^{-10} \text{ m/s}^2 \sqrt{\text{Hz}}$
Proof-mass positioning error	$6 \times 10^{-8} \text{ m} \sqrt{\text{Hz}}$
Absolute / relative scale factors	$10^{-3} / 10^{-5}$
Absolute / relative misalignment	$10^{-3} \text{ rad} / 10^{-5} \text{ rad}$

Because of launch delays, no actual data on the performance of GOCE can be given yet and the question remains if GOCE will meet the expectations set.

3.4.3 MEMS-technology used for miniaturize instruments

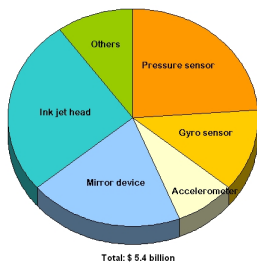


Figure 3.5: The MEMS market in 2005 [67].

MEMS is short for Micro-Electro-Mechanical Systems. Micro, since these systems have static or movable components with dimensions on the scale of a micrometer. MEMS combine the mechanical and electrical function in micro-devices, think of pressure sensors, accelerometers, gyroscopes and optical devices as well as chemical, biomedical and fluidic applications. Mechanical and electrical components are integrated within a single silicon chip, which creates the possibility of complete systems-on-a-chip. MEMS will allow the development of smart products, it will be able to increase the computational ability and thereby increase the possible applications.

When thinking of space applications, reliability, power consumption and size are critical criteria. Keeping this in mind, possible applications in the future, which rely on the same critical criteria, could even be as advanced as implantable sensors for medical applications.

MEMS are already widely used on Earth in a lot of different applications. Looking at the MEMS market of 2005 (figure 3.5), there are two major applications for MEMS devices: as active device for ink jet printer heads or micro mirror device for projectors or as passive device such as a sensor. Although the general applications are starting to expand, the market is still fairly small [67].

Gradiometers are mainly accelerometers confined in different directions, between which the difference in acceleration is measured. MEMS accelerometers are used on Earth in the automotive industry, among others as sensors for the airbag defolding mechanisms. Therefore it is more than logical to first look at the possibilities and operation of a MEMS accelerometer.

MEMS accelerometers

Most MEMS accelerometers consist of a suspended seismic mass that is displaced and measured, see figure 3.6. Thus the position of the seismic mass depends on the momentary acceleration sensed by the device. This displacement is then translated into for instance, a resistance in piezoelectric accelerometers or into capacitance in capacitive accelerometers [79]. State of the art read-out mechanisms in low-noise MEMS accelerometers are, including the two examples given above [13]:

- Piezoresistive
- Piezoelectric
- Resonant
- Thermal
- Electron tunneling
- Optical
- Capacitive

Capacitive, electron tunneling and optical read-outs have demonstrated displacement resolutions in the order of $10^{-13} \text{ m}/\sqrt{\text{Hz}}$. Electronic feedback and spring constant tuning are already standard techniques in MEMS accelerometers. A disadvantage regarding the standard MEMS techniques used is that silicon is not a good material for obtaining large proof mass. It has a low density compared to other materials that could be used, such as titanium (Ti, 4507 kg/m³), chromium (Cr, 7140 kg/m³), nickel (Ni, 8909 kg/m³), tantalum (Ta, 16 650 kg/m³) or platinum (Pt, 21 090 kg/m³). Next to that, the thickness is limited to wafer thickness, which typically is 0.5 or 0.8 mm. On the other hand, silicon is a very good material to make suspension springs, quality factors between 10^4 and 10^5 have been demonstrated in industry. Micro-machining techniques do offer high precision during fabrication, which can be very advantageous in realizing reliable read-out structures [13].

Possible approaches to get to a precision of $10^{-13} \text{ g}/\sqrt{\text{Hz}}$ using MEMS technology for accelerometry are [13]:

- A hybrid solution, e.g. to combine MEMS suspension/sensing/actuation with a large external proof mass

- To use the mass of entire wafers, by using a dense array of sensors such that the noise level is defined by the total mass: a 10 mm wafer weighs 10 grammes and a 30 mm wafer weighs already as much as 130 grammes. Other solutions are all wafer gradiometers or by using an array of accelerometers
- To use a free hanging electrostatically suspended proof mass to eliminate all damping. A side note is that MEMS accelerometers with electrostatic elevation are still in an infant state of development, but that there might be possibilities in the future

MEMS micro-gradiometer

It has been noted several times already that the GOCE-gradiometer is far to bulky to use for a mission to the (moons of) the outer planets. In the Netherlands, research is done at the University of Twente, MESA+ Institute of technology and SRON for gravity gradient sensor technology for future space missions. The concept design, see figure 3.7, is a single-axis micro-gradiometer etched from one silicon wafer. A sensitivity of $1 \text{ E}/\sqrt{\text{Hz}}$ is needed for planetary mission, see [13].

Table 3.2: Specifications of a micro-gravity gradiometer [13].

Low mass	$m = 1 - 3 \text{ kg}$
Low baseline	$b = 0.1 \text{ m}$
Mechanical quality factor	$Q = 10^5$
Lower operation temperature	$T = 77 \text{ K}$
Resonance frequency	$f = 1 \text{ Hz}$
Displacement resolution	$\Delta x = 10^{-11} \text{ m}$
Energy-coupling efficiency	$\alpha_e \cong 1$
Silicon wafer	0.3 m diameter, 0.8 mm thick

The noise level is an indication of accuracy and sensitivity of the instrument, given by equation 3.20 in units of $\text{E}/\sqrt{\text{Hz}}$. Normally the exact values of the noise level of an instrument are known after several tests done after fabrication. In this case, since the gradiometer is still in the design phase, the noise level for computational purposes is assumed to be $0.1 \text{ E}/\sqrt{\text{Hz}}$ for frequencies of 10^{-3} Hz and higher. For the lower frequencies the noise level is assumed to be $1/f$ noise [23].

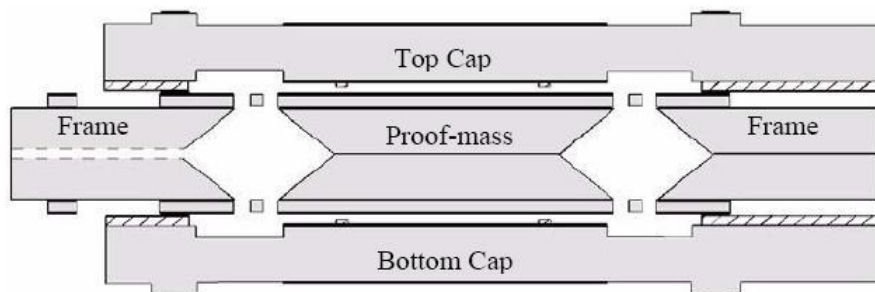


Figure 3.6: Cross-section of a MEMS accelerometer [67].

The specifications of this ideal concept design are given in table 3.2. Simulations of this ideal concept design prove that, if temperature stability can be guaranteed, the sensor noise is most dominant around one Herz [13]. Moreover the sensor has a low resonance frequency of 1 Hz, but feedback is needed to make the system fast enough. The springs of the ideal concept are extremely weak compared to their mass: for a mass of 39 grammes, the spring stiffness is $k = 10^{-6} - 10^{-1}$ N/m. Because these springs are designed for a zero gravity environment, they are, compared to the mass, too weak to support on Earth. The springs which are used during production and lab testing are much stiffer: $k = 1.4$ N/m. On the ideal concept some more restrictions have to be made: cubesats, the perfect testbed for MEMS sensors, have size restrictions (8×8 cm) to which the concept gradiometer must stick. To improve the sensitivity of the gradiometer, extra masses are attached to the structure [13].

Further simulations were done using the more realistic concept design. In the design maximum length springs which should survive Earth gravity in one axis ($3 \text{ cm} \times 0.5 \text{ mm} \times 50 \mu\text{m}$) were used and four extra masses (Pyrex block of $1 \times 1 \times 5$ cm, 11.2 gram each) were attached to the top and bottom of the test masses. This resulted in a resonance frequency of 2 Hz. First simulations of the gradiometer with the attached masses ([5], 2006) showed a total sensitivity of $17 \text{ E}/\sqrt{\text{Hz}}$, while later simulations ([13], 2007) give a total sensitivity of $2.6 \text{ E}/\sqrt{\text{Hz}}$. Still improvements have to be made to bring the sensitivity below $1 \text{ E}/\sqrt{\text{Hz}}$.

The final design of the gradiometer will be focused on mission requirements. The design of the gradiometer however is beyond the scope of this research and will not be treated any further.

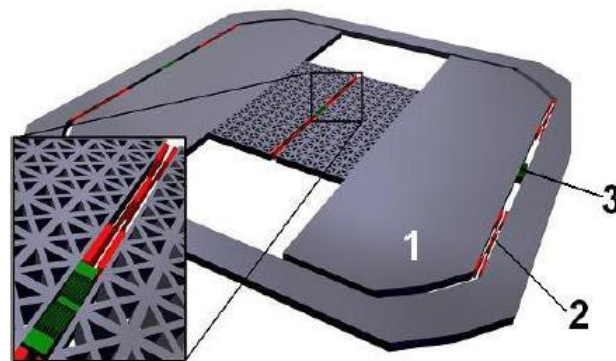


Figure 3.7: The proposed micro-gradiometer. The green parts are capacitive read outs and the elements in red are springs. The figure shows the proof mass (1), the spring (2), and the capacitive read-out (3) [23].

The gravity field of a planet

Mapping the gravitational field of a planet or satellite tells something about the interior of that particular body. Small variations in the gravitational field can be caused by varying densities of rocks and structures beneath the surface. This chapter will go into more detail on theory of gravitational fields and how the gravity field is determined. Section 4.1 gives the most common way to represent the gravitational potential, in spherical harmonics, and alternative ways of representing the gravity field. Section 4.2 describes how the gravity gradients are determined. The theory of the tidal potential is treated in section 4.3. This chapter concludes with the tidal parameters of Titan as suggested in literature.

4.1 Gravitational potential

The gravitational potential of a planetary body is, in absence of seismic data, the most powerful source of information concerning its internal structure [55]. The total perturbing potential, V is given by the sum of the gravitational potential V_g and the rotational potential V_r [7]:

$$V = V_g(r, \vartheta, \lambda) + V_r(r, \vartheta, \lambda) \quad (4.1)$$

where r stands for the radial distance, ϑ the colatitude and λ the longitude of the measurement point. The gravitational potential which acts on the satellite is given by [7]:

$$V_g(r, \vartheta, \lambda) = -\frac{GM}{r} \left[1 - \sum_{n=0}^{\infty} \left(\frac{R_e}{r} \right)^n J_n P_n(\cos \vartheta) \right] \quad (4.2)$$

again r stands for the radial distance, ϑ the colatitude and λ the longitude of the measurement point, furthermore is G the gravitational constant, M the mass of the planet, R_e the equatorial radius of the planet, J_n the gravitational moments and $P_n(\cos \vartheta)$ the Legendre polynomials (see appendix C). The rotational potential is defined as [7]:

$$V_r(r, \vartheta, \lambda) = -\frac{1}{2} r^2 \omega_{rot}^2 \sin^2 \vartheta \quad (4.3)$$

with ω_{rot} the rotational period of the planet.

This section will start with an explanation of the terms hydrostatic and isostatic equilibrium and how they are used in the theory of the gravitational potential. Next, the formulae of the moment of inertia of a planet are described. The spherical harmonic representation of the gravitational potential, which is the most widely used method of describing the gravitational potential, is given and this section concludes with alternative representations of the gravitational potential.

4.1.1 Hydrostatic and isostatic equilibrium

For rotating bodies, the effective gravity is less than the gravitational attraction calculated for a non-rotating planet, since the centrifugal force induced by rotation is directed outwards from the planet. The equipotential surface must thus be derived from the sum of the gravitational potential (equation 4.2) and the rotational potential (equation 4.3):

$$V_g(r, \vartheta, \lambda) + V_r(r, \vartheta, \lambda) = \text{constant} \quad (4.4)$$

The equipotential surface of the Earth is called the geoid. For other planets and satellites this name geoid is used often too. Sometimes other words are used, for instance the equipotential of the moon is called the luneoid. Deviations in the observed gravity data with respect to (theoretical) geoid models provide information on the structure of the crust and mantle of a planet. Before the observed data can be used for comparison to the models, several corrections will have to be made. The then derived low-degree harmonics are accredited to (large-scale) dynamic processes, like the sinking of the subducting oceanic slab and post-glacial rebound, and in models described by dynamic isostasy. The higher degree harmonics are usually well explained by the static isostatic conditions (like mountains), using Airy's or Pratt's hypothesis, see following sections.

Hydrostatic equilibrium

The internal structure of a spherical body is determined by the balance between gravity and pressure. The increase in pressure (Δp), or force per unit area, is given by [7]:

$$\Delta p = -g_p \rho \Delta z \quad (4.5)$$

where g_p is the gravitational acceleration, ρ the density and Δz the increase in height. Both the gravitational acceleration and the density depend on altitude. The balance between temperature, pressure and density of the planets atmosphere and interior is called hydrostatic equilibrium, which is given by [7]:

$$p(r) = - \int_{r_0}^{r_1} g_p(\tilde{r}) \rho(\tilde{r}) d\tilde{r} \quad (4.6)$$

here p is the pressure, r_0 and r_1 the lower and upper boundary respectively, ρ again the density and \tilde{r} the radial distance integrated over. Assuming the density of the planet is constant, the pressure in the center of the planet, p_c is given by equation 4.6 as:

$$p_c = \frac{3GM^2}{8\pi R^4} \quad (4.7)$$

where G is the gravitational constant, M the mass of the planet and R the radius of the planet. This value sets the lower limit to the pressure in the center of the planet, since normally the density increases with radial distance. As equations 4.6 and 4.7 show, the gravity field indirect gives information on the interior of a planet. The upper limit of the central pressure is given by [60]:

$$p_c = \left(\frac{\rho_c}{\bar{\rho}} \right)^{4/3} p_{c,low} \quad (4.8)$$

where $p_{c,low}$ is the value for the lower limit of the pressure given by equation 4.7, $\bar{\rho}$ the mean density of a planet and ρ_c the density of the planets core.

Isostatic equilibrium

The concept of isostatic equilibrium is based on the theory of hydrostatic equilibrium, as described above. On geological time scale, mountains in isostatic equilibrium behave the same as icebergs float on water; the rigid surface layers (the lithosphere) ‘float’ on the highly viscous ‘fluid’ layers (the asthenosphere). A mountain in isostatic equilibrium is compensated by a deficiency of mass underneath, since the volume of the mountain submerged in the upper mantle is lighter than the mantle material displaced. The total mass of the material displaced is equal to the total mass of the mountain [7]. This does not hold for all mountains on the Earth, certain areas (such as the Himalayas) are not in isostatic equilibrium, which has forced researchers to identify other reasons to explain their topographic heights. For instance at the Himalayas it is believed that the force of the impacting Indian and Eurasian plates forces the mountains upwards ([7] and [80]).

The deficiency or addition of mass at deeper layers of mountains or oceans are computed assuming isostatic equilibrium and using Airy’s or Pratt’s hypothesis. Airy’s hypothesis assumes a constant density for all the crustal layers and a larger value for the fluid mantle material. As can be seen on the right of figure 4.1, a mountain of height h_1 is compensated by the depth of the continental root, h_2 . Here the Airy condition applies [80]:

$$\rho_C h_1 = (\rho_M - \rho_C) h_2 \tag{4.9}$$

with ρ_C the density of the crust and ρ_M the density of the mantle. Underneath the crust–mantle boundary (under the dashed line and the mountain in the right figure of figure 4.1) there is hydrostatic equilibrium, because the amount of mass above this level is everywhere the same. This model proves to be a reasonable approximation for mountain ranges. As shown, within one column the Airy isostatic model can have various densities, whereas the Pratt’s hypothesis assumes that each column has a uniform density, see the left picture of figure 4.1. The height of the column above the depth where all columns are in hydrostatic equilibrium, is thus dependent on the density of the specific column and given by [80]:

$$\rho_1 h_1 = \rho_2 h_2 = \rho_3 h_3 \tag{4.10}$$

with ρ_i the densities and h_i the heights above the crust–mantle boundary of the different columns, $i = 1, 2, 3$. Pratt’s hypothesis approximates the condition for a continental plateau quite well.

Corrections applied to the observed data

Before gravity measurements can be used to determine if a region is in isostatic equilibrium several corrections have to be made on the observed data. The free–air gravity correction projects the observed data on a reference height, which usually coincides with the reference ellipsoid of the planet. Above continental areas the Bouguer correction is applied to compensate for the extra mass between the surface of the Earth and the reference ellipsoid. After these corrections have been applied and local surface topography has been taken into account, the remaining differences

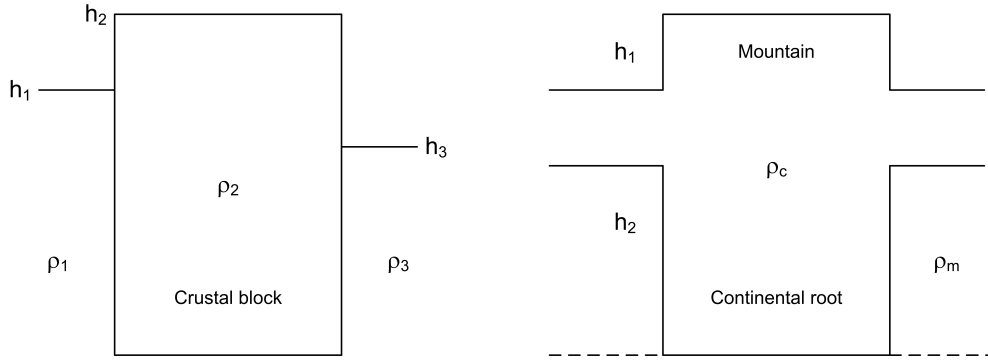


Figure 4.1: Static isostatic equilibrium: left Pratt isostasy and right Airy isostasy [80].

are then of geophysical interest [80].

The variation in surface gravity can be found by solving equation 4.4 and is given as function of latitude, φ , by [7]:

$$g(\varphi) = g_0(1 + C_1 \sin^2 \varphi + C_2 \sin^4 \varphi) \quad (4.11)$$

in which C_1 and C_2 are constants and g_0 the unperturbed surface gravity of a celestial body with radius R given by [22]:

$$g_0 = \frac{GM}{R^2} \quad (4.12)$$

In addition to this, the height at which the measurements are made has to be taken into account. Assuming that there is only air present above sea level up to an altitude h above the geoid, the free-air correction is equal to $2h/R$ ($h \ll R$, where R is the radius of the celestial body) [80]:

$$\Delta g_{FAA} \approx -\frac{2g_0 h}{R} \quad (4.13)$$

On the other hand, if there is a large slab of rock at the latitude of measurement, the free-air correction should be decreased by the gravitational attraction of rocks. This correction is known as the Bouguer correction [7]. The Bouguer correction can be found by considering axisymmetric ring elements, where the symmetry axis is aligned with the point where the gravity is observed. The ring element between the radial distance from the symmetry axis r and $r + dr$ has a volume of $dV = 2\pi r dr dz$ where z is the coordinate in the direction of the symmetry axis. The ring element is then situated at a distance of $\sqrt{r^2 + z^2}$ from the point where the gravity is observed, hence the vertical component of the gravity due to this ring element is given by [80]:

$$g(dV) = \frac{2\pi G \rho r dr dz}{r^2 + z^2} \times \frac{z}{\sqrt{r^2 + z^2}} \quad (4.14)$$

When integrating equation 4.14 over a plate with $0 < z < h$ and $0 < r < \infty$ the Bouguer correction becomes [80]:

$$\Delta g_B = \int_h^0 \int_\infty^r g(dV) dr dz = 2\pi \rho G h \quad (4.15)$$

where ρ is the density of the rocks and h again the height above the geoid. The Bouguer correction itself can be corrected using terrain correction factor, δg_T , which is based on a topographic map. Combining all these correction factors, the difference between the observed gravity, $g_p(obs)$, and the value expected the point of measurement, known as the Bouguer gravity anomaly, g_B , is ([7] and [80]):

$$\begin{aligned} g_B &= g_{obs} - \Delta g_{FAA} - \Delta g_B + \delta g_T \\ &= g_{(obs)} + \frac{2g_0 h}{R} - 2\pi\rho Gh + \delta g_T \end{aligned} \quad (4.16)$$

These lateral variations in density distributions result in gravity anomalies, which cause deviations in the measured geoid with respect to a spheroid calculated for a rotating, spherically symmetric, fluid planet. The geoid height anomaly, Δh_g , which is the geoid radius minus the spheroid radius, is used to express all these deviations and is related to the measured anomalies in the gravitational potential [7]:

$$g(\varphi)\Delta h_g = -\Delta V_g \quad (4.17)$$

For an isostatic density distribution this can be approximated by [7]:

$$\Delta h_g = -\frac{2\pi G}{g_p(\varphi)} \int_0^D \Delta\rho(z)z dz \quad (4.18)$$

where $\Delta\rho(z)$ is the anomalous density at depth z and D the compensation depth below which there are no horizontal gradients in density. The depth is measured downwards as positive and $z = 0$ corresponds to the geoid surface. The effective gravitational attraction is always normal to the geoid, so that there is a trough in the geoid where there is a negative gravity anomaly or positive potential anomaly (mass deficit), and there is a bulge in the geoid if there is a positive gravity anomaly or a negative potential anomaly (mass excess) [80].

4.1.2 Moment of inertia of a planet

The moment of inertia (MoI) of a planet, I_p , is computed using [24]:

$$I_p = \frac{8\pi}{3} \int_0^R \rho(r)r^4 dr \quad (4.19)$$

with r radial distance, R is the radius and ρ the density of the planet.

Undifferentiated (see section 2.3) models are characterized by the mass fraction of rock (silicate) with respect to the total mass of the body. The silicate mass fraction is given by [56]:

$$f_{silicate} = \frac{\rho_{sil}(\bar{\rho} - \rho_{ice})}{\bar{\rho}(\rho_{sil} - \rho_{ice})} \quad (4.20)$$

or similar the ice mass fraction [63]:

$$f_{ice} = 1 - \frac{\rho_{sil}(\bar{\rho} - \rho_{ice})}{\bar{\rho}(\rho_{sil} - \rho_{ice})} = 1 - f_{silicate} \quad (4.21)$$

where in both equations ρ_{sil} is the density of silicate present in the core, ρ_{ice} the density of ice present in the core and $\bar{\rho}$ the mean density of the planet. Differentiated models are characterized by the radius of the core (R_c) [56]:

$$R_c = \left(\frac{\bar{\rho} - \rho_M}{\rho_c - \rho_M} \right)^{1/3} R \quad (4.22)$$

with $\bar{\rho}$ again the mean density of the planet, ρ_c the density of the core, ρ_m the density of the mantle and R the radius of the planet.

4.1.3 Spherical harmonic representation of the gravitational potential

The gravitational field can be expressed in terms of a potential $V_g(\mathbf{r})$, which is defined as the integral over the gravitational force, $F_g(\mathbf{r})$, divided by the mass [7]:

$$V_g(\mathbf{r}) = - \int_{\infty}^r \frac{F_g(\tilde{\mathbf{r}})}{M} d\tilde{\mathbf{r}} \quad (4.23)$$

In general $V_g(\mathbf{r})$ satisfies Poisson's equation [7]:

$$\nabla^2 V_g = 4\pi\rho G \quad (4.24)$$

and, in empty space, where the density $\rho = 0$, $V_g(\mathbf{r})$ satisfies Laplace's equation [7]:

$$\nabla^2 V_g = 0 \quad (4.25)$$

The general solution to Laplace's equation can be written in spherical coordinates. For a non rotating fluid body in hydrostatic equilibrium this is given by:

$$V_g = -\frac{GM}{r} \quad (r \geq R) \quad (4.26)$$

with G the gravitational constant, M the mass of the body in question and r the radial distance. Equation 4.26 only holds outside the sphere (R represents the radius of the body). In reality planets are not perfect spheres and there are two general effects that produce these deviations [22]:

1. An equilibrium response of the planet to perturbing potentials
2. The deviation of the planet from symmetry due to departures from hydrostatic equilibrium

Thus solving Laplace's equation for an axisymmetric body, the gravitational potential is defined using a harmonic expansion [49]:

$$V_g = -\frac{GM}{r} \sum_{n=0}^{\infty} \sum_{m=0}^n \left(\frac{R}{r} \right)^n P_{nm}(\sin \phi) (C_{nm} \cos(m\lambda) + S_{nm} \sin(m\lambda)) \quad (4.27)$$

where [49]:

$$C_{nm} = \frac{2 - \delta_{0m}}{M} \frac{(n-m)!}{(n+m)!} \int \frac{r^n}{R^n} P_{nm}(\sin \phi') \cos(m\lambda') \rho(\mathbf{r}) dV \quad (4.28)$$

$$S_{nm} = \frac{2 - \delta_{0m}}{M} \frac{(n-m)!}{(n+m)!} \int \frac{r^n}{R^n} P_{nm}(\sin \phi') \sin(m\lambda') \rho(\mathbf{r}) dV \quad (4.29)$$

Usually the normalized coefficients are used. The most important (numerical) reason is that stable recursive schemes exist for the normalized Legendre functions whereas this is not necessary the case for the unnormalized Legendre functions. Thus by normalizing the coefficients the Legendre functions are mathematically better manageable. The normalization is defined by [49]:

$$\begin{Bmatrix} \bar{C}_{nm} \\ \bar{S}_{nm} \end{Bmatrix} = \sqrt{\frac{(n+m)!}{(2-\delta_{0m})(2n+1)(n-m)!}} \begin{Bmatrix} C_{nm} \\ S_{nm} \end{Bmatrix} \quad (4.30)$$

The normalized gravitational potential is now defined as [49]:

$$V_g(r, \phi, \lambda) = -\frac{GM}{r} \sum_{n=0}^{\infty} \sum_{m=0}^n \left(\frac{R_e}{r}\right)^n \bar{P}_{nm}(\sin \phi) (\bar{C}_{nm} \cos(m\lambda) + \bar{S}_{nm} \sin(m\lambda)) \quad (4.31)$$

where:

- V_g is the gravitational potential
- G is the universal gravitational constant of $6.673 \cdot 10^{-11} \text{ m}^3/\text{kg s}^2$
- M is the mass of the body
- R_e is the equatorial radius
- m is the spherical harmonic order, n is the spherical harmonic degree
- r, ϕ and λ are the distance, latitude and longitude respectively
- \bar{P}_{nm} are the fully normalized Legendre functions, given by [49]:

$$\bar{P}_{nm} = \sqrt{\frac{(2-\delta_{0m})(2n+1)(n-m)!}{(n+m)!}} P_{nm} \quad (4.32)$$

$$P_{nm}(x) = (1-x^2)^{m/2} \frac{d^m}{dx^m} P_n(x) \quad (4.33)$$

$$P_n(x) = \frac{1}{2^n n!} \frac{d^n}{dx^n} (x^2-1)^n \quad (4.34)$$

See appendix C too.

- \bar{C}_{nm} and \bar{S}_{nm} are the normalized spherical harmonic coefficients, describing the dependence of the potential on the internal mass distribution of the body of interest. An approximation of the size of these two coefficients on Earth is given by the empirical Kaula rule [33]:

$$\bar{C}_{nm}, \bar{S}_{nm} \approx \frac{10^{-5}}{n^2} \quad (4.35)$$

The geopotential coefficients with $m = 0$ are called the zonal coefficients, they describe the part of the potential that does not depend on the longitude. By inspection of equation 4.31 it can be seen that the terms S_{n0} vanish. For simplification the notation:

$$J_n = -C_{n0} \tag{4.36}$$

for the zonal coefficients is often used. If then the origin of the coordinate system coincides with the center of mass of the body, the gravitational coefficients C_{10} , C_{11} , S_{11} are equal to zero. Similarly C_{21} and S_{21} vanish as long as the z -axis is aligned with the main axis of inertia of the body. Rotating fluid bodies in hydrostatic equilibrium have $J_n = 0$ for all odd n , this has been found to be a very good approximation for the giant planets [7]. The sectoral harmonics are the terms with $m = n$, where the Legendre function reduces to a constant and a $(\cos \phi)^m$ term, this implies that there is no change of sign when following a certain meridian. The other components ($m < n$) are called the tesseral harmonics. The physical meaning of the zonal, sectoral and tesseral harmonics is illustrated in figure 4.2. Figure 4.3 shows what is this means for the higher order spherical harmonics.

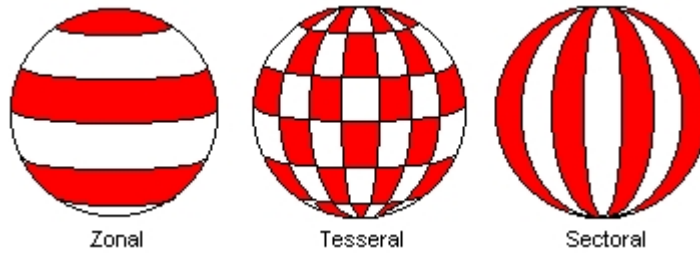


Figure 4.2: The different types of spherical harmonics [14].

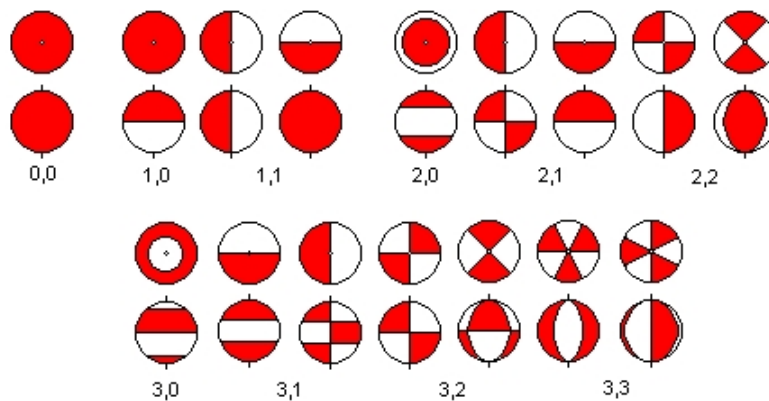


Figure 4.3: The physical interpretation of the higher order coefficients of the spherical harmonics [14].

A rotating planet which consists of an incompressible fluid of uniform density takes the form of a Maclaurin spheroid. From the solution for the equipotential surface (equation 4.4) it follows that the second harmonic, J_2 is related to the centrifugal and gravitational potentials ([7] and [22]):

$$J_2 = \frac{q r}{2} \quad (\rho = \text{constant}) \tag{4.37}$$

where

$$q_r = \frac{\omega_{rot}^2 R^3}{GM} \quad (4.38)$$

with again G the gravitational constant, M the mass, R the radius and ω_{rot} the rotational period of the planet. Usually the density (ρ) increases toward the center, such that $J_2 < q_r/2$. The ratio between J_2 and q_r is given by the so-called response coefficient Λ_2 [7]:

$$\Lambda_2 = \frac{J_2}{q_r} \quad (4.39)$$

The coefficient Λ_2 contains information on the spatial distribution of the mass in the planet's interior. Rotating planets with high-density cores have small values of Λ_2 , whereas bodies with a more homogeneous density distribution have large values of Λ_2 . The oblateness of a planet in hydrostatic equilibrium is related to the rotation period and the second harmonic [7]:

$$\frac{R_e - R_p}{R_e} \approx \frac{3}{2} J_2 + \frac{q_r}{2} \quad (4.40)$$

Here, R_e is the equatorial radius of the body and R_p the polar radius.

4.1.4 Alternative representations of gravitational fields

The standard representation of gravitational fields is in terms of spherical harmonics (SH). When using spherical harmonics, the only way to improve resolution is to increase the number of terms in the expansion. The estimation procedure requires matrices of dimension $(N+1)^2$ to be solved if an expansion complete to degree N is used. These matrices are full because coefficients of the SH expansion are not associated with any particular spatial location. Thus changes anywhere on the globe, change the SH expansion and the other way around: changing even a single coefficient in the model has a global effect in terms of mass distribution. It is noted by [36] too that it is extremely difficult to adjust the spatial frequency content of a spherical harmonic degree locally.

When modeling the gravitational fields of extraterrestrial bodies of very irregular shape, spherical harmonic expansions may also be a sub-optimal choice and an alternative representation may be able to describe the field with less parameters. According to [36] there are several possibilities for alternative representations of gravitational fields. The most common are:

- Source representation
- Representation by a mass layer on the surface of the body
- Representation by point masses
- Representation by multi quadratic functions
- Representation by radial basis functions
- Representation by integrals

Source representation

The gravitational potential of a volume mass distribution is given by Newton's integral [36]:

$$V_g(\mathbf{x}) = G \int_G \frac{\rho(\mathbf{y})}{|\mathbf{x} - \mathbf{y}|} d\Omega(\mathbf{y}) \quad (4.41)$$

where ρ is the mass density in kg/m^3 and $d\Omega$ the volume element. V is valid everywhere in \mathbb{R}^3 , but it can only be used if the mass density of the sources is available. When a model of the mass density and geometry of the body is available, a numerical integration can be used to approximate the gravitational potential given by equation 4.41 at a point \mathbf{x} :

$$V_g(\mathbf{x}) = G \sum_{i=1}^I \sum_{j=1}^J w_i v_j r(\vartheta_j, \lambda_j) f(r_i, \vartheta_j, \lambda_j) \quad (4.42)$$

The complete derivation is given in [36]. In equation 4.42 w_i and v_j denote the weights at the nodes r_i .

Representation by a mass layer on the surface of the body

The gravitational field of a body outside the masses can be represented by the gravitational potential of a thin layer of mass on the surface of a body. Alternatively, the mass layer may be located on a closed surface completely inside the body too. For instance, an internal sphere may be an appropriate choice for sphere-like bodies. If S is the surface on which the mass layer is defined, the gravitational potential generated by the mass layer is [36]:

$$V_g(\mathbf{x}) = G \iint_S \frac{\mu(\mathbf{y})}{|\mathbf{x} - \mathbf{y}|} dS(\mathbf{y}) \quad (4.43)$$

where μ is the layer density measured in kg/m^2 . A mass layer is also a suitable representation of time-varying gravity fields e.g., caused by mass transport in the atmosphere, on the surface or the shallow subsurface [36].

Representation by point masses

The gravitational field of a body outside the masses can be represented by the superposition of a finite number of point masses. A point mass located at \mathbf{y}_i of mass m_i generates a gravitational potential at point \mathbf{x} of [36]:

$$V_i(\mathbf{x}) = \frac{Gm_i}{|\mathbf{x} - \mathbf{y}|} \quad (4.44)$$

The superposition of I point masses located inside the body yields the gravitational potential [36]:

$$V_g(\mathbf{x}) = \sum_{i=1}^I V_i(\mathbf{x}) = G \sum_{i=1}^I \frac{m_i}{|\mathbf{x} - \mathbf{y}|} \quad (4.45)$$

How close $V(\mathbf{x})$ is to a given gravitational potential depends mainly on the number of point masses I and the choice of locations \mathbf{y}_i and masses m_i . If the point mass representation should be harmonic outside the body, then all the point masses must be located inside the body.

Representation by multi quadratic functions

The multi quadratic method was originally designed to model topography, but can be used to interpolate gravity field functions. The gravitational potential is represented by a mathematical surface by superposition of quadratic kernel functions. These functions, denoted as $K(\mathbf{x}, \mathbf{y}_i)$, are quadratic in the point \mathbf{x} and centered at the points \mathbf{y}_i , which are located on a reference surface. The coefficients a_i are determined from given values of V at a set of points using interpolation or approximation [36]:

$$V_g(\mathbf{x}) = \sum_{i=1}^I a_i K(\mathbf{x}, \mathbf{y}_i) \quad (4.46)$$

Representation by radial basis functions

The gravitational potential of a body outside its masses can be written as a superposition of spherical radial basis functions (SRBF), functions which when restricted to a sphere only depend on the spherical angle with respect to a fixed point \mathbf{y}_i [36]:

$$V_g(\mathbf{x}) = G \sum_{i=1}^I a_i K(\mathbf{x}, \mathbf{y}_i) \quad (4.47)$$

where K is a SRBF defined as [36]:

$$K(\mathbf{x}, \mathbf{y}_i) = \sum_{n=0}^{\infty} k_n \left(\frac{|\mathbf{y}_i|}{|\mathbf{x}|} \right)^{n+1} P_n(\hat{\mathbf{x}} \cdot \hat{\mathbf{y}}_i) \quad (4.48)$$

where \mathbf{y}_i are the nodal points or centers of the SRBF, $\hat{\mathbf{x}} = \frac{\mathbf{x}}{|\mathbf{x}|}$, $\hat{\mathbf{y}} = \frac{\mathbf{y}}{|\mathbf{y}|}$ and k_n the Legendre coefficients. The argument of the Legendre polynomial is given by the cosine of the angle ψ between \mathbf{x} and \mathbf{y} :

$$\hat{\mathbf{x}} \cdot \hat{\mathbf{y}}_i = \cos \psi \quad (4.49)$$

The quality of the gravitational potential depends on the choice of $\{k_n : n = 1, \dots\}$, the number I of SRBF's used and the location of the centers.

Representation by integrals

The most simple example of representing the gravitational potential by integral is the Poisson integral [36]:

$$V_g(\mathbf{x}) = \frac{|\mathbf{x}|^2 - R^2}{4\pi R} \int_{\sigma_R} V(\mathbf{y}) |\mathbf{x} - \mathbf{y}|^{-3} d\sigma_R(\mathbf{y}) \quad (4.50)$$

where σ_R is the surface of a sphere with radius R and $d\sigma_R = R^2 \sin \theta d\theta d\lambda$ a surface element.

4.2 Gravity gradients

In total nine gravity gradient elements can be derived. These nine gradients together form the gravity tensor:

$$\Gamma = \begin{bmatrix} V_{xx} & V_{yx} & V_{zx} \\ V_{xy} & V_{yy} & V_{zy} \\ V_{xz} & V_{yz} & V_{zz} \end{bmatrix} \quad (4.51)$$

The unit of the gravity gradient tensor is Eötvös, one Eötvös is equal to $10^{-9} / \text{s}^2$. Only five of the nine components are independent. This is due to (1) the symmetry of the gravity tensor, because the gravitational potential is curl-free. This means that the double derivative first taken with respect to x and then with respect to y ($\frac{\partial^2}{\partial x \partial y}$) is equal to the double derivative first taken with respect to y and then to x ($\frac{\partial^2}{\partial y \partial x}$), hence $V_{xy} = V_{yx}$, $V_{xz} = V_{zx}$ and $V_{yz} = V_{zy}$. The other reason is that the trace of the gravity tensor is zero, since the gravitational potential is harmonic outside the masses of the gradiometer [35].

4.2.1 Gravity gradients of point mass

From a large distance, a more or less spherical celestial body can be seen as a point mass. The gravitational potential of a point mass is defined by:

$$V_g = -\frac{GM}{|\mathbf{x}|} \quad (4.52)$$

with G the gravitational constant, M the mass of the body under consideration and \mathbf{x} the measurement point in a Titan centered reference frame. When defining \mathbf{x} in spherical coordinates, $|\mathbf{x}| = r$, where r represents the radial distance, composed of the radius of the body and the altitude above the surface of the body: $r = R + h$. The gravity gradients are given by [33] as:

$$\frac{\partial^2 V}{\partial x^2} = GM \left(\frac{1}{r^3} - \frac{3x^2}{r^5} \right) \quad (4.53)$$

Where x is the x -coordinate of the measurement point x_P . Hence to find all the elements of the gravity tensor the double derivative of equation 4.45 with respect to the x -, y - and z -coordinate of the measurement point have to be taken:

$$V_{xx} = GM \frac{r^2 - 3x_P^2}{r^5} \quad (4.54)$$

$$V_{yy} = GM \frac{r^2 - 3y_P^2}{r^5} \quad (4.55)$$

$$V_{zz} = GM \frac{r^2 - 3z_P^2}{r^5} \quad (4.56)$$

$$V_{xy} = V_{yx} = -GM \frac{3x_P y_P}{r^5} \quad (4.57)$$

$$V_{xz} = V_{zx} = -GM \frac{3x_P z_P}{r^5} \quad (4.58)$$

$$V_{yz} = V_{zy} = -GM \frac{3y_P z_P}{r^5} \quad (4.59)$$

4.2.2 Gravity gradients of the single layer method

The gravitational potential as defined in the single layer method is given by equation 4.43. Assuming the density of the layer of mass, μ , is constant in an area σ , equation 4.43 can be rewritten as:

$$V_g(\mathbf{x}) = G\mu \iint_{\sigma} \frac{1}{|\mathbf{x} - \mathbf{y}|} d\sigma(\mathbf{y}) \quad (4.60)$$

Parameterizing equation 4.60 such that it can easily be used for computations:

$$V_g(\mathbf{x}) \cong G\mu \sum_{i=1}^I \frac{\Delta\sigma_i}{|\mathbf{x} - \mathbf{y}_i|} \quad \text{with} \quad \Delta\sigma_i = \frac{\sigma}{I} \quad (4.61)$$

To find the elements of equation 4.51 the double derivative w.r.t. \mathbf{x} of the gravitational potential (equation 4.61) is computed:

$$\partial_{jj} V_g \cong G\mu \sum_{i=1}^I \frac{\partial^2}{\partial |\mathbf{x}|^2} \frac{1}{|\mathbf{x} - \mathbf{y}_i|} \Big|_{\mathbf{x}_j} \Delta\sigma_i \quad (4.62)$$

The vector \mathbf{x} indicates the point in the global coordinate system (see figure 4.4) at which the gradient is computed. Vector \mathbf{y} indicates the source point or, in other words, the mass anomaly. In cartesian coordinates the location of these two points are given as x, y, z , with the subscript P to indicate that the coordinate belongs to the measurement point P and the subscript Q to indicate that the coordinate belongs to the mass anomaly. Thus measurement point \mathbf{x} and source point \mathbf{y} are defined in cartesian coordinates as:

$$\mathbf{x} = \begin{pmatrix} x_P \\ y_P \\ z_P \end{pmatrix} \quad \mathbf{y} = \begin{pmatrix} x_Q \\ y_Q \\ z_Q \end{pmatrix} \quad (4.63)$$

Now the double derivatives according to equation 4.62 can be computed:

$$V_{xx} = G\mu \sum_{i=1}^I \frac{3(x_P - x_Q)^2 - \ell^2}{\ell^5} \Delta\sigma_i \quad (4.64)$$

$$V_{yy} = G\mu \sum_{i=1}^I \frac{3(y_P - y_Q)^2 - \ell^2}{\ell^5} \Delta\sigma_i \quad (4.65)$$

$$V_{zz} = G\mu \sum_{i=1}^I \frac{3(z_P - z_Q)^2 - \ell^2}{\ell^5} \Delta\sigma_i \quad (4.66)$$

$$V_{xy} = V_{yx} = G\mu \sum_{i=1}^I \frac{3(x_P - x_Q)(y_P - y_Q)}{\ell^5} \Delta\sigma_i \quad (4.67)$$

$$V_{xz} = V_{zx} = G\mu \sum_{i=1}^I \frac{3(x_P - x_Q)(z_P - z_Q)}{\ell^5} \Delta\sigma_i \quad (4.68)$$

$$V_{yz} = V_{zy} = G\mu \sum_{i=1}^I \frac{3(z_P - z_Q)(y_P - y_Q)}{\ell^5} \Delta\sigma_i \quad (4.69)$$

where $\ell = |\mathbf{x} - \mathbf{y}| = \sqrt{(x_P - x_Q)^2 + (y_P - y_Q)^2 + (z_P - z_Q)^2}$.

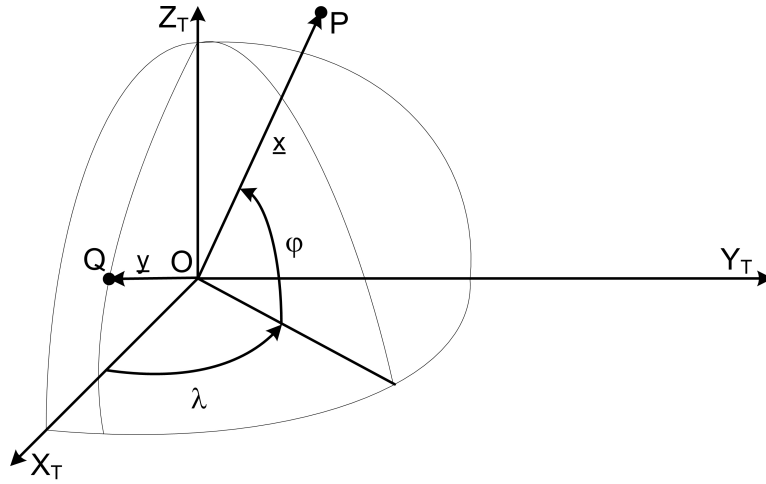


Figure 4.4: Measurement point P and location of the mass anomaly Q in a Titan centered reference system.

4.2.3 Gravity gradients of the point mass method

The representation of the gravitational potential by a point mass is given by equation 4.45:

$$V_g(\mathbf{x}) = \sum_{i=1}^I V_i(\mathbf{x}) = G \sum_{i=1}^I \frac{m_i}{|\mathbf{x} - \mathbf{y}_i|}$$

Computing the gravity gradients:

$$\partial_{jj} V_g(\mathbf{x}) = G \sum_{i=1}^I \frac{\partial^2}{\partial |\mathbf{x}|^2} \frac{1}{|\mathbf{x} - \mathbf{y}_i|} \Big|_{\mathbf{x}_j} m_i \quad (4.70)$$

which results, using the same analogy as in the previous section, in:

$$V_{xx} = G \sum_{i=1}^I \frac{3(x_P - x_Q)^2 - \ell^2}{\ell^5} m_i \quad (4.71)$$

$$V_{yy} = G \sum_{i=1}^I \frac{3(y_P - y_Q)^2 - \ell^2}{\ell^5} m_i \quad (4.72)$$

$$V_{zz} = G \sum_{i=1}^I \frac{3(z_P - z_Q)^2 - \ell^2}{\ell^5} m_i \quad (4.73)$$

$$V_{xy} = V_{yx} = G \sum_{i=1}^I \frac{3(x_P - x_Q)(y_P - y_Q)}{\ell^5} m_i \quad (4.74)$$

$$V_{xz} = V_{zx} = G \sum_{i=1}^I \frac{3(x_P - x_Q)(z_P - z_Q)}{\ell^5} m_i \quad (4.75)$$

$$V_{yz} = V_{zy} = G \sum_{i=1}^I \frac{3(z_P - z_Q)(y_P - y_Q)}{\ell^5} m_i \quad (4.76)$$

where again $\ell = |\mathbf{x} - \mathbf{y}| = \sqrt{(x_P - x_Q)^2 + (y_P - y_Q)^2 + (z_P - z_Q)^2}$.

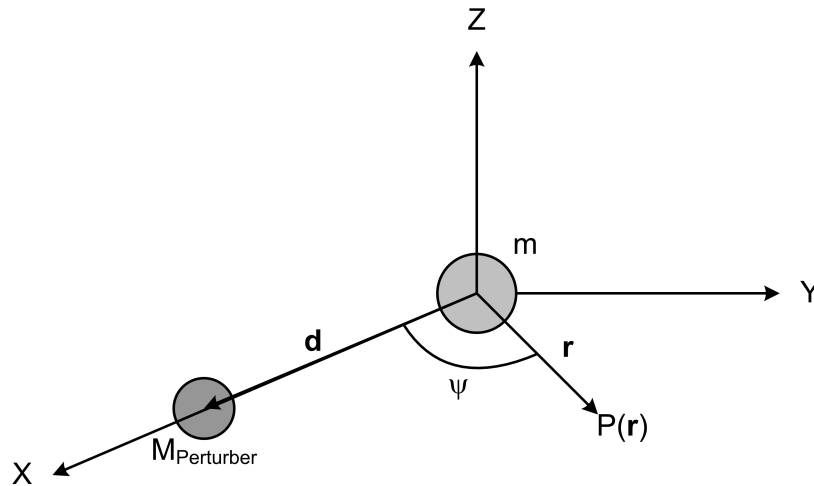


Figure 4.5: The body with mass m is perturbed by a body with mass $M_{perturber}$. The local gravity field is measured at point $P(\mathbf{r})$.

4.3 Tidal potential

Tides on a celestial body are generated by other celestial bodies in the relative vicinity of the body. The tidal potential is a measure of the gravitational influence of one body on another. This section will start with the general theory of the tide generating potential, which will be applied to the Titan–Saturn system later on. Next to that the theory on the tidal Love numbers and the induced tidal potential is treated.

4.3.1 Background theory on the tidal potential

Consider a celestial body of mass m , which is orbited by a perturbing object of mass $M_{perturber}$, see figure 4.5. The distance between the perturbed mass and the perturbing mass, given in the reference frame with the origin at the center of mass of the perturbed mass (the celestial body with mass m), is defined as distance d . Now, the tidal potential can be split into two terms: the first term is the gravitational potential produced by the perturbing mass. The second term, the rotational potential, results from the fact that the chosen reference frame is not an inertial one. The total perturbing potential at measurement point $P(\mathbf{r})$ is now given by [22]:

$$V_{perturbing} = \frac{GM_{perturber}}{|\mathbf{d} - \mathbf{r}|} - \left(\frac{GM_{perturber}}{d^2} \right) x \quad (4.77)$$

If ψ is the angle between the vectors \mathbf{d} and \mathbf{r} , the expansion in Legendre polynomials can be given by ([22] and [32]):

$$V_{tidal} = V_t(\mathbf{r}) = \frac{GM_{perturber}}{d} \sum_{n=2}^{\infty} \left(\frac{r}{d} \right)^n P_n(\cos \psi) \quad (4.78)$$

Considering Titan for the mass being perturbed by Saturn, equation 4.78 can be rewritten for the Titan–Saturn case as ([32] and [55]):

$$V_t(\mathbf{r}) = \frac{GM_S}{a} \sum_{n=2}^{\infty} \left(\frac{r}{a} \right)^n P_n(\cos \psi) \quad (4.79)$$

Here, M_S is the mass of Saturn, P_n the associated Legendre polynomials, r the radial distance of measurement point P, $s = a$, the semi-major axis of the orbit of Titan around Saturn and ψ the angle between the directions to the perturbing body Saturn and to the measurement point P from the mass center of Titan. The amplitude of the tidal deformation and the associated energy are determined by the tide-raising potential and by the internal structure of the satellite. For a synchronous eccentric orbit, the time-dependent part of the tide-raising potential of Saturn on Titan can be written as [66]:

$$V_{time} = -\frac{GM_S R^2}{a^3} 3e \left[\frac{1}{2} (3 \sin^2 \vartheta \cos^2 \lambda - 1) \cos(nt) + \sin^2 \vartheta \sin(2\lambda) \sin(nt) \right] \quad (4.80)$$

where M_S is the mass of Saturn, R is the radius from the center of mass of Titan to the measurement point ($R = R_T$ at the surface of Titan), a the semi major axis of the orbit of Titan, $e = 0.0292$ the orbital eccentricity of Titan, ϑ and λ are the co-latitude and longitude (with $\lambda = 0$ at the sub-Saturn longitude) t the time and n is the orbital angular frequency:

$$n = \sqrt{\frac{GM}{a^3}} \quad (4.81)$$

4.3.2 Tidal Love numbers

A dimensionless number can be defined to give the constant of proportionality between the perturbing potential, V_t and the tidal displacement of the surface of the planet, δr [22]:

$$\delta r = \frac{hV_t}{g_0} \quad (4.82)$$

where h is the displacement Love number and g_0 the unperturbed surface gravity given by equation 4.12. For a Maclaurin spheroid the displacement Love number is given by $h = 5/2$ [22], but in general the value for h will be smaller. There are two main reasons for this:

1. The planet will generally have some degree of central concentration
2. The planet may not be able to relax to hydrostatic equilibrium over a tidal cycle

If the last is the case and the planet acts as an elastic body over a tidal cycle, with a uniform density ρ and an elastic shear modulus μ , the displacement Love number is then given by [22]:

$$h = \frac{5/2}{1 + \frac{19\mu}{2g_0\rho R}} \quad (4.83)$$

If a body is in hydrostatic equilibrium, the value of the fluid Love number k_f will give the moment of inertia from the Radau equation [22]:

$$\frac{I_p}{MR^2} = \frac{2}{3} \left[1 - \frac{2}{5} \left(\frac{4 - k_f}{1 + k_f} \right)^{1/2} \right] \quad (4.84)$$

with I_p the moment of inertia given by equation 4.19. The other way around, the moment of inertia can be used to estimate the value for k_f , after which the value for the quadrupole moment

C_{22} is given by [55]:

$$C_{22} = -k_f \frac{q_t}{12} \quad (4.85)$$

where q_t is the tidal parameter given by:

$$q_t = -3 \frac{M_{perturber}}{m} \left(\frac{R}{d} \right)^3 \quad (4.86)$$

here, $M_{perturber}$ is the mass of the perturbing body, m the mass, R the radius of the body being perturbed and s the distance between the two bodies, see figure 4.5.

4.3.3 Induced tidal potential

The deformation of the surface of a planet in the response to tides are smaller than they would be if the planet is in hydrostatic equilibrium, because elastic forces tend to maintain the spherical shape of a planet. The tidal response of a planet affects its own external gravitational field too, therefore a tidally induced potential ($V_{tidal,induced}$) can be defined. This potential up to an order two is given as [22]:

$$V_{tidal,induced} = V_{t,i} = J_{t2} GM \frac{R^2}{r^3} P_2(\cos \psi) \quad (4.87)$$

Again a response coefficient can be defined [22]:

$$J_{t,i} = \Lambda_{2,0} q_t \quad (4.88)$$

with the tidal parameter, q_t given as in equation 4.86. For a liquid or perfect elastic planet, the tidal response coefficient $\Lambda_{2,0}$ from equation 4.88 would be the same as the rotational response coefficient as defined in equation 4.39. Of course, a planet is neither fully liquid or a perfect elastic planet, so the tidal and rotational $\Lambda_{2,0}$ are often different. Evaluated at the surface of a planet, instead of $\Lambda_{2,0}$, the Love number of degree 2 is used [22]:

$$k_2 = \frac{V_{tidal,induced}}{V_{tidal}} = \frac{3/2}{1 + \frac{19\mu}{2g_0\rho R}} \quad (4.89)$$

this gives the following relation between k_2 and h_2 for a body in hydrostatic equilibrium:

$$h_2 = \frac{5}{3} k_2 \quad (4.90)$$

4.3.4 Tidal dissipation

Following the assumptions that a body is incompressible, the rotation is synchronous and uniform and the body is small enough that the displacement Love number satisfies equation 4.90, the energy dissipation is given as [91]:

$$\frac{dE}{dt} = \frac{21}{2} \frac{k_2}{Q_{tidal}} \frac{GM^2 n R^5 e^2}{a^6} \quad (4.91)$$

where k_2 is the second degree Love number (equation 4.89), Q the effective tidal dissipation factor, G the gravitational constant, a the orbital semi-major axis, M the mass of the primary body, n the orbital mean motion (equation 4.81). R the radius of the satellite and e the orbital eccentricity. Equation 4.91 only holds if the eccentricity of the orbit is small, the average rate of energy dissipation is dependent on the eccentricity and for zero obliquity given as [91]:

$$\frac{dE}{dt} = \frac{21}{2} \frac{k_2}{Q} \frac{GM^2 n R^5 e^2}{a^6} \zeta(e) \quad (4.92)$$

where $\zeta(e)$ represents the eccentricity dependent factor [91]:

$$\zeta(e) = \frac{2}{7} \frac{f_0(e)}{\beta^{15}} - \frac{4}{7} \frac{f_1(e)}{\beta^{12}} + \frac{2}{7} \frac{f_2(e)}{\beta^9} \quad (4.93)$$

with

$$\begin{aligned} f_0(e) &= 1 + \frac{31}{2}e^2 + \frac{255}{8}e^4 + \frac{185}{16}e^6 + \frac{25}{64}e^8 \\ f_1(e) &= 1 + \frac{15}{2}e^2 + \frac{45}{8}e^4 + \frac{5}{16}e^6 \\ f_2(e) &= 1 + 3e^2 + \frac{3}{8}e^4 \end{aligned} \quad (4.94)$$

and

$$\beta = \sqrt{1 - e^2} \quad (4.95)$$

For arbitrary obliquity, η , $\zeta(e)$ in equation 4.92 can be replaced with $\zeta(e, \eta)$ [91]:

$$\zeta(e, \eta) = \frac{2}{7} \frac{f_0(e)}{\beta^{15}} - \frac{4}{7} \frac{f_1(e)}{\beta^{12}} \cos \beta + \frac{1}{7} \frac{f_2(e)}{\beta^9} \left(1 + (\cos \eta)^2\right) + \frac{3}{14} \frac{e^2 f_3(e)}{\beta^{13}} (\sin \eta)^2 \cos(2\chi) \quad (4.96)$$

where

$$f_3(e) = 1 - \frac{11}{6}e^2 + \frac{2}{3}e^4 + \frac{1}{6}e^6 \quad (4.97)$$

and χ the measure of the longitude of the node of the equator on the orbit with respect to the pericenter of the orbit. For a satellite in non-synchronous rotation the rate of dissipation is given as [91]:

$$\frac{dE}{dt} = \frac{21}{2} \frac{k_2}{Q} \frac{GM^2 n R^5 e^2}{a^6} \zeta_{ns}(e, \cos \eta) \quad (4.98)$$

with $\zeta_{ns}(e, \cos \eta)$ given as:

$$\zeta_{ns}(e, \cos \eta) = \frac{2}{7} \left[F_0(e) - \frac{(F_1(e))^2}{F_2(e)} \frac{2 \cos^2 \eta}{1 + \cos^2 \eta} \right] \quad (4.99)$$

where

$$\begin{aligned}
 F_0(e) &= \frac{f_0(e)}{\beta^{15}} \\
 F_1(e) &= \frac{f_1(e)}{\beta^{12}} \\
 F_2(e) &= \frac{f_2(e)}{\beta^9}
 \end{aligned}
 \tag{4.100}$$

with $f_0(e)$, $f_1(e)$ and $f_2(e)$ given in equation 4.94 and β in equation 4.95.

4.4 Tidal parameters of Titan

Since the Voyager missions, scientists have tried to solve the mystery of Titan’s relative high eccentricity. Different interior models have been set up, in order to compute among other values the associated tidal dissipation, the decay of the eccentricity over time and the tidal Love numbers. This section will treat the most important models given in the literature and will summarize the conclusions drawn with respect to the interior of Titan. A summary of all the models treated is given in appendix D.

Tidal Love numbers of Titan

Several basic simulations made of the interior of Titan in order to compute Love numbers and dissipation rates has been described in [63]. Here three models are used, a uniform density model, a volatile-poor model and a volatile-rich model. Model A is a uniform model, based on the mean density of Titan of 1881 kg/m^3 . The ice mass fraction given by equation 4.21 is set to 0.45, where $\rho_{ice} = 1200 \text{ kg/m}^3$ $\rho_{rock} = 3500 \text{ kg/m}^3$. For model B a volatile-poor scenario is chosen, suggesting a development in analogue of the Jovian satellites Ganymede and Callisto. In this model the rocky core of 1900 km is overlain with a layer of ice-VI with a thickness of 200 km, an ice V layer of 75 km, an ice-II layer of 300 km and the outer ice-I is 100 km thick, see figure 4.6. In the last model, the volatile-rich scenario, the water-ice is replaced with ammonia-ice and instead of the ice-II layer a subsurface $\text{NH}_3\text{-H}_2\text{O}$ ocean is included underneath a 150 km thick ice-I shell. The high-pressure ice between the core and the ocean is assumed to be ice-V [63].

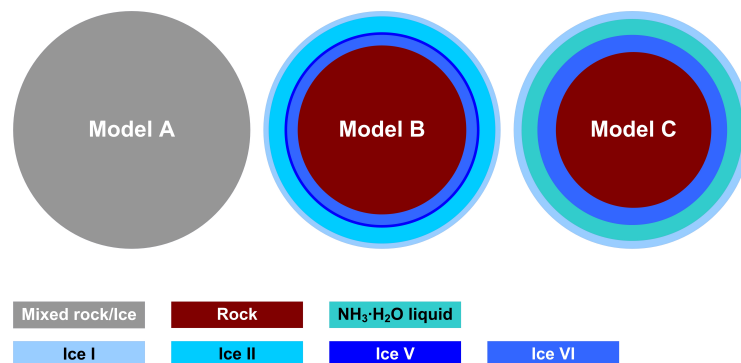


Figure 4.6: The three interior models used in the simulation of [63]. Model A is a homogeneous sphere of ice and rock, model B based on a differentiated volatile-poor scenario and model C on a volatile-rich scenario [63].

To compute the dissipation rates, the model used in [63] requires the Love numbers h_2 and k_2 and the mass load coefficients h'_2 and k'_2 . The values used are given in table 4.1 together with the fluid Love numbers h_f and k_f .

Table 4.1: Complex Love numbers, mass load coefficients and fluid Love numbers for the three different models given in figure 4.6 [63].

	Model A		Model B		Model C	
	\Re	$100 \times \Im$	\Re	$100 \times \Im$	\Re	$100 \times \Im$
h_2	0.1192	-0.3225	0.0587	-0.0796	1.1900	-0.5673
k_2	0.0716	-0.1935	0.0263	-0.0288	0.3590	-0.1711
h'_2	-0.0795	0.2150	-0.0797	0.1414	-2.7530	1.3130
k'_2	-0.0477	0.1290	-0.0325	0.0508	-0.8307	0.3961
h_f	2.5000	–	1.9020	–	1.4300	–
k_f	1.5000	–	0.9253	–	0.4304	–

Using these values the dissipation rates due to ocean loading are computed, the values are given in table 4.2. For comparison the background dissipation rates due to the body and loading tides have been given too. The body dissipation represents the energy dissipation in Titan’s interior caused by tidal forcing and the load dissipation represents the energy dissipation due to surface traction caused by tidal forcing. Together these form the global tidal dissipation rate. The figures and equations used for these computations can be found in [63].

From the values in table 4.2 it can be seen that dissipation due to ocean loading is minor compared to the tidal background dissipation. The values for the zero–depth ocean are due to atmospheric load. The influence of different types of oceans, a methane–rich ocean, an ethane–rich ocean and a sludge ocean, has been incorporated in the simulations. For the computation of the values in table 4.2 an ethane–rich ocean is used. The dissipation values for the more viscous and dense sludge ocean prove to be a magnitude higher, but not significant. The solid tidal dissipation rates range from 8.6×10^9 W up to 5.8×10^{10} W in the non–ocean case (models A and B) and for the ocean case (model C), the total dissipation varies between 5.2×10^{10} and 7.0×10^{10} W. This is smaller than the radiogenic component for which the values are given to be between 4.04×10^{11} and 5.15×10^{11} W. Nonetheless, according to these models the current eccentricity of Titan’s orbit is not consistent with the dissipation rates computed, which indicates that the orbit should be circular by now [63]. The models used in [63] do most probably not represent Titan’s interior structure of today, a global ocean is therefore very unlikely. Only volatile–poor interior and ocean with a depth greater than 500 m is considered possible in [63], though this conflicts the theories on the formation and conservation of the volatile rich atmosphere (see section 2.5). Other possible explanations given for Titan’s high eccentricity are that the origin of the eccentricity has a more recent past, or that Titan’s interior has changed significantly over time [63].

Table 4.2: The dissipation rates for the various interior models of Titan. The loading dissipation for the zero–depth ocean is due to the atmosphere, f_b denotes the bottom friction coefficient [63].

Ocean depth [m]	Tidal dissipation rates [W]			Total dissipation
	Dissipation due to tidal forcing in the interior	Dissipation due to surface traction	Dissipation due to an internal ocean	
Model A ($f_b = 0.0042$)				
0	5.8×10^{10}	6.9×10^4	–	5.8×10^{10}
100	5.8×10^{10}	1.0×10^9	2.1×10^{12}	2.2×10^{12}
400	5.8×10^{10}	1.0×10^9	3.3×10^{10}	9.2×10^{10}
600	5.8×10^{10}	1.0×10^9	9.8×10^9	6.9×10^{10}
1000	5.8×10^{10}	1.0×10^9	2.1×10^9	6.1×10^{10}
Model B ($f_b = 0.0042$)				
0	8.6×10^9	7.5×10^4	–	8.6×10^{10}
100	8.6×10^9	1.1×10^9	2.2×10^{12}	2.2×10^{12}
400	8.6×10^9	1.1×10^9	3.5×10^{10}	4.4×10^{10}
600	8.6×10^9	1.1×10^9	1.0×10^{10}	2.0×10^{10}
1000	8.6×10^9	1.1×10^9	2.2×10^9	1.2×10^{10}
Model C ($f_b = 0.0065$)				
0	5.1×10^{10}	2.3×10^4	–	5.1×10^{10}
100	5.1×10^{10}	3.4×10^8	1.8×10^{10}	7.0×10^{12}
400	5.1×10^{10}	3.4×10^8	2.9×10^8	5.2×10^{10}
600	5.1×10^{10}	3.4×10^8	8.5×10^7	5.2×10^{10}
1000	5.1×10^{10}	3.4×10^8	1.8×10^7	5.2×10^{10}

Influence of a dense atmosphere on the Love numbers

The induced potential that will perturb the Cassini spacecraft during the Titan flybys represents the tidal response of the solid body (assuming no global ocean the loading tide defined previously is zero, see [63]) and the atmosphere. Equation 4.89 can then be rewritten as [32]:

$$V_{t,i(n=2)}(r = R_e) = (k_2^s + k_2^a) V_2(r = R_e) \quad (4.101)$$

k_2^s is the Love number due to the solid body and k_2^a the Love number due to the atmosphere. The effect of a dense atmosphere can be two–fold, it contributes directly to the tidal potential and it induces a load on the body under consideration. Assuming that the atmosphere is in hydrostatic equilibrium and that it can be approximated by a thin layer, the degree–two tidal potential Love number induced by the atmosphere, from now on referred to as the atmospheric Love number k_2^a , can be written as [32]:

$$k_2^a = (1 + k_2^l) \frac{4\pi}{5} \frac{R_T^2}{g_0 M_S} \left(\frac{a}{R_T} \right)^3 \tilde{p}_{S_2} \quad (4.102)$$

where g_0 is the surface gravity (equation 4.12), R_T the radius of Titan, M_S the mass of Saturn and a the semi–major axis of the orbit of Titan around Saturn. The solid body deformation as result of the atmospheric loading is represented by a load Love number, k_2^l , and the tidal forcing is represented by the amplitude \tilde{p}_{S_2} of the degree–two atmospheric tide exerted by Saturn. The value of \tilde{p}_{S_2} is only known by modeling, the most recent, time–dependent numerical simulations

[75] show that at the sub-Saturn point (SP) the surface pressure varies by 1.5 hPa throughout the orbit. The likely effect of topography was not implemented in the simulations of [32] and it was assumed that the atmosphere was locally in hydrostatic equilibrium.

Using three different interior models as proposed in [63] and described above, models A, B and C, and the according parameters, the load Love numbers, k_2^l , solid body Love numbers, k_2^s , and atmospheric Love numbers, k_2^a , are computed and given in table 4.3. As can be seen, for all three interior models, the atmospheric Love number is less than 2% of the total Love number, and according atmospheric effect can most likely be neglected when studying the interior structure of Titan from the Love number measurements [32].

Table 4.3: Love numbers as a function of three interior models [32].

Love number	Model A	Model B	Model C
k_2^s	7.16×10^{-2}	2.63×10^{-2}	3.590×10^{-1}
k_2^l	-4.77×10^{-2}	-3.25×10^{-2}	-8.307×10^{-1}
k_2^a	4.04×10^{-4}	4.10×10^{-4}	7.18×10^{-5}
$\frac{k_2^a}{k_2} \times 100$	0.561	1.537	0.020
k_2	0.072004	0.02671	0.3590718

Determining the tidal Love number from Cassini radio tracking data

As the previous sections have shown, a model with internal ocean gives significantly larger values for the Love numbers k and h than the models without. According to the research presented in [72], when the Love number k_2 is larger than 0.3 an internal ocean exists, since the low degree harmonics of Titan's gravity field reflect the response of the body to perturbing potentials due to Titan's rotation, Saturn's tides and to internal stresses. The quadrupole moments of Titan can be measured by the Cassini Radio Science Subsystem (RSS) and will be used to determine the degree-two Love numbers of Titan. If this can be done with sufficient accuracy, this will pose restrictions on the possibilities for the interior structure. How this is done and with what accuracy is presented in [57] and in short described here.

The total perturbing potential is the sum of a static, denoted by lowercase s , and a periodic, denoted by a lower case p , part [55]:

$$V = V_s + V_p \tag{4.103}$$

The secular part of the perturbing potential V_s is responsible for permanent deformation of the planet. The induced potential at the surface of Titan is proportional to this, with a coefficient of proportionality given by the fluid Love number k_f . The periodic term, V_p , changes over the orbital period of Titan. The induced potential at the surface of Titan is therefore proportional to V_p , with a coefficient of proportionality of the second degree Love number, k_2 , see equation 4.89 [55].

At the surface of Titan, the induced tidal potential is described by the dimensionless coefficients [57]:

$$\begin{aligned} J_2 &= J_{2,s} + J_{2,p} & (4.104) \\ &= k_f \frac{(2q_r - q_t)}{6} - k_2 \frac{q_t}{2} e \cos(M - \delta) \end{aligned}$$

$$\begin{aligned} C_{22,s} &= C_{22,s} + C_{22,p} & (4.105) \\ &= -k_f \frac{q_t}{12} - k_2 \frac{q_t}{4} e \cos(M - \delta) \end{aligned}$$

$$\begin{aligned} S_{22,s} &= S_{22,s} + S_{22,p} & (4.106) \\ &= S_{22,s} - \frac{1}{3} k_2 q_t e \sin(M - \delta) \end{aligned}$$

Here, q_t is the tidal parameter given by equation 4.86, M is the mean anomaly of Titan at the time of the Cassini encounter and δ accounts for a possible lag of the tidal bulge [57]. The Love number is defined as complex number as [57]:

$$\begin{aligned} k_2 &= \Re(k_2) + \Im(k_2) & (4.107) \\ &= k_2 \cos \delta - (k_2 \sin \delta) i \end{aligned}$$

From the assumption that Titan is in hydrostatic equilibrium, a priori values of the coefficients J_2 , C_{22} and S_{22} can be computed and are given in [57] as:

$$J_2 = 4.93 \times 10^{-5} + 4.84 \times 10^{-7} \cos(M - \delta) \quad (4.108)$$

$$C_{22} = 1.48 \times 10^{-5} + 2.42 \times 10^{-7} \cos(M - \delta) \quad (4.109)$$

$$S_{22} = 3.23 \times 10^{-7} \sin(M - \delta) \quad (4.110)$$

where the a priori Love number is assumed to be $k_2 = 0.3$ (following [72]). When Titan has an internal ocean, covered by a high viscosity ice-I layer, the phase lag angle $\delta = 0^\circ$. In the oceanless case, hence only an outer shell of low-viscosity ice-I, the values for the possible phase lag angles used in [57] are $\delta = 5^\circ, 10^\circ, 15^\circ, 20^\circ, 25^\circ$ and 30° . Figure 4.7 shows how the a priori value of J_2 behaves for the different phase lag angles, along a complete orbit (mean anomaly $0 \leq E \leq 360$), the figures for C_{22} and S_{22} can be found in appendix D.

To determine k_2 , [57] uses the JPL Orbit Determination Program, in which k_2 will follow from the determination of the static parts of J_2 , C_{22} and S_{22} for a number of N flybys. A direct estimation of k_2 is not possible due to the lack of satellite tide modes in this program. The method this program uses a weighted least squares procedure to minimize the penalty function F [57]:

$$\begin{aligned} F &= \sum_{j=1}^N \left[\frac{(J_{2j} - J_{2s} - a_j k_{re} - \bar{a}_j k_{im})}{\sigma_{J_{2j}}} \right]^2 & (4.111) \\ &+ \left[\frac{(C_{22j} - C_{22s} - b_j k_{re} - \bar{b}_j k_{im})}{\sigma_{C_{22j}}} \right]^2 \\ &+ \left[\frac{(S_{22j} - S_{22s} - c_j k_{re} - \bar{c}_j k_{im})}{\sigma_{S_{22j}}} \right]^2 \end{aligned}$$

where J_{2j} , C_{22j} and S_{22j} are the estimated values of the quadrupole coefficients for the j -flyby and

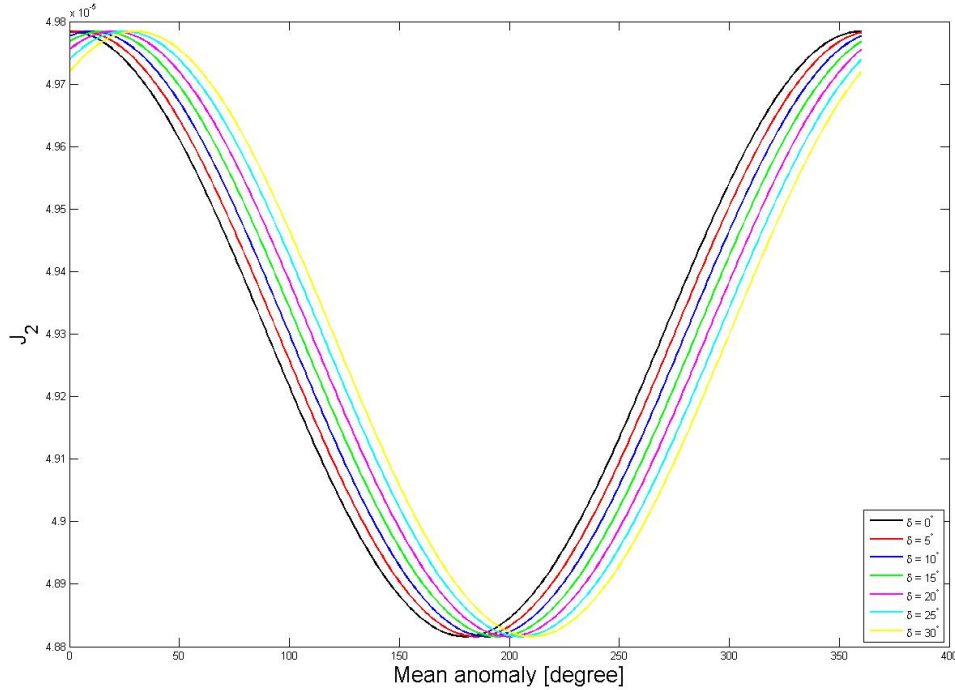


Figure 4.7: A priori values of J_2 for different phase lag angles δ , given by equation 4.108 [57].

$\sigma_{J_{2j}}$, $\sigma_{C_{22j}}$ and $\sigma_{S_{22j}}$ are the corresponding uncertainties. The parameters a_j , \bar{a}_j , b_j , \bar{b}_j , c_j and \bar{c}_j are known geometrical quantities. The flybys the Cassini orbiter has made until now do not provide a high enough accuracy in the determination of k_2 . Therefore future flybys are needed to make a better estimation of the second-degree Love number [57].

Nevertheless some estimations are made by [57] regarding the interior of Titan. Two interior cases are distinguished: the (a) elastic and (b) viscoelastic case. Both cases are characterized by the viscosity of the mantle. If the viscosity of the mantle is large enough, an elastic model can be used (case (a)). Assuming the tidal response is instantaneous, the corresponding Love number will be a real value. Considering then an internal ocean underneath an 100 km thick shell, the value for k_2 will lie between 0.42 and 0.48. If no sub-surface ocean is present the Love number is expected to be approximately 0.03. According to [57], taking the probabilities into account, if the observed Love number $k_2^{obs} > 0.225$ an internal ocean is present, if the value of $k_2^{obs} < 0.225$, Titan has no internal ocean.

In the viscoelastic case (case (b)) it is assumed that both the high-pressure ices and the ice-I shell have equal viscosities, estimated between 5×10^{13} Pa s and 1×10^{16} Pa s, having equal probabilities. Consider again a sub-surface ocean with an ice-I shell thickness of 20–100 km (having equal probabilities too), then a range of possible values for the true (complex) Love number can be found. The same can be done when considering an oceanless Titan, with an ice-I shell of 160 km and high-pressure ice with a thickness of 745 km. In [57] the results are given in two figures, shown here in figure 4.8. The white dots illustrate the possible values for the Love number k_2 , the black line represents the points where the probability distributions in the ocean and oceanless

cases are equal. Using this line as a decision marker, [57] claims that a successful prediction of the presence or absence of an ocean can be made with a 93% certainty. Thus the (still) expected data from the Cassini orbiter will allow to test the hypothesis of an interior liquid water ocean on Titan with a high degree of confidence.

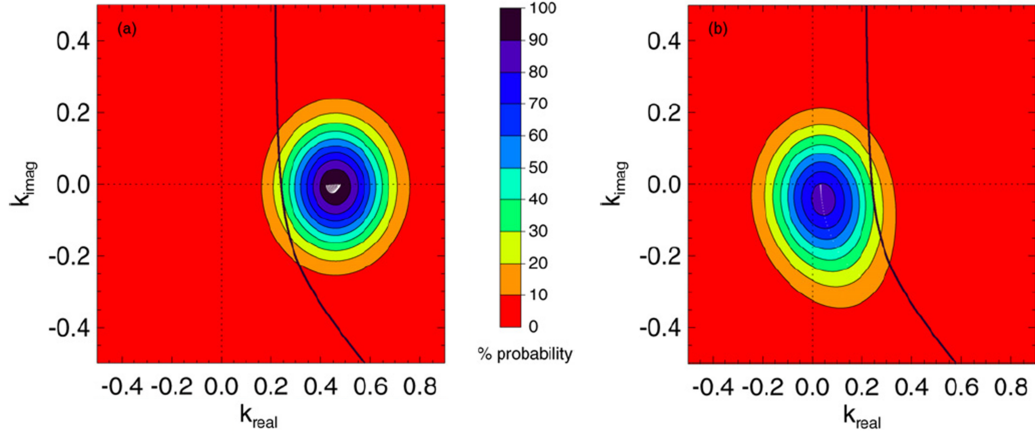


Figure 4.8: Picture (a) (left) shows the expected probability distribution of the observed values for the (complex) Love number, for the case of an ocean with a viscoelastic ice layer between 20 and 100 km thick. The underlying high-pressure ice is assumed to be viscoelastic too. The cluster of white dots illustrate the range of possible real values. Picture (b) (right) shows the same, but then for an oceanless case. The black line marks the points where the probability distributions in the ocean and oceanless cases are equal [57].

Tidal dissipation of Titan

For any planet or moon, the global tidal dissipation rate due to the body tide, \dot{E}_{diss} , is proportional to the imaginary part of the second degree Love number ($\Im(k_2)$) [73] and given for Titan as:

$$\dot{E}_{diss} = \frac{dE}{dt} = -\frac{21}{2} \frac{R^5(n)^5 e^2}{G} \Im(k_2) \quad (4.112)$$

where G is the gravitational constant, R is the radius of Titan, n is the orbital angular frequency and e the orbital eccentricity of Titan. Tidal dissipation tends to make the orbit of satellites circular and their rotation synchronous with their revolution. The change in eccentricity due to the tidal dissipation is given as [71]:

$$\frac{de}{dt} \frac{e}{1-e^2} = \frac{-a}{GM_S M_T} \frac{dE}{dt} \quad (4.113)$$

where M_S is the mass of Saturn, M_T the mass for Titan, G the gravitational constant, e the orbital eccentricity and a the semi-major axis of the orbit of Titan around Saturn. Equation 4.113 does not take the expansion of Titan's orbit due to dissipation of tides raised by Titan on Saturn into account. However according to [71], the effect of dissipation within Saturn corresponds to less than 2% of the effect of dissipation within Titan on the eccentricity variation and therefore it can be neglected.

Orbital resonance of Galilean satellites forces Io's and Europa's orbit to be eccentric, despite their strong tidal dissipation. The eccentricity of Titan's orbit is relatively high ($e = 0.0292$), but for

Titan no such orbital resonance is known and the tidal dissipation within Titan's interior is expected to be large enough to circularize its orbit [63]. Tidal heating within a decoupled ice shell contributes less than 10% to the total heat production and is more than ten times lower than radiogenic heating, for the models investigated. The interior and ocean models tested in [63] are given in figure 4.6. The dissipation rates for the various interior models found by [63] range in value from $8.6 \cdot 10^9$ up to $5.8 \cdot 10^{10}$ W in the absence of a global ocean.

According to [73] a liquid water layer has a very strong influence on the distribution of dissipation within both the deep interior of the satellite and the outer ice-I layer. This is concluded from the generic model for large icy satellites that was set up, by using a new method of tidal dissipation computations, where the tidal dissipation rate is related to the radial distribution of the rigidity. The model uses a generic approach and does not reproduce the dissipation for each individual satellite, but it identifies the influence of each internal layer. This model is, according to [73], a useful tool to study the coupled thermal-orbital evolution of satellites, which for Titan has been done in [71]. The global model shows, in analogy to other studies like [62], that the primary effect of a sub-surface ocean on the tidal deformation is mainly controlled by the radial displacement of this subsurface ocean. The tidal strain rate is almost constant with depth, its maximum at the poles and minimum at the equator. These characteristics seem not to be sensitive to variations of ice rheology parameters within the outer ice-I layer. Next to that in [71] the effect of different amount of radiogenic heating in the silicate core and a range of values for viscosity of the high-pressure phases of ice is investigated. It is concluded there that these effects are of second order compared to the effect of ammonia.

The effect of ammonia is presented and discussed in [62]. Several simulations are made, among other things the temperature of a convective sublayer and subsurface ocean, surface heat flow, core density, MoI factor, radial displacement Love number h_2 and potential Love number k_2 as function the ice thickness of the upper ice-I shell. All simulations are done for a subsurface ocean containing 5% and 15% ammonia and for different core heat production rates. In these simulations it is assumed that Titan is fully differentiated, the effects of pressure and temperature on the density can be neglected and that the specific heat production rate is twice as large as the chondritic value. It is shown that the Love numbers depend linearly on the ice shell thickness, but it is commented that the data will not be unambiguous. The Love numbers do not only depend on chemistry, but on the rheological properties of the Titan too. The MoI factor for a differentiated Titan will be smaller than 0.38, the value if Titan would be undifferentiated. Once the Love numbers are determined using the Cassini fly-bys, additional constraints can be set to reduce uncertainties in the model used [62]. The most important figures and values presented in [62] can be found in appendix D.

Depending on the composition of the subsurface ocean, ammonia can strongly depress the melting temperature of water ice. So as the ice-I shell thickens the ocean thins, the ammonia in the ocean becomes more concentrated and the melting temperature declines even more. This would make the melting temperature at the base of the ice shell drop too. On the other hand for a given change in the thickness of the ice-I shell the resulting change in the oceanic ammonia concentration depends on whether a silicate mantle or high-pressure ices underlie the ocean. One of the determined radial structures is shown in figure 4.9. An ocean composition of 15% is assumed and

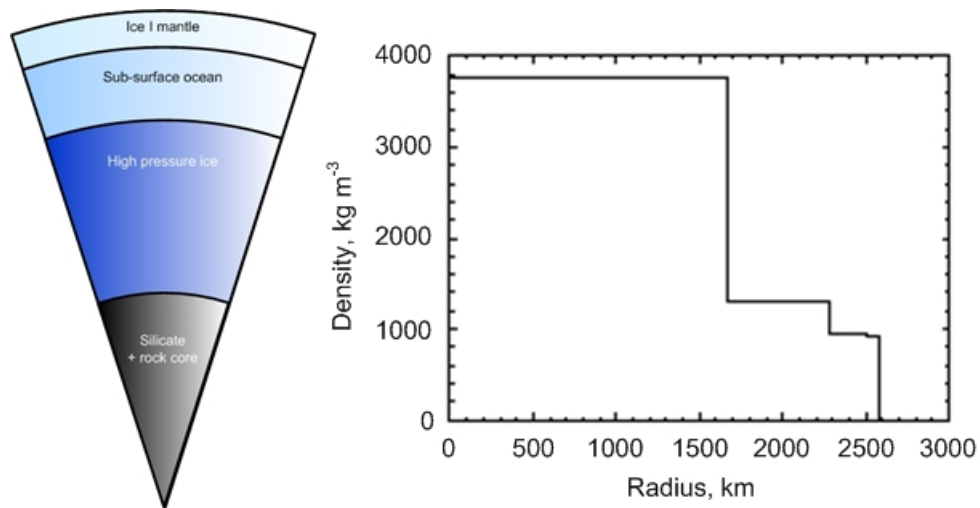


Figure 4.9: Radial structure and density distribution of Titan according to [62]. A primordial ammonia–water ocean composition of 15 wt.% NH_3 is assumed. The interior structure model is optimized for a rock–to–ice ratio of 55:45. The ice–I layer is 69 km thick and entirely conductive. The subsurface ocean extends over a depth of 224 km and is underlain by a high–pressure ice layer of 612 km thickness. The rocky core has a radius of 1671 km and a mean density of 3800 kg/m^3 . The satellite’s density distribution is associated with a MoI factor of 0.304 and the radiogenic heat flow amount to $3.35 \times 10^{11} \text{ W}$, corresponding to a total surface heat flow per unit area of about 4 mW/m^2 [62].

the model is optimized for a rock–to–ice ratio of 55:45.

Modeling the gravity field of the lakes on the surface of Titan

It is chosen to model the gravity field using the single layer method, which approximates the lakes on the surface of Titan as a thin mass layer. The gradients of Titan are modeled under the assumption that Titan is a spherical symmetrical, which will be explained in section 5.1. Here it is not chosen to make a model using SH, because this representation has some drawbacks. To get a better resolution, the coefficients in the expansion have to be increased. Next to that the SH representation is not connected to a particular spatial location. Thus changing one of the many coefficients has global effect, which makes it extremely difficult to adjust the spatial frequency content of a spherical harmonic degree locally [36]. Another major drawback is the oscillatory character of the SH functions. This has as a consequence that in a border area, for instance between a lake and the solid surface, the functions will oscillate continuously to find the appropriate approximation, which will result in many unknowns. These reasons make the SH representation not a very efficient method to solve for a model of the lakes.

Section 5.1 shows how the modeling of the gravitational potential and the gravity gradients is done. Defining the reference frame and selecting the lakes for the computations is described in section 5.2. Finally the tidal potential caused by Saturn is resolved in section 5.3.

5.1 Modeling the gravity field

The gravity field is modeled to resolve the signal the gradiometer will receive when floating over a lake. To do this, Titan is modeled under the assumption the moon is spherical symmetrical and the lakes are modeled using the single mass layer method as explained in section 4.1 and the corresponding gravity gradients as explained in section 4.2.

5.1.1 Modeling the gravity field of Titan

Assuming that Titan is spherical symmetrical, having a constant density ($\bar{\rho} = 1881 \text{ kg/m}^3$) the gravitational potential is thus given by equation 4.52:

$$V = \frac{GM}{r} \quad (5.1)$$

with $r = R + h$, R the radius of Titan and h the measurement altitude. A positive sign convention is used in equation 5.1, because this is more convenient when using this representation together

with the single layer method.

Considering the possible interior build up of Titan (see figure 2.6) and given the different possibilities given by several models (see table D.1), one could approximate the layers by several spherical shells on top of each other. In [34] the derivation for the gravitational field of a homogeneous spherical shell is given, hence for an arbitrary point on the the z -axis the gravitational potential of a spherical shell with constant density (ρ) is given by [34]:

$$V(0, 0, z) = 2\pi G\rho \begin{cases} \left(R_2^2 - \frac{2}{3z} R_1^3 - \frac{z^2}{3} \right) & \text{for } R_1 < |z| < R_2 \\ \frac{2}{3z} (R_2^3 - R_1^3) & \text{for } |z| > R_2 \\ (R_2^2 - R_1^2) & \text{for } |z| < R_1 \end{cases} \quad (5.2)$$

To see if this approximation is valid, the gravitational potential of the different models, assuming the interior is build up from homogeneous spherical, are compared to the point mass approximation. The result of this comparison is given in figure 5.1.

As can be seen in figure 5.1, the differences are not very large. Therefore it is assumed that the gravitational potential of Titan can be approximated with equation 5.1. Thus the gradients are given as (in analogy of equations 4.54 through 4.59):

$$\begin{aligned} V_{xx} &= GM \frac{3x_P^2 - r^2}{r^5} \\ V_{yy} &= GM \frac{3y_P^2 - r^2}{r^5} \\ V_{zz} &= GM \frac{3z_P^2 - r^2}{r^5} \\ V_{xy} &= V_{yx} = GM \frac{3x_P y_P}{r^5} \\ V_{xz} &= V_{zx} = GM \frac{3x_P z_P}{r^5} \\ V_{yz} &= V_{zy} = GM \frac{3y_P z_P}{r^5} \end{aligned}$$

5.1.2 Modeling the lakes as a single mass layer

The gravitational potential and gravity gradients of the lakes selected are modeled using the single layer method, given in equation 4.43 and equations 4.64 to 4.69 respectively. In these equations the point Q represents the source point, in this case the raster points of the lakes. This will be explained in more detail in section 5.2. The lakes can be seen as a thin layer of mass, with a homogeneous density. It is assumed that the lakes have the density of the hydrocarbon mixture I, given in table 2.4. The single layer method assumes that the lakes are located in a thin layer of mass, it uses the density per unit thickness and therefore the densities used have the unit of kg/m^2 . As shown in figure 5.1 all layers are of influence on the total gravitational potential, but that the difference is not significant, thus Titan can be represented by the equations given in the previous section. As consequence of this the surrounding of the lakes will be modeled using a density of $\bar{\rho}_{model} = 1881 \text{ kg}/\text{m}^2$. Because the density of the hydrocarbon mixture is less than the

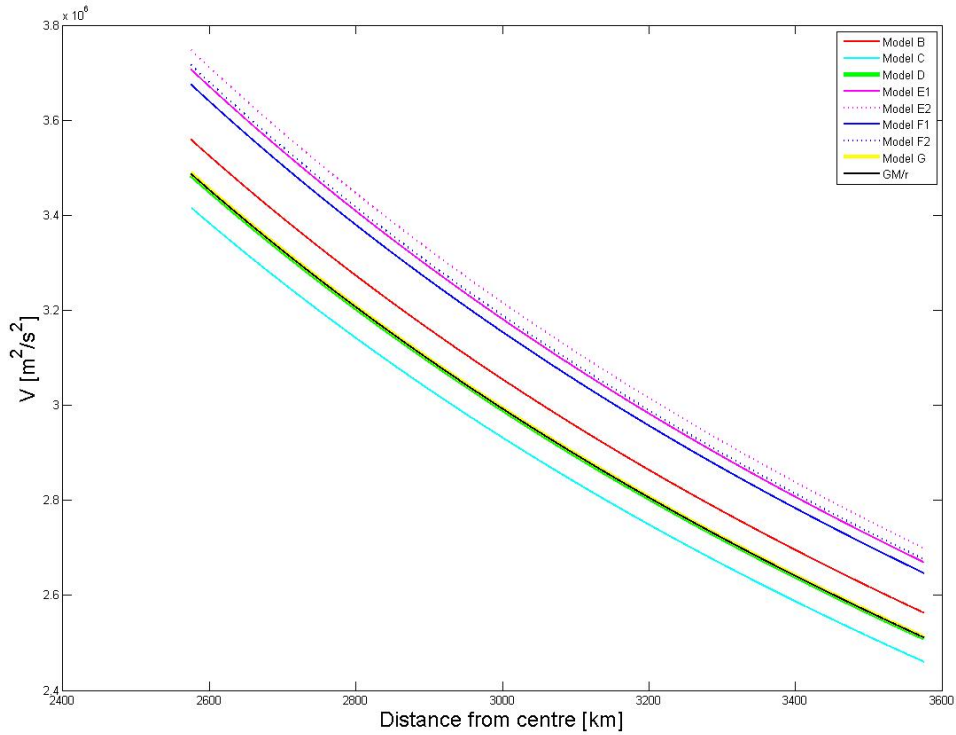


Figure 5.1: Gravitational potential for an arbitrary point on the z -axis computed for the different interior models given in table D.1.

mean density of Titan, $\rho_{lake} < \bar{\rho}_{Titan}$, the lake can be treated as extra mass on top of the homogeneous sphere that represents Titan, see figure 5.2. In this case though, there is no surplus of mass, but a mass deficit. To superimpose the outcome of the single layer computations of the lakes upon the point mass approximation of Titan, the density used in the single layer computations is negative and given as:

$$\Delta\mu = \mu_{lake} - \bar{\mu}_{Titan} \quad (5.3)$$

If the density of the lakes would be larger than that of Titan, equation 5.3 can be used too (e.g. a mass surplus). Only then the value for $\Delta\mu$ used in the computations would be positive.

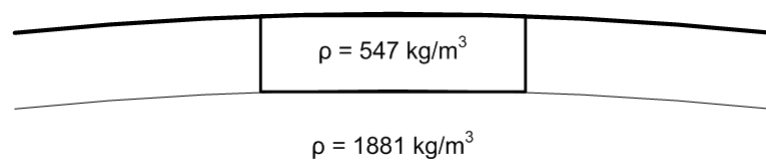


Figure 5.2: The lake can be seen as a ‘hole’ in the homogeneous sphere, because the density of the hydrocarbon mixture, $\rho_{lake} = 547 \text{ kg/m}^3$, is less than the mean density of Titan, $\bar{\rho} = 1881 \text{ kg/m}^3$.

5.2 Initial conditions: reference system and source points

Before setting up a model it is important to decide about the reference system in which the computations are done. One reference system has to be chosen, measurements done in different reference systems are hard to compare. The lakes at the northern hemisphere of Titan are used as source points for the models. How that is done is explained in this section too.

5.2.1 Reference coordinate system

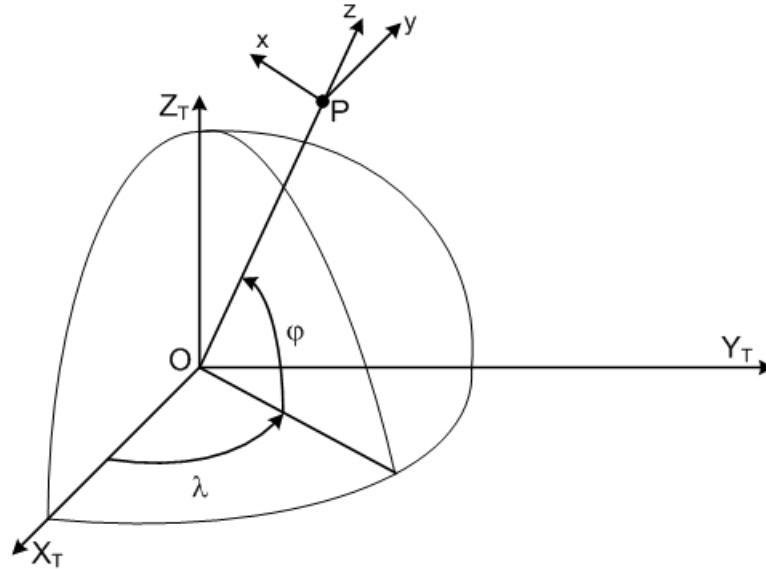


Figure 5.3: The global Titan reference system (X_T, Y_T, Z_T) and the local north-oriented reference system (x, y, z).

Figure 5.3 shows a schematic representation of Titan and the position of the gradiometer, point P , above the surface of Titan. Attached to Titan is a global cartesian coordinate system, indicated by the axes X_T, Y_T and Z_T , in which the signals of the gravity gradients are computed. The origin of this system is located at Titan's geometrical center and the Z -axis coincides with the mean rotational axis of Titan. The mean equatorial plane perpendicular to this axis forms the XY -plane and the XZ -plane is generated by the mean meridian plane of Titan's 'Greenwich' [77], i.e. 'zero-degree longitude' at Titan. The results of the modeling, however, are presented in a local astronomical reference system attached to the gradiometer. This system has its origin located at observation point P , the z -axis directed to the astronomical zenith, the x -axis directed to the north and the y -axis directed to the east. The local north-oriented reference system is indicated in figure 5.3 by small x, y, z . The transformation of the global Titan coordinate system to the local north-oriented reference system is given by [61] as:

$$\mathbf{R} = \begin{bmatrix} -\sin \varphi \cos \lambda & -\sin \varphi \sin \lambda & \cos \varphi \\ -\sin \lambda & \cos \lambda & 0 \\ \cos \varphi \cos \lambda & \cos \varphi \sin \lambda & \sin \varphi \end{bmatrix} \quad (5.4)$$

with the angles φ and λ as indicated in figure 5.3. The output of the measured gradients are collected in gradient tensor Γ_0 , measured in the global Titan reference system. The transformation

of this matrix into the final gradient tensor Γ , in the local north-oriented reference system is defined by:

$$\Gamma = \mathbf{R}\Gamma_0\mathbf{R}^T \quad (5.5)$$

where the subscript T indicates the transpose of the rotation matrix \mathbf{R} (equation 5.4).

Following the assumption that Titan is spherical symmetrical, the gradient tensor at the surface of the Titan ($r = R_T$) can be rewritten, in the local-north oriented reference system, as:

$$\Gamma = \frac{GM}{R_T^3} \begin{bmatrix} -1 & 0 & 0 \\ 0 & -1 & 0 \\ 0 & 0 & 2 \end{bmatrix} \quad (5.6)$$

Figure 5.4 shows the gradients in the local north-oriented reference system. For comparison, figure 5.5 shows the gradients in the Titan-centered reference frame. The difference between the two figures is obvious. The values of the gradients in the Titan-centered reference frame differ from the values given in the local north-oriented reference system, this stresses the importance of choosing one reference frame to present the results. The results in this thesis research are all given in the local north-oriented reference system.

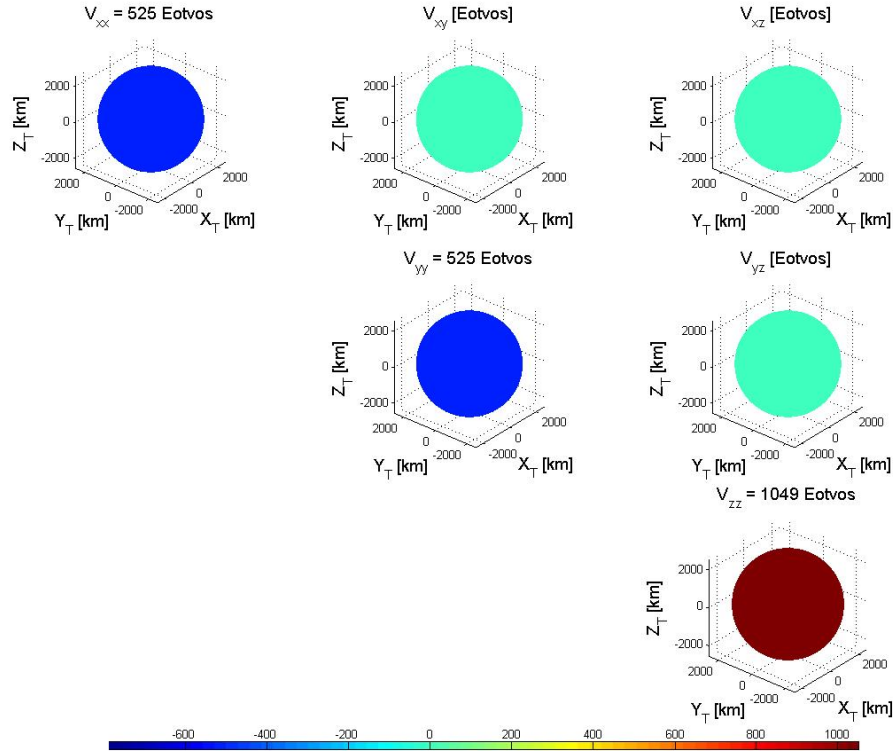


Figure 5.4: The gravity gradients at the surface of Titan, shown in the local north-oriented reference system. The dark red areas (maximum) in the plots have a value of 1049 E, the dark blue areas (minimum) a value of -525 E.

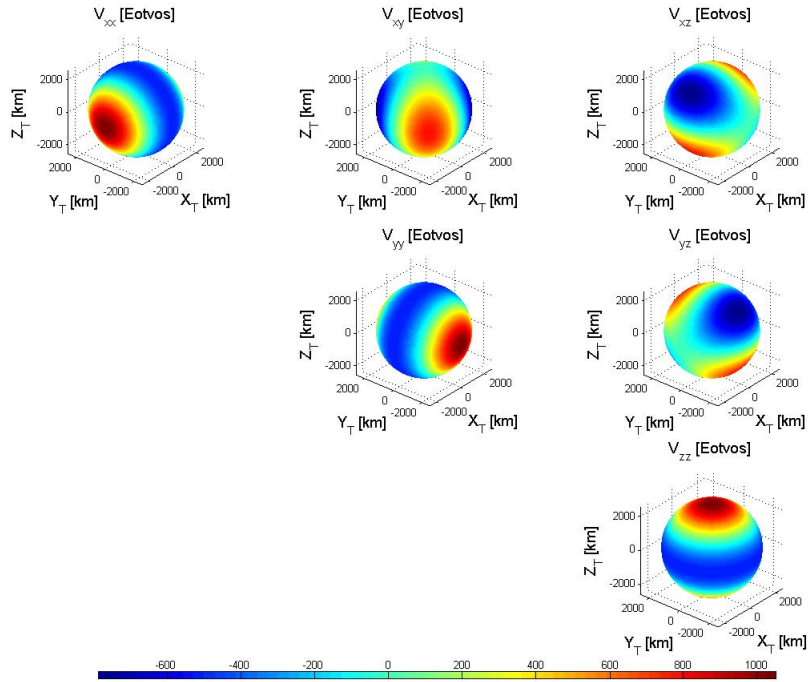


Figure 5.5: The gravity gradients at the surface of Titan shown in the Titan centered reference system. The dark red areas (maximum) in the plots have a value of 1049 E, the dark blue areas (minimum) a value of -525 E.

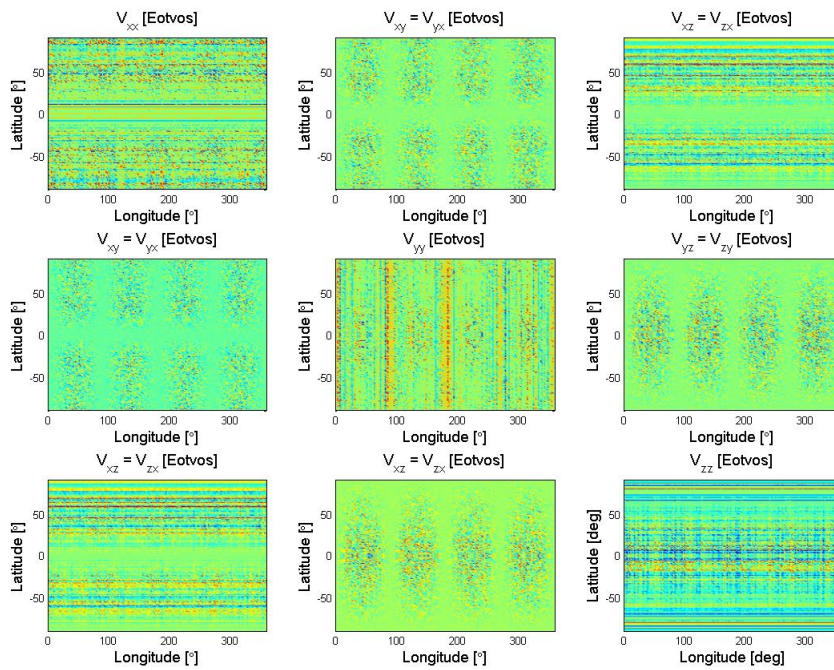


Figure 5.6: The gradients plotted in the local north-oriented reference system. The amplitude of the noise seen is of the order of 10^{-23} Eötvös.

By inspecting the gradients in the local north-oriented reference system (figure 5.6) more closely, noise features are visible. The amplitude of these features is of the order of 10^{-23} Eötvös. It is clear that these features are due to round off errors. MATLAB uses numerical methods to approximate analytical formulae, such as sine and cosine. The noise seen is a result of these approximations. It will be shown that this noise is of no influence on the simulations of the measurements done later on.

5.2.2 Selecting and discretizing the lakes from the northern hemisphere

In order to use lakes as source points for the computations in the single layer method, they have to be discretized. From the lakes seen in figure 2.8, two large lakes are selected. A raster is drawn over the lakes using squares of 1° by 1° . The coordinates of these squares are written down in a text-file, which can be read by the different MATLAB-files. Figure 5.7 shows the SAR image of the lakes on the left-hand side and the rasterized lakes using dots to signify the source points on the right-hand side. Each dot represents a square of 1° by 1° , corresponding to the area used per measurement point.

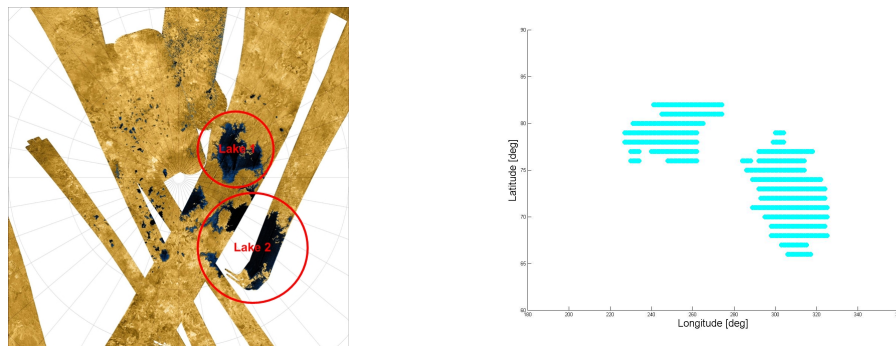


Figure 5.7: SAR image of the lakes at the northern hemisphere (left) and the discretization of the two largest lakes. Note that the reference system used is different in both pictures.

5.3 The tidal potential at the surface of Titan

The tidal potential of Titan can be split up in a static and a time-varying part. First the influence of several celestial bodies is simulated, to resolve if these bodies have a significant influence on Titan. Afterwards the time-varying part of the tidal potential caused by Saturn is investigated.

5.3.1 The tidal potential at the surface of Titan

The tidal potential at the surface of Titan due to the gravitational attraction of Saturn is given by equation 4.79:

$$V_t = \frac{GM_S}{a} \sum_{n=2}^{\infty} \left(\frac{R_T}{a} \right)^n P_n(\cos \theta)$$

where M_S is the mass of Saturn, a the semi-major axis of the orbit of Titan around Saturn, R_T is the radius of Titan and θ is the colatitude of the measurement location. According to [55], as the

Table 5.1: Estimation of the values for the tidal potential V_t , degree two and three, at the surface of Titan induced by several celestial bodies.

Celestial body	GM [km^3/s^2]	Distance [km]	$V_{t(n=2)}$ [m^2/s^2]	$V_{t(n=3)}$ [m^2/s^2]
Sun	$1.327 \cdot 10^{11}$	$1.4276 \cdot 10^9$	$1.2559 \cdot 10^{-4}$	$6.6243 \cdot 10^{-11}$
Saturn	$3.7928 \cdot 10^7$	1221000	57.371	$3.5380 \cdot 10^{-2}$
Mimas	2.503	1035460	$6.2079 \cdot 10^{-6}$	$4.5143 \cdot 10^{-9}$
Enceladus	7.206	982960	$2.0891 \cdot 10^{-5}$	$1.6003 \cdot 10^{-8}$
Tethys	41.21	926330	$1.4275 \cdot 10^{-4}$	$1.1604 \cdot 10^{-7}$
Dione	73.113	843580	$3.3535 \cdot 10^{-4}$	$2.9933 \cdot 10^{-7}$
Rhea	153.94	693930	$1.2685 \cdot 10^{-3}$	$1.3764 \cdot 10^{-6}$
Iapetus	120.51	2339840	$2.5903 \cdot 10^{-5}$	$8.3356 \cdot 10^{-6}$
Hyperion	0.37	279880	$4.6469 \cdot 10^{-5}$	$1.2502 \cdot 10^{-7}$

distance between Saturn and Titan is far larger than the radius of Titan ($a \gg R_T$), the Legendre polynomials only need to be expanded up to degree–two terms giving:

$$V_{t(n=2)} = \frac{GM_S R_T^2}{a^3} P_2(\cos \vartheta) \quad (5.7)$$

To verify if the third order influences can really be neglected, these are estimated too:

$$V_{t(n=3)} = \frac{GM_S R_T^3}{a^4} P_3(\cos \vartheta) \quad (5.8)$$

A complete overview of the Legendre polynomials up to order and degree three is given in appendix C. The Legendre functions needed in this case are P_2 and P_3 (second and third order) defined as [34]:

$$\begin{aligned} P_2(\cos \vartheta) &= \frac{1}{4} (1 + 3 \cos(2\vartheta)) \\ P_3(\cos \vartheta) &= \frac{1}{8} (3 \cos \vartheta + 5 \cos(3\vartheta)) \end{aligned} \quad (5.9)$$

The results of the estimations for the Titan–Saturn system are given in table 5.1. The distance between Titan and Saturn is approximated by the semi–major axis of the orbit of Titan and assuming Titan is located at the pericentre of its orbit. The formulae for the tidal influence of other celestial bodies can be constructed in the same way. Next to Saturn the tidal influence of the Sun, the Saturnian regular satellites and Hyperion are estimated and the results of these estimations are given in table 5.1 too. The distance between Titan and the Sun is given by the semi–major axis of the Saturnian system, the distances of the larger satellites of Saturn is approximated by the difference between the semi–major axes of Titan and the other satellite in orbit around Saturn. The GM values and the values for semi–major axes of the satellites are given by the JPL HORIZONS website [29], which has the most up–to–date values. If the tidal potential at balloon or satellite altitude h is to be estimated, R_T in equation 5.7 can be replaced by $r = R_T + h$. Since the balloon will be flying at a height between two and ten kilometers, the estimations at these heights will not deviate much from the estimations given in table 5.1.

As can be seen from table 5.1 tides generated on Titan by the other moons orbiting Saturn are

negligible. The influence of Saturn is significant, the minimum and maximum values of the tidal potential are around $-8.58 \text{ m}^2/\text{s}^2$ and $138.15 \text{ m}^2/\text{s}^2$ respectively for degree two and around $-0.12 \text{ m}^2/\text{s}^2$ and $0.29 \text{ m}^2/\text{s}^2$ respectively for degree three. The third order influences are indeed making a small difference and are thus negligible.

5.3.2 The time-varying part of the tidal potential

According to [75] the tidal potential varies due to the radial tide, caused by the varying Saturn–Titan distance and the librational tide, caused by the libration of the sub–Saturn point. The amplitude of this libration is $\tan^{-1}(2E) = 3.35^\circ$ along the equator, which corresponds to 150.5 km at Titan’s surface. The time-dependent part of the tide-raising potential of Saturn on Titan is given by equation 4.80:

$$V_{time} = -\frac{GM_S R^2}{a^3} 3e \left[\frac{1}{2} (3 \sin^2 \vartheta \cos^2 \lambda - 1) \cos(nt) + \sin^2 \vartheta \sin(2\lambda) \sin(nt) \right]$$

where M_S is the mass of Saturn, R is the radius from the center of mass of Titan to the measurement point ($R = R_T$ at the surface of Titan), a the semi major axis of the orbit of Titan, n is the orbital angular frequency, $e = 0.0292$ the orbital eccentricity of Titan, ϑ and λ are the co-latitude and longitude (with $\lambda = 0$ at the sub–Saturn longitude), and t the time. Due to the eccentricity of the orbit of Titan tidal flow occurs, if the orbit of Titan were completely circular there would be none. This can be clearly illustrated by plotting this time-varying part. Figure 5.8 shows this time-varying part of the tidal potential, starting at the position where Titan is at peri-saturnian at day 1, and subsequently day 4, day 8 and day 12 of the orbit of Titan around Saturn, but seen from a Titan centered reference system. From that point of view it looks as if Saturn orbits Titan, clearly indicated by the shift the tidal bulge makes. This tidal bulge, as consequence of the tidal forces introduced by Saturn, remains pointed to Saturn since the orbital and rotational period of Titan are equal to each other (see table 2.2): 15.946 Earth days. Appendix E gives the time-varying part for every day, during one orbit of Titan around Saturn. The dark blue areas in the figures correspond to the minimum value of $-12.868 \text{ m}^2/\text{s}^2$ and the darkest red areas correspond to the maximum value of $12.872 \text{ m}^2/\text{s}^2$.

The time-varying part of the gravitational potential is of an order less than the static part, thus of almost no influence on the total potential. Comparing these values with, for instance, Europa, the differences are of an order of magnitude lower and therefore the tidal potential has no significant influence on Titan.

Recent publications in Science ([43] and [64]) show that Titan spins approximately 0.36° per year faster than synchronous spin and that it appears to be accelerating, relative to synchronous spin, by 0.05° per day every 100 years [43]. This observed drift indicates that motion of the crust relative to the Titan centered reference system is permitted, which would not be the case for highly viscous ice. This means that the viscosity of the crust must be low enough for the tidal bulge to remain pointed to Saturn whereas the entire crust drifts eastward or westward depending on the season. This strongly suggests that there is an internal ocean on Titan and it is already believed that the anticipated determination of the tidal Love number k_2 , as explained in section 4.3, will confirm an internal liquid ocean [64].

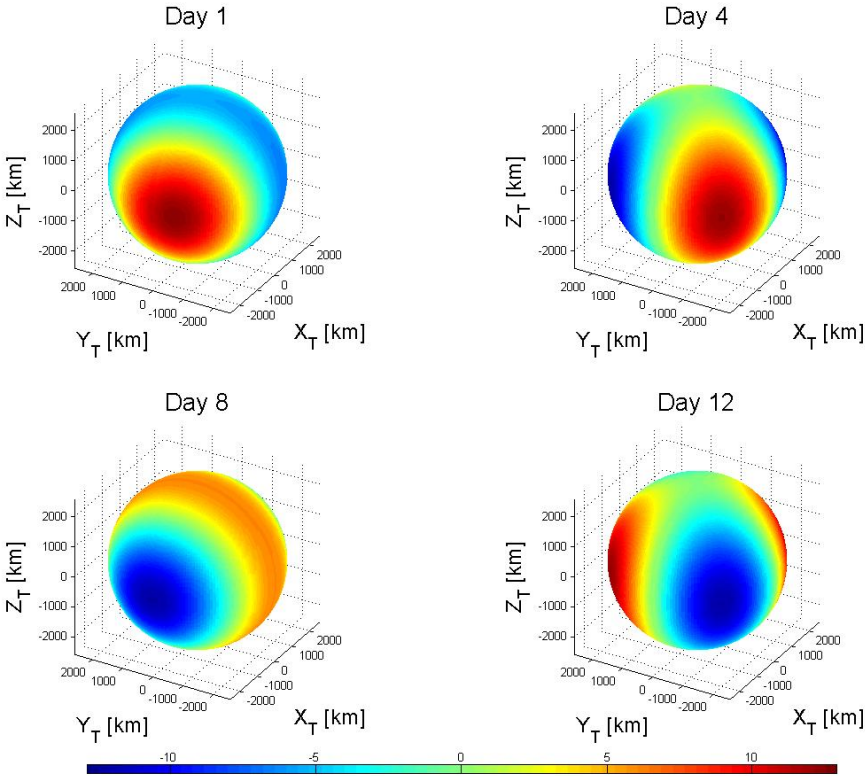


Figure 5.8: The time-dependent part of the tide-raising potential at days one, four, eight and twelve of an orbit of Titan around Saturn.

Analysis of the gradients measured in the vicinity of lakes on Titan

The gradiometer measures the gradients of the gravity field, therefore the analysis will focus on the gravity gradients of the gravitational field, and not on the gravitational potential. An analysis is made of the results of different scenarios, generated by the model that was explained in detail in section 5.1. First the gravitational potential and gravity gradients of the area surrounding the two selected lakes is simulated in section 6.1. Section 6.2 explains the layout of the problem and states the assumptions taken. The strength of the gradients against the measurement altitude will be investigated in section 6.3. Section 6.4 will look at the difference in measuring one or two lakes and section 6.5 shows the difference in measuring along different trajectories. Hereafter the density of the lakes and depth of the lakes are varied in sections 6.6 and 6.7 respectively. Section 6.8 finishes this chapter by looking with what accuracy the density of the lakes can be retrieved using the least-squares technique.

6.1 Gravitational potential and gravity gradients of the lake area

In previous sections it is stated that the gravitational potential is very sensitive to mass differences. To show this, a closer look is taken at the gravitational potential of the lakes and the influence of increasing depth underneath the surface of Titan. The gradiometer, however, does not measure the gravitational potential directly, but the gravity gradients. A first glance is taken at the gravity gradients in this section too.

6.1.1 Gravitational potential of the lakes

After computation of the gravitational potential for the two lakes that were selected in section 5.1, in a 1° by 1° grid and using a measurement altitude of 2 km, nice contour plots of the lakes are created, see figures 6.1 and 6.2. Figure 6.1 shows the gravitational potential of the smaller lake (lake 01), figure 6.2 of the larger lake (lake 02). The gravitational potential of Titan has not been added in these two pictures. The gravitational potential of the lakes are simulated separately in these two figures, figure F.2 in appendix F shows the gravitational potential of the two lakes and Titan, superimposed on each other.

To see the effect of sub-surface lakes on the gravitational potential, the depth of the lake underneath the surface of Titan is increased. The gravitational potential is used for this, because it clearly shows where the lakes are located. Figures 6.3 and 6.4 show the gravitational potential of both lakes combined, for a depth of 20 km underneath the surface of Titan and the right figure

for a depth of 100 km underneath the surface of Titan respectively. In appendix F the figures for a depth of 10, 30 and 40 km underneath the surface are given. It is clearly shown that the potential decreases as the depth of the lakes beneath the surface increases, clearly seen from the difference in shade of blue at the tip of the lakes, since the color bar of both the figures is the same. Note that the axes of both figures are different in scale. This is a good indication that the gravity gradients as a result of the subsurface lakes will be weaker.

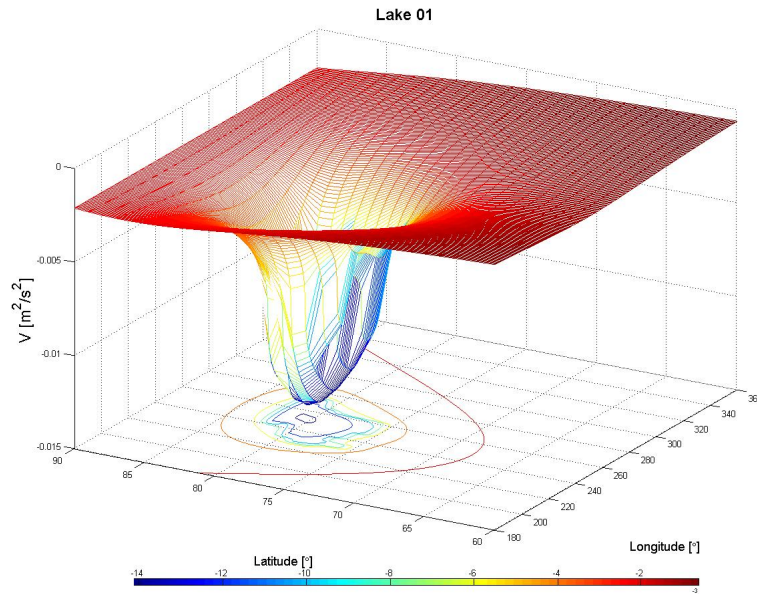


Figure 6.1: The gravitational potential [m^2/s^2] of lake 01 at a measurement altitude of 2 km.

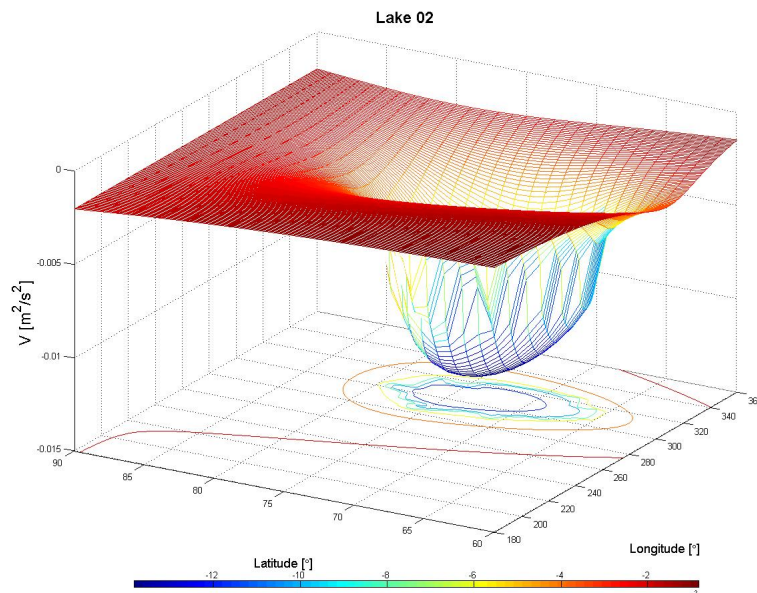


Figure 6.2: The gravitational potential [m^2/s^2] of lake 02 at a measurement altitude of 2 km.

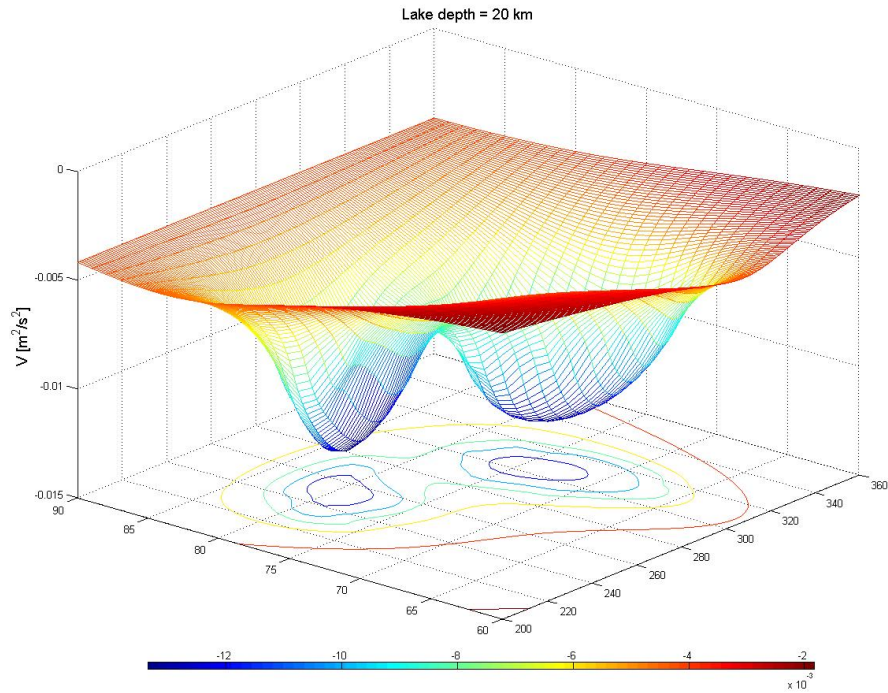


Figure 6.3: The gravitational potential [m^2/s^2] of the lakes 01 and 02 combined, located at a depth of 20 km underneath the surface of Titan. The values for Titan are not superimposed in this figure.

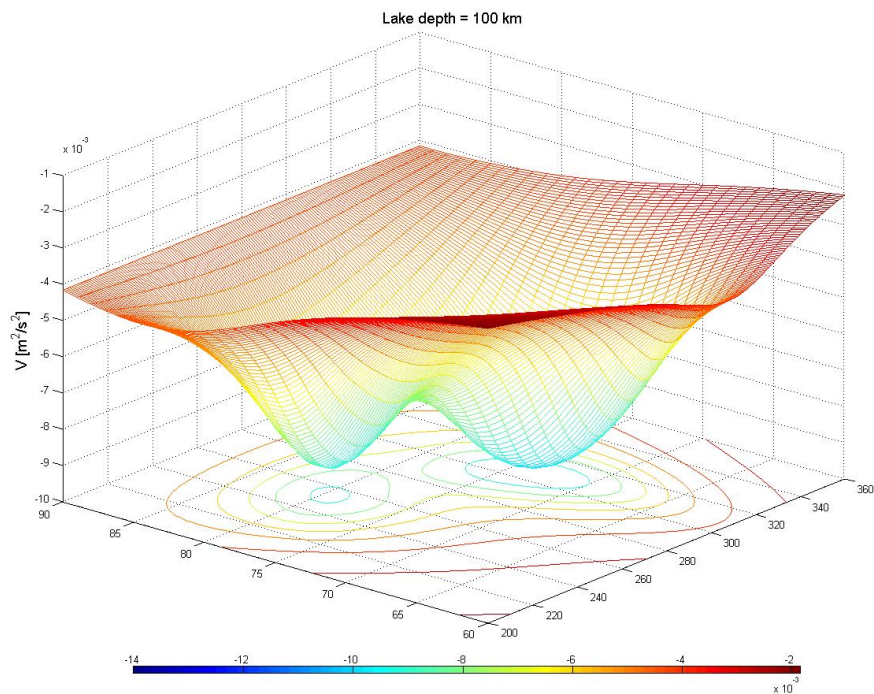


Figure 6.4: The gravitational potential [m^2/s^2] of the lakes 01 and 02 combined, located at a depth of 100 km underneath the surface of Titan. The values for Titan are not superimposed in this figure.

6.1.2 Gravity gradients of the lakes

The gravity gradients are modeled according to equations 4.64 to 4.69, as explained in section 5.1, in a 1° by 1° grid. Figure 6.5 and figure 6.6 give the results at a measurement altitude of 2 km, for lake 01 and lake 02 respectively. The values for Titan are not superimposed in this figure. Enlargement of all figures separately can be found in appendix F, only here the gradients of the two lakes are combined in one figure.

A few distinctive features can be seen directly. First of all the assumption that $V_{xy} = V_{yx}$, $V_{xz} = V_{zx}$ and $V_{yz} = V_{zy}$ is immediately clear in the results, the symmetry is seen in both figures. When looking more closely, it can be seen that the signal of the diagonal components is far stronger than that of the off-diagonal components. Next to that the values for V_{zz} are approximately twice as large as the value for V_{xx} and V_{yy} which was to be expected. Equation 5.6 already showed that the gradient V_{zz} of the spherical symmetrical model in the local north-oriented reference system is twice as large as the gradients V_{xx} and V_{yy} . The gradients of the lakes can be inspected in more detail in appendix F. In these figures the values for the two lakes and Titan are superimposed. Besides that, the figures in the appendix show two different ways of plotting the gradients. The left figure is a surface plot where the different colours represent the different values for the gradients and the right plot shows the same figure only in a 3D plot, where next to the colour the peaks represent the values of the gradients.

When having a closer look at the gradients, in figures F.6 to F.14 in appendix F, it can clearly be seen that the difference in gradients is not very large. The value for the gradient V_{xx} varies approximately 0.6 Eötvös between its constant value and the maximum. The other variations are given in table 6.1. In order to measure variations in the gradients in the diagonal direction, the gradiometer must be able to measure small differences, of approximately 0.1 Eötvös. The off-diagonal gradients have even smaller variations, the gradiometer must be able to sense differences in the gravity gradient of the order of 0.01 Eötvös for V_{yz} . The differences in V_{xy} are so small, that these might not be measured at all.

Table 6.1: The maximum difference in magnitude of the gravity gradients measured over the lakes.

Gradient	Maximum variation [Eötvös]	Gradient	Maximum variation [Eötvös]
ΔV_{xx}	0.6	$\Delta V_{xy} = \Delta V_{yx}$	$8 \cdot 10^{-4}$
ΔV_{yy}	0.6	$\Delta V_{xz} = \Delta V_{zx}$	0.35
ΔV_{zz}	0.5	$\Delta V_{yz} = \Delta V_{zy}$	0.015

6.2 Simulation of a passive balloon in the atmosphere of Titan

Assume a passive balloon, with in its gondola a gravity gradiometer, is safely released in the atmosphere of Titan. The trajectory such a balloon might follow is briefly touched in section 2.2, and more in depth discussed in [74]. Due to the prevailing zonal winds (section 2.5) a trajectory of a passive balloon will not vary in latitude very much. For more possible trajectories of passive

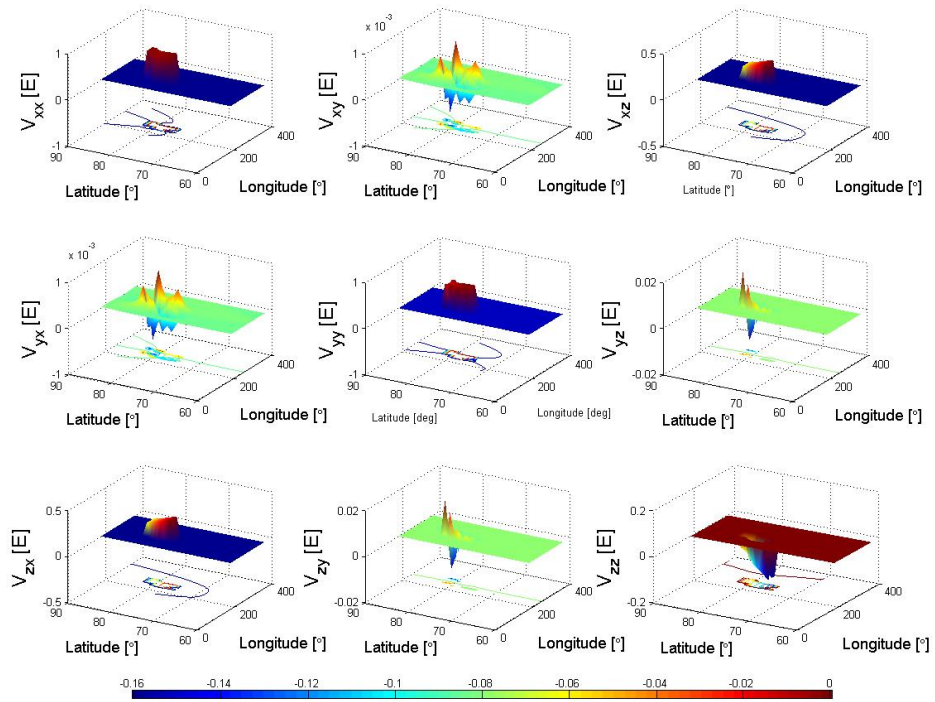


Figure 6.5: The gravity gradients of lake 01.

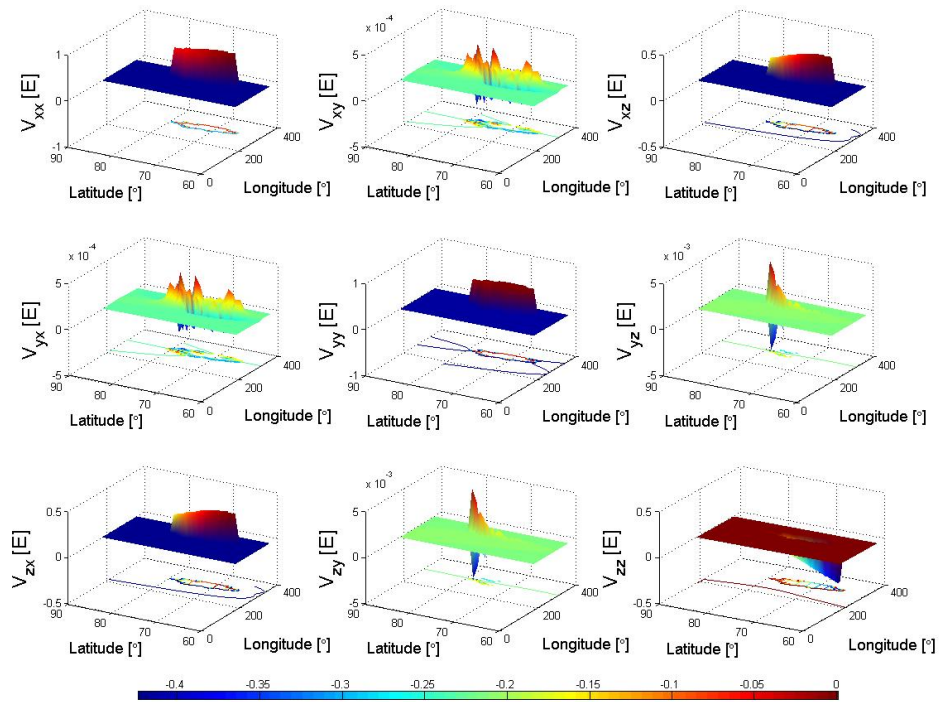


Figure 6.6: The gravity gradients of lake 02.

balloons see [74], keep in mind that these trajectories are only an indication and are based on a model of Titan's atmosphere. Based on these models, the trajectories chosen for the simulation will not change in latitude, only in longitude. Figure 6.7 shows an example of a trajectory simulated. The trajectory follows a latitude of 79°N , crossing both lakes. It is assumed that a passive balloon follows this trajectory, in the picture from left to right. Section 6.5 will look at other possible trajectories and make a comparison between them.

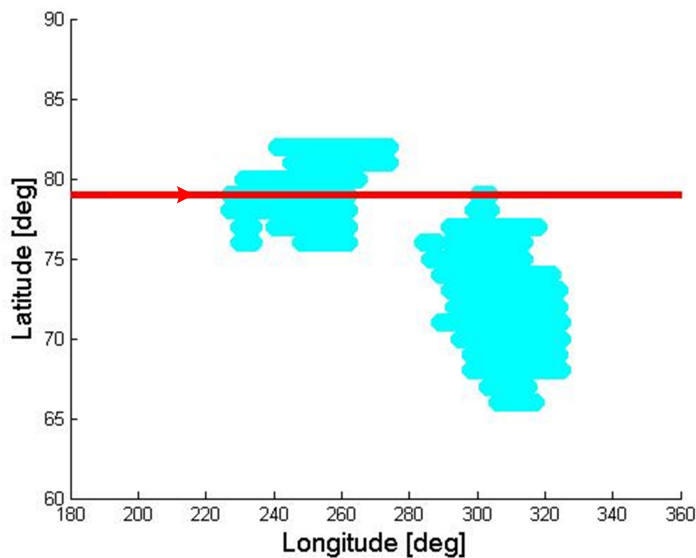


Figure 6.7: The trajectory along 79°N crossing both lakes selected in section 5.1.

Several important assumptions are made before starting the simulations:

- The gradiometer is oriented along the axis of the local north-oriented reference system
- The exact location of the balloon, and thus the gradiometer, is known
- The gradiometer is perfect, i.e. measurements are done instantaneously
- All gradients are measurable

The gradients are given in Eötvös.

6.3 Gradients measured at different altitudes throughout the atmosphere of Titan

The value for the gravitational potential decreases with altitude, as shown in figure 5.1. Consequently the gravity gradients decline with increasing altitude, thus it is interesting to see until which altitude the gradient is strong enough to be measured by the gradiometer. To simulate these measurements, the measurement point (i.e. the balloon with the gradiometer) is located in the middle of both lakes, see table 6.2 and figure 6.8, and the measurements are taken upwards. The red dot in figure 6.8 represents the location of the balloon, from where it is assumed to increase in altitude in a straight line upwards. The gradients of both lakes are simulated separately

to see if the size of the lakes have an influence on the strength of the gradients. The area of the lakes as used for the simulations is given in table 6.2 too.

Table 6.2: *The location of the measurement point and the area of the lakes.*

	Colatitude (ϑ)	Longitude (λ)	Area [km ²]
Lake 01	11°	245°	12 050
Lake 02	17°	308°	17 497

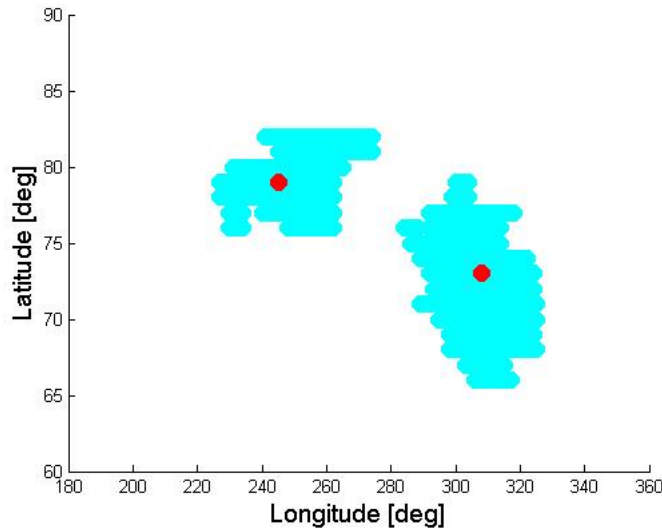


Figure 6.8: *Schematic representation of the location of the measurements. The red dot represents the balloon with in its gondola the micro-gravity gradiometer. The simulation is done by varying the altitude of the balloon, assuming it does not drift sideways.*

The first simulations (figure F.15 and F.16) are done up to an altitude of 1000 km, the approximate height of Titan’s atmosphere. The diagonal gradients (V_{xx} , V_{yy} and V_{zz}) look more or less constant, while the off-diagonal gradients (V_{xy} , V_{yz} and V_{xz}) rapidly become very small. After zooming in to measurements up to an altitude of 100 km (figures F.17 and F.18), the same decrease is seen in general. It is thus more promising to look at the first tens of kilometers. Section 2.2 shows that simulations of possible paths of passive balloons were made up to an altitude of 20 km, therefore the last simulations of a balloon floating in the middle of a lake, are zoomed in on the altitude range from 0 to 20 km.

The results up to an altitude of 20 km are given in figure 6.9 for the diagonal gradients and in figure 6.10 for the off-diagonal gradients. The decrease of the signal looks very steep, but note that the y-axis has a logarithmic scale. The gradients for both lakes are plotted next to each other, such that they can be easily compared. It is to be expected that the gradients from lake 02 is stronger, because the area of the lake is larger (more mass). Comparing the figures, the gradients from lake 02 is slightly stronger, but not significantly. Very clear from both figures is that the gradients are the strongest the first few kilometers and decrease with increasing altitude.

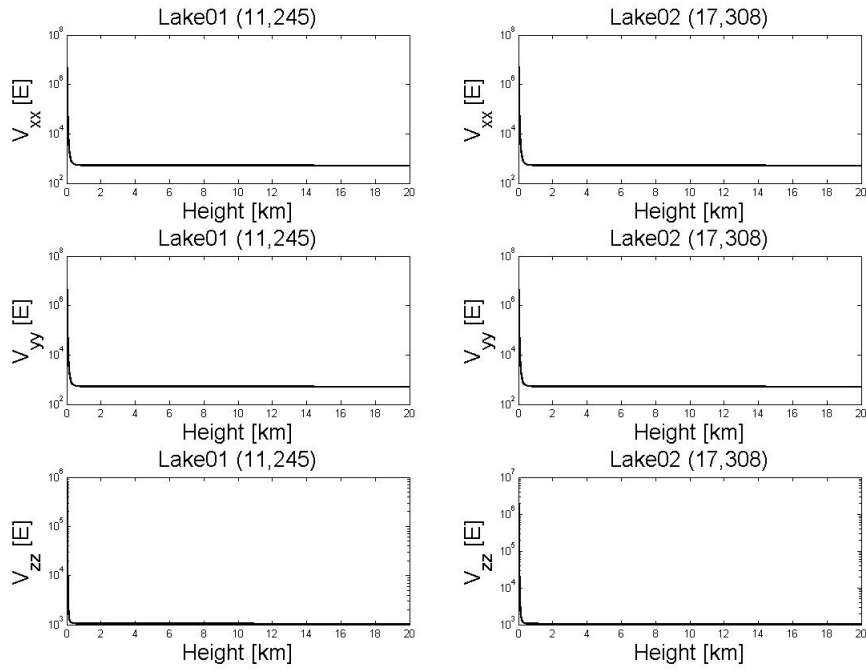


Figure 6.9: Diagonal gradients up to an altitude of 20 km, measured at the middle of lake 01 (left) and lake 02 (right). Note that the scale of the y-axis is logarithmic.

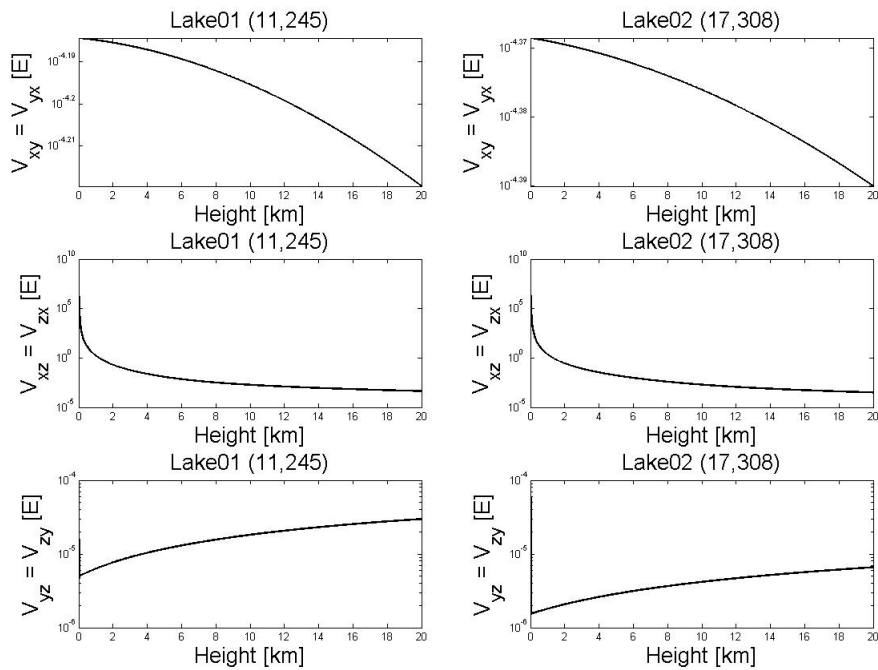


Figure 6.10: Off-diagonal gradients up to an altitude of 20 km, measured at the middle of lake 01 (left) and lake 02 (right). Note that the scale of the y-axis is logarithmic.

6.3.1 Gradients measured at different balloon altitudes

To show the difference between the strength of a gradient compared to the measurement altitude more precisely, a balloon trajectory is chosen as explained in section 6.2. The path chosen follows 79°N latitude, from 200° to 300° longitude, see figure 6.7, taking only lake 01 into account. The simulations are done at an altitude of 2, 6 and 10 km. The diagonal gradients (figure 6.11) decrease visibly with altitude, at an altitude of 10 km the signal of the lake is so small that it cannot be distinguished from the gradient that Titan produces. For the off-diagonal gradients (figure 6.12) this is less clear. V_{xz} decreases with altitude, while V_{yz} has the strongest signal at an altitude of 6 km, the weakest at 10 km and the strength of the gradient at an altitude of 2 km is in between both. The shape of the plot of V_{xy} is more or less the same every time, but at the crossing of the border of the lake the height of the smaller bump decreases with increasing altitude.

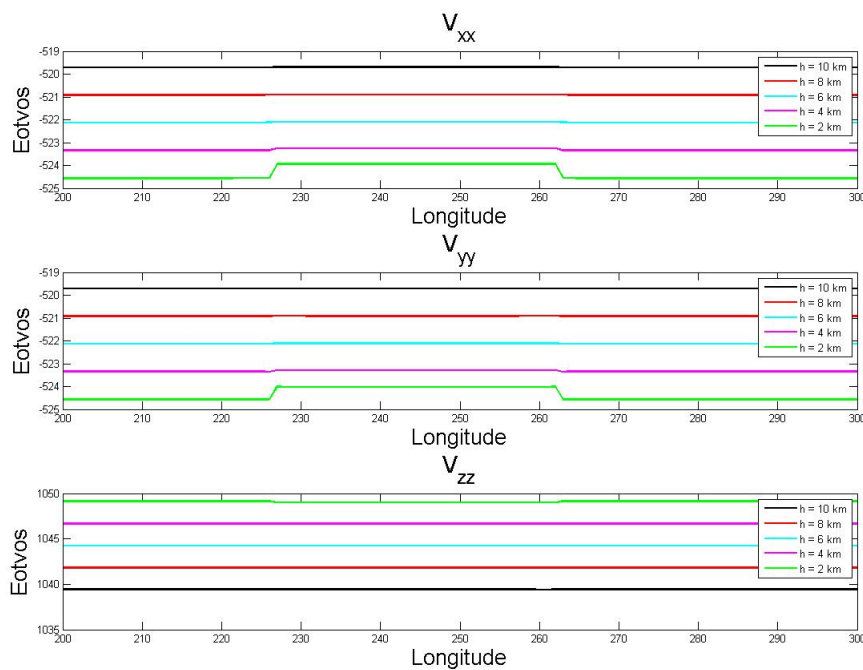


Figure 6.11: The diagonal gradients along a trajectory following 79°N at a measurement altitude of 2, 6 and 10 km, lake 01 only. The density of the lake is 547 kg/m³.

When looking at the same gradients at a measurement altitude of 10 km only (figures F.19 and F.20), variations, though relatively small when compared to the gradients at a measurement altitude of 2 km, can be seen. The difference seen in figure F.19 is ~ 0.011 Eötvös for V_{xx} , ~ 0.005 Eötvös for V_{yy} and ~ 0.0015 Eötvös for V_{zz} . This would mean that to measure these differences the gradiometer at least should have a sensitivity of ~ 0.001 Eötvös, which is very small compared to the ~ 1 Eötvös the industry want to achieve at the moment.

It is clear that it would be most preferable to fly a balloon at the lowest possible altitude. The variations in gradients are the largest and best visible at a measurement altitude of 2 km. On Titan, the highest features found until now are mountain ranges, see section 2.4, with a maximum

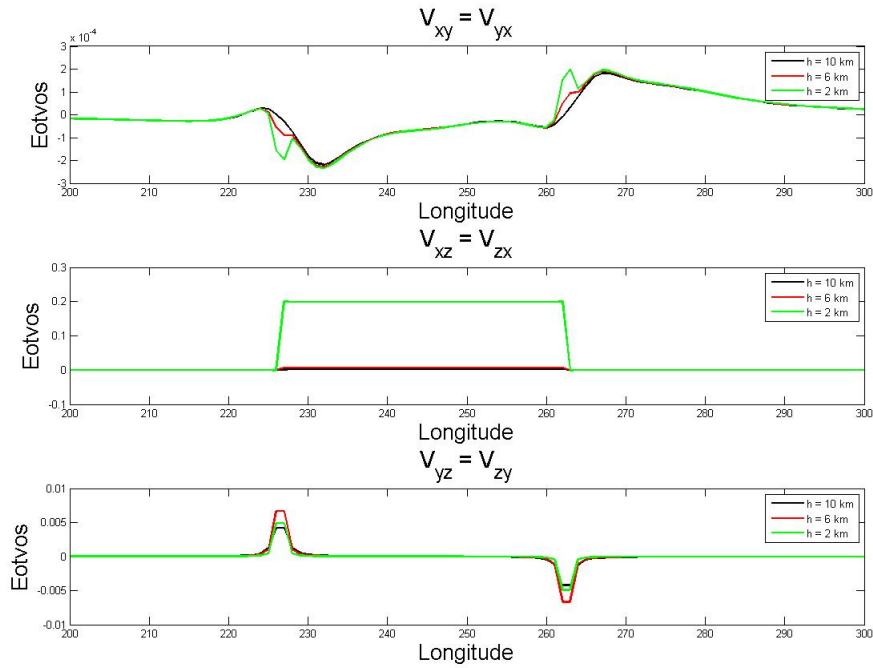


Figure 6.12: The off-diagonal gradients along a trajectory following $79^\circ N$ at a measurement altitude of 2, 6 and 10 km, lake 01 only. The density of the lake is 547 kg/m^3 .

height of 2 km. Considering the balloon trajectories described in [74], the lowest possible measurement altitude that seems feasible to fly the balloon is 2 km. Therefore the simulations will be done using this altitude as measurement altitude.

The balloon is assumed to float at a constant altitude, because when changing the altitude, the value of the gradients changes. Thus a change in observed gradient could not only be because of the crossing of the border of a lake, but because of an in- or decrease in balloon altitude too. The gradient tensor is related to this increase in altitude (equation 5.6):

$$\Gamma \sim \frac{GM}{(R+h)^3}$$

hence a change in gradient corresponds to a change in altitude (J. M. Smit, personal communication):

$$\Delta\Gamma \sim 3\Gamma \frac{\Delta h}{R} \tag{6.1}$$

Table 6.1 in section 6.1 gives the maximum differences of the gradients. At a measurement altitude of 2 km the maximum difference in the gradients V_{xx} and V_{yy} is 0.6 Eötvös. Computing the change in altitude according to equation 6.1, a change in gradients of 0.6 Eötvös corresponds with a change in altitude of 0.98 km. Thus when observing a change in gradient of 0.1 Eötvös, this could correspond with a change of balloon altitude of 0.16 km.

6.3.2 Fluctuation in the gradients of Titan

As mentioned in section 5.2, features with an amplitude of 10^{-23} Eötvös were visible in the simulation of the gradients of Titan after the transformation of the Titan-centered reference system to the local north-oriented reference system. To show that these features are of no influence on the measurements at 2 km altitude, the gradients of Titan are compared to the total gradients (that of lake 01 and Titan combined). Again the trajectory along 79°N is chosen, with left of figure 6.13 the simulated off-diagonal gradients of Titan only and right of figure 6.13 the simulated off-diagonal gradients of lake 01 with the gradients of Titan superimposed. The left figures clearly show fluctuations in the simulated trajectory, while the diagonal gradients show almost no variation, see figure F.21 in appendix F. When superimposing the gradients of Titan to the measurements of the lake, these fluctuations completely disappear. This proves that these fluctuations are of no influence in the simulations of the total gradients.

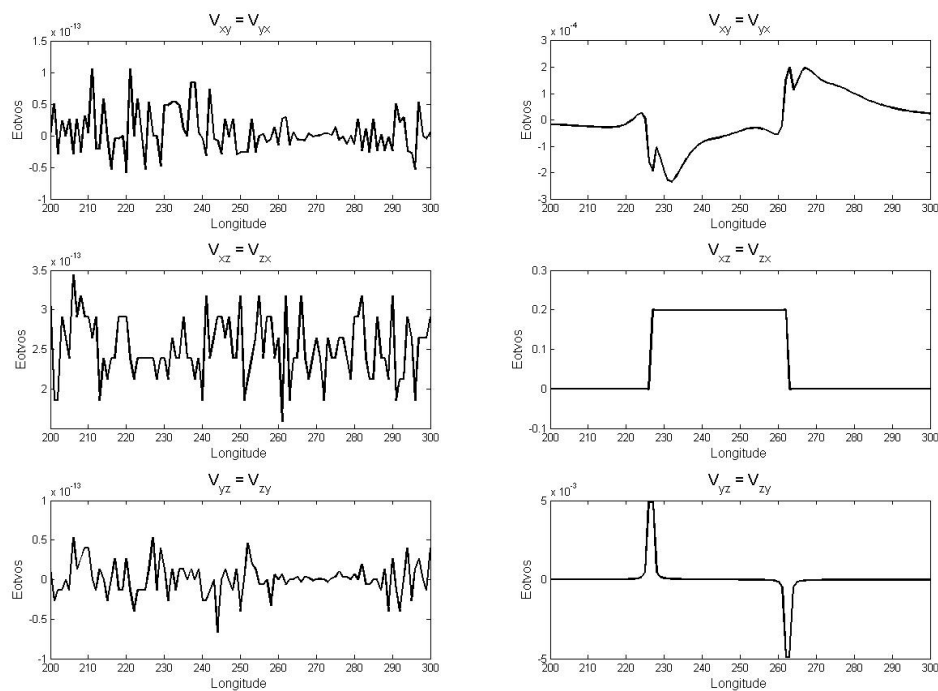


Figure 6.13: The off-diagonal gradients of Titan (left) and superimposed with the gradients of lake 01 (right) along a trajectory at 79°N , a measurement altitude of 2 km above the surface and a lake density of 547 kg/m^3 .

6.4 Combining the gradients of multiple lakes

Until now the simulations are focused on the first of the two lakes along a trajectory following 79°N latitude (see figure 6.7 again). Even if lake 02 is not crossed it still has a small influence on the measured gradients. This can be seen in figure 6.14, where the black line represents the measured gradients from lake 01 and the red line the measured gradients from lake 02. Combining both these measurements, which is a more closer approach to reality, the figure on the right of figure 6.14 is created. Here one can see that the measurements are influenced by both lakes. Looking

at the diagonal gradients (figure 6.14), lake 01 and lake 02 can be identified separately from each other, the first larger bump belongs to lake 01, while the second smaller bump belongs to lake 02. This bump is smaller, since the trajectory passes lake 02 very closely and crosses lake 01 completely. When looking at the off-diagonal gradients, figure 6.15, V_{xz} behaves the same as the diagonal gradients, where V_{yz} shows clearly separated bumps when crossing the borders of lake 01 and lake 02. Looking at the separate measurement of V_{xy} the borders of both lakes can clearly be distinguished, but when combining both measured gradients, this is not so well seen anymore. These figures show that for some measurements lake 01 cannot be distinguished from lake 02 and show the importance of having images of the area which is being observed and of knowing the location of the gradiometer during measurements.

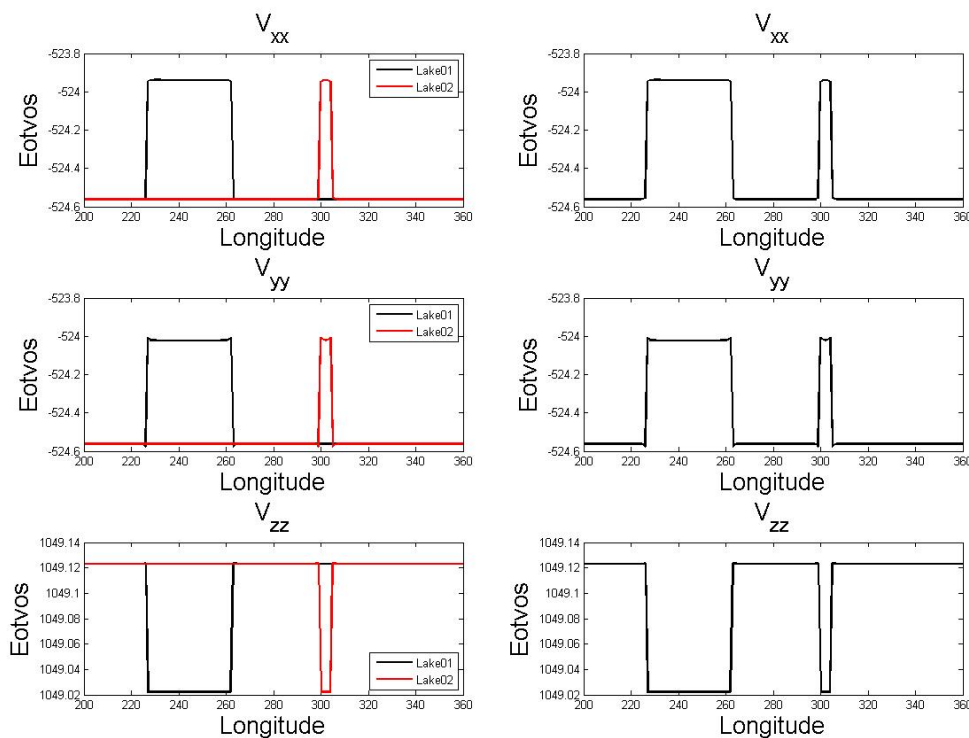


Figure 6.14: The diagonal gradients of lake 01 and lake 02 separately (left) and combined (right), both superimposed on Titan. The measurements are taken along a trajectory at 79°N , an altitude of 2 km above the surface and a lake density of 547 kg/m^3 .

6.5 Gradients along different trajectories of the balloon

The trajectory of the balloon is of importance to the measurements, the previous section showed that when crossing a second lake, measurements belonging to two different lakes might be hard to distinguish from each other. To see which trajectory can be used best for further simulations, i.e. which trajectory gives the most information, nine trajectories are selected and simulated. The trajectories used are: 85°N , 82°N , 79°N , 77°N , 74°N , 72°N , 69°N , 66°N , and 63°N , varying between flying past the lakes, crossing only one of the two lakes or crossing both. Figure 6.16 gives a visual representation of these trajectories, the flight direction is from left to right.

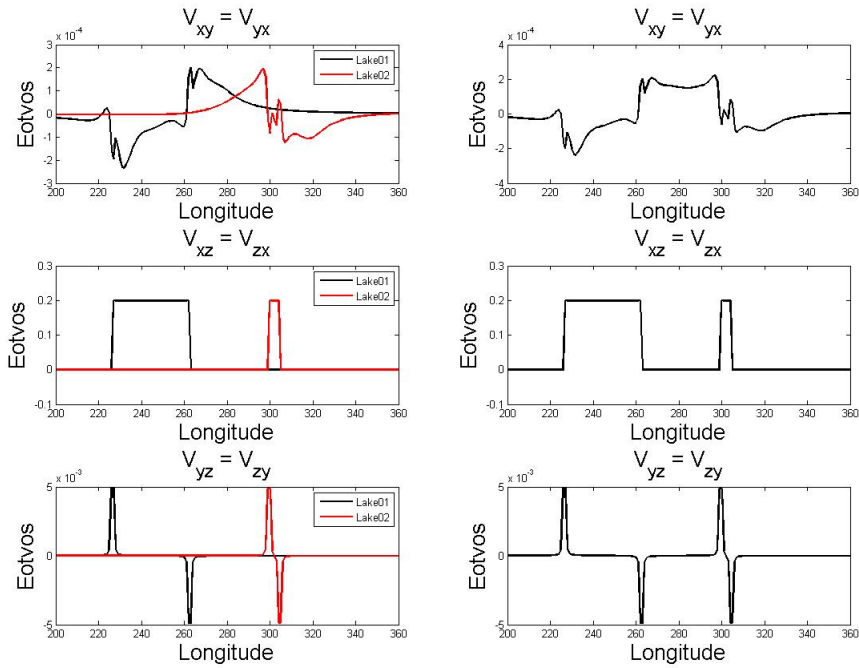


Figure 6.15: The off-diagonal gradients of lake 01 and lake 02 separately (left) and combined (right), both superimposed on Titan. The measurements are taken along a trajectory at 79°N, an altitude of 2 km above the surface and a lake density of 547 kg/m³.

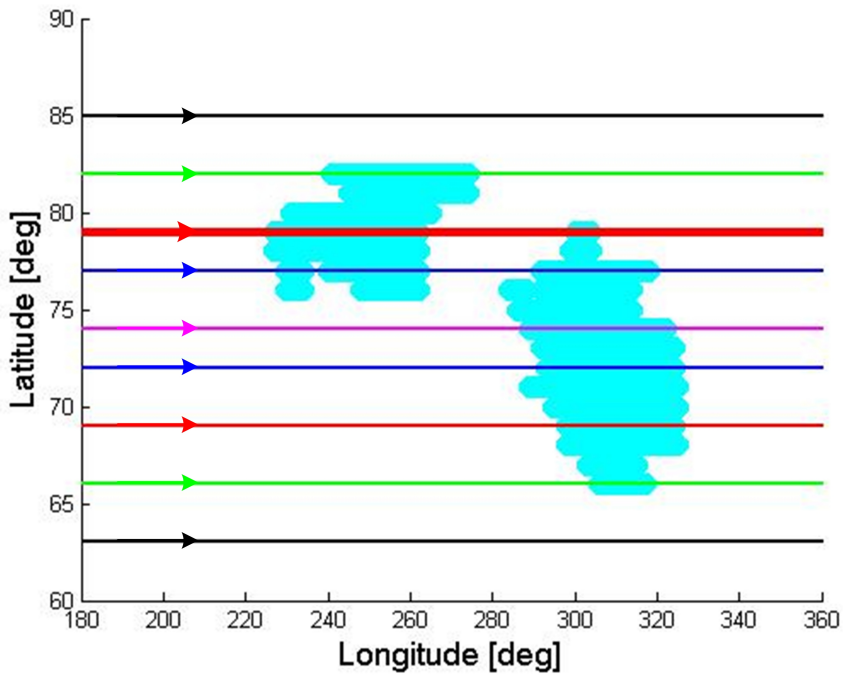


Figure 6.16: The different trajectories of the balloon as used in the simulations. The flight direction is from left to right and the thick red line represents the trajectory along 79°N, which is chosen for most the simulations.

6.5.1 The trajectories plotted in 2D

The trajectories are only plotted along varying longitude. To reduce the amount of information, two different plots are made, one of the trajectories from 63° to 72° and one of the trajectories from 74° to 85°. Figure 6.17 shows the gradient V_{xx} along the trajectories 63° till 72° (upper picture) and 74°–85° (lower picture). The figures of the trajectories for the gradients V_{yy} and V_{zz} and the off-diagonal gradients can be found in appendix F.

The diagonal gradients, V_{xz} and V_{xy} , all show more or less the same variations along longitude as the diagonal gradients. Figure 6.18 shows that along the trajectory of 85°N only the gradient of Titan is found. Along 82°N only a gradient due to lake 01 (first bump) is found; the same holds for a trajectory along 74°N: then the gradients belongs to lake 02 (second bump). Both the trajectories along 79°N and 77°N show two and three bumps respectively, representing gradients caused by lake 01 and lake 02. These two trajectories clearly give the most information, both on lake 01 and lake 02. To see which of the two trajectories will be used for further simulations, the off-diagonal gradients are inspected. V_{xy} (figure F.24) does not give a lot of information on its own, the lakes cannot be clearly distinguished in these measurements. In combination with the other two off-diagonal gradients, V_{xz} and V_{yz} , this information can be deduced and certain features in the V_{xy} plot can be assigned to lake borders, which will be shown later. On the other hand, looking at V_{yz} (figure 6.18), the lake borders can clearly be distinguished. The figure shows bumps at the border of each lake, inbound and outbound. The bumps are higher, representing a higher value for the gradient, along the trajectory of 79°N. Therefore the trajectory along 79°N is used for further simulations.

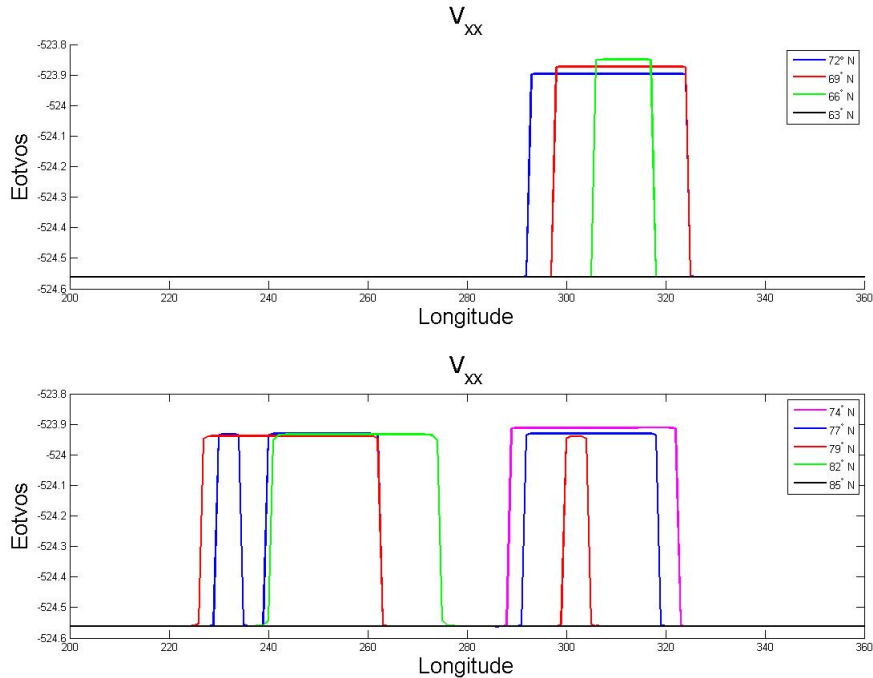


Figure 6.17: The gradient V_{xx} along different trajectories from 63° to 85°N plotted in a two dimensional way, at a measurement altitude of 2 km above the surface and a lake density of 547 kg/m³.

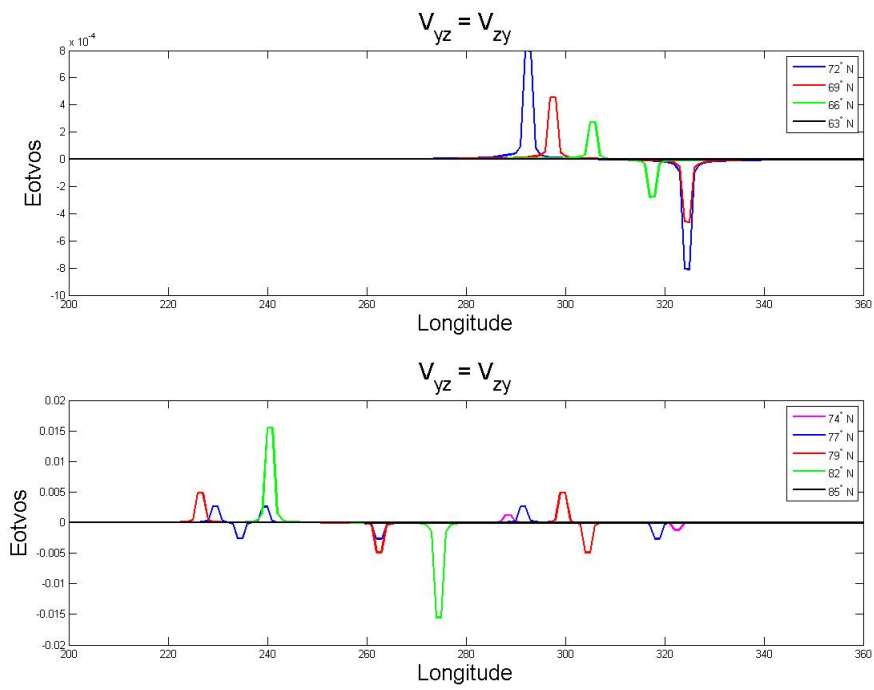


Figure 6.18: V_{yz} along different trajectories from 63° to 85°N plotted in a two dimensional way, at a measurement altitude of 2 km above the surface and a lake density of 547 kg/m³.

6.5.2 The trajectories plotted in 3D

The reason so many trajectories are chosen to be simulated is to see whether different trajectories together can provide extra information. The measurements described above are combined in a three dimensional plot, see figure 6.19 for the gradient V_{xx} . The figures for the other gradients can be found in appendix F.

When a measurement is taken very nearby or above the lake, a different gradient is measured than further away from the lake. Thus with very precise measurements, the contour of the lake, and maybe even the size, can be extracted from the measurements, as can be seen in figure 6.19. The only problem is that every mass difference gives a different value for the gradients. It could therefore be quite difficult to, with scattered measurements only, determine what physically is present at the measurement area. If a very dense network of measurements is available, it could give a very nice picture on the features present at the measurement area. A good example for this is figure F.6, which show the gravity gradient V_{xx} with a grid of 1° by 1° .

Depending on the mass differences, a mountain might for instance not be separated from a lake, which is located directly at the bottom of that mountain. The measurements might only reveal a very large mountain. Or when the lake is filled with a very dense fluid, it might look in the measurements as a small mountain. Thus to give a more precise geophysical interpretation, it would be useful to have (visual) information of the observed area. This was already emphasized in the previous section, where in some measurements the difference between lake 01 and lake 02 could not be distinguished.

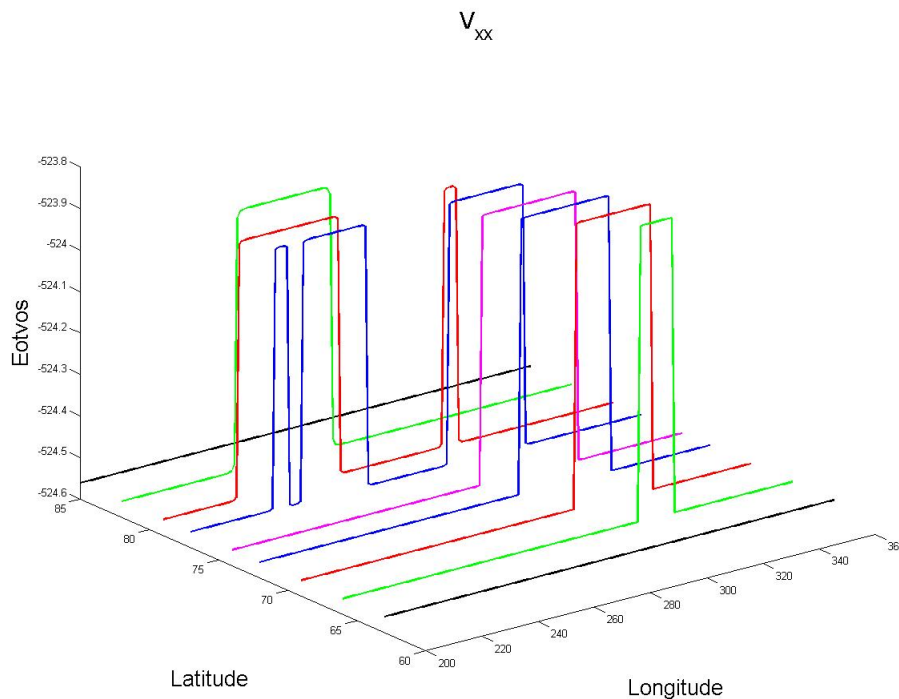


Figure 6.19: The gradient V_{xx} along different trajectories plotted in a three dimensional way, at a measurement altitude of 2 km above the surface and a lake density of 547 kg/m^3 .

6.6 Influence of different lake densities

One of the questions on the lakes of Titan is what the composition of the lakes is. Is it methane? Or a hydrocarbon mixture? A way to resolve this is looking at the density of the liquid in the lake. To show the influence of different densities on the measurements, different lake–densities are used in the simulation. The lake densities used are given in table 2.4, which are the density and composition of the two mixtures as suggested in [48], the density of pure methane and the density of pure ethane.

The densities range from 448.9 kg/m^3 to 649.43 kg/m^3 and as figure 6.20 shows, the difference between the plotted gradients is very small. It is therefore very hard to extract a very precise density of the fluid in the lake from the measurements and only when the lake area is known an estimation can be made. Even when using non–realistic values for the lake density, to enlarge the range of the plots, see figure 6.21, the differences stay within one Eötvös. It will be very hard to assign different densities to the measurements from these plots.

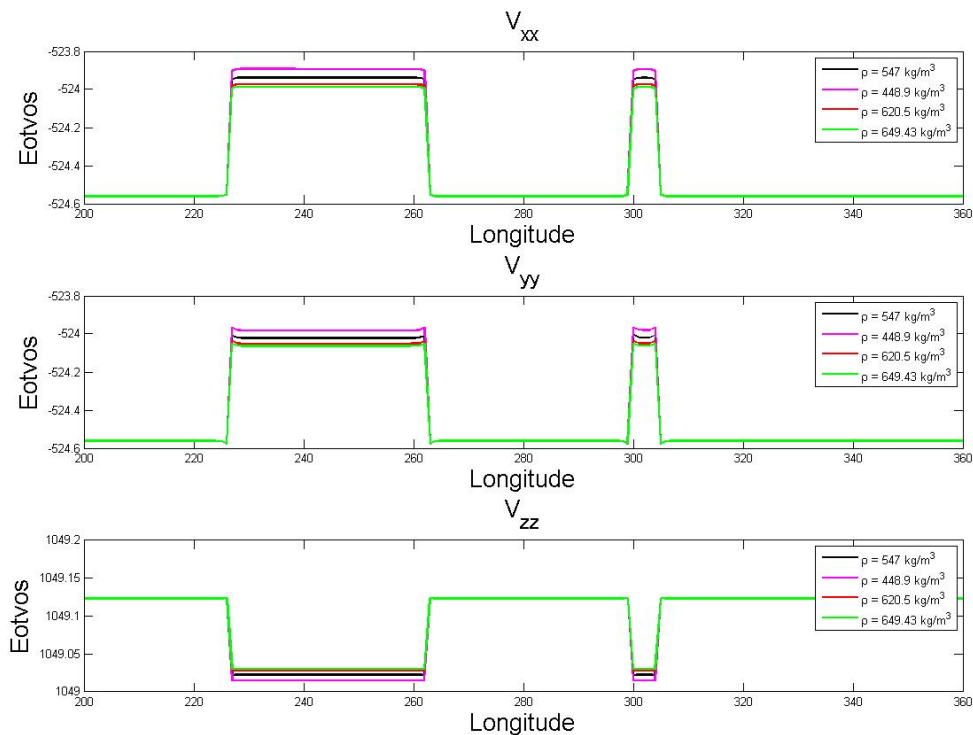


Figure 6.20: The diagonal gradients for different lake–densities. The measurements are taken along a trajectory at 79°N , an altitude of 2 km above the surface. The figures for the off–diagonal gradients can be found in appendix F.

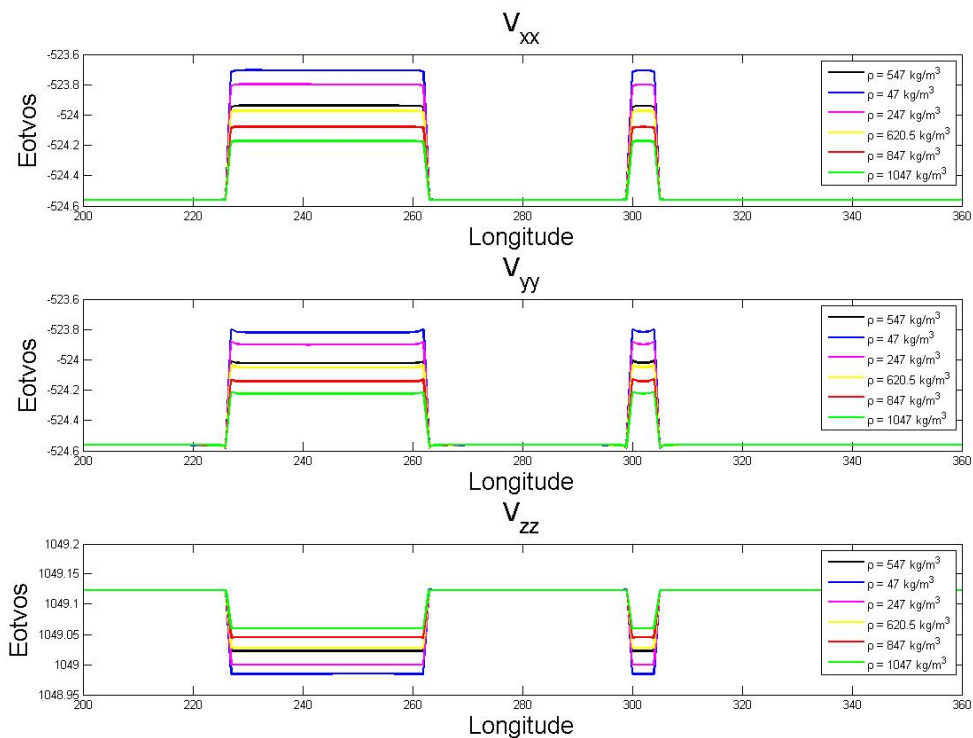


Figure 6.21: The diagonal gradients for different lake-densities. The measurements are taken along a trajectory at $79^\circ N$, an altitude of 2 km above the surface. The figures for the off-diagonal gradients can be found in appendix F.

6.7 Gradients due to subsurface lakes

Figure 6.22 shows that the gradients measured at an altitude of 2 km quickly decrease when the lake is located under the surface of Titan. Already at a distance of five kilometers below the surface almost nothing can be measured anymore, the only exception being V_{yz} (figure 6.23). The values for V_{yz} are, though very small, very close to each other, but still distinguishable. Thus, to be able to measure sub-surface lakes, the lakes should be located less deep than those simulated here, or have a higher density than simulated here (which would suggest a different composition than that of the surface lakes). Inspection of V_{yz} to find sub-surface lakes could be possible, but it should be known then whether the observed region is fairly flat, thus that it is certain that the measurements inspected do not belong to other surface features.

Figures 6.22 and 6.23 compare the gradients from deeper located lakes with the gradients of a surface lake at a measurement altitude of 2 km. When plotting the gradients due to a lake located at a depth of 10 km, still a small variation can be seen, see figures F.33 and F.34 in appendix F. The off-diagonal gradients show a much smaller difference than the diagonal gradients and will be harder to measure. Thus the variations in the gradients are present, but will only be detected if the gradiometer is able to sense variations of at least 0.001 Eötvös.

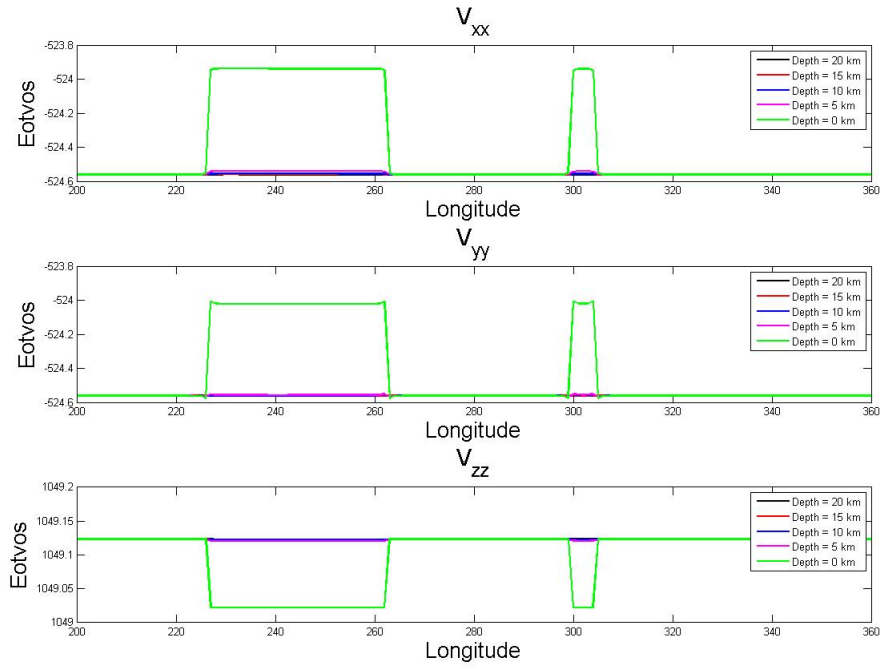


Figure 6.22: The diagonal gradients for sub-surface lakes at different depths. The measurements are taken along a trajectory at 79°N, an altitude of 2 km above the surface and using a density of 547 kg/m³.

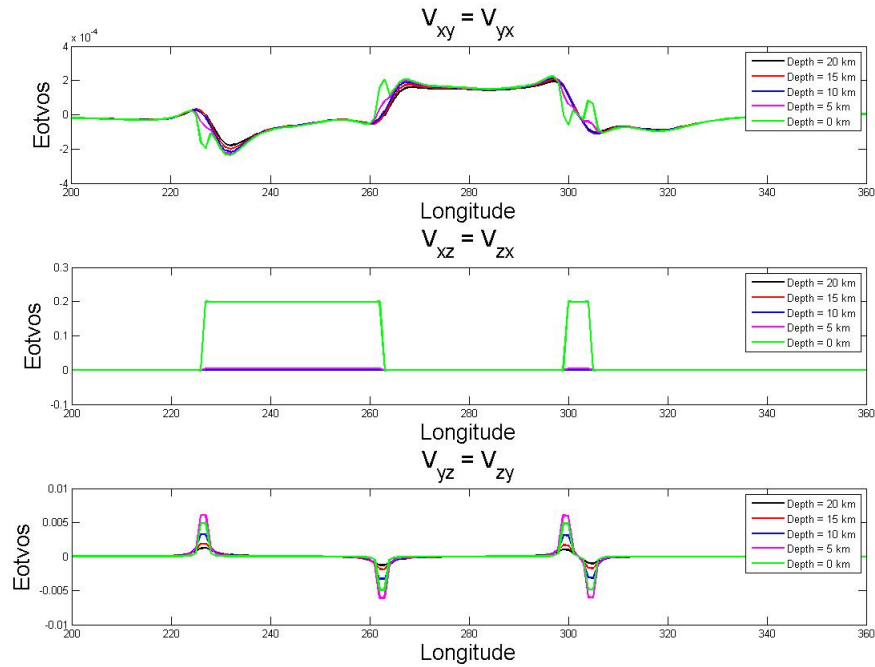


Figure 6.23: The off-diagonal gradients for sub-surface lakes at different depths. The measurements are taken along a trajectory at 79°N, an altitude of 2 km and using a density of 547 kg/m³.

6.8 Determining the lake density using the least-squares method

The least squares method is an analytical method widely used to retrieve data from satellite observations using a simple linear model. Using this method, the variance of the density of the lakes is computed from the simulations along different trajectories. First the theoretical background on the least-squares method is explained, next it is applied to the system of gradient equations of the single layer method. Next the density is retrieved from the simulations and the variance of different observations sets is computed.

6.8.1 Theoretical background on the least-squares method

The least squares method is an analytical method widely used to retrieve data from satellite observations using a simple linear model. In general, a system can be described by a simple linear model:

$$\mathbf{y} + \epsilon = A\mathbf{x} \quad (6.2)$$

where \mathbf{y} is the observation vector, A the design matrix, \mathbf{x} the parameter vector and ϵ the residual vector. The classical formula for least-squares adjustment with regularization is given as [8]:

$$\hat{\mathbf{x}} = \left(A^T C_y^{-1} A + C_x^{-1} \right)^{-1} \left(A^T C_y^{-1} \mathbf{y} \right) \quad (6.3)$$

Assuming that the covariance matrix for the data noise C_y is pre-defined and uncorrelated, it is given as [8]:

$$C_y = \sigma_y^2 I \quad (6.4)$$

where σ stands for the variance of the data. A similar representation holds for the covariance matrix of the model (\mathbf{x}) ([8]):

$$C_x = \sigma_x^2 I \quad (6.5)$$

In most cases the covariance matrix is a diagonal matrix, the diagonals consisting of the variances. Inserting equations 6.4 and 6.5 into equation 6.3 results in:

$$\hat{\mathbf{x}} = \left(A^T C_y^{-1} A + \alpha I \right)^{-1} A^T C_y^{-1} \mathbf{y} \quad (6.6)$$

where the so-called regularization parameter, α is defined by [8]:

$$\alpha = \frac{\sigma_y^2}{\sigma_x^2} \quad (6.7)$$

Considering the data noise non-correlated and stationary ('white noise') and a priori knowledge about the unknown parameters \mathbf{x} is totally absent, this equation reduces to:

$$\hat{\mathbf{x}} = \left(A^T A + \alpha I \right)^{-1} A^T \mathbf{y} \quad (6.8)$$

When the matrix A is ill-conditioned, regularization has to be applied. To check this, the condition number of the matrix can be computed. The condition number of a matrix measures the sensitivity of the solution of a system of linear equations to errors in the data. It gives an indication of the accuracy of the results from matrix inversion and the linear equation solution. Values near one indicate a well-conditioned matrix.

A priori knowledge about the unknown parameters is assumed to be totally absent. In this case $\sigma_x^2 \rightarrow \infty$, hence $\alpha \rightarrow 0$. Then the least-squares adjustment formula reduces further to [8]:

$$\hat{\mathbf{x}} = (A^T A)^{-1} A^T \mathbf{y} \quad (6.9)$$

The variance of the parameter vector, i.e. the bounds in which the solution is given, can be computed by:

$$C_{\hat{\mathbf{x}}} = (X^T C^{-1} X)^{-1} = \sigma_{\hat{\mathbf{x}}}^2 \quad (6.10)$$

The residual vector is found when comparing the observations with the approximation of the observations. The approximation of the observations is found by multiplying the least-squares solution $\hat{\mathbf{x}}$ with the original design matrix A . Hence, the residual vector is given by:

$$\boldsymbol{\epsilon} = \mathbf{y} - A\hat{\mathbf{x}} \quad (6.11)$$

The least-squares error of the observations is the length of this vector and thus given by [37]:

$$\text{LS error} = \|\mathbf{y} - A\hat{\mathbf{x}}\| \quad (6.12)$$

The root mean square (rms) or quadratic mean is a statistical measure of the magnitude of a varying quantity. The rms for a set of n values $\{x_1, x_2, \dots, x_n\}$ is defined as:

$$\text{rms} = \sqrt{\frac{1}{n} \sum_{i=1}^n x_i^2} \quad (6.13)$$

6.8.2 The least-squares method applied to the system of gradient equations

In order to retrieve the density, the system of gravity gradients described by equation 4.62 will be described by a simple linear model (equation 6.2):

$$\mathbf{y} + \boldsymbol{\epsilon} = X\boldsymbol{\mu}$$

where $\bar{\mathbf{y}}$ is the observation vector, composed of the measurements of the gradients, $\boldsymbol{\mu}$ the parameter vector, which in this case is the difference in density between the lake density and the mean density of Titan in kg/m^2 as explained in section 5.1. Keep in mind that the single layer method uses the density per unit area, thus given in kg/m^2 . The design matrix, X , consists of all parameters, except the density μ at the right hand side of equation 4.62. The solution to this system is given as (following equation 6.6, no regularization needed ($\alpha = 1$)):

$$\hat{\boldsymbol{\mu}} = (X^T C_y^{-1} X)^{-1} (X^T C_y^{-1} \mathbf{y}) \quad (6.14)$$

In order to compute this solution, the covariance matrix of the measurements has to be given. The covariance matrix consists of the variances on the diagonal of the matrix and the co-variances on the off-diagonals of the matrix. The variance with which the density is computed is given by equation 6.10:

$$C_{\hat{\mu}} = \left(X^T C_y^{-1} X \right)^{-1} = \sigma_{\hat{\mu}}^2 \quad (6.15)$$

A simple rule of thumb is used in order to see if the measurements done have a high enough accuracy. This rule of thumb gives that the density computed using the least-squares method is larger than three times the variance found:

$$\hat{\mu} \geq 3\sigma_{\hat{\mu}} \quad \Rightarrow \quad \frac{3\sigma_{\hat{\mu}}}{\hat{\mu}} \leq 1 \quad (6.16)$$

6.8.3 Variance of the computed lake density for different observation sets

The computations as explained previously are done for four different observation sets and combinations of these sets. All these observations have a surface lake, that is the distance of the lake underneath the surface of Titan is equal to zero. The observation sets used are:

- Measurements along a trajectory of 79°N and a measurement altitude of 2 km
- Measurements along a trajectory of 79°N and a measurement altitude of 6 km
- Measurements along a trajectory of 77°N and a measurement altitude of 2 km
- Measurements along a trajectory of 77°N and a measurement altitude of 6 km

Each observation set contains the measurements of all the gradients (the complete tensor), but it can be imagined that during a measurement campaign not all gradients are available. Therefore the density of the lake is computed using different configurations: (i) using the full gradient tensor, (ii) using half the tensor (diagonals and three of the off-diagonals) (iii) using the diagonals only (V_{xx} , V_{yy} and V_{zz}) (iv) using only V_{xx} , (v) using only V_{yy} , and (vi) using only V_{zz} . The results of the computations are given in figure 6.24. The y-axis represents $\frac{3\sigma_{\hat{\mu}}}{\hat{\mu}}$. The red line is the 'border' set at one, as given in equation 6.16. All the measurements below this line thus give a sufficiently enough accuracy. On the x-axis the measurements are represented by a number. The numbers 1 to 9 represent the following observation sets and combinations of the four sets, described above:

1. 79°N, h = 2 km
2. 79°N, h = 6 km
3. 77°N, h = 2 km
4. 77°N, h = 6 km
5. a combination of 79°N, h = 2 km and 79°N, h = 6 km
6. a combination of 79°N, h = 2 km and 77°N, h = 2 km
7. a combination of 79°N, h = 2 km and 77°N, h = 6 km
8. a combination of 79°N, h = 2 km and 79°N, h = 6 km and 77°N, h = 2 km

9. a combination of all four: 79°N , $h = 2 \text{ km}$ and $h = 6 \text{ km}$ and 77°N , $h = 2 \text{ km}$ and $h = 6 \text{ km}$

The different configurations ((i) to (vi)) for all nine observation sets are computed. Three different values for the resolution will be used: (1) a study at SRON showed that in an ideal setup a resolution of 0.17 Eötvös rms could be reached (J. M Smit, personal communication), (2) the minimum value needed for planetary missions, 1 Eötvös rms (section 3.4) and (3) a resolution of 2.6 Eötvös rms (section 3.4).

Figure 6.24 shows the results for $\sigma_{ij} = 0.17 \text{ Eötvös rms}$. The figures for the other two values can be found in appendix G. Figure 6.24 directly shows that two measurement combinations have a too large value for $\frac{3\sigma_{\hat{\rho}}}{\hat{\rho}}$: 2 and 4. Both measurement set 2 and 4 represent the measurements along a single trajectory at a measurement altitude of 6 km. This indicates that when only having one set of measurements at higher altitude, the density cannot be computed with enough accuracy. The values accompanying these measurements can be found in table G.1 in appendix G. Figure 6.25 zooms in on the region below 1 (indicated by the red line), to get a closer look at the other datasets. For all sets hold that when resolving the density using the gradient V_{zz} only (indicated by the cross: \times) the accuracy with which the measurements are resolved is the lowest, for instance measurement set 1 (79°N , $h = 2 \text{ km}$) resolves the density as $\hat{\rho} = 547 \pm 351 \text{ kg/m}^2$. Using only V_{xx} or V_{yy} , regarding computing the density using the least-squares technique, gives more or less the same accuracy: $\hat{\rho} = 547 \pm 65 \text{ kg/m}^2$. Using the diagonal gradients, half the tensor or the full gradient tensor to compute the density, do not give a significant difference in accuracy, $\hat{\rho} = 547 \pm 41.5 \text{ kg/m}^2$. Again, all these results can be found in table G.1 in appendix G.

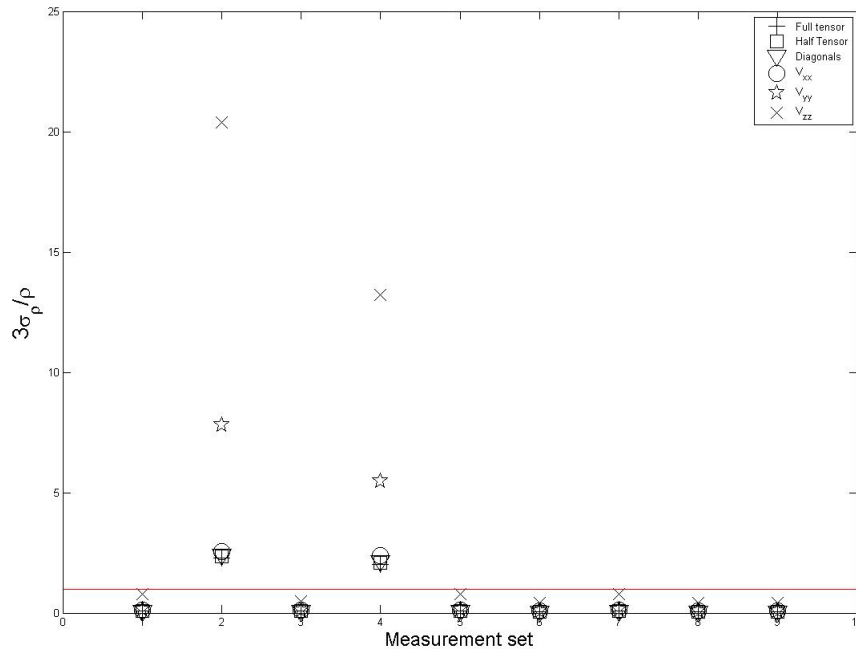


Figure 6.24: The results of the least-squares estimation for nine different observation sets, $\sigma_{ij} = 0.17 \text{ Eötvös}$. The configurations indicated below the red line comply with the rule of thumb given by equation 6.16.

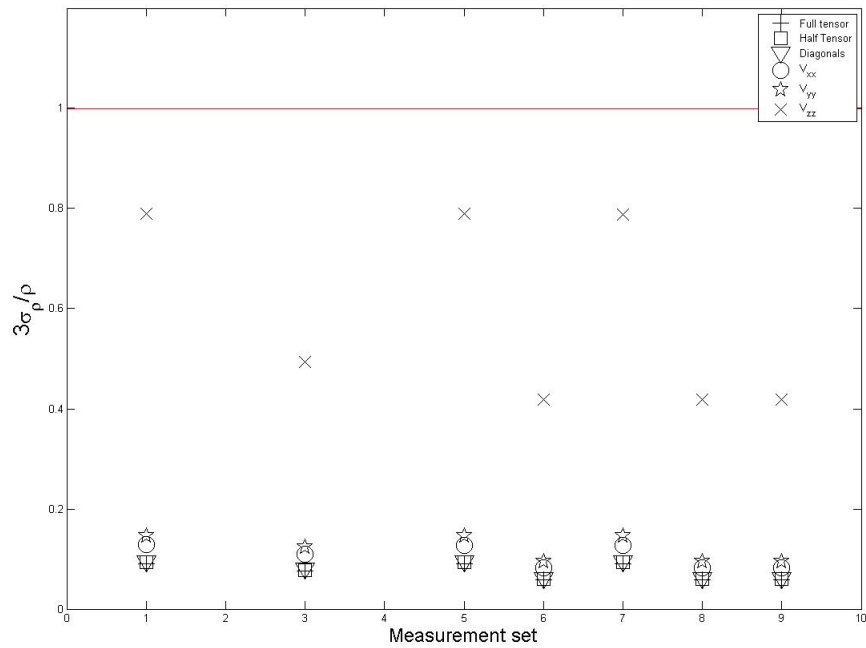


Figure 6.25: The results of the least-squares estimation zoomed in on the part below the red line, $\sigma_{ij} = 0.17$ Eötvos.

Measurements sets 6, 8 and 9 give the highest accuracy. Table 6.3 shows the part of the table presented in appendix G, consisting only of these three measurement sets. Comparing the values belonging to each configuration between the measurement sets, it can be seen that these values are very similar to each other. Two things can be concluded from this: (1) using the observations made at the lowest measurement altitude (in this case 2 km), the same accuracy is reached as when combining these with observations at higher measurement altitudes and (2) the same accuracy is reached when using the full tensor or the diagonals only, thus the off-diagonal measurements are not necessary.

Table 6.3: The density and variance [kg/m²] computed for measurement sets 6,8 and 9 using the least-squares technique.

Observations used	Computed density $\hat{\rho}$ [kg/m ²]	Variance $\sigma_{\hat{\rho}}$ [kg/m ²]
<i>Measurement set 6</i>	<i>79°N and 77°N, 2 km</i>	
Full tensor	547	25.9
Half tensor	547	26.6
Diagonals only	547	27.5
V _{xx} only	547	36.9
V _{yy} only	547	42.3
V _{zz} only	547	186.3
<i>Measurement set 8</i>	<i>79°N, 2 km, 6 km and 77°N, 2 km</i>	
Full tensor	547	25.8
Half tensor	547	26.6
Diagonals only	547	27.5
V _{xx} only	547	36.9
V _{yy} only	547	42.3
V _{zz} only	547	186.2
<i>Measurement set 9</i>	<i>79°N, 2 km, 6 km and 77°N, 2 km, 6 km</i>	
Full tensor	547	25.8
Half tensor	547	26.6
Diagonals only	547	27.5
V _{xx} only	547	36.9
V _{yy} only	547	42.3
V _{zz} only	547	186.1

Discussion

The goal of this thesis work was to investigate if a perfect MEMS micro-gradiometer on board a hot air balloon floating in the atmosphere of Titan can detect (sub-) surface lakes. Furthermore it is investigated if the density of those lakes can be resolved from the observed gradients using the least-squares technique and consequently what accuracy is of the computed density is. Regarding to these goals first several conclusions are given and this chapter finishes with recommendations for future work.

7.1 Conclusions

This thesis work has focused on the gradients of the gravitational potential as consequence of two large lakes found on the Northern polar region of Titan. It is assumed that a perfect gradiometer is placed in a gondola underneath a balloon in the atmosphere of Titan. The influence of swinging and rotating balloon motions have been omitted, since this is beyond the scope of this project. The gravity gradients, i.e. the second derivative of the gravitational potential, were modeled using two superimposed methods: a spherical symmetrical model representing Titan and the mass layer method representing the lakes. The mass layer method assumes that the gravitational potential of the lakes can be represented by a single mass layer on the surface of Titan.

The gradiometer is oriented along the axes of the local north-oriented reference system and it is assumed that the exact location of the gradiometer with respect to the Titan-centered reference system is known. The gradients are given in Eötvös units and the gradiometer is assumed to make perfect measurements, without any noise sources. The density of the lakes is computed from the observations using the least-squares technique. To account for the noise in the gradiometer measurements, the least-squares computations are done using different values of the resolution of all components of the gradient tensor: $\sigma_{ij} = 0.17$ Eötvös rms, $\sigma_{ij} = 1$ Eötvös rms and $\sigma_{ij} = 2.6$ Eötvös rms.

Different simulations were done in order to see what the effect is of altitude, of different trajectories along which measurements can be done, of different measurement step sizes, of different densities of the lakes and of the location of the lakes with respect to the surface of Titan. Next to that the influence of noise on the measurements was investigated and it was computed with what accuracy the density can be retrieved from the observations, using the least-squares technique.

First of all it can be concluded that the diagonal gradients give a larger difference in magnitude than the off-diagonal gradients, and are thus better measurable. Especially the gradient V_{xy} (and V_{yx}) is very weak, the difference in magnitude is of the order of 10^{-4} Eötvös which is too small to

be measured by the gradiometer. The maximum difference in magnitude of the diagonal gradients is 0.5–0.6 Eötvös. This is measurable by the gradiometer, because the target resolution of the gradiometer is 0.1 Eötvös.

The strength of the gravity gradients decreases with altitude and it was shown that the measurements at higher altitudes do not give a sufficiently enough accuracy. The accuracy reached at a measurement altitude of 2 km, using only one set of observations, is $547 \pm 42.6 \text{ kg/m}^3$, while at a measurement altitude of 6 km this is $547 \pm 1075 \text{ kg/m}^3$. The observations at 6 km altitude do not satisfy $\mu \geq 3\sigma_\mu$, which is used to verify if the accuracy is good enough, too. Thus it can be concluded that for accurate measurements it is desirable that the balloon should fly at the lowest altitude possible.

The trajectory chosen is of great influence on the measurements. Not only the altitude, as mentioned above, is of importance, but the path chosen (latitude, longitude) has influence. The hot-air balloon will be a passive balloon, therefore the trajectory of the balloon is completely dependent on the winds that are present on Titan and the location where the balloon will be released. Due to the prevailing zonal winds the trajectories will most probably not vary along latitude very much. If a trajectory could be set on beforehand, the trajectory along 76°N to 79°N will give the most information regarding the two lakes selected for observation in this thesis work.

Every mass difference is measured by the gradiometer and gives different values for the gradients. It could therefore be quite difficult to, with scattered measurements only, determine what physically is present at the measurement area. The simulations were done for the two lakes combined and separately and show that, depending on the trajectory chosen, the two lakes cannot always be separated in the measurement plots. Even when having measurements along more different trajectories this proves to be quite difficult. Ideally, visual information on the location of the balloon should be available, thus measurements could be linked to the images to give a correct geophysical interpretation. This can be seen back in the least-squares computations for the density too, in comparing two trajectories, 79°N and 77°N , both measuring at an altitude of 2 km. The trajectory along 77°N crosses a larger part of both lakes compared to the trajectory along 79°N , which can directly be seen in the accuracy reached for the density computed: 547 ± 36.0 Eötvös against 547 ± 42.6 Eötvös respectively. Concluding, if visual information is available, the chance that the interpretation of the results is correct is higher and it gives the possibility to determine on beforehand where the balloon should fly to make more useful measurements.

The simulations are done with a one degree stepsize, i.e. the gradients are computed with intervals of one degree. This corresponds to one measurement approximately every 45 kilometers. To detect both lakes a step size between 1° and 5° is needed in the simulations. A gradiometer sampling speed of 10 Hz and a balloon speed computed according to the simulations done in [74] of 0.3–1 m/s the gradiometer will be able to detect both lakes used in the simulations.

Changing the density of the lakes did not have a significant influence on the values for the gravity gradients. The differences in magnitude found were not larger than one Eötvös and it will be very hard to exactly determine the composition of the lake since all values used for the simulation have similar effects. But, if the composition of the lake is the expected ethane mixed with other

hydrocarbons, the gradients do show enough variation to determine the presence of the lake.

The deeper the lake is located underneath the surface of Titan, the smaller the difference in gradients will be. The simulations show that a lake located 10 km underneath the surface of Titan has a maximum difference of 0.006 Eötvös. Concluding from the simulations done in this study, it will not be possible to detect lakes with a density of 547 kg/m^3 below 5 km underneath the surface of Titan with the micro-gradiometer.

A last conclusion can be made regarding the least-squares technique. This study shows that when computing the density of the lake using the least-squares method, it does not matter whether the full gravity tensor is used or only the diagonals of the tensor, both give the same variances. If only one of the diagonal gradients is used, the best result is achieved when using V_{xx} or V_{yy} . Less accurate results are achieved when using V_{zz} only. This is rather counter intuitive: the gradient V_{zz} is twice as large in magnitude as the gradients V_{xx} and V_{yy} , thus a smaller variance is expected. The computations do show that when combining more sets of observations, for instance along different trajectories and at different measurement altitudes, the accuracy can be increased too.

7.2 Recommendations

Following this research several recommendations can be made. The recommendations made are separated into two parts: (1) on the simulations and modeling done and (2) concerning the feasibility of the gradiometer measurements.

To simulate the gravity gradients of the lakes, the mass layer method is used. A comparison to other alternative methods, for instance the point mass method, has not been made. At the moment there is no comparison whatsoever, to indicate what the performance is of the single layer method. Gravitational data (Love number k_2 and gravitational moments C_{22} and S_{22}) are anticipated in the near future, which will limit the possibilities for Titan's interior structure. When this data is available a comparison should be made between the spherical harmonic representation and the mass layer method. Next to that the relations between the two methods need to be worked out more specifically.

Only two large lakes have been implemented. The choice was made on basis of the images available by Cassini-Huygens. The smaller lakes seen on these images have not been considered, but it is not investigated if the gradients of these separate small lakes can be distinguished from each other or if they show up as a large lake. It is recommended to investigate whether the gradiometer is sensitive enough to distinguish the smaller lakes from their surroundings and what the minimum area of the lakes is to create measurable gradients.

All motions of the balloon have been omitted. Of course these motions will have a large influence on the accuracy of the measurements if not corrected for. It is recommended to model these motions, including swinging and rotations of the gondola as well as variations in altitude, to see if these motions do not disturb the gradiometer measurements too much. The balloon trajectory is geometry based, it is a straight line at constant altitude and constant latitude measuring at regular intervals. The speed of the balloon and deviations from this straight line have not been imple-

mented. This could be done by coupling the data obtained by the balloon trajectory simulations made by Tokano and Lorenz [74] using the GCM model and a timewise measurement interval to the gravitational models used in this study. The observation sets created using such a model will allow for a more realistic approximation of the gravity gradients as measured by a gradiometer in the gondola of the balloon.

It was assumed that the gradiometer is perfect and measures instantaneously, but noise can be of a considerable influence on the measurements. To improve modeling, the noise sources of the gradiometer have to be considered.

Recent research has shown that Titan does not rotate synchronously with respect to Titan. What this will implicate for the tidal potential and body tides has not been investigated in this study. Combining this with the anticipated gravitational data, research could be done on the tidally induced stresses in the interior of Titan.

The research on balloon-borne gradiometry is very limited. Only a few tests have been done in the past to verify the feasibility of a gradiometer on board the gondola of a balloon. The motions the balloon undergoes, and especially their influence on the gradiometer measurements, have not been well characterized and documented. It is therefore recommended that more experience with balloon-borne gradiometry is gained and studies are done to the feasibility of balloon-borne gradiometry, before sending the micro-gradiometer with the balloon to Titan.

The micro-gradiometer is still in the development phase. During the development it should be aimed to make the gradiometer as sensitive as possible and reduce the gradiometer noise to a minimum. If a high sensitivity can be achieved, the balloon will be able to fly higher than the recommended 2 km, which might be preferable for other (atmospheric) measurement equipment on board of the gondola of the balloon. Next to that the gradiometer might be able to detect sub-surface lakes below the in this study limited 5 km.

References

- [1] ATREYA, S. K., ADAMS, E. Y., NIEMANN, H. B., DEMICK–MONTELARA, J. E., OWEN, T. C., FULCHIGNONI, M., FERRI, F., AND WILSON, E. H. Titan’s methane cycle. *Planetary and Space Science* 54 (2006), 1177–1187.
- [2] BILLS, B. G., AND NIMMO, F. Forced obliquity and moments of inertia of Titan. *Icarus* 196 (2008), 293–297.
- [3] CHAKRABARTY, I. Gravitational Waves: An Introduction. *physics.ed-ph* (August 19, 1999), 1–22.
- [4] COUSTENIS, A. TANDEM, Titan and Enceladus mission, A proposal in response to the ESA Cosmic Vision Plan. For the TANDEM Consortium, 2007.
- [5] CUPERUS, R., FLOKSTRA, J., AND WIEGERINK, R. J. Miniaturized gravity gradiometer. In *Proceedings 7th international workshop on low temperature electronics* (June 2006).
- [6] CYGNUS RESEARCH INTERNATIONAL. Power spectral density function, July 22, 2005. <http://www.cygres.com/0cnPageE/Glosry/Spec.html> (accessed October 04, 2007).
- [7] DE PATER, I., AND LISSAUER, J. J. *Planetary Sciences*. Cambridge University Press, 2001.
- [8] DITMAR, P. AE4-E10: Inverse Problems, Lecture notes, May 22, 2007.
- [9] ESA COSMIC VISION 2015–2025. Tandem, August 01, 2008. <http://sci.esa.int/science-e/www/object/index.cfm?fobjectid=42286> (accessed August 11, 2008).
- [10] ESA LIVING PLANET PROGRAMME. GOCE, July 19, 2007. <http://www.esa.int/esaLP/LPgoce.html> (accessed September 18, 2007).
- [11] ESA SCIENCE & TECHNOLOGY. Cassini–Huygens, July 15, 2008. <http://sci.esa.int/science-e/www/object/index.cfm?fobjectid=34962> (accessed August 28, 2007)
<http://sci.esa.int/science-e/www/object/index.cfm?fobjectid=43032> (accessed August 11, 2008).
- [12] FARLEX. The free dictionary, 2008. <http://www.thefreedictionary.com/equinox> (accessed August 11, 2008).
- [13] FLOKSTRA, J. Gravity gradiometers for space applications. Lecture slides, April 19, 2007.
- [14] FORTES, A. D., Created: July 06, 2000 – Last revised: March 21, 2001. <http://mysite.du.edu/~jcalvert/math/harmonic/harmonic.htm> (accessed September 21, 2007).

- [15] FULCHIGNONI, M., ET AL. *In situ* measurements of the physical characteristics of Titan's environment. *Nature* 438 (December 8, 2005), 785–791.
- [16] GFZ POTSDAM. CHAMP Gravity field recovery, June 30, 2000.
http://www.gfz-potsdam.de/pb1/op/champ/science/index_SCIENCE.html (accessed September 19, 2007).
- [17] GIBBARD, S. G., MACINTOSH, B., GAVEL, D., MAX, C. E., DE PATER, I., ROE, H. G., GHEZ, A. M., YOUNG, E. F., AND MCKAY, C. P. Speckle imaging of Titan at 2 microns: surface albedo, haze optical depth, and tropospheric clouds 1996–1998. *Icarus* 169 (2004), 429–439.
- [18] GRIFFITH, C. A., ET AL. The evolution of Titan's mid-latitude clouds. *Science* 313 (October 21, 2005), 474–475.
- [19] GRIFFITH, C. A., ET AL. Evidence for polar ethane cloud on Titan. *Science* 313 (September 15, 2006), 1620–1622.
- [20] HAAGMANS, R., FLOBERGHAGEN, R., PIEPER, B., AND DRINKWATER, M. ESA's Gravity mission GOCE. BR-209, June 2006.
- [21] HELDEN, A. v. Huygens, Titan, and Saturn's rings. In *Proceedings of the International Conference 'Titan – From discovery to Encounter'* (2004), K. Fletcher, Ed., SP-1278, European Space Agency.
- [22] HUBBARD, W. B. *Planetary Interiors*. Van Nostrand Reinhold Company, 1984.
- [23] HUIBREGTSE, J. N. The gravitational field of Europe and the gravitational impact of Jupiter on a micro-gradiometer in orbit around Europe, Internship at SRON, July 03, 2007. Internship report.
- [24] IESS, L., RAPPAPORT, N. J., TORTORA, P., LUNINE, J. I., ARMSTRONG, J. W., ASMAR, S. W., SOMENZI, L., AND ZINGONI, F. Gravity field and interior of Rhea from Cassini data analysis. *Icarus* 190 (2007), 585–593.
- [25] ISRAËL, G., ET AL. Complex organic matter in Titan's atmospheric aerosols from *in situ* pyrolysis and analysis. *Nature* 438 (December 08, 2005), 796–799.
- [26] JEKELI, C. Balloon Gravimetry Using GPS and INS. *IEEE AES Magazine June* (1992), 9–15.
- [27] JEKELI, C. Airborne vector gravimetry using precise, position-aided inertial measurement units. *Bulletin Géodésique* 69 (1994), 1–11.
- [28] JET PROPULSION LABORATORY, CALIFORNIA INSTITUTE OF TECHNOLOGY. Voyager, the Interstellar Mission, January 14, 2003.
<http://voyager.jpl.nasa.gov/index.html> (accessed on May 23, 2008).
- [29] JET PROPULSION LABORATORY, CALIFORNIA INSTITUTE OF TECHNOLOGY. Solar system Dynamics, HORIZONS Web-Interface, September 24, 2007.
<http://ssd.jpl.nasa.gov/horizons.cgi\#top> (accessed February 26, 2008).

- [30] JET PROPULSION LABORATORY, CALIFORNIA INSTITUTE OF TECHNOLOGY. Cassini–Huygens – mission to Saturn & Titan, June 30, 2008.
<http://saturn.jpl.nasa.gov/news/features/feature20080627c.cfm> (accessed August 11, 2008).
- [31] KAMP, A. Space instrumentation engineering, lecture notes ae4–880. Delft University of Technology, Faculty of Aerospace Engineering, February 2006.
- [32] KARATEKIN, O., AND VAN HOOLST, T. The effect of a dense atmosphere on the tidally induced potential of Titan. *Icarus* 183 (2006), 230–232.
- [33] KAULA, W. M. *Theory of Satellite Geodesy*. Blaisdell Publishing Company, 1966.
- [34] KLEES, R. Planetary Gravity Fields, Part 1: Basics, November 09, 2007.
- [35] KLEES, R. Planetary Gravity Fields, Part 2: Space–borne gravimetry, November 23, 2007.
- [36] KLEES, R. Planetary Gravity Fields, Part 3: Advanced aspects of space–borne gravimetry, December 19, 2007.
- [37] LAY, D. C. *Linear algebra and its applications*. Addison Wesley Longman, 1997.
- [38] LAZAREWICZ, A. R. Balloon–borne, high–altitude gravimetry. *Adv. Space Res.* 5 (1985), 79–82.
- [39] LAZAREWICZ, A. R., SCHILINSKI, B. J., COWIE, R. J., RICE, C. L., MOSS, P., CARTER, L. N., AND LEYH, C. Balloon–borne, high altitude gravimetry: The flight of DUCKY 1a (October 1983), DUCKY II (October 1985). *Abstracts of the interim scientific report (DUCKY 1a) and of the final scientific report (DUCKY II)* (12/1985 and 10/1087), Abstract.
- [40] LOPES, R. M. C., MITCHELL, R. T., WALL, S. D., MITRI, G., JANSSEN, M., OSTRO, S., KIRK, R. L., HAYES, A. G., STOFAN, E. R., LUNINE, J. I., LORENZ, R. D., WOOD, C., RADEBAUCH, J., PAILLOU, P., ZEBKER, H., AND PAGANELLI, F. The Lakes and Seas of Titan. *EOS* 88, 51 (December 18, 2007), 569–576.
- [41] LORENZ, R. D. A review of balloon concepts for Titan. *JBIS* 61 (2008), 2–13.
- [42] LORENZ, R. D., MITCHELL, K. L., KIRK, R. L., HAYES, A. G., AHARONSON, O., ZEBKER, H. A., PAILLOU, P., RADEBAUCH, J., LUNINE, J. I., JANSSEN, M. A., WALL, S. D., LOPES, R. M., STILES, B., OSTRO, S., MITRI, G., AND STOFAN, E. R. Titan’s inventory of organic surface materials. *Geophysical research letters* 35 (2008), 1–6.
- [43] LORENZ, R. D., STILES, B. W., KIRK, R. L., ALLISON, M. D., PERSI DEL MARMO, P., IESS, L., LUNINE, J. I., OSTRO, S. J., AND HENSLEY, S. Titan’s rotation reveals an internal ocean and changing zonal winds. *Science* 319 (March 21, 2008), 1649–1651.
- [44] LORENZ, R. D., ZARNECKI, J. C., TOWNER, M. C., LEESE, M. R., BALL, A. J., HATHI, B., HAGERMANN, A., AND GHAFOR, N. A. L. Descent motions of the Huygens probe as measured by the Surface Science Package (SSP): Turbulent evidence for a cloud layer. *Planetary and Space Science* 55 (2007), 1936–1948.
- [45] MATSON, D. Titan and Saturn System Mission (TSSM), Joint Science Definition Team (JSDT), March 31, 2008.

- [46] MCKAY, C. P., COUSTENIS, A., SAMUELSON, R. E., LEMMON, M. T., LORENZ, R. D., CABANE, M., RANNOU, P., AND DROSSART, P. Physical properties of the organic aerosols and clouds on Titan. *Planetary and Space Science* 49 (2001), 79–99.
- [47] MITCHELL, R. T. The Cassini mission at Saturn. *Acta Astronautica* 61 (2007), 37–43.
- [48] MITRI, G., SHOWMAN, A. P., LUNINE, J. I., AND LORENZ, R. D. Hydrocarbon lakes on Titan. *Icarus* 186 (2007), 385–394.
- [49] MONTENBRUCK, O., AND GILL, E. *Satellite Orbits*, third ed. Springer, 2000.
- [50] NIEMANN, H. B., ET AL. The abundances of constituents of Titan’s atmosphere from the GCMS instrument on the Huygens probe. *Nature* 438 (December 08, 2005), 779–784.
- [51] RADEBAUCH, J., LORENZ, R. D., KIRK, R. L., LUNINE, J. I., STOFAN, E. R., LOPES, R. M., WALL, S. D., AND CASSINI RADAR TEAM. Mountains on Titan observed by Cassini radar. *Icarus* 192 (2007), 77–91.
- [52] RANNOU, P., HOURDIN, F., LEBONNOIS, S., LUZ, D., AND MADELEINE, J. B. Titan atmosphere database, Users Guide. Tech. rep., Laboratoire de Météorologie Dynamique, Service d’Aéronomie, Institut Pierre–Simon Laplace, January 17 2006.
- [53] RANNOU, P., HOURDIN, F., MCKAY, C. P., AND LUZ, D. A coupled dynamics–microphysics model of Titan’s atmosphere. *Icarus* 170 (2004), 443–462.
- [54] RANNOU, P., LEBONNOIS, S., HOURDIN, F., AND LUZ, D. Titan atmosphere database. *Advances in Space Research* 36 (2005), 2194–2198.
- [55] RAPPAPORT, N., BERTOTTI, B., GIAMPIERI, G., AND ANDERSON, J. D. Doppler measurements of the quadrupole moments of Titan. *Icarus* 126 (1997), 313–323.
- [56] RAPPAPORT, N. J., IESS, L., TORTORA, P., ANABTAWI, A., ASMAR, S. W., SOMENZI, L., AND ZINGONI, F. Mass and interior of Enceladus from Cassini data analysis. *Icarus* 190 (2007), 175–178.
- [57] RAPPAPORT, N. J., IESS, L., WAHR, J., LUNINE, J. I., ARMSTRONG, J. W., ASMAR, S. W., TORTORA, P., DI BENEDETTO, M., AND RACIOPPA, P. Can Cassini detect a subsurface ocean in Titan from gravity measurements? *Icarus* 194 (2008), 711–720.
- [58] RISHBETH, H., YELLE, R. V., AND MENDILLO, M. Dynamics of Titan’s thermosphere. *Planetary and Space Science* 48 (2000), 51–58.
- [59] RUMMEL, R. How to climb the gravity wall. *Space Science Reviews* 108 (2003), 1–14.
- [60] SAGAN, C., AND DERMOTT, S. F. The tide in the seas of Titan. *Nature* 300 (December 1982), 731–733.
- [61] SEEBER, G. *Satellite Geodesy*. de Gruyter, 1993.
- [62] SOHL, F., HUSSMANN, H., SCHWENTKER, B., SPOHN, T., AND LORENZ, R. D. Interior structure models and tidal Love numbers of Titan. *Journal of Geophysical Research* 108, E12 (2003), 5130.

- [63] SOHL, F., SEARS, W. D., AND LORENZ, R. D. Tidal dissipation on Titan. *Icarus* 115 (1995), 278–294.
- [64] SOTIN, C., AND TOBIE, G. Titan’s hidden ocean. *Science* 319 (March 21, 2008), 1629–1630.
- [65] STOFAN, E. R., ET AL. The lakes of Titan. *Nature* 445 (2007), 61–64.
- [66] STROBEL, D. F. Gravitational tidal waves in Titan’s upper atmosphere. *Icarus* 182 (2006), 251–258.
- [67] TANAKA, M. An industrial and applied review of new MEMS devices features. *Microelectronic Engineering* 84 (2007), 1341–1344.
- [68] TANDEM. Titan and enceladus mission.
<http://www.lesia.obspm.fr/cosmicvision/tandem/> (accessed August 05, 2008).
- [69] TEANBY, N. A., IRWIN, P. G. J., KOK, DE, R., NIXON, C. A., COUSTENIS, A., ROYER, E., CALCUTT, S. B., BOWLES, N. E., FLETCHER, L., C., H., AND TAYLOR, F. W. Global and temporal variations in hydrocarbons and nitriles in Titan’s stratosphere for northern winter observed by Cassini/CIRS. *Icarus* 193 (2008), 595–611.
- [70] THE JOHNS HOPKINS UNIVERSITY APPLIED PHYSICS LABORATORY. Titan Explorer Flagship Mission Study. Prepared for NASAs Planetary Science Division, January 2008.
- [71] TOBIE, G., GRASSET, O., LUNINE, J. I., MOCQUET, A., AND SOTIN, C. Titan’s internal structure inferred from a coupled thermal–orbital model. *Icarus* 175 (2005), 496–502.
- [72] TOBIE, G., LUNINE, J. I., AND SOTIN, C. Episodic outgassing as the origin of atmospheric methane on Titan. *Nature* 440 (March 02, 2006), 61–64.
- [73] TOBIE, G., MOCQUET, A., AND SOTIN, C. Tidal dissipation within large icy satellites: Application to Europa and Titan. *Icarus* 177 (2005), 534–549.
- [74] TOKANO, T., AND LORENZ, R. D. GCM simulation of balloon trajectories on Titan. *Planetary and Space Science* 54 (2006), 685–694.
- [75] TOKANO, T., AND NEUBAUER, F. M. Tidal winds on Titan caused by Saturn. *Icarus* 158 (2002), 499–515.
- [76] TOMASKO, M. G., ET AL. Rain, winds and haze during the Huygens probe’s descent to Titan’s surface. *Nature* 438 (December 08, 2005), 765–778.
- [77] TORGE, W. *Geodesy*. de Gruyter, 1980.
- [78] UNIVERSITY OF TEXAS. GRACE – Gravity Recovery And Climate Experiment, February 24, 2004.
http://www.csr.utexas.edu/grace/gallery/animations/measurement/measurement_wm.html (accessed September 18, 2007).
- [79] VARADAN, V. K., VARADAN, V. V., AND SUBRAMANIAN, H. Fabrication, characterization and testing of wireless MEMS-IDT based microaccelerometers. *Sensors and Actuators A* 90 (2001), 7–19.

- [80] VERMEERSEN, B. Earth–Oriented Space Research, Part I: The Solid Earth. Delft University of Technology, Delft Institute for Earth–Oriented Space Research, Delft, March 04, 2002.
- [81] WAKKER, K. F. Astrodynamics–I, Course ae4–873, Part 1. Delft University of Technology, Faculty of Aerospace Engineering, August 2005.
- [82] WEBBOOK, N. C. NIST Standard Reference Database Number 69, June 2005.
<http://webbook.nist.gov/chemistry/> (accessed March 14, 2008).
- [83] WERTZ, J. R. *Mission Geometry; Orbit and Constellation Design and Management*. Kluwer Academic Press, Inc., 2001.
- [84] WIKIPEDIA. Isostasy — Wikipedia, the free encyclopedia, September 23, 2007.
<http://en.wikipedia.org/wiki/Isostasy> (accessed September 24, 2007).
- [85] WIKIPEDIA. Orbital resonance — Wikipedia, The Free Encyclopedia, August 18, 2007.
http://en.wikipedia.org/wiki/Orbital_resonance (accessed August 28, 2007).
- [86] WIKIPEDIA. Serpentinization — Wikipedia, the free encyclopedia, July 30, 2007.
<http://en.wikipedia.org/wiki/Serpentinization> (accessed September 03, 2007).
- [87] WIKIPEDIA. Chondrites — Wikipedia, the free encyclopedia, July 15, 2008.
<http://en.wikipedia.org/wiki/Chondrites> (accessed August 14, 2008).
- [88] WIKIPEDIA. Chondrule — Wikipedia, the free encyclopedia, July 5, 2008.
<http://en.wikipedia.org/wiki/Chondrule> (accessed August 14, 2008).
- [89] WIKIPEDIA. Lithophile — Wikipedia, the free encyclopedia, April 26, 2008.
<http://en.wikipedia.org/wiki/Lithophile> (accessed August 14, 2008).
- [90] WIKIPEDIA. Roche limit — Wikipedia, the free encyclopedia, May 05, 2008.
http://en.wikipedia.org/wiki/Roche_Limit (accessed May 22, 2008).
- [91] WISDOM, J. Tidal dissipation at arbitrary eccentricity and obliquity. *Icarus* 193 (2008), 637–640.
- [92] YAZDI, N., AND KHALIL, N. An All-Silicon Single-Wafer Micro-g Accelerometer with a Combined Surface and Bulk Micromachining Process. *Journal of Microelectromechanical Systems* 9, 4 (December 2000), 544–550.
- [93] ZARNECKI, J. C., ET AL. A soft solid surface on Titan as revealed by the Huygens Surface Science Package. *Nature* 438 (December 08, 2005), 792–795.
- [94] ZHU, X., AND STROBEL, D. F. On the maintenance of thermal wind balance and equatorial superrotation in Titan’s stratosphere. *Icarus* 176 (2005), 331–350.

Definitions

Chondrite Chondrites are stones of meteoric origin, characterized by the small round granules called chondrules. Chondrites are divided into about fifteen distinct groups on the basis of their mineralogy, bulk chemical and oxygen isotopic compositions. Each chondrite group has a distinctive mixture of chondrules, refractory inclusions, matrix (dust), other components and a characteristic grain size. The various chondrite groups likely originated on separate asteroids or groups of related asteroids. The groups are divided into four categories: ordinary, carbonaceous, enstatite and other chondrites [87].

Ordinary chondrites Ordinary chondrites are the most common type of meteorite that fall on Earth, about 80% of all meteorites and over 90% of chondrites are ordinary chondrites.

Carbonaceous chondrites Carbonaceous chondrites make up less than 5% of the chondrites that fall on Earth. There are many groups of carbonaceous chondrites, but most of them are distinguished chemically and isotopically. CI (Ivuna type) chondrites entirely lack chondrules, but are mostly composed of fine-grained material that is altered largely by water on the parent asteroid. The CI chondrites are highly oxidized, brecciated (type of rock structure) rocks, containing abundant magnetite and sulfate minerals, but lacking metallic Fe.

Enstatite chondrites Only 2% of the chondrites that fall on Earth are enstatite chondrites and are among the most chemically reduced rocks known. Unlike in most other chondrites, the minerals in enstatite chondrites contain almost no iron oxide; metallic Fe–Ni and Fe-bearing sulfide minerals contain nearly all of the Fe. Enstatite chondrites contain a variety of unusual minerals that can only form in extremely reducing conditions, including oldhamite (CaS), niningerite (MgS), perryite (Fe–Ni silicide), and alkali sulfides. Enstatite chondrites can be divided into two groups: EH (high metal) and EL (low metal).

The EH chondrites contain small chondrules (~0.2 mm) and high ratios of siderophile (iron loving) elements to Silicate. Somewhat more than 10% of the rock is composed of metal grains and a diagnostic feature of EH chondrites is that the Fe–Ni metal contains ~3 wt% elemental silicon. The EL chondrites contain larger chondrules (≥ 0.5 mm) and low ratios of siderophile elements to Si. The Fe–Ni metal contains ~1 wt% Si.

Other chondrites This category contains the R (Rumuruti type) chondrites, a very rare group and the K (Kakangari type) grouplet.

Chondrule The small round granules found in chondrites are called chondrules. Chondrules are formed as molten or partially molten droplets in space, before being accreted to their parent asteroids. Chondrites represent the oldest solid material within the solar system and are

believed to be the building blocks of the planetary system. Most chondrules are composed primarily of the silicate minerals olivine and pyroxene, surrounded by material composed of feldspar, that may either be glassy or crystalline. Small amounts of other minerals are often present, including Fe sulfide (troilite), metallic Fe–Ni, oxides such as chromite, and phosphates such as merrillite [88].

Clathrate A type of chemical substance where a guest molecule is trapped or contained in another type of lattice, for example a clathrate hydrate has a lattice of water molecules which encloses molecules of a trapped gas.

Equinox One of the two moments of the year when the Sun is directly above a planet's equator. On Earth the vernal equinox occurs on March 20 or 21, marking the beginning of spring, and the autumnal equinox on September 22 or 23, marking the beginning of autumn in the Northern Hemisphere (and the reverse in the Southern Hemisphere). The days on which an equinox falls have about equal periods of sunlight and darkness [12].

Gravitational wave Einstein's general theory of relativity predicts that two stars revolving around each other in a bound orbit suffer accelerations, and as a result generate gravitational radiation. Gravitational waves carry away energy and momentum at the expense of the orbital decay of two stars, thereby causing the stars to gradually spiral towards each other and giving rise to shorter and shorter periods. This anticipated decrease of the orbital period of a binary pulsar was first observed in PSR 1913+16 by Taylor and Weisberg [3].

Gravity assist A planetary gravity assist or swing-by is the use of the relative movement and gravity of a planet to change the plane and/or velocity of the spacecraft's trajectory. With respect to the planet, the spacecraft approaches on a hyperbolic trajectory. It swings by the planet at 'periplanet' and leaves on the other leg of the hyperbolic trajectory at the same velocity *with respect to the planet* at which it came in [83].

Isostasy Isostasy is a term used in geology to refer to the state of gravitational equilibrium between the Earth's lithosphere and asthenosphere such that the tectonic plates 'float' at an elevation which depends on their thickness and density. It is invoked to explain how different topographic heights can exist at the Earth's surface [84].

Lithophile Lithophiles are micro-organisms that can live within the pore spaces of sedimentary and in cracked igneous (formed by the cooling and hardening of magma or molten lava) rocks to depths down to nearly three kilometers, where the temperature is approximately 75°C. The lithophiles that live in surface rocks make use of photosynthesis for energy, the lithophiles that live in deeper rocks extract energy from the minerals around them and extract carbon dioxide from water that seeps down the cracks they live in [89].

Orbital resonance In celestial mechanics, an orbital resonance occurs when two orbiting bodies exert a regular, periodic gravitational influence on each other, usually due to their orbital periods being related by a ratio of two small integers. Orbital resonances greatly enhance the mutual gravitational influence of the bodies. In most cases, this results in an unstable interaction, in which the bodies exchange momentum and shift orbits until the resonance no longer exists. Under some circumstances, a resonant system can be stable and self-correcting, so that the bodies remain in resonance [85].

Prograde In the direction that the planet rotates.

Roche limit The Roche limit is the distance within which a celestial body, held together only by its own gravity, will disintegrate due to a second celestial body's tidal forces. Inside the Roche limit, orbiting material will tend to be pulled apart and form rings, while outside the limit, material will tend to accrete. The term is named after Édouard Roche, the French astronomer who first calculated this theoretical limit in 1848 [90] and given as [7]:

$$\frac{a_R}{R_p} = 2.456 \left(\frac{\rho_p}{\rho_s} \right)^{\frac{1}{3}} \quad (\text{A.1})$$

where a_R is the Roche limit for tidal disruption, R_p and ρ_p the radius and density of the planet in question respectively, and ρ_s the density of the satellite in question.

Serpentinization A geological low-temperature and metamorphic (physical and/or chemical changes caused temperatures greater than 150 to 200 C and pressures of 1500 bars) process involving heat and water in which low-silica mafic (silicate mineral or rock that is rich in magnesium and iron) and ultramafic (igneous rocks with very low silica content) rocks are oxidized and hydrolyzed with water into serpentinite (a type of rock).

Peridotite, a dense, coarse-grained igneous rock, consisting mostly of the minerals olivine and pyroxene, at and near the sea floor and in mountain belts is converted to serpentine, brucite, magnetite, and other minerals – some rare, such as awaruite (Ni_3Fe), and even native iron. In the process large amounts of water are absorbed into the rock increasing the volume and destroying the structure.

The reaction is exothermic and large amounts of heat energy are produced in the process. Rock temperatures can be raised by about 260°C , providing an energy source for formation of non-volcanic hydrothermal vents. The magnetite-forming chemical reactions produce hydrogen gas and combined with the sulfates and carbonates methane and hydrogen sulfide is formed [86].

Sideral day The interval between two successive passages of the vernal equinox across the observer's meridian [81].

Synchronous An orbit is called synchronous when the orbital period of the satellite is equal to its rotational period. As result the satellite is always in the same position w.r.t the celestial body it is orbiting.

Tidal Love number The measure of elastic deformation of a body in response to tidal perturbations [7].

Properties of methane and ethane

Properties of methane and ethane computed at a pressure of 1.5 bar, the surface pressure of Titan. More details can be found in the NIST Chemistry–WebBook [82].

Table B.1: *Properties of methane (CH₄) at a pressure of 1.5 bar [82].*

Temperature [K]	Density [kg/m ³]	Volume [m ³ /kg]	Viscosity [uPa*s]	Phase	Sound Spd. [m/s]
91.694	450.23	0.0022211	198.49	liquid	1530.5
92.694	448.90	0.0022277	192.44	liquid	1521.3
93.694	447.56	0.0022344	186.68	liquid	1512.1
94.694	446.21	0.0022411	181.19	liquid	1502.9
95.694	444.86	0.0022479	175.97	liquid	1493.6
96.694	443.50	0.0022548	170.98	liquid	1484.2
97.694	442.14	0.0022617	166.21	liquid	1474.8
98.694	440.77	0.0022688	161.66	liquid	1465.4
99.694	439.40	0.0022759	157.30	liquid	1455.9

Table B.2: *Properties of ethane (C₂H₆) at a pressure of 1.5 bar [82].*

Temperature [K]	Density [kg/m ³]	Volume [m ³ /kg]	Viscosity [uPa*s]	Phase	Sound Spd. [m/s]
91.352	650.47	0.0015373	1226.6	liquid	1990.9
92.352	649.43	0.0015398	1176.8	liquid	1985.8
93.352	648.38	0.0015423	1129.9	liquid	1980.3
94.352	647.33	0.0015448	1085.7	liquid	1974.6
95.352	646.27	0.0015473	1044.1	liquid	1968.7
96.352	645.21	0.0015499	1004.8	liquid	1962.6
97.352	644.14	0.0015525	967.68	liquid	1956.3
98.352	643.07	0.0015550	932.64	liquid	1949.8
99.352	641.99	0.0015576	899.53	liquid	1943.2

Table B.3: *Additional data methane (CH₄) and ethane (C₂H₆) [82].*

Methane	
Critical temperature (T_c)	190.564 K
Critical pressure (P_c)	45.992 bar
Critical density (ρ_c)	162.66 kg/m ³
A centric factor	0.01142
Normal boiling point	111.667 K
Ethane	
Critical temperature (T_c)	305.33 K
Critical pressure (P_c)	48.718 bar
Critical density (ρ_c)	207. kg/m ³
A centric factor	0.0993
Normal boiling point	184.552 K

Legendre polynomials

The Legendre functions are given by ([34]):

$$P_{nm}(x) = (1 - x^2)^{m/2} \frac{d^m}{dx^m} P_n(x)$$

$$P_n(x) = \frac{1}{2^n n!} \frac{d^n}{dx^n} (x^2 - 1)^n$$

$$P_{nm}(\cos \varphi) = \sin^m \varphi \frac{d^m P_n(\cos \varphi)}{d(\cos \varphi)^m}$$

Which gives up to degree and order three:

n	m	$P_{nm}(x)$	$P_{nm}(\sin \varphi)$
0	0	1	1
1	0	x	$\sin \varphi$
1	1	$(1 - x^2)^{1/2}$	$\cos \varphi$
2	0	$\frac{1}{2} (3x^2 - 1)$	$\frac{1}{4} (1 + 3 \cos 2\varphi)$
2	1	$3x (1 - x^2)^{1/2}$	$\frac{3}{2} \sin 2\varphi$
2	2	$3(1 - x^2)$	$\frac{3}{2} (1 - \cos 2\varphi)$
3	0	$\frac{1}{2} x (5x^2 - 3)$	$\frac{1}{8} (3 \cos \varphi + 5 \cos 3\varphi)$
3	1	$\frac{3}{2} (5x^2 - 1) (1 - x^2)^{1/2}$	$\frac{3}{8} (\sin \varphi - 5 \sin 3\varphi)$
3	2	$15(1 - x^2)x$	$\frac{15}{4} (\cos \varphi - \cos 3\varphi)$
3	3	$15(1 - x^2)^{3/2}$	$\frac{15}{4} (3 \sin \varphi - \sin 3\varphi)$

Tidal parameters of Titan

Interior models of Titan

Since the Voyager missions, scientists have tried to solve the mystery of Titan's relative high eccentricity. Different interior models have been set up, in order to compute among other values the associated tidal dissipation, the decay of the eccentricity over time and the tidal Love numbers. Here an overview of all the interior models encountered in literature.

Table D.1: *Different interior models of Titan.*

Layer		Density [kg/m ³]	Thickness [km]	Reference	
<i>Model A</i>	uniform	$f_{ice} = 0.45$	1881	[63]	
		$\rho_{ice} = 1200$			
		$\rho_{rock} = 3500$			
<i>Model B</i>	Core	Silicate/iron	2990	1900	[63]
	High-pressure ice	Ice VI	1430	200	
	High-pressure ice	Ice V	1280	75	
	Mantle	Ice II	1180	300	
	Crust	Ice I	930	100	
<i>Model C</i>	Core	Silicate/iron	2990	1900	[63]
	High-pressure ice	Ice VI	1430	225	
	Subsurface ocean	Ammonia water	950	300	
	Mantle/crust	Ice I	930	150	
<i>Model D</i>	Core	rock-to-ice ratio of 55:45	3800	1671	[62]
	High-pressure ice	Ice V	1310	612	
	Subsurface ocean	Ammonia-water 15 wt.% NH ₃	950	224	
	Mantle/crust	Ice I	917	69	

Continued on the next page

TableD.1 – continued from previous page

Layer	Density	Thickness	Reference	
			[kg/m ³]	[km]
<i>Model E</i>				
				[58]
Core type 1		CI chondrite	3300	1875
	High–pressure ice	Ice V	1310	500
Core type 2		liquid iron	8000	910
		EH enstatite	3300	800
	High–pressure ice	Ice V	1310	665
	Subsurface ocean	Ammonia water 5 wt.% NH ₃	1000	74
	Mantle/crust	Ice I	917	126
<i>Model F</i>				
				[58]
Core type 1		CI chondrite		1875
	High–pressure ice	Ice V	1310	425
Core type 2		liquid iron	8000	910
		EH enstatite	3300	800
	High–pressure ice	Ice V	1310	590
	Subsurface ocean	Ammonia water 15 wt.% NH ₃	1000	208
	Mantle/crust	Ice I	917	67
<i>Model G</i>				
				[55]
Core		Silicate/iron	3300	1875
	High–pressure ice	Ice VI	1310	510
	Mantle/crust	Ice I	920	190

Determining the tidal Love number from Cassini radio tracking data

From the assumption that Titan is in hydrostatic equilibrium, a priori values of the coefficients J_2 , C_{22} and S_{22} can be computed and are given in [57] as:

$$\begin{aligned}
 J_2 &= 4.93 \times 10^{-5} + 4.84 \times 10^{-7} \cos(M - \delta) \\
 C_{22} &= 1.48 \times 10^{-5} + 2.42 \times 10^{-7} \cos(M - \delta) \\
 S_{22} &= 3.23 \times 10^{-7} \sin(M - \delta)
 \end{aligned}$$

where the a priori Love number is assumed to be $k_2 = 0.3$ (following [72]) . When Titan has an internal ocean, covered by a high viscosity ice–I layer, the phase lag angle $\delta = 0^\circ$. In the oceanless case, hence only an outer shell of low–viscosity ice I, the values for the possible phase lag angles used in [57] are $\delta = 5^\circ, 10^\circ, 15^\circ, 20^\circ, 25^\circ$ and 30° . Figures D.1 and D.2 show how the a priori value

of C_{22} and S_{22} behave for the different phase lag angles, along a complete orbit (mean anomaly $0 \leq E \leq 360$).

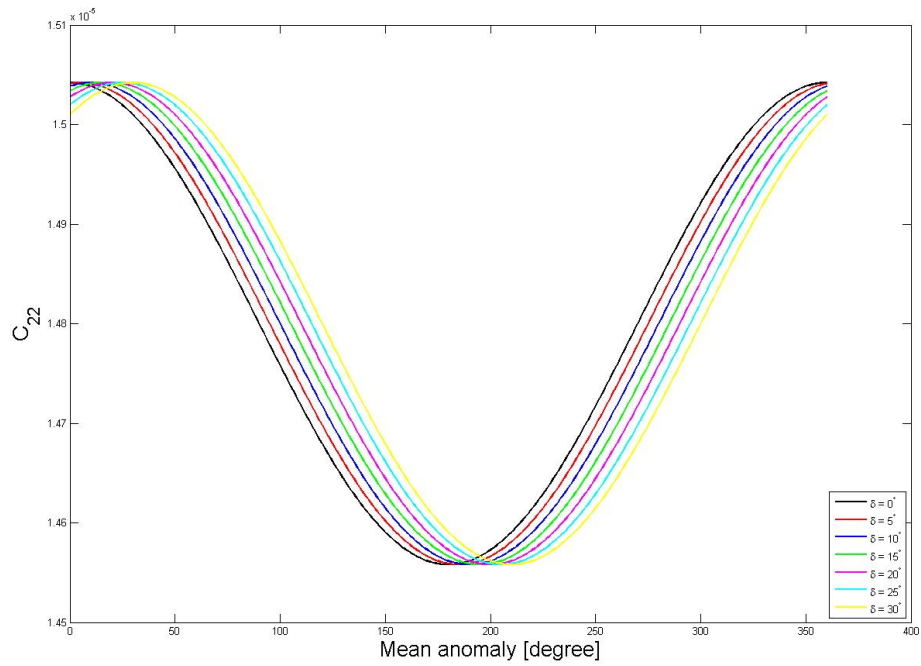


Figure D.1: A priori values of C_{22} for differet phase lag angles δ , given by equation 4.109 [57].

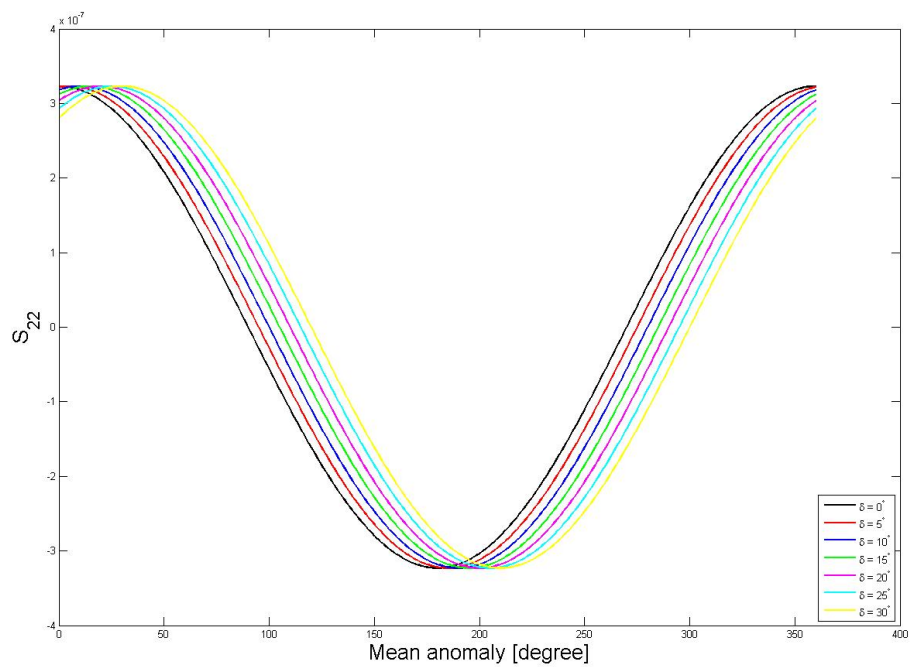


Figure D.2: A priori values of S_{22} for differet phase lag angles δ , given by equation 4.110 [57].

Effect of ammonia on tidal parameters of Titan

The effect of ammonia is presented and discussed in [62]. The most important figures and values presented in [62] can be found here.

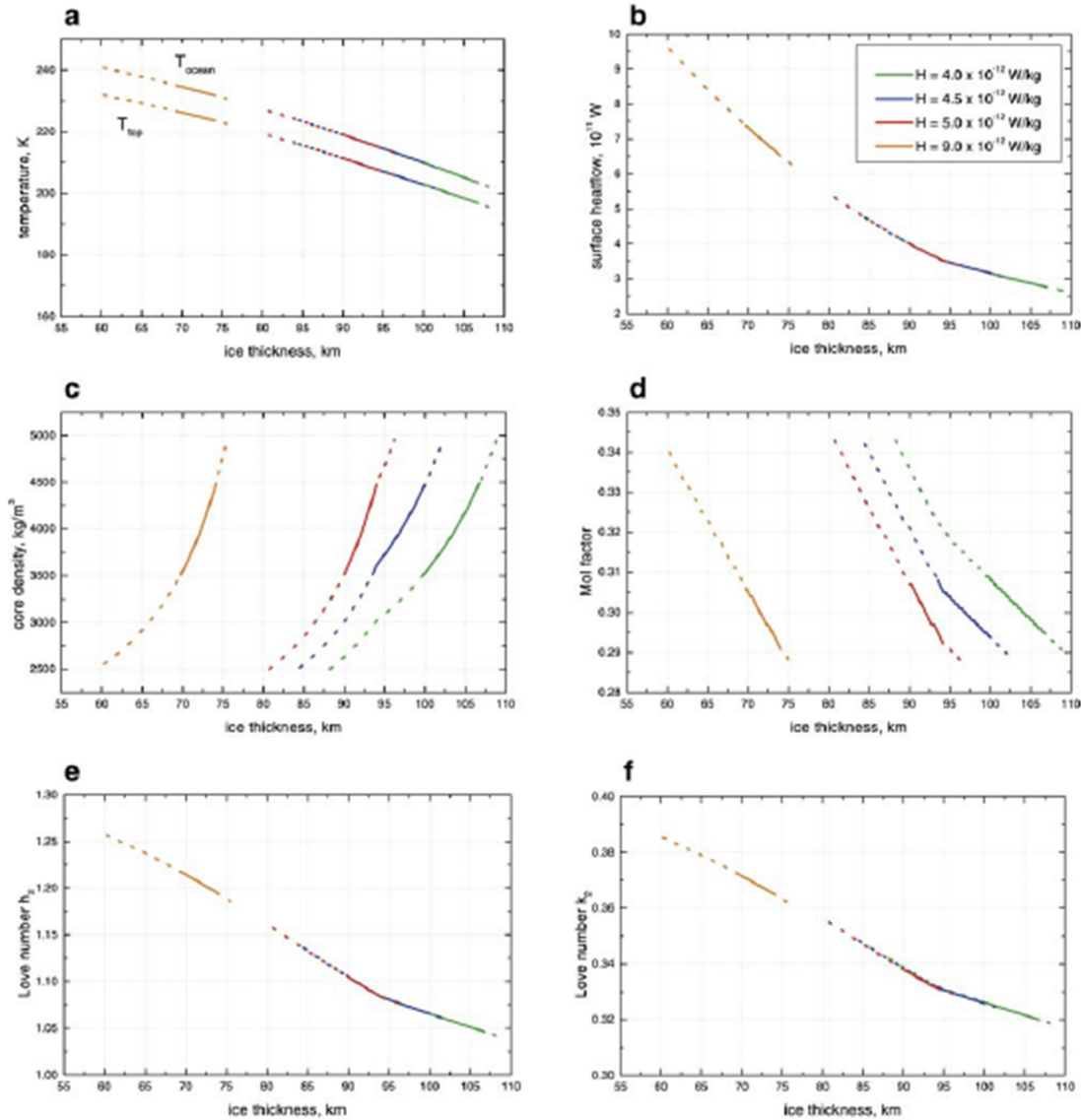


Figure D.3: Summary of the model results for a primordial ammonia–water ocean composition of 5 wt.% NH_3 and different core heat production rates H as a function of ice–I layer thickness: (a) Temperatures of the convective sublayer T_{int} and subsurface ocean T_{ocean} , (b) surface heat flow, (c) core density, (d) Mol factor, (e) radial displacement Love number h_2 , (f) potential Love number k_2 . From left to right, there are four partly overlapping sets of curves in each figure that correspond to $H = 9 \times 10^{-12}$ W/kg, $H = 5 \times 10^{-12}$ W/kg, $H = 4.5 \times 10^{-12}$ W/kg, and $H = 4 \times 10^{-12}$ W/kg. Solid curve branches indicate model results consistent with core densities of anhydrous rock and iron between 3500 and 4500 kg/m^3 [62].

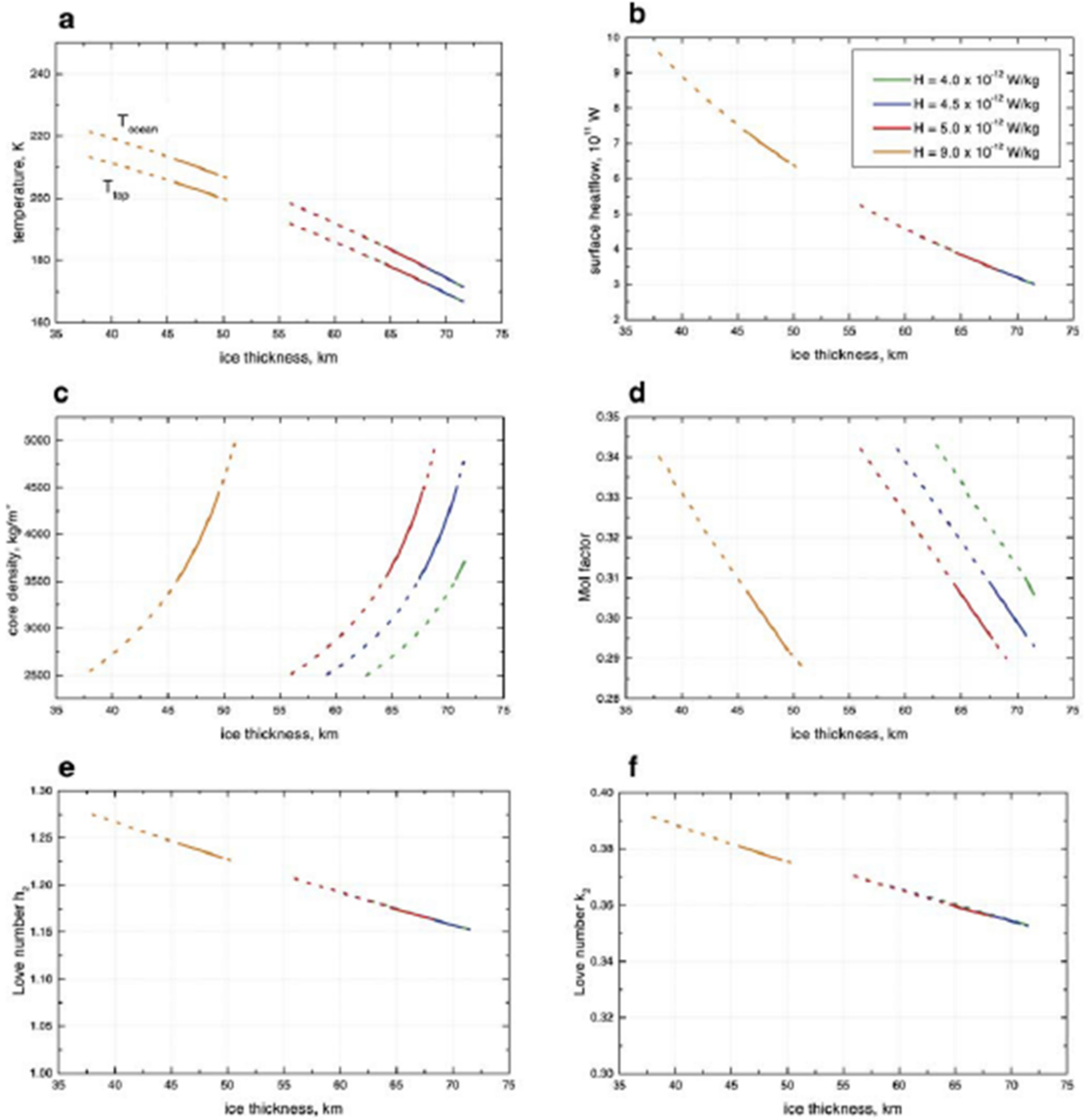


Figure D.4: Summary of the model results for a primordial ammonia–water ocean composition of 15 wt.% NH_3 and different core heat production rates H as a function of ice–I layer thickness: (a) Temperatures of the convective sublayer T_{int} and subsurface ocean T_{ocean} , (b) surface heat flow, (c) core density, (d) Mol factor, (e) radial displacement Love number h_2 , (f) potential Love number k_2 . From left to right, there are four partly overlapping sets of curves in each figure that correspond to $H = 9 \times 10^{-12}$ W/kg, $H = 5 \times 10^{-12}$ W/kg, $H = 4.5 \times 10^{-12}$ W/kg, and $H = 4 \times 10^{-12}$ W/kg. Solid curve branches indicate model results consistent with core densities of anhydrous rock and iron between 3500 and 4500 kg/m^3 [62].

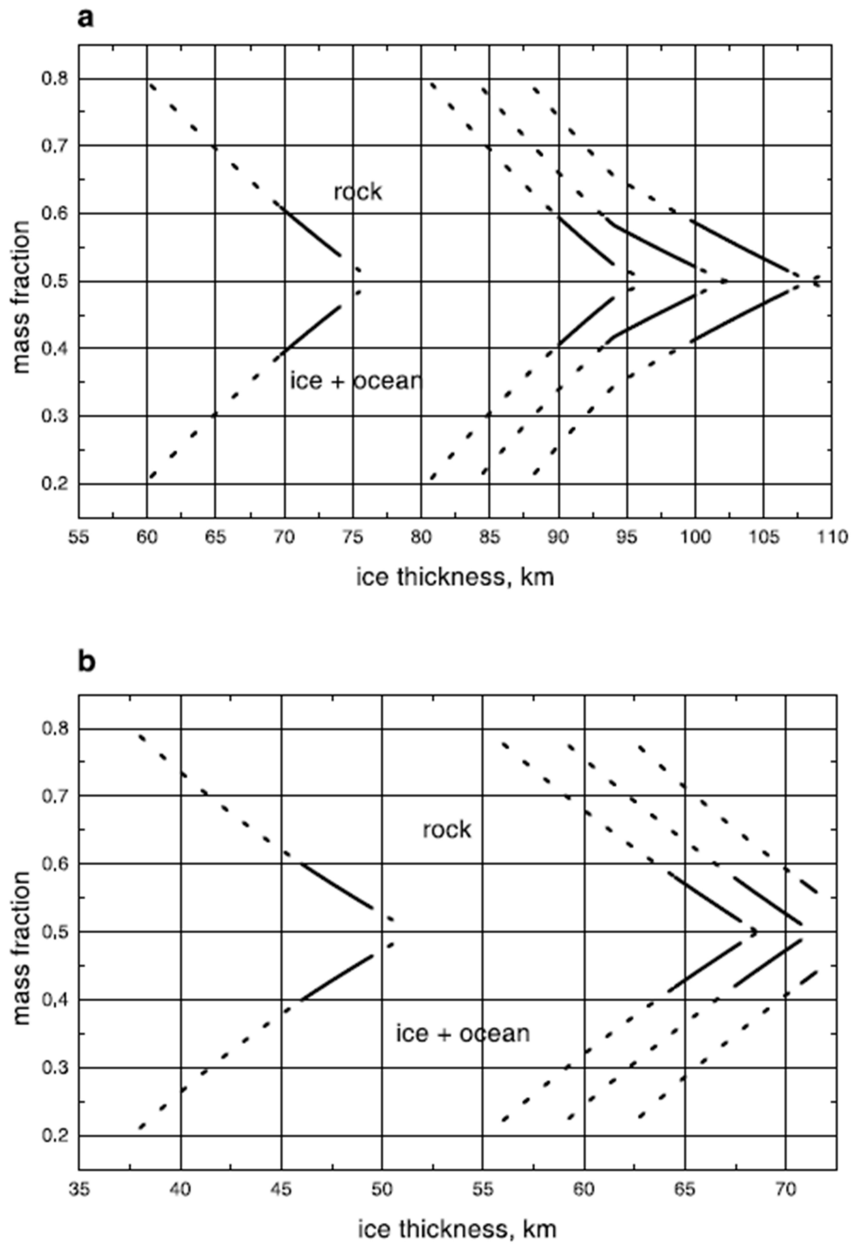


Figure D.5: Mass fractions of rock/iron and ice plus subsurface ocean for various core heat production rates H as a function of ice-I layer thickness. From left to right, there are four sets of curves in each figure that correspond to $H = 9 \times 10^{-12}$ W/kg, $H = 5 \times 10^{-12}$ W/kg, $H = 4.5 \times 10^{-12}$ W/kg, and $H = 4 \times 10^{-12}$ W/kg, respectively: (a) primordial ammonia-water ocean composition of 5 wt.% NH_3 , (b) 15 wt.% NH_3 . Solid curve branches indicate model results consistent with core densities of anhydrous rock and iron between 3500 and 4500 kg/m³ [62].

Time-dependent part of the tide-raising potential

The time-dependent part of the tide-raising potential of Saturn on Titan can be written as [66]:

$$V_{time} = -\frac{GM_S R^2}{a^3} 3e \left[\frac{1}{2} (3 \sin^2 \vartheta \cos^2 \lambda - 1) \cos(nt) + \sin^2 \vartheta \sin(2\lambda) \sin(nt) \right]$$

where M_S is the mass of Saturn, R is the radius from the center of mass of Titan to the measurement point ($R = R_T$ at the surface of Titan), a the semi-major axis of the orbit of Titan, n is the orbital angular frequency, $e = 0.0292$ the orbital eccentricity of Titan, ϑ and λ are the co-latitude and longitude (with $\lambda = 0$ at the sub-Saturn longitude) and, t the time. An orbit of Titan around Saturn corresponds to 15.95 Earth days and is synchronous with respect to Saturn.

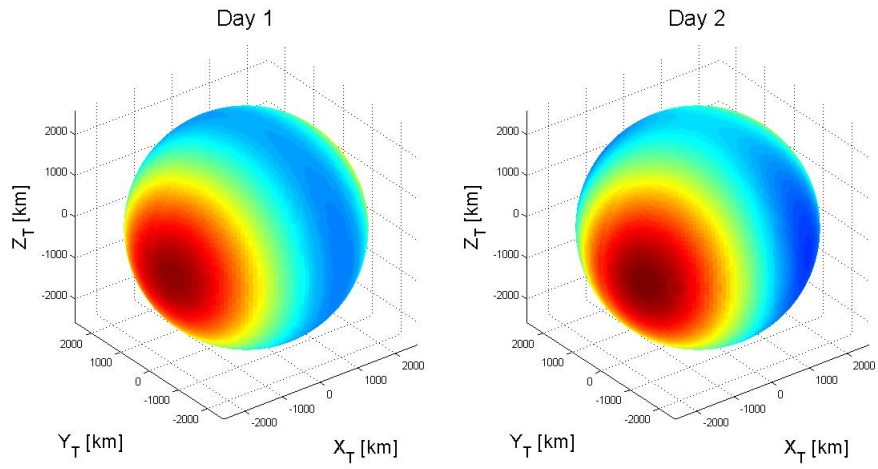


Figure E.1: The time-dependent part of the tide-raising potential on day one and day two of the orbit of Titan around Saturn.

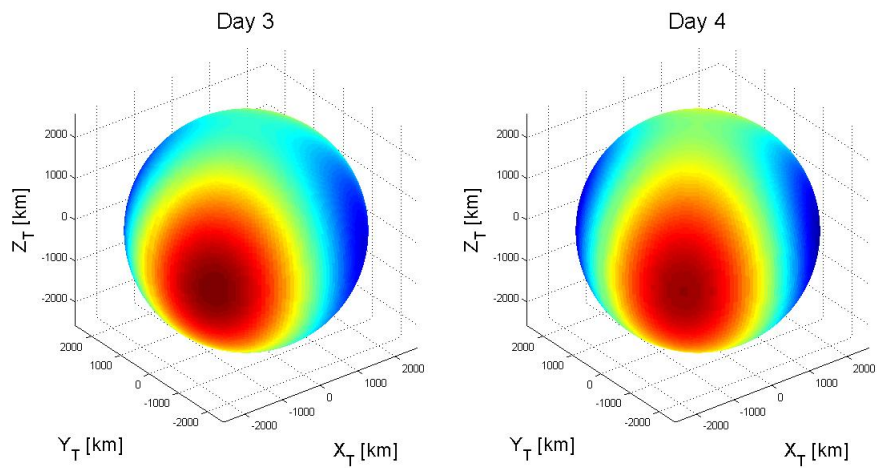


Figure E.2: The time-dependent part of the tide-raising potential on day one and day two of the orbit of Titan around Saturn.

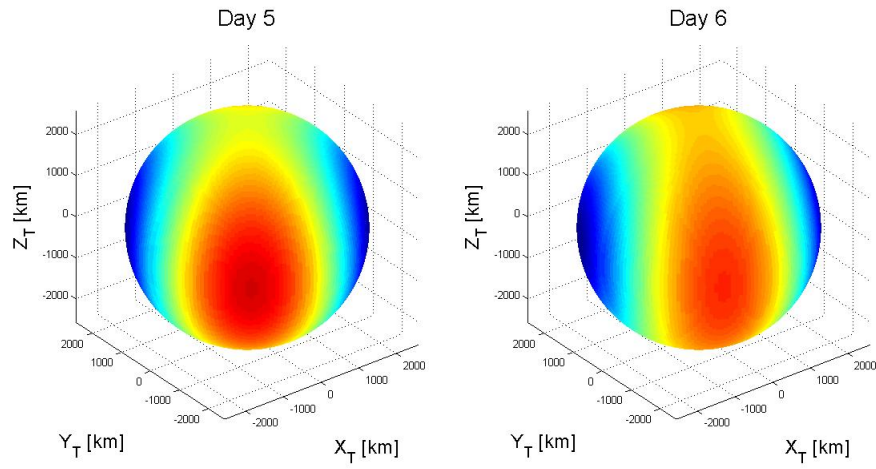


Figure E.3: *The time-dependent part of the tide-raising potential on day five and day six of the orbit of Titan around Saturn.*

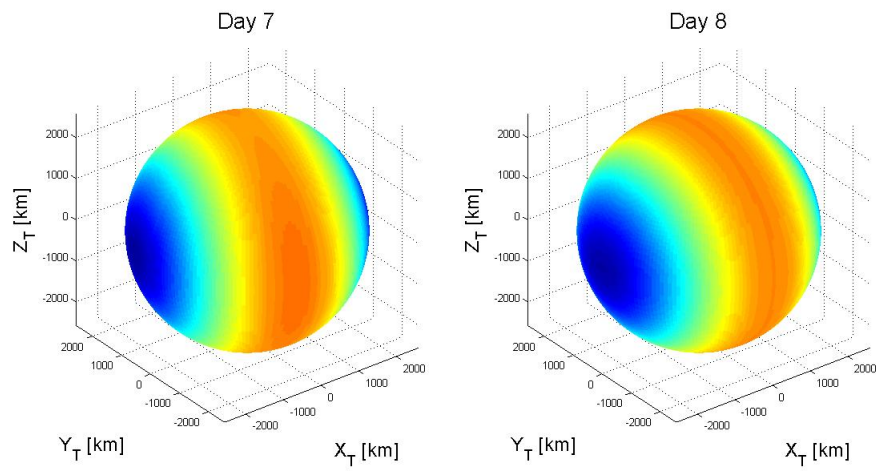


Figure E.4: *The time-dependent part of the tide-raising potential on day seven and day eight of the orbit of Titan around Saturn.*

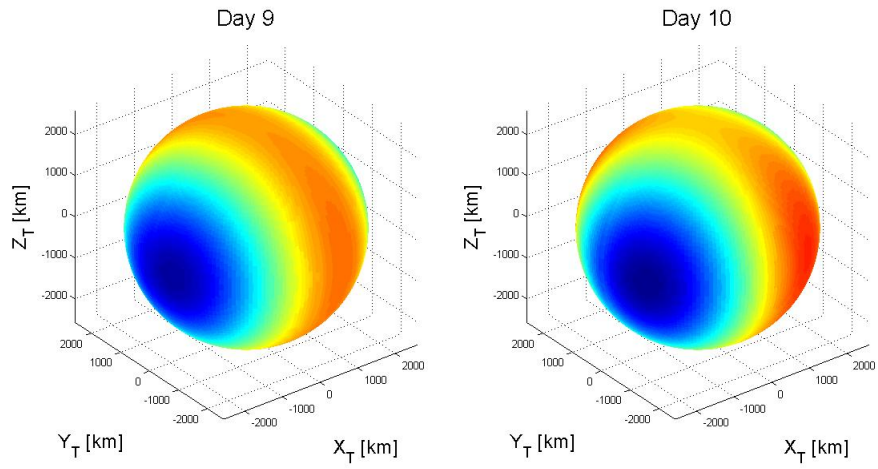


Figure E.5: The time-dependent part of the tide-raising potential on day nine and day ten of the orbit of Titan around Saturn.

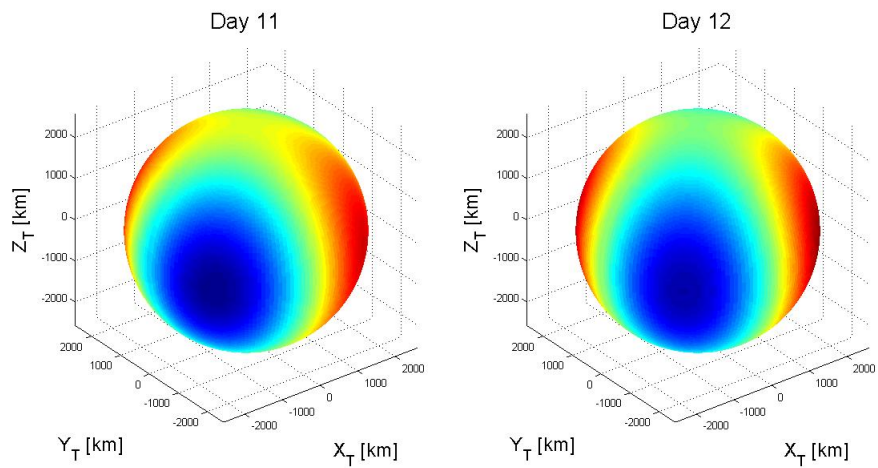


Figure E.6: Time-dependent part of the tide-raising potential on day eleven and day twelve of the orbit of Titan around Saturn.

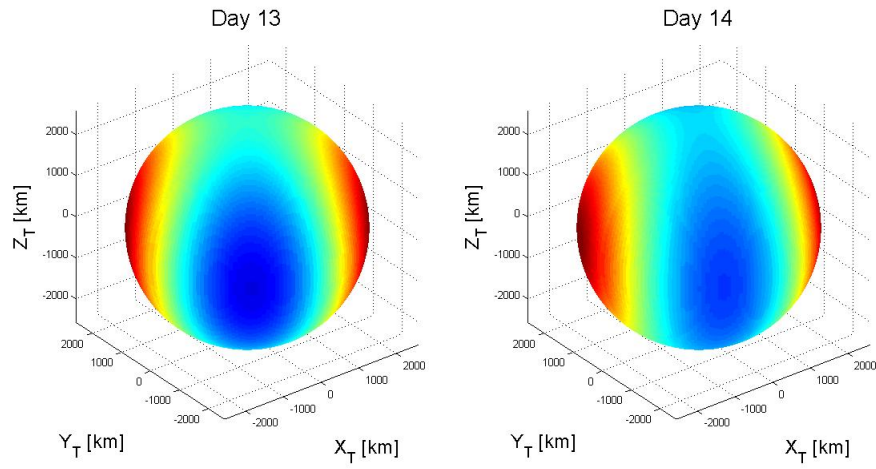


Figure E.7: The time-dependent part of the tide-raising potential on day thirteen and day fourteen of the orbit of Titan around Saturn.

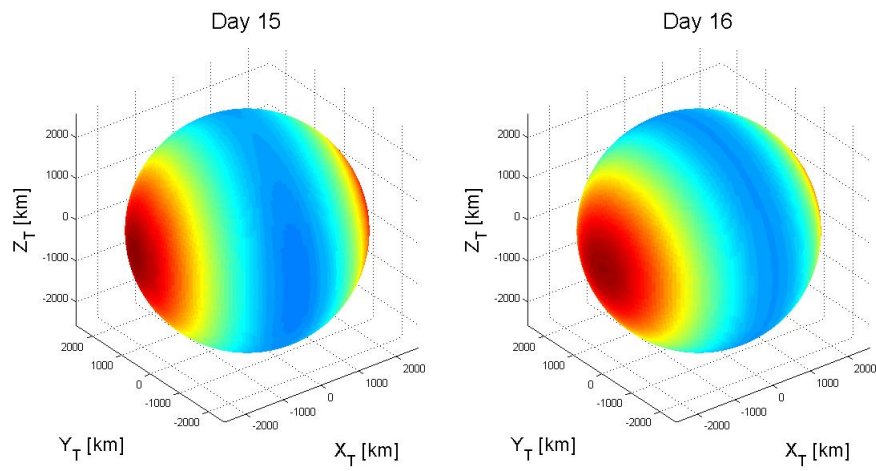


Figure E.8: The time-dependent part of the tide-raising potential on day fifteen and day sixteen of the orbit of Titan around Saturn.

Miscellaneous figures belonging to chapter 6

Gravitational potential of the lakes

The gravitational field of a body outside the masses can be represented by the gravitational potential of a thin layer of mass on the surface of a body and is given by equation 4.43:

$$V(\mathbf{x}) = G \iint_S \frac{\mu(\mathbf{y})}{|\mathbf{x} - \mathbf{y}|} dS(\mathbf{y})$$

where μ is the layer density measured in kg/m^2 . The left picture of figure F.1 shows the gravitational potential of the smaller lake (lake 01), the right of the larger lake (lake 02) with the gravitational potential superimposed on each other and the gravitational potential of the sphere. Figure F.2 shows the same, only the two lakes combined in one figure.

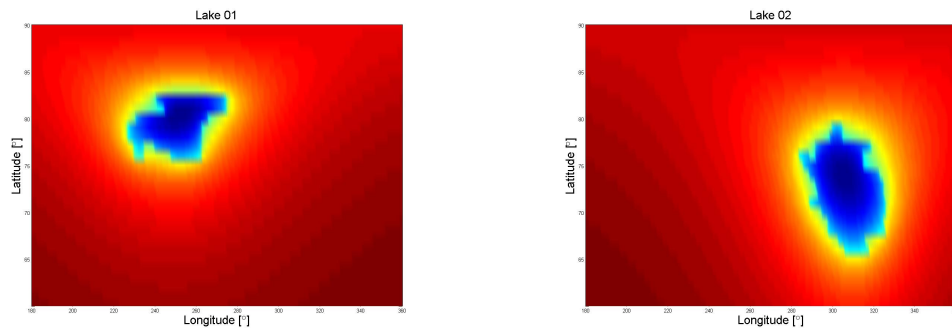


Figure F.1: *The gravitational potential of lake 01 (left) and lake 02 (right).*

To see the effect of sub-surface lakes on the gravitational potential, the distance of the lake underneath the surface of Titan is increased. The gravitational potential is used for this, because it clearly shows where the lakes would be. Note that the axes of the figures are different in scale, a good indication that the gravity gradients as a result of the subsurface lakes will be weaker too.

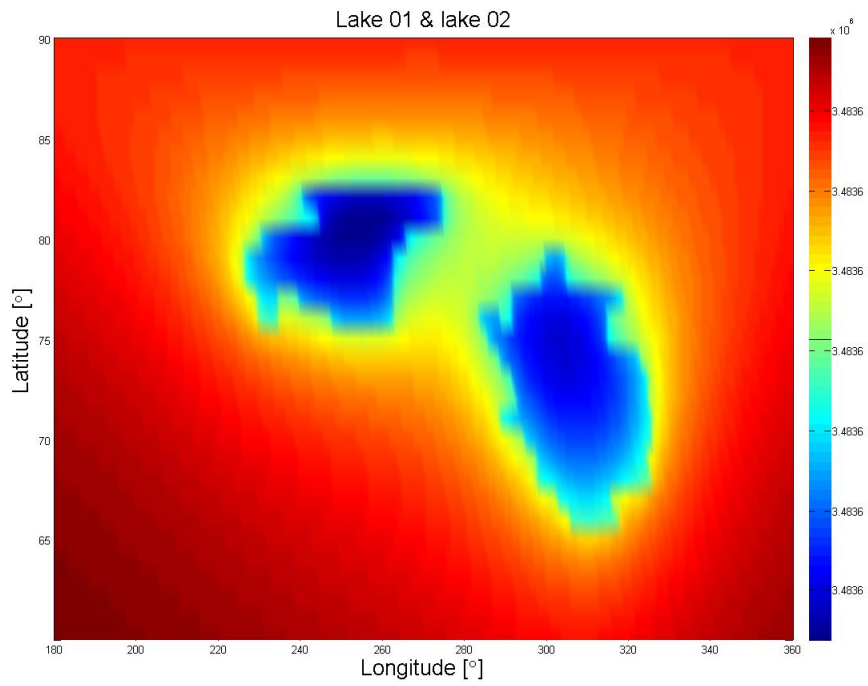


Figure E.2: The gravitational potential of lake 01 and lake 02 combined in one figure. The gravitational potential of the sphere Titan is superimposed to that of both the lakes in this figure.

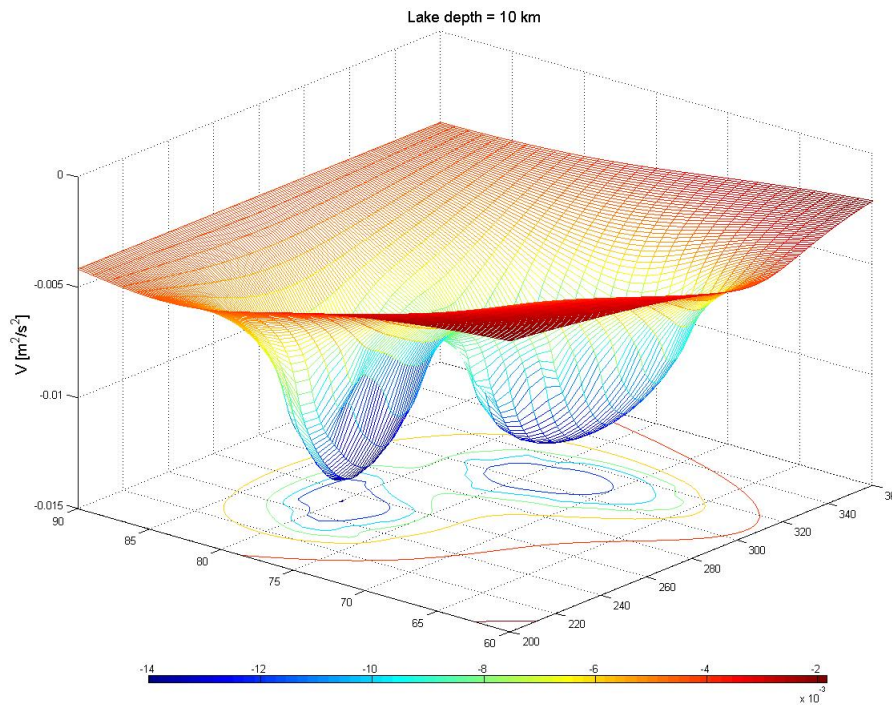


Figure E.3: The gravitational potential [m^2/s^2] of the lakes 01 and 02 combined, 10 km underneath the surface of Titan. The values for the sphere Titan are not superimposed in this figure.

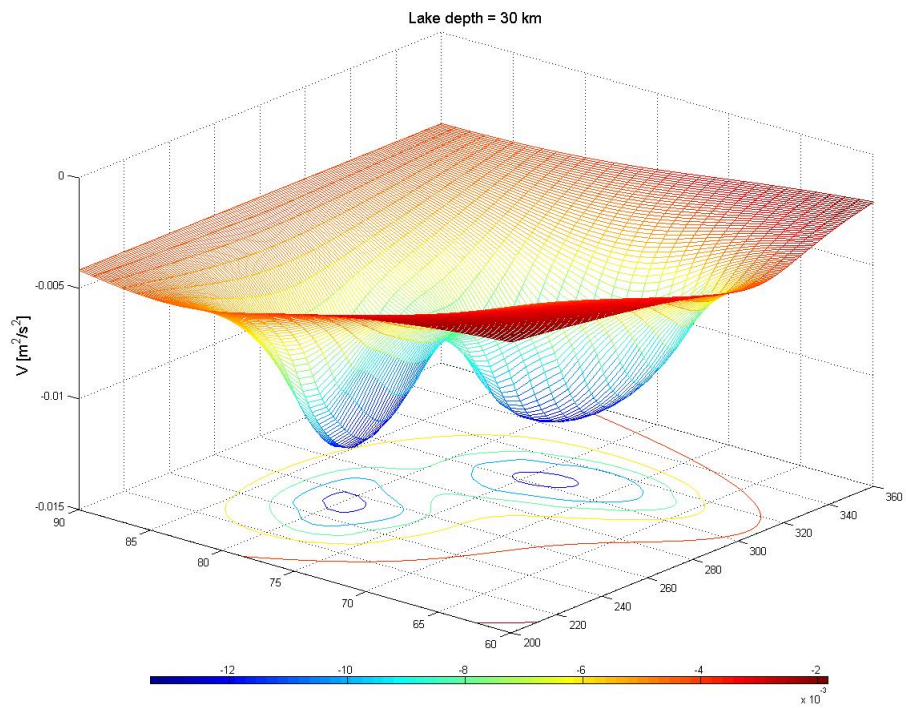


Figure E.4: The gravitational potential [m^2/s^2] of the lakes 01 and 02 combined, 30 km underneath the surface of Titan. The values for the sphere Titan are not superimposed in this figure.

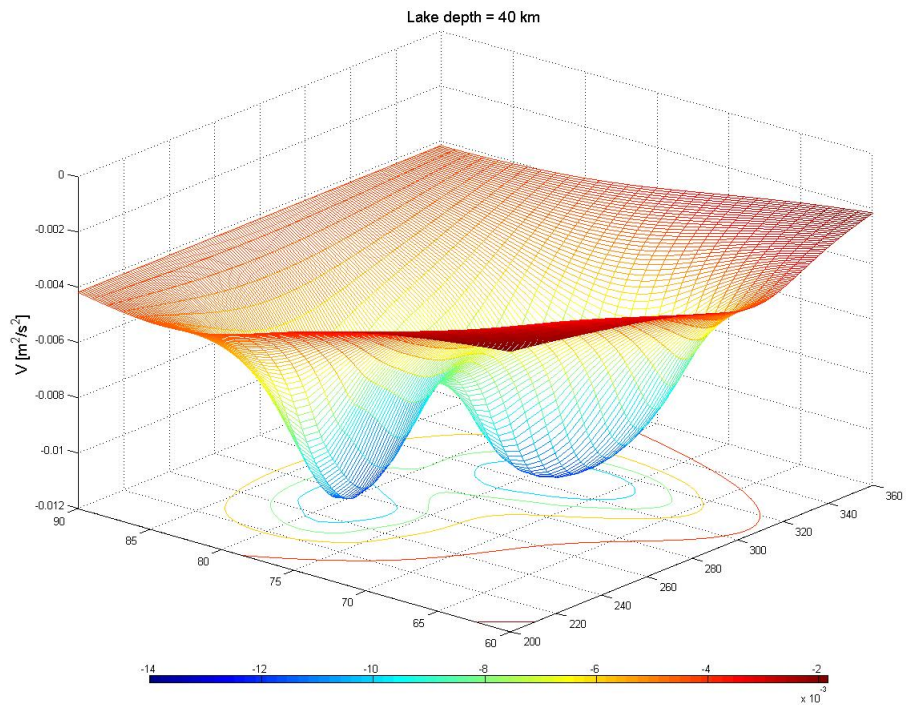


Figure E.5: The gravitational potential [m^2/s^2] of the lakes 01 and 02 combined, 40 km underneath the surface of Titan. The values for the sphere Titan are not superimposed in this figure.

Gravity gradients of the lakes

The gravity gradients are modeled according to equations 4.64 to 4.69:

$$\begin{aligned}
 V_{xx} &= G\mu \sum_{i=1}^I \frac{3(x_P - x_Q)^2 - \ell^2}{\ell^5} \Delta\sigma_i \\
 V_{yy} &= G\mu \sum_{i=1}^I \frac{3(y_P - y_Q)^2 - \ell^2}{\ell^5} \Delta\sigma_i \\
 V_{zz} &= G\mu \sum_{i=1}^I \frac{3(z_P - z_Q)^2 - \ell^2}{\ell^5} \Delta\sigma_i \\
 V_{xy} &= V_{yx} = G\mu \sum_{i=1}^I \frac{3(x_P - x_Q)(y_P - y_Q)}{\ell^5} \Delta\sigma_i \\
 V_{xz} &= V_{zx} = G\mu \sum_{i=1}^I \frac{3(x_P - x_Q)(z_P - z_Q)}{\ell^5} \Delta\sigma_i \\
 V_{yz} &= V_{zy} = G\mu \sum_{i=1}^I \frac{3(z_P - z_Q)(y_P - y_Q)}{\ell^5} \Delta\sigma_i
 \end{aligned}$$

where $\ell = |\mathbf{x} - \mathbf{y}| = \sqrt{(x_P - x_Q)^2 + (y_P - y_Q)^2 + (z_P - z_Q)^2}$. The figures give the results at a measurement height of 2 km. The values for the two lakes and the sphere are superimposed, the left figure is a surface plot where the different colours represent the different values for the gradients and the right plot shows the same figure only in a 3D plot, where next to the colour the peaks represent the values of the gradients.

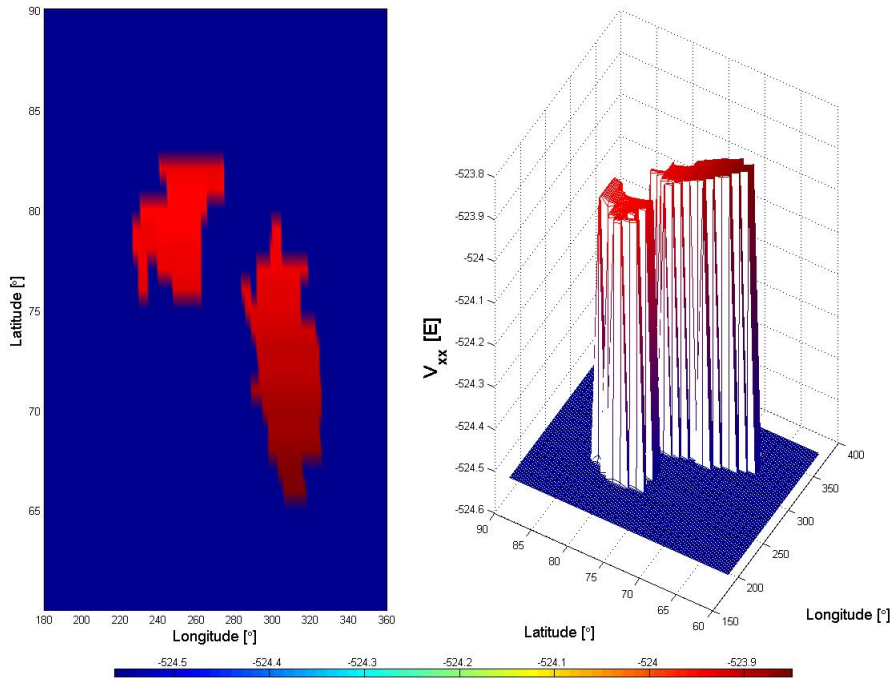


Figure E.6: The gravity gradient V_{xx} of lake 01 and lake 02 combined in one figure. The gradients of the sphere Titan are superimposed to that of both the lakes in this figure.

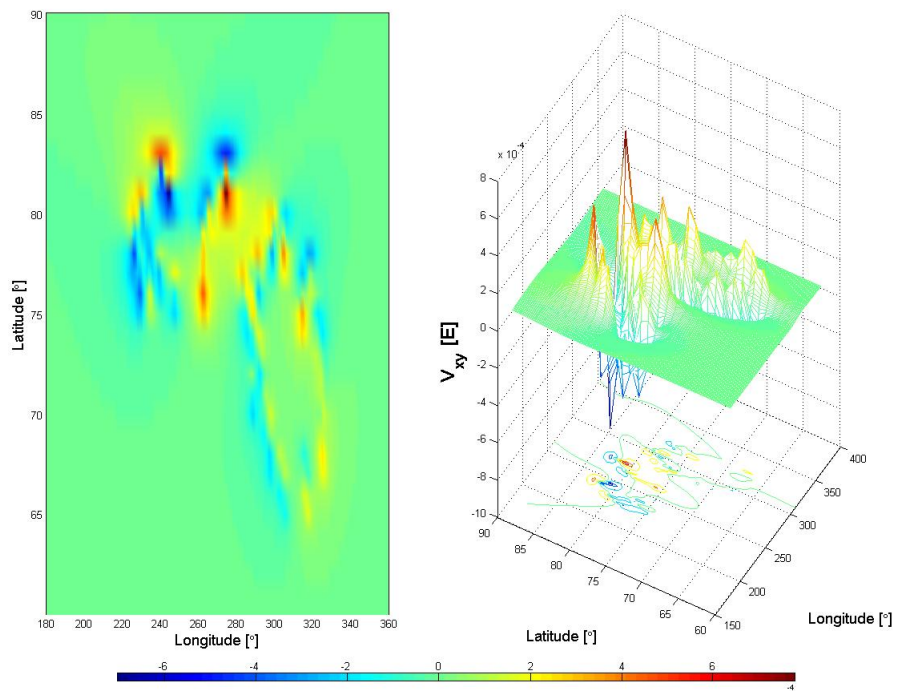


Figure E.7: The gravity gradient V_{xy} of lake 01 and lake 02 combined in one figure. The gradients of Titan are superimposed to that of both the lakes in this figure.

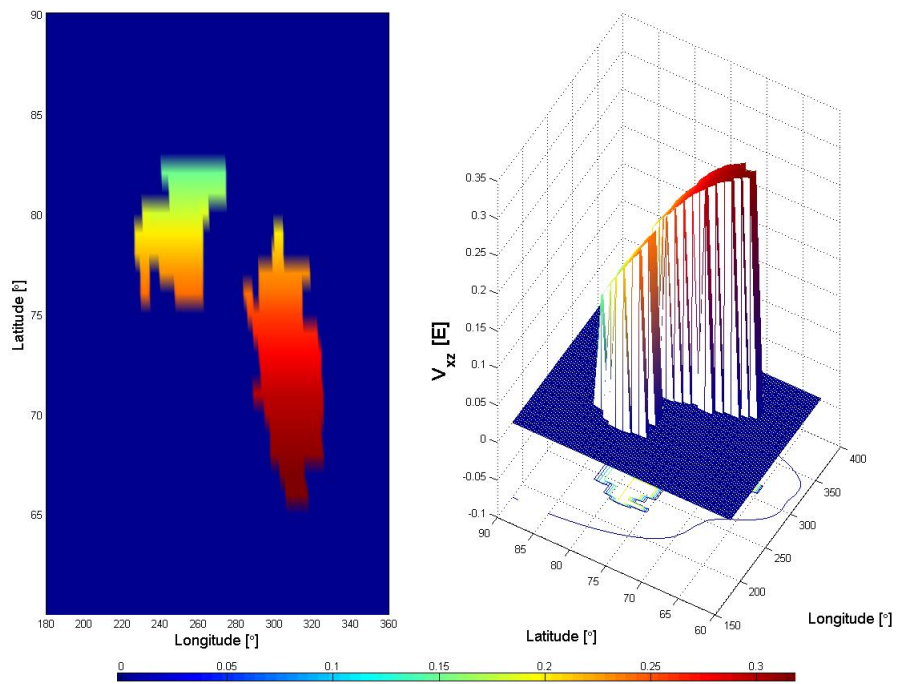


Figure E.8: The gravity gradient V_{xz} of lake 01 and lake 02 combined in one figure. The values for gradients of Titan are superimposed to that of both the lakes in this figure.

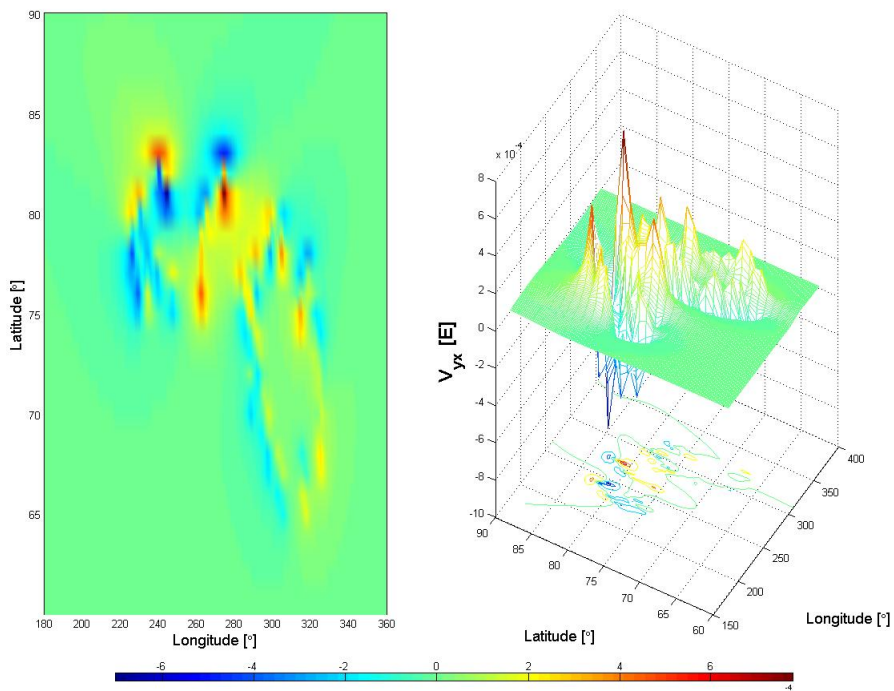


Figure E.9: The gravity gradient V_{yx} of lake 01 and lake 02 combined in one figure. The values for gradients of Titan are superimposed to that of both the lakes in this figure.

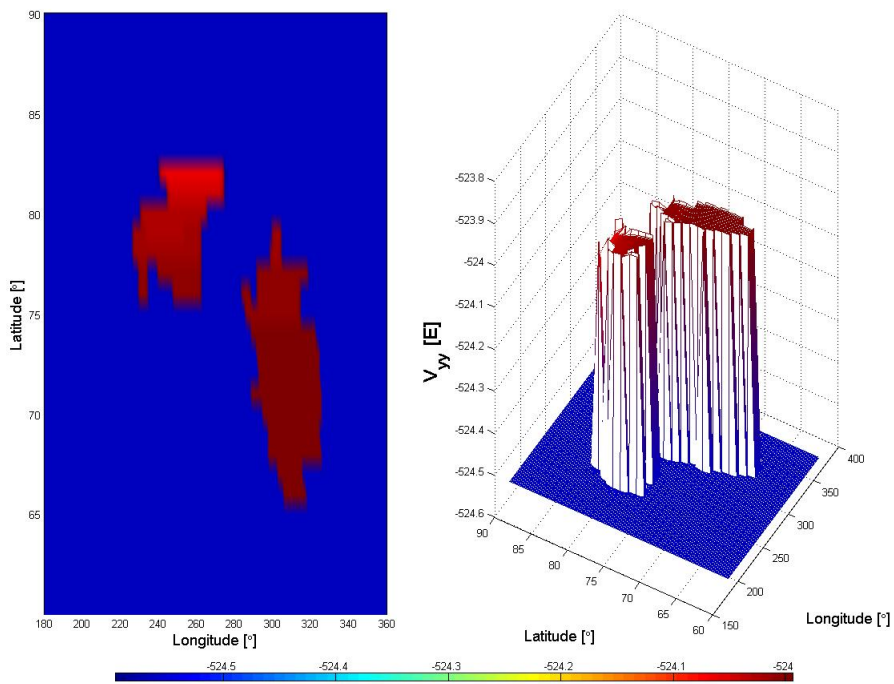


Figure E.10: The gravity gradient V_{yy} of lake 01 and lake 02 combined in one figure. The values for gradients of Titan are superimposed to that of both the lakes in this figure.

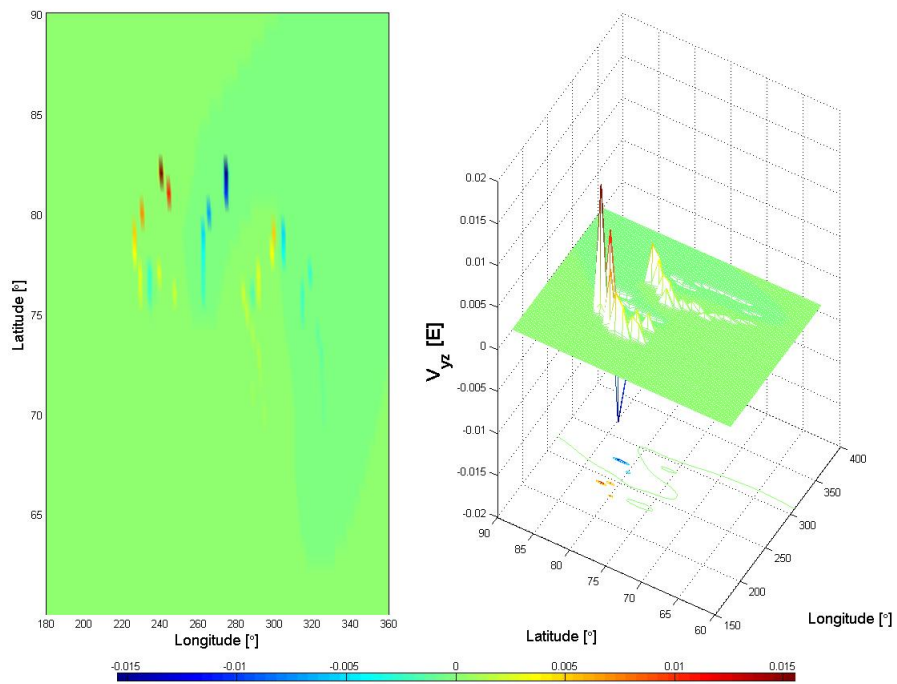


Figure F.11: The gravity gradient V_{yz} of lake 01 and lake 02 combined in one figure. The values for gradients of Titan are superimposed to that of both the lakes in this figure.

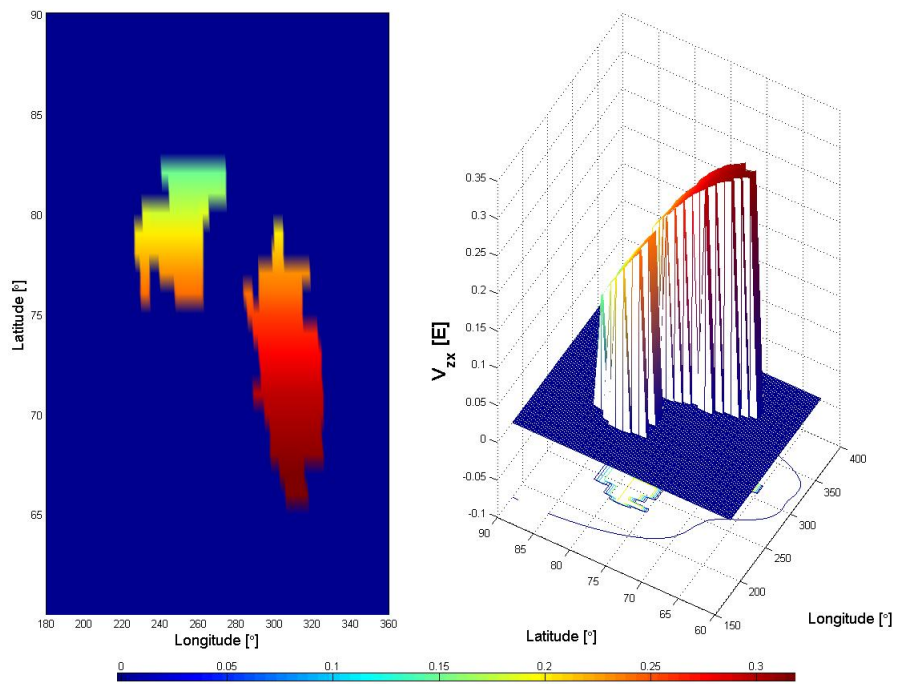


Figure F.12: The gravity gradient V_{zx} of lake 01 and lake 02 combined in one figure. The values for gradients of Titan are superimposed to that of both the lakes in this figure.

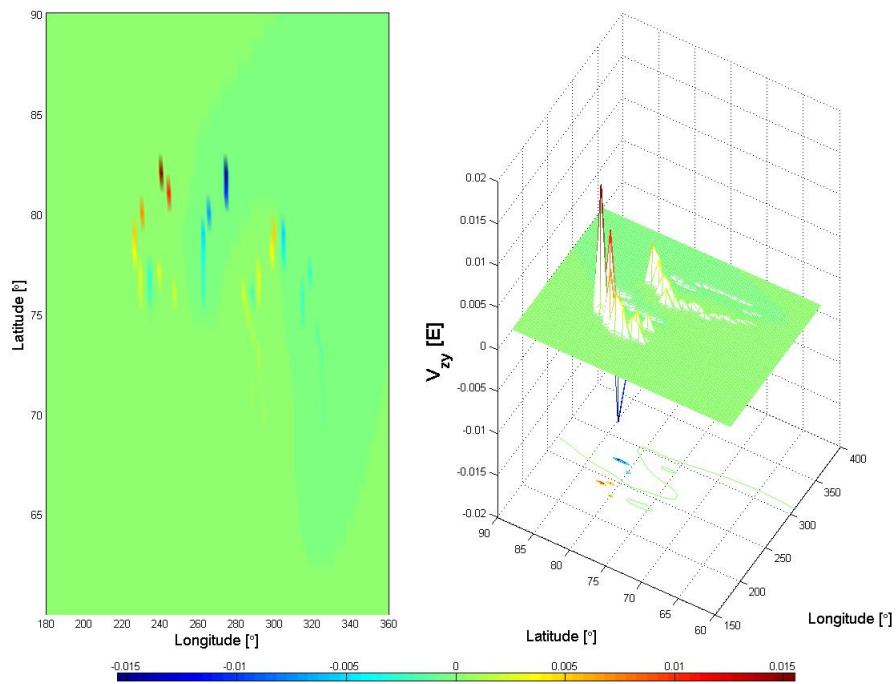


Figure E.13: The gravity gradient V_{zy} of lake 01 and lake 02 combined in one figure. The values for gradients of Titan are superimposed to that of both the lakes in this figure.

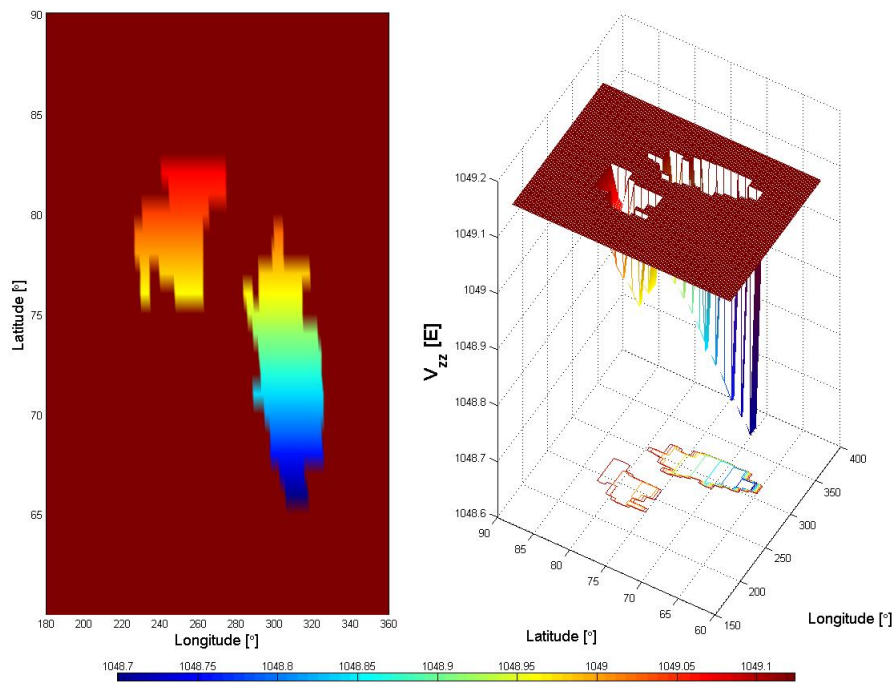


Figure E.14: The gravity gradient V_{zz} of lake 01 and lake 02 combined in one figure. The values for gradients of Titan are superimposed to that of both the lakes in this figure.

Gradients measured at different altitudes throughout the atmosphere of Titan

The gravity gradients decline with increasing height, thus it is interesting to see until which height the gradient is strong enough to be measured by the gradiometer. The measurement point (e.g. the balloon) is located in the middle of both lakes, see table F.1 and the measurement are taken upwards. The following figures show the diagonal and off-diagonal gradients up to an height of 1000 km, followed by the figures up to a height of 100 km.

Table F.1: The location of the measurement point and the area of the lakes.

	Colatitude (ϑ)	Longitude (λ)	Area [km ²]
Lake 01	11°	245°	12 050
Lake 02	17°	308°	17 497

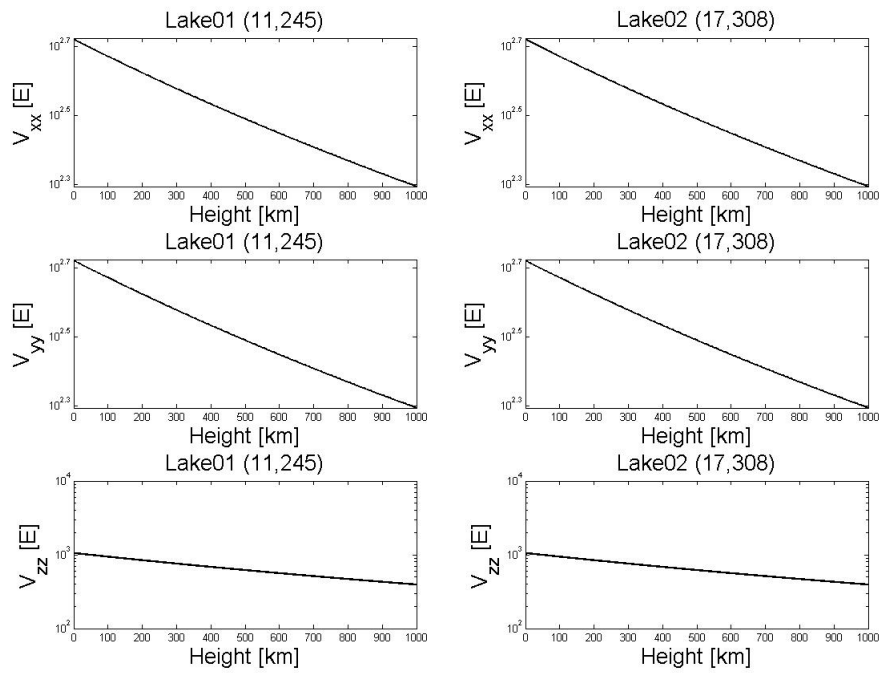


Figure F.15: Diagonal gradients up to an altitude of 1000 km, measured at the middle of lake 01 (left) and lake 02 (right).

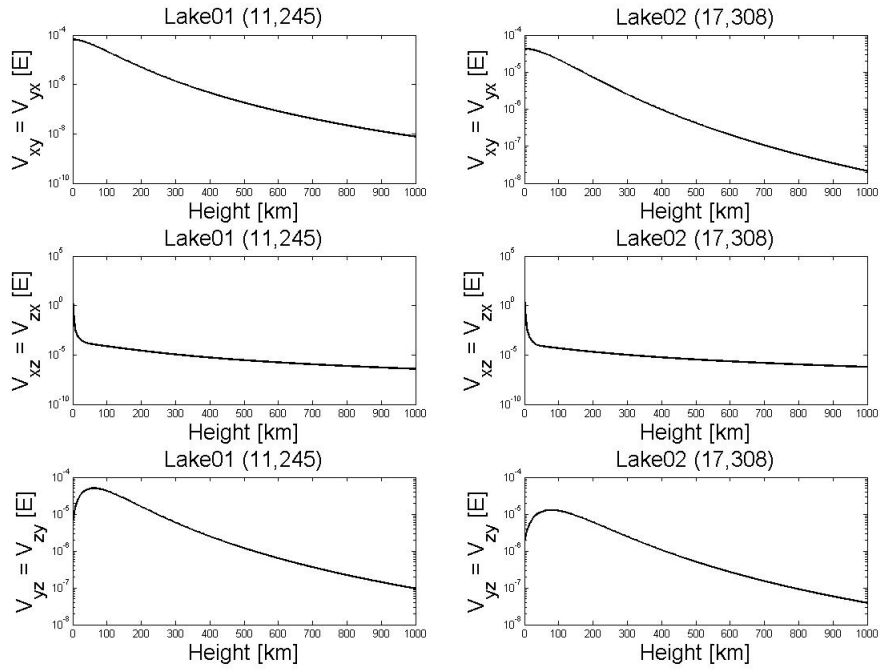


Figure F.16: Off-diagonal gradients up to an altitude of 1000 km, measured at the middle of lake 01 (left) and lake 02 (right).

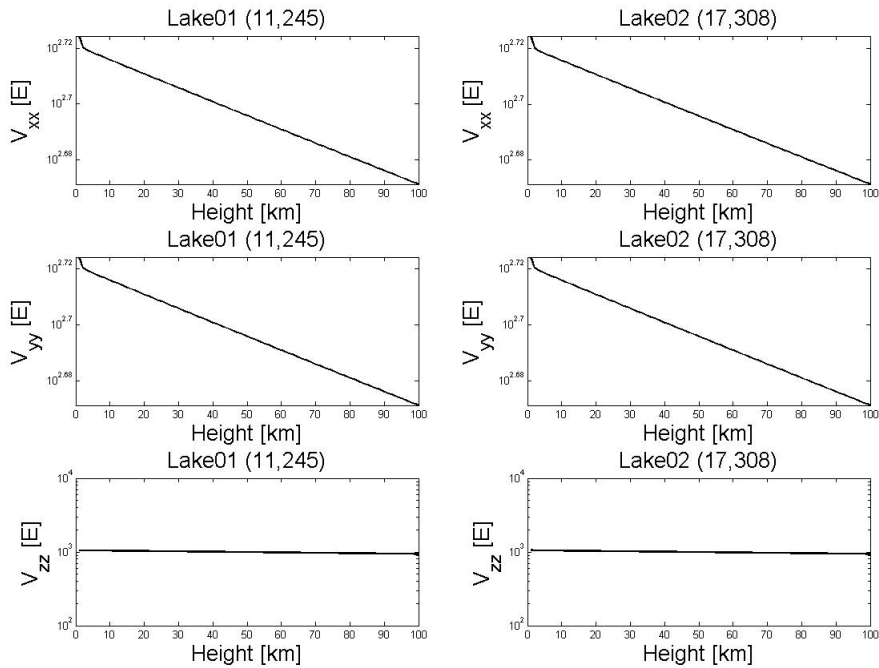


Figure F.17: Diagonal gradients up to an altitude of 100 km, measured at the middle of lake 01 (left) and lake 02 (right).

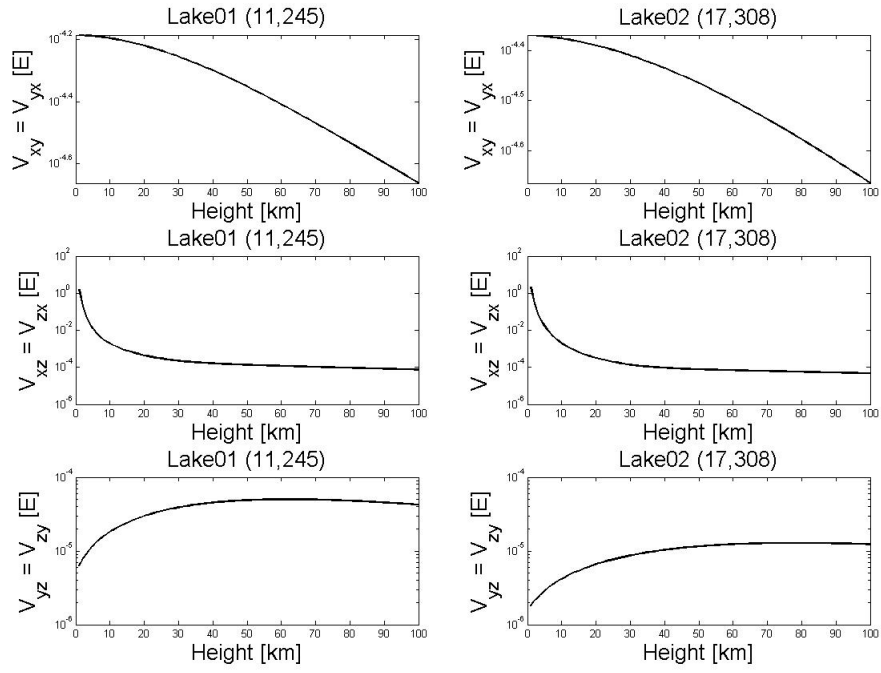


Figure F.18: Off-diagonal gradients up to an altitude of 100 km, measured at the middle of lake 01 (left) and lake 02 (right).

Gradients measured at different balloon altitudes

When looking at the same gradients at a measurement altitude of 10 km only, variations, though relatively small when compared to the gradients at a measurement altitude of 2 km, can be seen. The difference seen in figure F.19 is ~ 0.011 Eötvös for V_{xx} , ~ 0.005 Eötvös for V_{yy} and ~ 0.0015 Eötvös for V_{zz} .

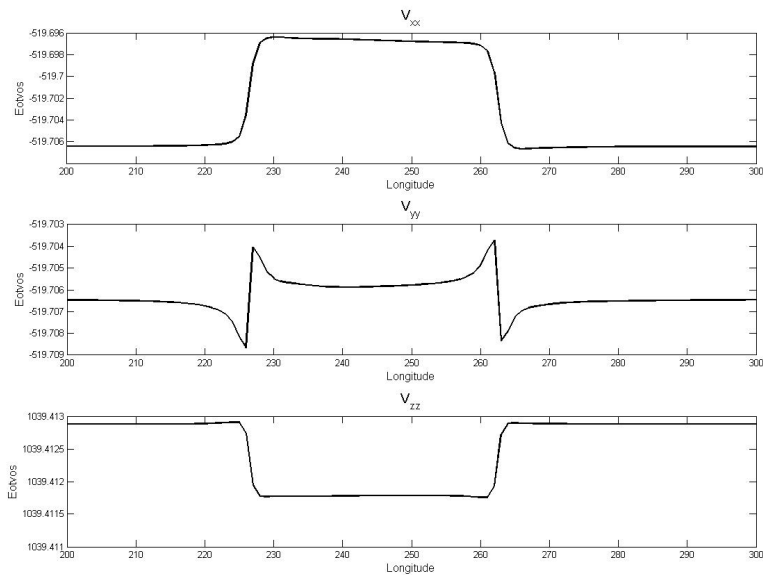


Figure F.19: The diagonal gradients along a trajectory following 79°N at a measurement altitude of 10 km, lake 01 only. The density of the lake is 547 kg/m^3 .

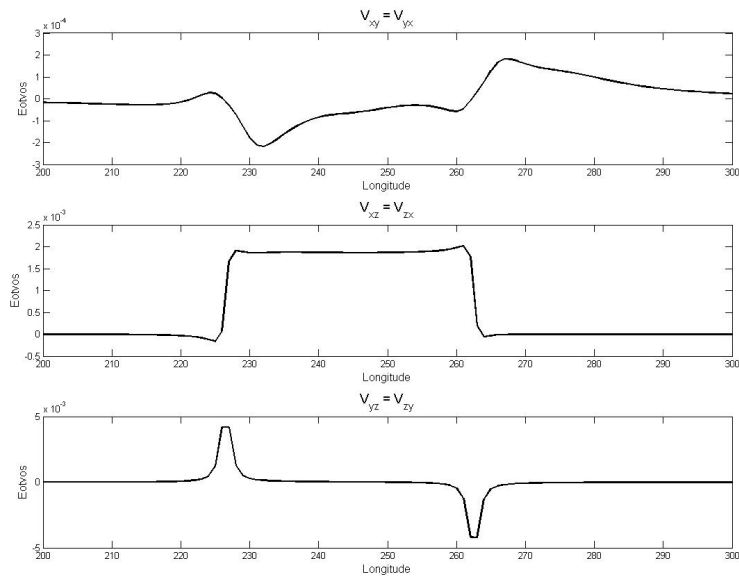


Figure F.20: The off-diagonal gradients along a trajectory following 79°N at a measurement altitude of 10 km, lake 01 only. The density of the lake is 547 kg/m^3 .

Fluctuations in the gradients of Titan

Features with an amplitude of 10^{-23} Eötvös were visible in the simulation of the gradients of Titan after the transformation of the Titan-centered reference system to the local north-oriented reference system. Here it is shown that these fluctuations have no influence on the simulated total diagonal gradients of lake 01.

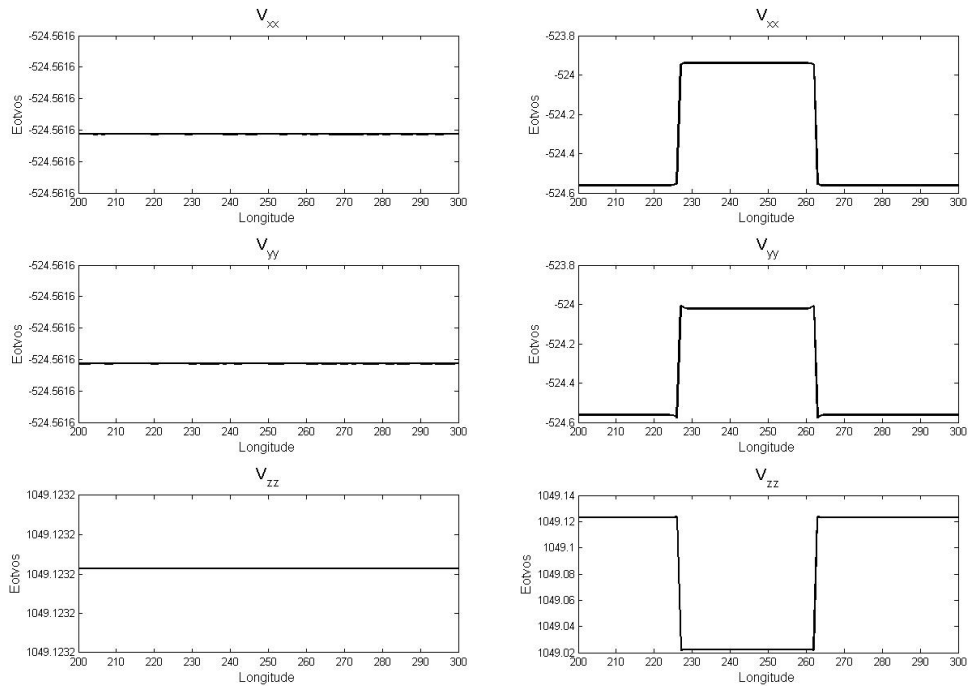


Figure F.21: The diagonal gradients of Titan (left) and superimposed with the gradients of lake 01 (right) along a trajectory at 79°N , an altitude of 2 km above the surface and a lake density of 547 kg/m^3 .

The trajectories plotted in 2D

The trajectories are plotted along longitude. To reduce the amount of information, two different plots are made, one of 63° – 72° and one of 74° – 85° .

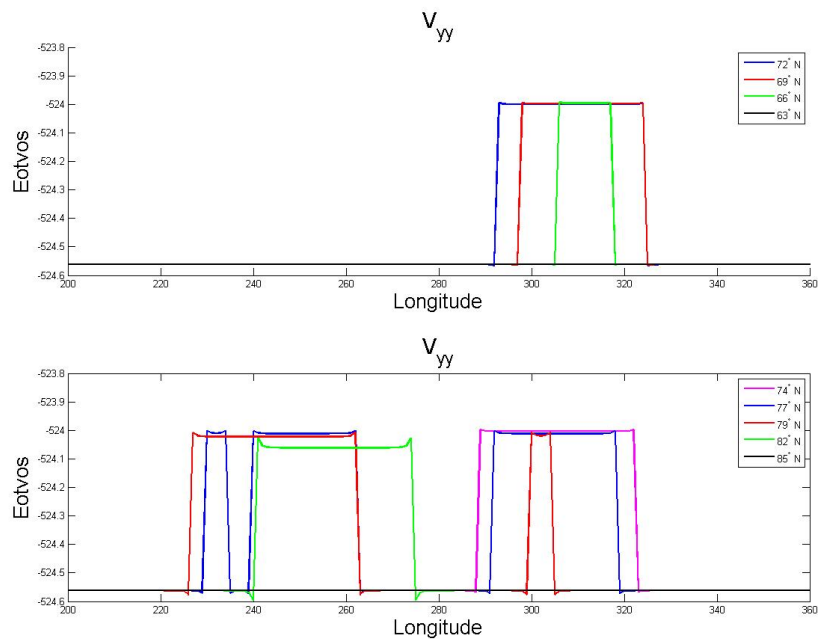


Figure E.22: The gradient V_{yy} along different trajectories from 63° to 85° N plotted in a two dimensional way, at a measurement altitude of 2 km above the surface and a lake density of 547 kg/m^3 .

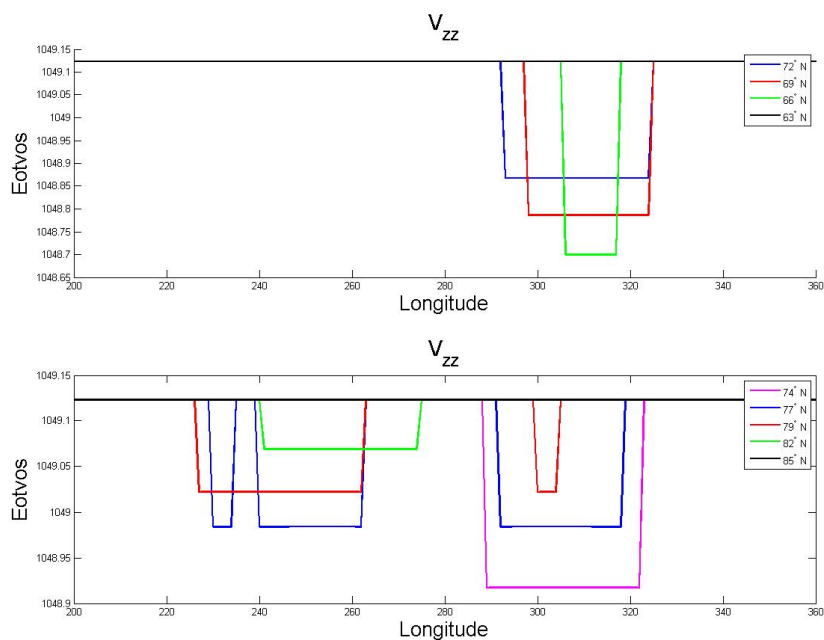


Figure E.23: The gradient V_{zz} along different trajectories from 63° to 85° N plotted in a two dimensional way, at a measurement altitude of 2 km above the surface and a lake density of 547 kg/m^3 .

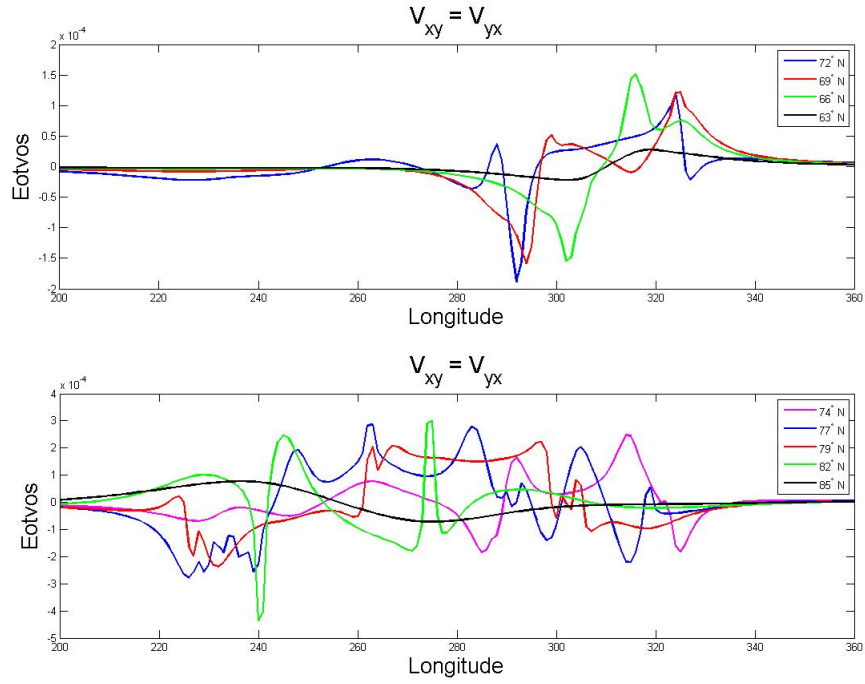


Figure F.24: The gradient V_{xy} along different trajectories from 63° to 85° N plotted in a two dimensional way, at a measurement altitude of 2 km above the surface and a lake density of 547 kg/m^3 .

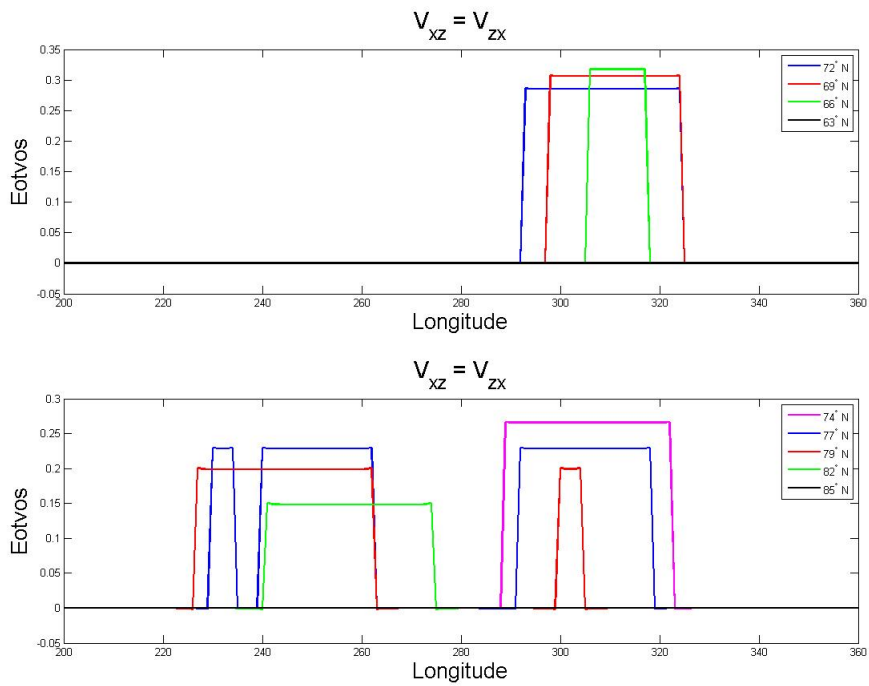


Figure F.25: The gradient V_{xz} along different trajectories from 63° to 85° N plotted in a two dimensional way, at a measurement altitude of 2 km above the surface and a lake density of 547 kg/m^3 .

The trajectories plotted in 3D

The measurements done for the two dimensional case are combined in a three dimensional plot.

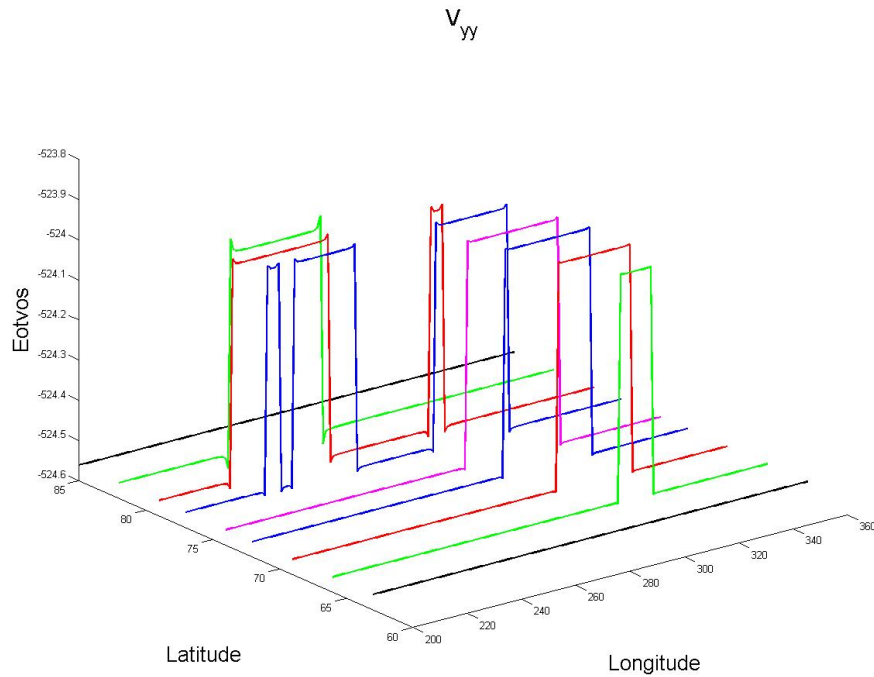


Figure E.26: The measured gradient V_{yy} along nine different trajectories plotted in a three dimensional way, at a measurement altitude of 2 km above the surface and a density of 547 kg/m^3 .

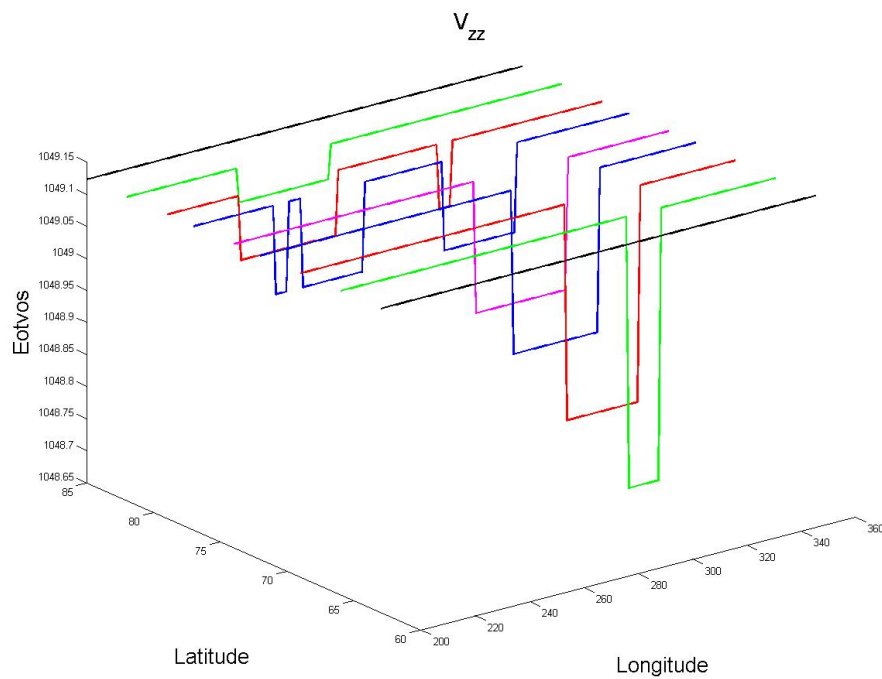


Figure E.27: The measured gradient V_{zz} along nine different trajectories plotted in a three dimensional way, at a measurement altitude of 2 km above the surface and a density of 547 kg/m^3 .

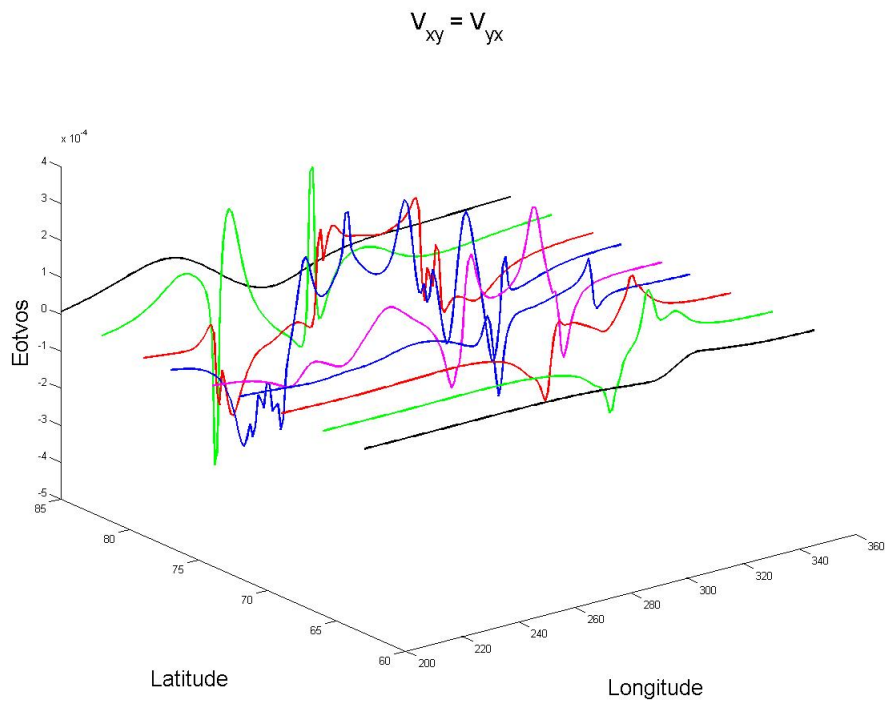


Figure F.28: The measured gradient V_{xy} along nine different trajectories plotted in a three dimensional way, at a measurement altitude of 2 km above the surface and a density of 547 kg/m^3 .

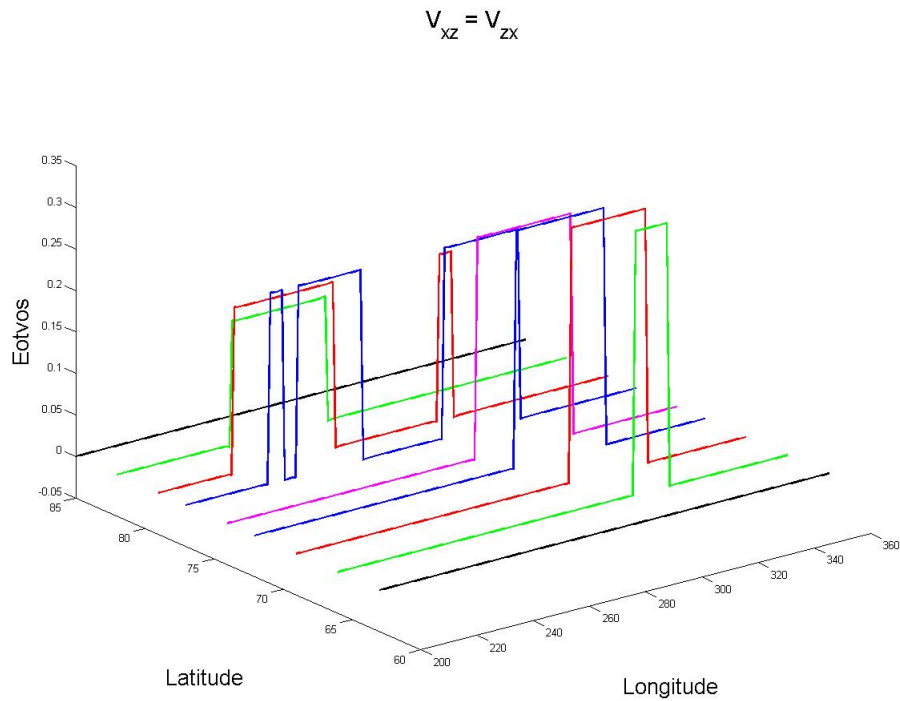


Figure F.29: The measured gradient V_{xz} along nine different trajectories plotted in a three dimensional way, at a measurement altitude of 2 km above the surface and a density of 547 kg/m^3 .

$$V_{yz} = V_{zy}$$

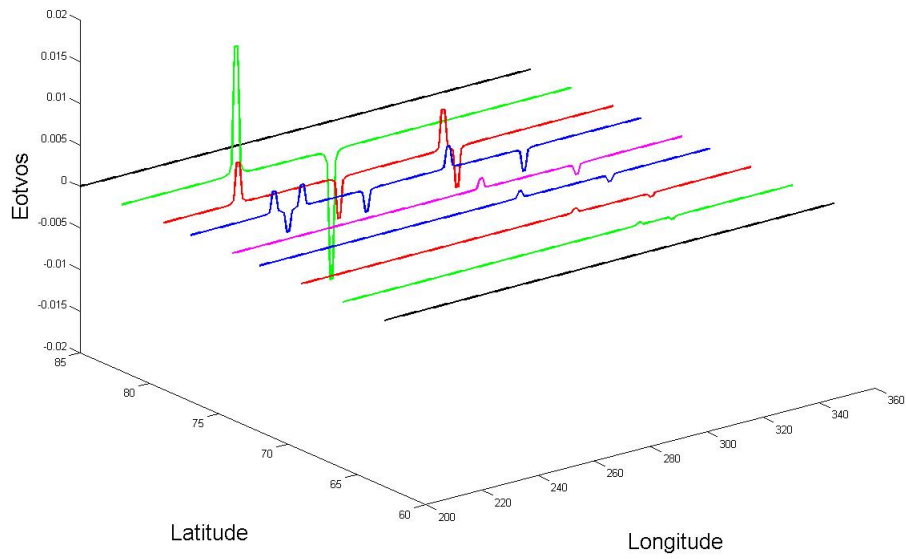


Figure E.30: The measured gradient V_{yz} along nine different trajectories plotted in a three dimensional way, at a measurement altitude of 2 km above the surface and a density of 547 kg/m^3 .

Influence of different densities

To show the influence of different densities on the measurements, different lake–densities are used in the simulation. The lake densities used are given in table 2.4, which are the density and composition of the two mixtures as suggested in [48], the density of pure methane and the density of pure ethane.

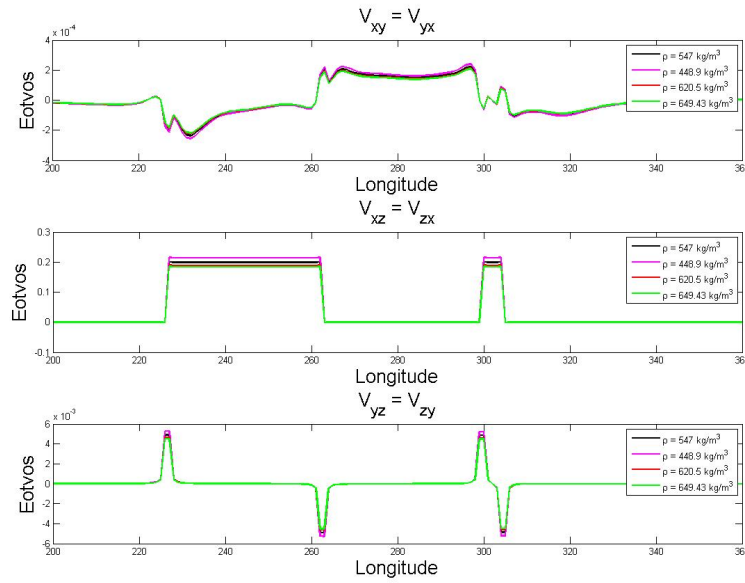


Figure F31: The off–diagonal gradients for different lake–densities. The measurements are taken along a trajectory at 79°N, an altitude of 2 km above the surface.

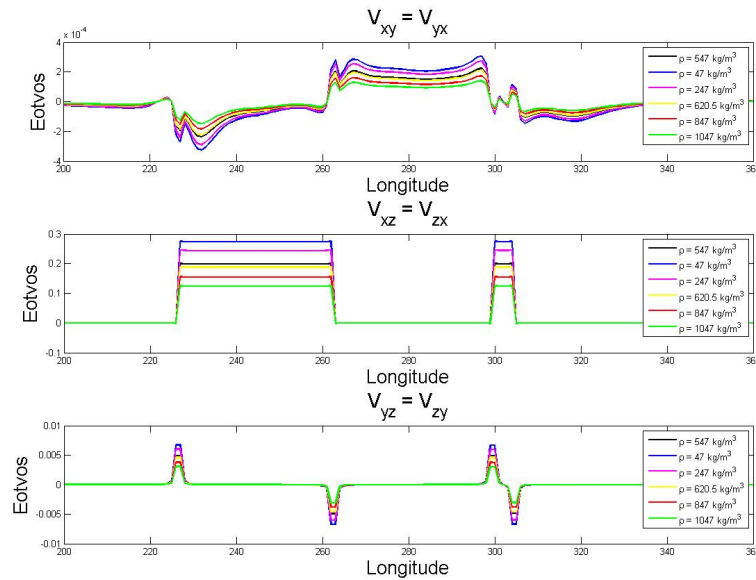


Figure F32: The off–diagonal gradients for different lake–densities. The measurements are taken along a trajectory at 79°N, an altitude of 2 km above the surface.

Gradients due to subsurface lakes

Figures 6.22 and 6.23 compare the gradients from deeper located lakes with the gradients of a surface lake at a measurement altitude of 2 km. When plotting the gradients due to a lake located at a depth of 10 km, still a small variation can be seen, see figures F.33 and F.34.

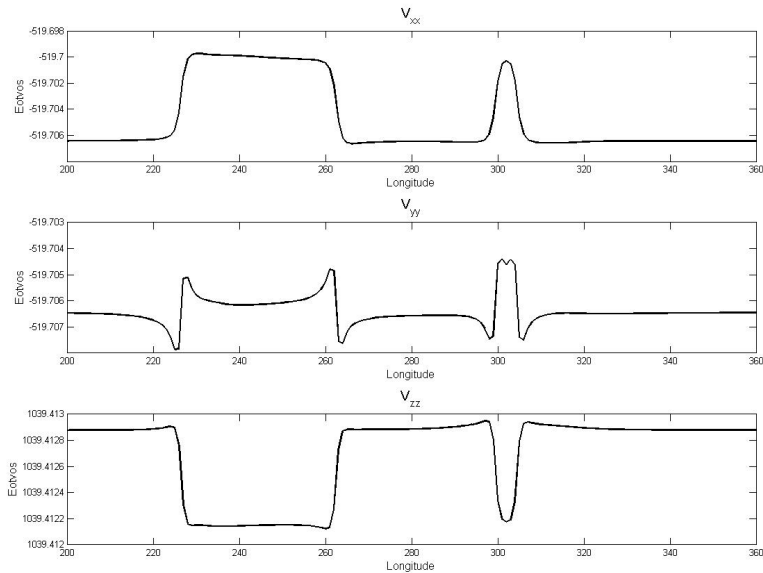


Figure F.33: The diagonal gradients for sub-surface lakes at a distance of 10 km underneath the surface of Titan. The measurements are taken along a trajectory at 79°N , an altitude of 2 km above the surface and using a density of 547 kg/m^3 .

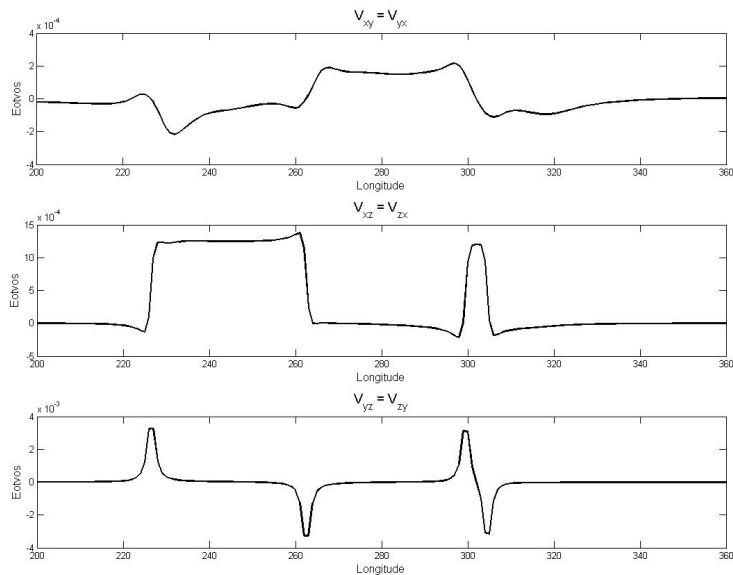


Figure F.34: The off-diagonal gradients for sub-surface lakes at a distance of 10 km underneath the surface of Titan. The measurements are taken along a trajectory at 79°N , an altitude of 2 km above the surface and using a density of 547 kg/m^3 .

Computed layer density of the lakes and variance of the observations

Least squares solution for the niine observation sets

A simple rule of thumb is used in order see if the measurements done have a high enough accuracy. This rule of thumb gives that the density computed using the least-squares method is larger than three times the variance found:

$$\mu \geq 3\sigma_{\mu} \quad \Rightarrow \quad \frac{3\sigma_{\mu}}{\mu} \leq 1$$

The result which is computed using the least-squares method (equation 6.14) is the difference in density ($\Delta\mu$) as explained in equation 5.3. Thus the density of the lake is computed as:

$$\mu_{lake} = \Delta\mu + \bar{\mu}_{Titan}$$

Table G.1: The density and variance [kg/m²] computed using the least-squares technique. A total gravity gradient noise of 0.17 E/√Hz, 1 E/√Hz and 2.6 E/√Hz are used for the computations.

Observation sets used	Computed density $\hat{\mu}$ [kg/m ²]	$\sigma_{ij} = 0.17 \text{ E}$		$\sigma_{ij} = 1 \text{ E}$		$\sigma_{ij} = 2.6 \text{ E}$	
		$\sigma_{\hat{\mu}}$ [kg/m ²]	$\frac{3\sigma_{\hat{\mu}}}{\hat{\mu}}$	$\sigma_{\hat{\mu}}$ [kg/m ²]	$\frac{3\sigma_{\hat{\mu}}}{\hat{\mu}}$	$\sigma_{\hat{\mu}}$ [kg/m ²]	$\frac{3\sigma_{\hat{\mu}}}{\hat{\mu}}$
<i>Measurement set 1: 79°N, 2 km</i>							
Full tensor	547	40.4	0.091	238	0.534	618	1.39
Half tensor	547	41.5	0.093	244	0.549	634	1.43
Diagonals only	547	42.6	0.096	251	0.564	652	1.47
V _{xx} only	547	57.0	0.128	335	0.753	871	1.96
V _{yy} only	547	65.4	0.147	385	0.866	1001	2.25
V _{zz} only	547	351	0.790	2065	4.64	5370	12.1
<i>Measurement set 2: 79°N, 6 km</i>							
Full tensor	547	1021	2.30	6007	13.5	15617	35.1
Half tensor	547	1047	2.35	6158	13.8	16011	36.0
Diagonals only	547	1075	2.42	6321	14.2	16435	37.0

Continued on next page

TableG.1 – continued from previous page

Observation sets used	Computed density $\hat{\rho}$ [kg/m ²]	$\sigma_{ij} = 0.17 \text{ E}$		$\sigma_{ij} = 1 \text{ E}$		$\sigma_{ij} = 2.6 \text{ E}$	
		$\sigma_{\hat{\rho}}$ [kg/m ²]	$\frac{3\sigma_{\hat{\rho}}}{\hat{\rho}}$	$\sigma_{\hat{\rho}}$ [kg/m ²]	$\frac{3\sigma_{\hat{\rho}}}{\hat{\rho}}$	$\sigma_{\hat{\rho}}$ [kg/m ²]	$\frac{3\sigma_{\hat{\rho}}}{\hat{\rho}}$
V_{xx} only	547	1139	2.56	6700	15.0	17419	39.2
V_{yy} only	547	3473	7.81	20429	45.9	53116	119.5
V_{zz} only	547	9059	20.4	53288	120	138550	311.6
<i>Measurement set 3: 77°N, 2 km</i>							
Full tensor	547	33.7	0.076	198	0.445	515	1.16
Half tensor	547	34.8	0.078	205	0.46	532	1.20
Diagonals only	547	36.0	0.081	212	0.476	551	1.24
V_{xx} only	547	48.5	0.109	285	0.642	742	1.67
V_{yy} only	547	55.4	0.125	326	0.733	848	1.91
V_{zz} only	547	220	0.494	1292	2.91	3360	7.56
<i>Measurement set 4: 77°N, 6 km</i>							
Full tensor	547	903	2.03	5312	11.9	13811	31.1
Half tensor	547	931	2.09	5475	12.3	14235	32.0
Diagonals only	547	961	2.16	5654	12.7	14699	33.1
V_{xx} only	547	1062	2.39	6250	14.1	16251	36.5
V_{yy} only	547	2440	5.49	14355	32.3	37322	83.9
V_{zz} only	547	5882	13.2	34598	77.8	89955	202
<i>Measurement set 5: 79°N, 2 and 6 km</i>							
Full tensor	547	40.4	0.091	237	0.534	617	1.39
Half tensor	547	41.4	0.093	244	0.548	634	1.43
Diagonals only	547	42.6	0.096	251	0.564	652	1.47
V_{xx} only	547	56.9	0.128	335	0.753	870	1.96
V_{yy} only	547	65.4	0.127	385	0.866	1001	2.25
V_{zz} only	547	351	0.789	2064	2.46	5366	12.1
<i>Measurement set 6: 79°N and 77°N, 2 km</i>							
Full tensor	547	25.9	0.058	152	0.342	396	0.889
Half tensor	547	26.6	0.060	157	0.353	407	0.916
Diagonals only	547	27.5	0.062	162	0.364	421	0.946
V_{xx} only	547	36.9	0.083	217	0.489	565	1.27
V_{yy} only	547	42.3	0.095	249	0.560	647	1.45
V_{zz} only	547	186	0.419	1096	2.46	2849	6.41
<i>Measurement set 7: 79°N, 2 km and 77°N, 6 km</i>							
Full tensor	547	40.3	0.091	237	0.534	618	1.39
Half tensor	547	41.4	0.093	244	0.548	634	1.42

Continued on next page

TableG.1 – continued from previous page

Observation sets used	Computed density $\hat{\rho}$ [kg/m ²]	$\sigma_{ij} = 0.17 \text{ E}$		$\sigma_{ij} = 1 \text{ E}$		$\sigma_{ij} = 2.6 \text{ E}$	
		$\sigma_{\hat{\rho}}$ [kg/m ²]	$\frac{3\sigma_{\hat{\rho}}}{\hat{\rho}}$	$\sigma_{\hat{\rho}}$ [kg/m ²]	$\frac{3\sigma_{\hat{\rho}}}{\hat{\rho}}$	$\sigma_{\hat{\rho}}$ [kg/m ²]	$\frac{3\sigma_{\hat{\rho}}}{\hat{\rho}}$
Diagonals only	547	42.6	0.096	251	0.564	652	1.47
V _{xx} only	547	56.9	0.128	335	0.752	870	1.96
V _{yy} only	547	65.4	0.147	385	0.865	1000	2.25
V _{zz} only	547	351	0.788	2062	4.637	5360	12.1
<i>Measurement set 8: 79°N, 2 km, 6 km and 77°N, 2 km</i>							
Full tensor	547	25.8	0.058	152	0.342	395	0.889
Half tensor	547	26.6	0.060	157	0.352	407	0.916
Diagonals only	547	27.5	0.062	162	0.364	421	0.946
V _{xx} only	547	36.9	0.083	217	0.488	564	1.27
V _{yy} only	547	42.3	0.095	249	0.560	647	1.45
V _{zz} only	547	186	0.419	1095	2.46	2848	6.40
<i>Measurement set 9: 79°N, 2 km, 6 km and 77°N, 2 km, 6 km</i>							
Full tensor	547	25.8	0.058	152	0.342	395	0.889
Half tensor	547	26.6	0.060	157	0.352	407	0.916
Diagonals only	547	27.5	0.062	162	0.364	420	0.946
V _{xx} only	547	36.9	0.083	217	0.488	564	1.27
V _{yy} only	547	42.3	0.095	249	0.559	647	1.45
V _{zz} only	547	186	0.419	1095	2.46	2847	6.40

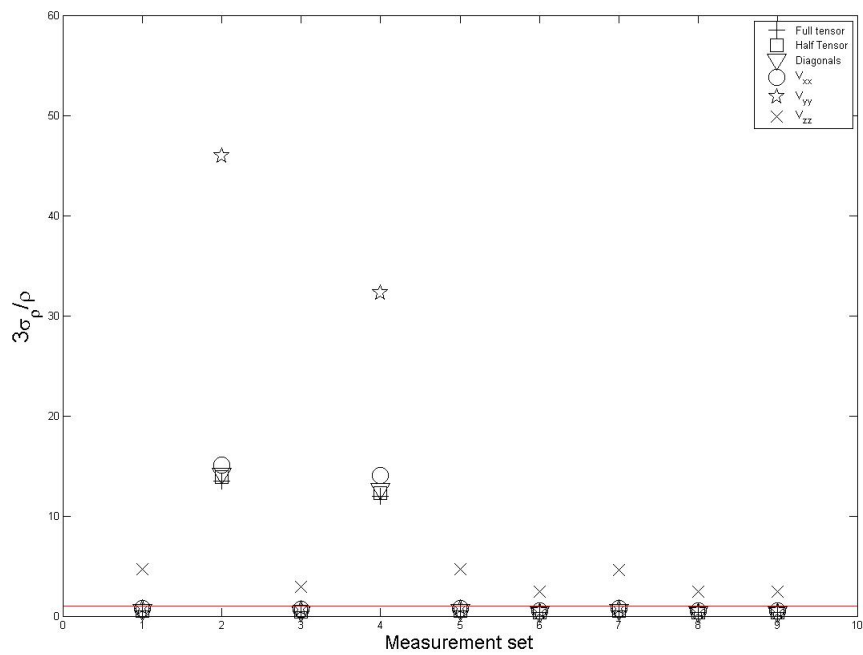


Figure G.1: The results of the least-squares estimation for nine different observation sets, $\sigma_{ij} = 1$ Eötvös. The configurations indicated below the red line comply with the rule of thumb given by equation 6.16.

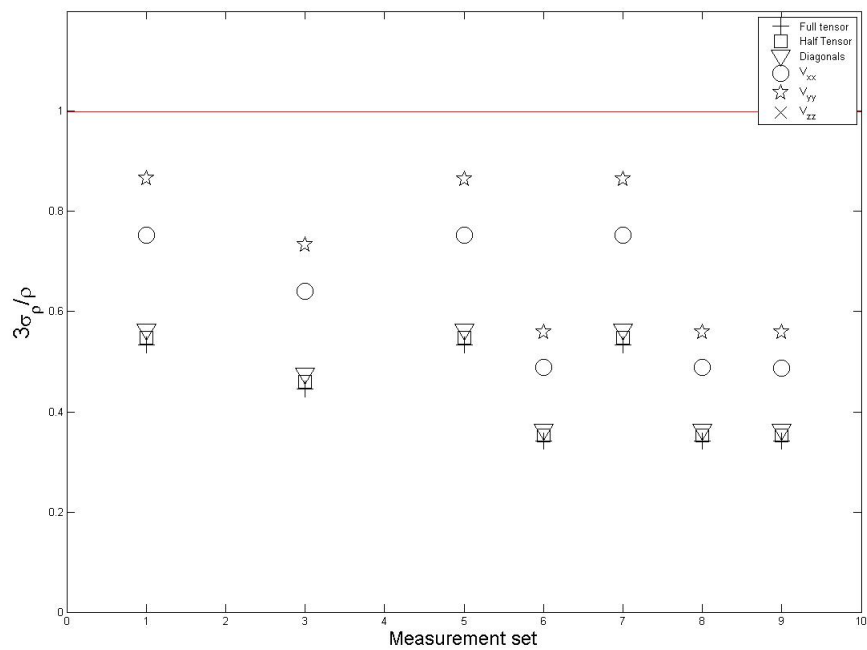


Figure G.2: The results of the least-squares estimation zoomed in on the part below the red line, $\sigma_{ij} = 1$ Eötvös.

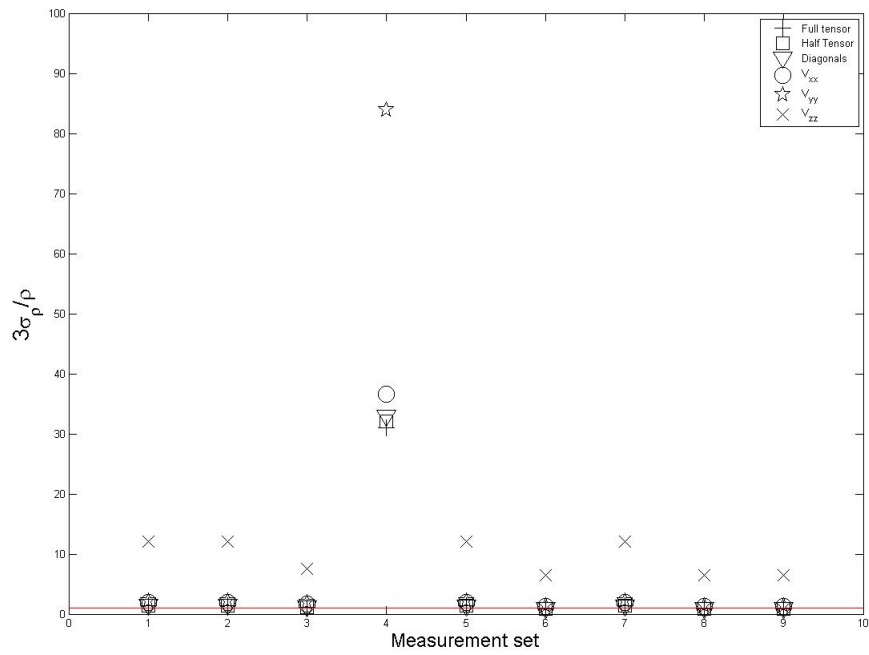


Figure G.3: The results of the least-squares estimation for nine different observation sets, $\sigma_{ij} = 2.6$ Eötvös. The configurations indicated below the red line comply with the rule of thumb given by equation 6.16.

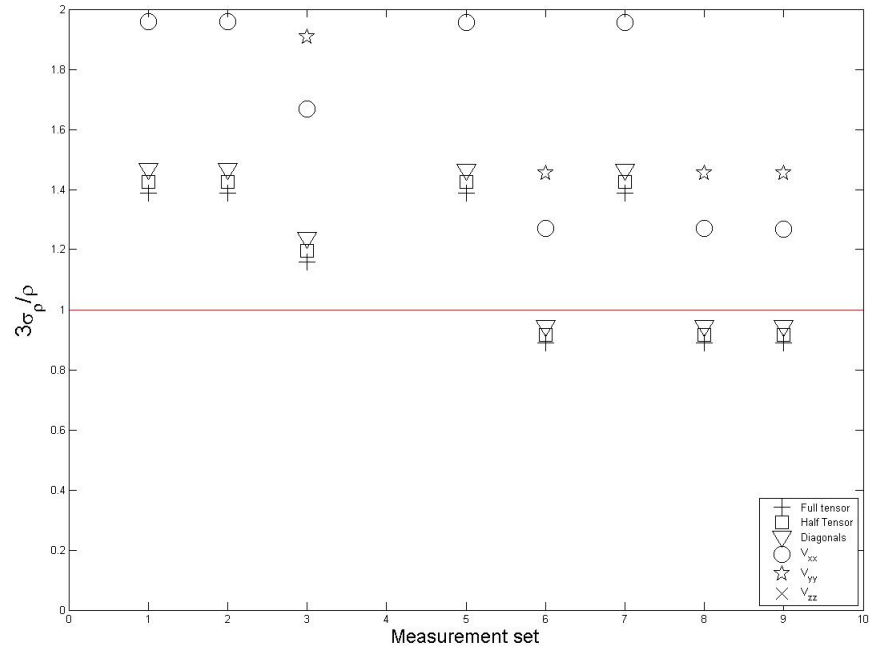


Figure G.4: The results of the least-squares estimation zoomed in on the part below the red line, $\sigma_{ij} = 2.6$ Eötvös.